Various aspects of quantum transport through single molecules
Amechanical break-junction study

Stefani, Davide

DOI
10.4233/uuid:f6120a10-0a29-43f8-b900-bb62c856e74b

Publication date
2019

Document Version
Final published version

Citation (APA)
Stefani, D. (2019). *Various aspects of quantum transport through single molecules: Amechanical break-junction study*. [Dissertation (TU Delft), Delft University of Technology].
https://doi.org/10.4233/uuid:f6120a10-0a29-43f8-b900-bb62c856e74b

Important note
To cite this publication, please use the final published version (if applicable).
Please check the document version above.

VARIOUS ASPECTS OF QUANTUM TRANSPORT THROUGH SINGLE MOLECULES

A MECHANICAL BREAK-JUNCTION STUDY

VARIOUS ASPECTS OF QUANTUM TRANSPORT THROUGH SINGLE MOLECULES

A MECHANICAL BREAK-JUNCTION STUDY

Dissertation

for the purpose of obtaining the degree of doctor
at Delft University of Technology
by the authority of the Rector Magnificus prof. dr. ir. T.H.J.J. van der Hagen
chair of the Board for Doctorates
to be defended publicly on
Tuesday 23 April 2019 at 15:00 o'clock

by

Davide STEFANI

Master of Science in Physics, Università degli Studi di Padova, Italy,
born in Vicenza, Italy.

This dissertation has been approved by the promotors.

Composition of the doctoral committee:

Rector Magnificus,	Chairperson
Prof. dr. ir. H.S.J. van der Zant,	Delft University of Technology, promotor
Prof. dr. M. Mayor,	University of Basel, Switzerland, promotor
Independent members:	
Prof. dr. N. Agraït,	Universidad Autónoma de Madrid, Spain
Prof. dr. T. Albrecht,	University of Birmingham, United Kingdom
Prof. dr. P.C. Steeneken,	Delft University of Technology
Dr. J. M. Thijssen,	Delft University of Technology
Dr. ir. M.L. Perrin,	Swiss Federal Laboratories for Materials Science and Technology, Switzerland
Prof. dr. Y.M. Blanter,	Delft University of Technology, reserve member

Keywords: single-molecule, charge transport, mechanically controllable break-junction, quantum interference, biomolecules, nanotechnology

Printed by: Gildeprint, Enschede

Cover: Artistic representation of a single-molecule junctions. Art and design by D. Stefani.

Casimir PhD Series, Delft-Leiden 2019-20

ISBN 978-90-8593-396-0

An electronic version of this dissertation is available at
http://repository.tudelft.nl/.

Al Marco e ai miei nonni

Contents

Summary

This dissertation concerns transport measurements in single-molecule junctions using the mechanically controlled break junction (MCBJ) technique. It describes various aspects that play a role in charge transport through single molecules, in order to develop the necessary knowledge to ultimately develop electronic devices based on intrinsic molecular functionality.

In chapter 1 we give a short introduction to molecular electronics. We briefly recall the first steps of the field and compare the principal techniques that drive it. We then mention the most important aspects needed to understand transport at the nanoscale and provide a toy model to describe it. Finally, we introduce the experimental setup and fabrication of the samples used during the measurements.

Chapter 2 introduces the measurement protocols and basic data analysis of MCBJ experiments, and offers an insight into the amount of information that can be extracted from a relatively simple system. The model system of our choice is an oligo(phenylene-ethynylene) consisting of three rings (OPE3 in short), which represents a paradigmatic model system for molecular-scale electronics. By probing thousands of single-molecule junctions in different conditions, we show that their creation involves independent events justifying the statistical tools that are used. By combining room- and low-temperature experiments, we estimate the level alignment and the electronic couplings to the leads using the single-level model and show that the dominant transport mechanism for electrons through the OPE3 molecule is off-resonant tunneling.

Chapter 3 shows the role of the anchoring configurations in single-molecule junctions. The conductance histogram of a C_{60}-diazafluorene molecule exhibits three conductance peaks which are related to three binding modes of the diazafluorene anchoring groups to the gold electrodes. Density functional theory calculations confirm the existence of multiple binding configurations and the calculated transmission functions are consistent with experimentally determined conductance values. These results reveal that the binding geometry can have a large impact on the molecular conductance, and appropriate anchoring groups should be accordingly selected.

Chapter 4 presents how a clever molecular design allows us to manipulate the electronic properties of a molecule by tuning quantum interference effects. The possibility of inducing changes in the orbital structure through external stimuli can provide functionality on the single-molecule level that can be employed for sensing or switching purposes if the associated conductance changes are sizable upon application of the stimuli. Here, we show that the room-temperature conductance of a spring-like molecule can be mechanically controlled up to an order of magnitude by compressing or elongating it. Quantum-chemistry calculations indicate that the large conductance variations are the result of destructive quantum interference effects between the frontier orbitals that can be lifted by applying either compressive or tensile strain to the molecule. When periodically modulating the electrode separation, a conductance modulation at double the driving frequency is observed, provid-

ing a direct proof for the presence of quantum interference. Furthermore, oscillations in the conductance occur when the stress built up in the molecule is high enough to allow the anchoring groups to move along the surface in a stick-slip-like fashion.

Chapter 5 contains a study of the influence of the environment on the molecular junction, *i.e.*, what happens when we measure molecules in solution. When performed in water rather than in air, measurements of single OPE3 molecules show a lower conductance, higher dispersion and steeper plateau. Preliminary measurements in other polar solvents show a similar behavior. Density functional theory calculations show that the effects of the water environment cannot be explained with the intuitive description of water as a dielectric continuum. This is because the role of water is not limited to electrostatic interactions, but also includes competing effects on the coupling to the leads, the molecular orbitals, the anchoring dynamic, and the molecular geometry. Knowing the effects of an aqueous environment is important in the prospect of studying molecules that are involved in biological processes, which are naturally found in solution

Chapter 6 presents a study on the length and amino acid composition of peptides and their role on their ability to transport charge. The measurements show that peptides are not good conductors, as they have similar properties to other non-conjugated molecules like alkanes. Many different conductance values are found, which can be related to different metastable configurations of the molecular junction. The results suggest that the ability of some peptides to fold into non-linear configurations might be beneficial to electron transport, as is the presence of tryptophan and cysteine in the chain composition.

Chapter 7 presents preliminary results on four projects that are currently still in progress. The first is an initial approach to characterize the transmission dip of the molecule presented in Chapter 4 by performing measurements at cryogenic temperature. In the second, the role of bulky side groups is investigated in the OPE3 family of molecules. In the third, the influence of anchoring and bulky side groups on the electronic paths is studied on a family of porphyrins. Finally, the topic of molecular switches is touched upon with a section on pseudo-rotaxane molecules.

In appendix A, details are given on the clustering technique that has been employed in some of the chapters and the limitations of the technique are discussed.

SAMENVATTING

Dit proefschrift beschrijft transportmetingen in juncties van individuele moleculen gebruikmakend van de mechanisch regelbare breekjunctie (MCBJ) techniek. Het beschrijft een aantal aspecten die een rol spelen in ladingstransport door individuele moleculen, gericht op het verkrijgen van de noodzakelijke kennis om functionele apparaten te ontwerpen die gebaseerd zijn op intrinsieke moleculaire functionaliteiten.

In hoofdstuk 1 geven we een korte introductie tot het onderzoeksveld van de moleculaire elektronica. We beschrijven in het kort de eerste stappen van het onderzoeksveld en vergelijken de belangrijkste technieken die het drijven. We noemen vervolgens de aspecten die nodig zijn om ladingstransport op de nanoschaal te begrijpen en verstrekken een simpel model om het te beschrijven. Ten slotte introduceren we de experimentele opstelling en de fabricage van de devices die tijdens de metingen werden gebruikt.

Hoofdstuk 2 introduceert de meetprotocollen en data-analyse van MCBJ-experimenten en geeft een idee van de hoeveelheid informatie die kan worden afgeleid uit een relatief eenvoudig systeem. Ons modelsysteem is een oligo(fenyleen-ethynyleen) bestaande uit drie ringen (kortweg OPE3), wat een paradigmatisch modelsysteem voor elektronica op moleculaire schaal vertegenwoordigt. Door duizenden juncties van individuele moleculen in verschillende configuraties te meten, laten we zien dat hun creatie gepaard gaat met onafhankelijke gebeurtenissen die de gebruikte statistische hulpmiddelen rechtvaardigen. Door het combineren van experimenten bij kamertemperatuur en lage temperatuur kunnen we de uitlijning van de energieniveaus en de elektronische koppelingen naar de elektrodes inschatten met behulp van een model met een enkel energieniveau. We tonen aan dat het dominante transportmechanisme voor elektronen door het OPE3-molecuul niet-resonante tunneling is.

Hoofdstuk 3 toont de rol van de verankeringsconfiguraties in juncties van individuele moleculen. Het geleidingshistogram van een C_{60}-diazafluorene molecuul toont drie geleidingspieken die gerelateerd zijn aan drie bindingswijzen van de diazafluoreen-verankeringsgroepen aan de goudelektroden. Dichtheidsfunctionaalberekeningen bevestigen het bestaan van meerdere bindingsconfiguraties en laten zien dat de berekende transmissiefuncties overeenkomen met het experimenteel bepaalde geleidingsvermogen. Deze resultaten tonen aan dat de bindingsgeometrie een enorme impact kan hebben op de moleculaire geleiding, en dat geschikte verankeringsgroepen overeenkomstig moeten worden geselecteerd.

Hoofdstuk 4 laat zien hoe een slim moleculair ontwerp ons in staat stelt om de elektronische eigenschappen van een molecuul te manipuleren door kwantuminterferentie-effecten te variëren. De mogelijkheid om veranderingen in de orbitale structuur teweeg te brengen door externe stimuli kan functionaliteit verschaffen op het niveau van een enkel molecuul dat gebruikt kan worden voor detectie- of schakeldoeleinden als de bijbehorende geleidingsveranderingen aanzienlijk zijn. Hier laten we zien dat het geleidingsvermogen van een verend molecuul bij kamertemperatuur mechanisch tot op een ordegrootte kan worden

geregeld door het samen te drukken of te verlengen. Kwantumchemieberekeningen tonen aan dat de grote geleidingsvariaties het resultaat zijn van destructieve kwantuminterferentie-effecten tussen de buitenste orbitalen die opgeheven kunnen worden door ofwel compressieve druk of trekspanning op het molecuul aan te brengen. Wanneer de afstand tussen de elektroden periodiek wordt gemoduleerd, wordt een conductantiemodulatie waargenomen met een dubbele aandrijffrequentie, waardoor een direct bewijs wordt geleverd voor de aanwezigheid van kwantuminterferentie. Bovendien treden oscillaties in de geleiding op wanneer de spanning die is opgebouwd in het molecuul hoog genoeg is om de verankeringsgroepen op een "stick-slip"-achtige manier langs het oppervlak te laten bewegen.

Hoofdstuk 5 bevat een onderzoek naar de invloed van de omgeving op de moleculaire junctie, namelijk wat er gebeurt als we moleculen in oplossing meten. Metingen van individuele OPE3-moleculen vertonen een lager geleidingsvermogen, hogere dispersie en een steiler plateau indien uitgevoerd in water in plaats van in lucht. Voorlopige metingen in andere polaire oplosmiddelen vertonen een vergelijkbaar gedrag. Dichtheidsfunctionaalberekeningen tonen aan dat de effecten van de wateromgeving niet kunnen worden verklaard met de intuïtieve beschrijving van water als een diëlektrisch continuüm. Dit komt doordat de rol van water niet beperkt is tot elektrostatische interacties, maar ook concurrerende effecten bevat met de koppeling met de elektrodes, de moleculaire orbitalen, de verankeringsdynamiek en de moleculaire geometrie. Het begrijpen van de effecten van een waterhoudende omgeving is belangrijk om moleculen te bestuderen die betrokken zijn bij biologische processen, die van nature in oplossing worden gevonden.

Hoofdstuk 6 presenteert een studie naar de lengte en aminozuursamenstelling van peptiden en hun rol in hun vermogen om lading te transporteren. De metingen tonen aan dat peptiden geen goede geleiders zijn omdat ze vergelijkbare eigenschappen hebben als andere niet-geconjugeerde moleculen zoals alkanen. Er worden veel verschillende geleidingswaarden gevonden die kunnen worden gerelateerd aan verschillende metastabiele configuraties van de moleculaire junctie. De resultaten suggereren dat het vermogen van sommige peptiden om zich in niet-lineaire configuraties te vouwen gunstig kan zijn voor elektronentransport, evenals de aanwezigheid van tryptofaan en cysteïne in de ketensamenstelling.

Hoofdstuk 7 presenteert voorlopige lopende resultaten voor vier projecten. Het eerste project gaat over de karakterisatie van de transmissiedip van het molecuul in Chapter 4 door metingen bij cryogene temperaturen uit te voeren. In het tweede project wordt de rol van zijgroepen op de OPE3-familie van moleculen onderzocht. In het derde deel wordt de invloed van verankering en zijgroepen op elektronische routes bestudeerd in een familie van porfyrines. Ten slotte wordt het onderwerp van moleculaire machines besproken met een sectie over pseudo-rotaxane moleculen.

In appendix A worden meer details gegeven over de clusteringstechniek die in sommige hoofdstukken is gebruikt en worden de beperkingen van de techniek besproken.

PREFACE

Doing experiental physics at the forefront of science is not a walk in the park. Things go wrong all the time and in ways and moments that no one could have predicted. The challenges that one encounters while doing experimental physics are, of course, part of what makes this profession interesting and fun, but they are also something that a physicist should always keep in mind when designing, performing and interpreting experiments.

Molecular electronics is, if possible, an even tougher challenge. Each experiment involves a huge number of variables, only a few of which can be controlled or even measured. In mechanically controlled break junction (MCBJ) experiments, the dynamics of junction formation depends on factors like temperature, wire tension, electric field, adhesion mechanics, local concentration, diffusion rates, and many others. Some of these parameters are fixed, some are not; some of them we can control, some we cannot. This means that there is a huge number of possible outcomes for each breaking event, and our task is, then, to make some sense out of them, which is no easy feat. Because of these limitations, we need to start from simple systems so that we can build some knowledge and then, hopefully, transfer it to more complex scenarios.

Oligo(phenylene-ethynylene) (OPE3) is one of the simplest molecules available and is a great platform to learn molecular electronics with MCBJs. We gained a lot of insight from molecules like this one, and it helped us to build a foundation for the theory of molecular electronics. However, even for this simple system, not all is yet understood and even these 'simple' molecules still hold many mysteries.

Regardless, the drive to go beyond is always there, and it pulls us to take a stab at more complex molecules like proteins. These systems challenge what we thought we understood from the simple models, taking us back to the drawing board and making us question the interpretation of our findings.

This is the endless cycle of science. The cycle through which knowledge is built and progress is made. Trending towards a more accurate 'truth'. This cycle never stops, but it is particularly fast and devastating when a field is not yet mature. Molecular electronics is still at this stage, so much so that even replicating experimental results is not straightforward. For this reason, claims should always be made with caution and taken with a grain of salt, because the temptation of confirmation bias can help to establish (wrong) beliefs which delay the advances of the field.

This thesis may not be groundbreaking, but I hope that it can be a cobble, placed in a useful spot, that scientists of the future generation can build on. Just a piece of the puzzle that will someday show a clearer picture. So to you who have been so kind to read these words, I offer this work hoping it can be of some help.

Davide Stefani
Paris, December 19, 2018

1

INTRODUCTION

In this chapter we give a short introduction to molecular electronics. We briefly recall the first steps of the field and compare the principal techniques that drive it. We then mention the most important aspects needed to understand transport at the nanoscale and provide a toy model to describe it. Finally, we introduce the experimental setup and fabrication of the samples used during the measurements.

1

1.1. Molecular electronics

The field of molecular electronics was initially born as the ultimate terminus of Moore's law. In the pursuit of miniaturization of electrical components, it is inevitable that a limit is eventually going to be reached, and this will happen when electronic components consist of a single element. Molecules are the smallest units that preserve the chemical properties of a certain substance, therefore they represent the natural limit for the size of electrical components. This thought gave the impulse to build devices based on the functionality of a few (or even a single) molecules.

The first proof of principle for molecular-scale electronics can be found in the experiment of Hans Kuhn on the tunneling of electrons through monolayers of fatty acid salt [1]. This experiment inspired Ratner and Aviram to propose their famous unimolecular diode, which started and gave the first fuel to the field [2]. In the following years, scientists developed different ways of contacting molecules [3] and, using the properties of organic molecules, it was possible to replicate electronic components, observing diode-like (rectification, and negative differential conductance) [4–6], transistor [7–9], and different kinds of switching behaviours in molecular junctions [10, 11]. Despite all the discoveries and advances achieved since then, the recent improvements in silicon-based technology allowed to create components with smallest parts having a size as little as 5 nm – the same order of magnitude of single molcules [12, 13]. Since the investment in the silicon industry incomparably outclasses that put into single-molecule technologies, the engineering gap between the two technologies is most likely never going to be filled.

Even though its application in present-day technology is limited, molecular electronics, because of the small sizes involved, offers the possibility to investigate charge and heat transport at a scale where physics is dominated by quantum mechanics, even at room temperature [14, 15]. The great variety of electrical, mechanical and optical properties of molecules can give rise to interesting new physical phenomena, which makes molecular electronics a very attractive field of basic research. Thanks to the highly developed tools of molecular synthesis, transport, binding, optical, and structural properties of molecules can be finely tuned to obtain the desired functionality. Moreover, a deeper understanding of the fundamental mechanisms that govern electronic transport at the nanoscale will be crucial for the integration of molecular electronics into future technology. Special properties of organic molecules can lead to electronic functionalities that are not available to conventional solid-state devices, thus giving molecular electronics some major advantages over silicon-based technology [16]. For example, the electronic behaviour of a device can be modified via molecular recognition (by the presence of a specific molecule), providing both switching and sensing capabilities at the single-molecule scale.

1.2. Molecular devices

In the first molecular devices, molecules were investigated in ensembles. This is a powerful and still widely used method, in particular for molecules that are poor conductors and cannot be studied in a single-molecule device [17, 18]. This approach exploits one of the unique properties of molecules with a certain chemistry, *i.e.* their ability to self-assemble into an ordered monolayer film when they are deposited on the right surface. The measurements of self-assembled monolayers in eutectic GaIn junctions are an example of such a

technique [19, 20]. However, the possible presence of collective effects makes it difficult to deconvolute the intrinsic properties of the individual molecules [21]. This makes this approach less ideal for fundamental studies, but the high reliability of these junctions makes them very promising candidates for applications in technological devices.

The techniques employed to study single molecules can be divided into two main classes [15, 22–24]. The first employs fixed electrodes, which results in junctions that are very stable and particularly well suited for studies at varying temperature and magnetic field. One of the most noticeable in this class is the electromigration technique [25–27]. Because the electrodes are in direct contact with the substrate, it is relatively straightforward to add a third electrode for gating purposes, allowing to mimic experiments performed on solid-state devices. With these tools it was possible to study phenomena like Coulomb blockade [7], Kondo effect [28, 29], Franck–Condon blockade [30], vibrational excitations [31–33], and electronic excitations [34]. The main drawbacks of this technique are the low junction yield (the probability of having a single molecule bridging the electrodes), which makes the acquisition of large statistical data sets impractical, and the limited control over the electrode geometry, which means that the exact junction configuration is largely unknown.

The second class of techniques for single-molecule studies utilizes devices with moving electrodes. Thanks to their flexibility, many junctions can be repeatedly formed using the same electrodes, which results in the possibility of gathering statistical information on the molecule. The price to pay for this flexibility is the lower stability and shorter lifetime of the junctions. The two principal approaches in this class are the Scanning Tunneling Microscope Break Junctions (STM-BJ) technique and the Mechanically Controlled Break Junctions (MCBJ) technique.

The main advantages of the STM-BJ are its speed, versatility and commercial availability [35]. In this technique one electrode is a sharp tip, whereas the other is a metallic surface. The asymmetry in the geometry makes it easier to measure in asymmetric conditions, *e.g.*, in presence of a temperature gradient or having different materials for the tip and the substrate [36, 37]. Moreover, in this technique it is possible to image the surface of the substrate to obtain information on its cleanliness and it is easier to passivate the tip for measurements in polar solutions and with electrochemical gating [38–42]. Electrochemical way of gating is particularly interesting because it promises, in principle, to have 100% gating efficiency from the applied electrochemical potential to the energy level shift of the electrodes [43].

In the MCBJ technique [44, 45], on the other hand, two sharp tips are used as electrodes in a more symmetrical geometry. These can be obtained following two main approaches: the notched-wire MCBJs and the lithographic MCBJs. MCBJs utilize a flexible substrate to transform the vertical displacement of a pushing rod into the horizontal separation of the electrodes. Becaues of their geometry, these devices have a built-in reduction of the pushing rod vs. electrode displacement. This grants a higher mechanical stability, yielding junction lifetimes of many hours even at room temperature, and higher accuracy on the positioning of the electrodes compared to STM-BJ, at the cost of lower actuation speed. However, because of the suspended bridge geometry, gating is more challenging, but was achieved both with solid-state [46–49] and electrochemical gating [41, 50]. Finally, it is possible to combine the MCBJ technique with gap-mode Raman spectroscopy to track *in-situ* the molecular junction formation while performing charge transport measurements [51].

Metals and superconductors are the main materials employed in the electrodes, however, graphene has made an important appearance in molecular devices as well [52–54]. Due to its unique electrical and optical properties, graphene offers an attractive platform to study new effects in molecular junction, like optical tuning of the electrode properties [55]. Moreover, the extremely small thickness of graphene has been employed in DNA sequencing through nanopore recognition [56, 57].

Despite the tremendous progress that has been achieved in recent years, single-molecule devices still struggle to have robust and reliable contacting mechanisms and reproducibility is still not taken for granted [58]. The lack of direct imaging of the molecular junction in the BJ techniques makes it hard to identify if the electrodes are bridged by a single target molecule, by multiple molecules, or by some contaminant or metallic grain that could mimic the electrical behaviour of a molecule. This brought some controversy about the switching behaviour observed in rotaxane molecules [59] because it was later shown that it could also arise from the metal electrodes alone or the metal-molecule interface [60]. Since the properties of molecules can only be infered through indirect measurements, it is crucial that the phenomena are observed consistently and analysed with robust stastical tools.

In this thesis, I will approach this realm by investigating the various aspects that play a role in charge transport throught single molecules: internal orbital structure, anchoring groups, junction configuration, local environment, bulky side groups, *etc*. I will start by studying a relatively simple rod-like molecule to learn some basic insight on the aspects of quantum transport and single-molecule experiments. Afterwards, I will show how the properties of the anchoring groups can have a huge influence on the observed features. I will then show how a clever molecular design allows us to manipulate the electronic properties of a molecule by tuning quantum interference effects. Subsequently, I will present the study of the environment of the molecular junction, *i.e.*, what happens when we measure molecules in solution. Knowing the effects of an aqueous environment is important in the prospect of studying molecules that are involved in biological processes, which are naturally found in solution. A first step into this direction will be presented in this thesis, with a chapter on peptides. The final chapter will be a summary of the works that are currently in progress. Among them are a study on the role of bulky groups on the molecular conductance, the identification of transport pathways across a family of porphyrin molecules, and a proof of concept of how bistable molecules can be used as molecular machines. In the appendix, I will present a machine-learning based method for the analysis of the large amount of data that the MCBJ technique can produce.

1.3. Charge transport through a single-molecule

This section introduces the basic theoretical concepts needed to understand how charge transport across a molecular junction takes place. The discussion is based on Ref. [61–63], which provide a more exhaustive introduction to molecular transport.

1.3.1. Relevant dimensions and energy scales

In classical physics, the current flowing through an electrical circuit follows Ohm's law. This is used to describe macroscopic objects, in which the quantum effects that each individual electron experiences is averaged out and have therefore no influence on the outcome.

However, when the physical dimensions of the system become *small enough* (we will define what 'enough' means in a moment), Ohm's formula is not valid anymore and the laws of quantum mechanic take over. This means that effects like, for example, the quantization of energy or the particle-wave dualism become relevant.

PHYSICAL DIMENSIONS

Let us consider a simple system in which two electrodes are connected by a smaller bridge. When we apply a voltage difference across the electrodes, a current will start flowing from the source electrode to the drain. An electric current is a flow of electric charges (electrons or holes) throught a matarial, and along their path they can bounce and scatter against the atoms of the material itself. The average distance that electrons can travel between these scattering events is called *mean free path* (l_e), whereas the *phase coherence length* (l_ϕ) is the average distance that an electron travels between two events that cause it to change its phase substantially. Finally, the *Fermi wavelength* is the de Broglie wavelength (*i.e.*, the wavelength corresponding to the electron wavefunction) of the electrons present near the Fermi energy level, and is usually denoted with λ_F. In the classical limit, the physical dimensions of the system L_i ($i = x,\ y,\ z$) are large compared to these lengths, *i.e.*, $L_i \gg l_e,\ l_\phi,\ \lambda_F$. In this situation we can use Drude's model to describe the system, which leads to Ohm's law. On the other hand, if the dimensions of the systems are comparable to l_e, l_ϕ, and λ_F, we enter the quantum limit. In a single-molecule junction formed with a small organic molecule the relevant physical dimensions are $L_y,\ L_z \approx 0.5$ nm, $L_{\text{mol}} \approx 2$ nm, the mean free path in gold nano-electrodes is typically $l_e > 100$ nm [64, 65] and the Fermi wavelength of gold is $\lambda_F \approx 0.5$ nm. Therefore single-molecule junctions belong to the quantum world.

If the bridge shrinks to a size smaller than the mean free path or phase coherence length, charge transport becomes, respectively *ballistic* or *coherent*. In the ballistic regime the charge-carriers suffer few to no scattering events as they traverse the bridge, which leads to the quantization of the conductance [66]. In this regime the conductance comes from the transmission of the system; for a single transport channel, its upper limit is the quantum of conductance, $1\ \text{G}_0 = \frac{2e^2}{h} \approx 77.5\,\mu\text{S}$, in the case of perfect transmission ($\mathcal{T} = 1$). For coherent transport the phase of the electron becomes important, leading to constructive and destructive interference of the electron wavefunctions, an example of which is represented by the Aharonov-Bohm effect [67, 68]. Transport can either be *elastic*, if the electrons do not experience interactions that cause them to lose or gain energy while they flow through the bridge, or *inelastic* if they do. The same interactions that cause the loss of coherence (electron-electron, electron-phonon, electron-photon) are usually responsible for inelastic collisions, although it has to be noted that incoherent transport can still be elastic.

ENERGY SCALES

The small size of the molecule forces the charge carriers to be spatially confined on the molecule. This causes them to have a discrete energy spectrum in which the levels are separated by a certain energy. In general, the *confinement energy* (Δ), *i.e.* the energy separation between two levels, is larger the smaller the molecule is (the higher the confinement). The order of magnitude of Δ can be obtained from the particle-in-a-box model, which, for a cube with a side of 1 nm, yields $\Delta = \sum_i \frac{\hbar^2}{2m_e}\left(\frac{\pi}{L_i}\right)^2 \approx 1.2$ eV.

Another consequence of the spatial confinement is that the electrons feel a repulsion due to the electrostatic interaction. This can be quantified with the *charging energy*, $E_C = e^2/2C$, where e is the electron charge, and C the capacitance of the molecule to its environment. An estimate of the charging energy can be calculated from the self-capacitance of a metallic sphere with radius r, which is given by $C = 4\pi\varepsilon_0 r$. Choosing a diameter of 1 nm yields a self-capacitance of about $5 \cdot 10^{-20}$ F, which results in a charging energy of about 1.4 eV.

The third important energy is the *thermal energy* $E_{\text{th}} = k_B T$, where k_B is the Boltzmann constant and T the temperature, which determines the broadening of the energy features as a result of thermal fluctuations. At room temperature the thermal energy is about 25 meV, while at 4 K this energy is 0.36 meV.

Confinement, charging and thermal energy are important parameters that influence the properties of charge transport, for example determining the coupling regime (1.3.3). Comparing the thermal energy to the confinement and charging energies estimated above shows that $E_{\text{th}} < \Delta, E_C$, which indicates that quantum effects in molecular junctions can be observed even at room temperature.

1.3.2. Molecular orbitals

The electrons of an isolated molecule occupy discrete energy levels called molecular orbitals (MOs), whose shape is determined by the potential landscape created by the nuclei 1.1c. According to the *Aufbau principle*, electrons fill the MOs with the lowest available energy before occupying higher levels. Each orbital can host at most two electrons which, as dictated by the *Pauli exclusion principle*, must have opposite spin.

The highest occupied molecular orbital (HOMO) is separated from the lowest unoccupied molecular orbital (LUMO) by an energy gap, called HOMO-LUMO gap. The HOMO and LUMO are to single molecules what the valence band and conduction band are for inorganic semiconductors. Moreover, according to Koopman's theorem, the first ionization energy (IE) of a molecular system is equal to the negative of the HOMO (and a similar relation between electron affinity and LUMO can derived) [69, 70]. The HOMO-LUMO gap in isolated single molecules is of the order of a few eV, considerably larger than the thermal energy even at room temperature. Therefore, thermal excitations can be safely neglected in isolated molecules. In general terms, the size of the energy gap gets smaller when the size of the molecule becomes large because of the lesser confinement felt by the valence electrons [71].

1.3.3. Charge transport

Because the MOs appear at discrete energies, the density of states of a molecule in gas phase is given by a series of discrete levels represented by Dirac delta functions. When a molecule approaches a metal surface, it will initially interact with it through van der Waal's forces (Fig. 1.2). This interaction is usually pretty weak (10–100 meV) and does not cause a considerable overlap between the wave-function of the molecule and the one of the metal. Therefore, charge transfer is negligible in this process (called *physisorption*). Under the attraction of the van der Waal's forces, the molecule is drawn closer to the metal surface, and interactions between the two increase. At this point, because of the increased screening from the electrons in the metal and the formation of image charges in the electrodes,

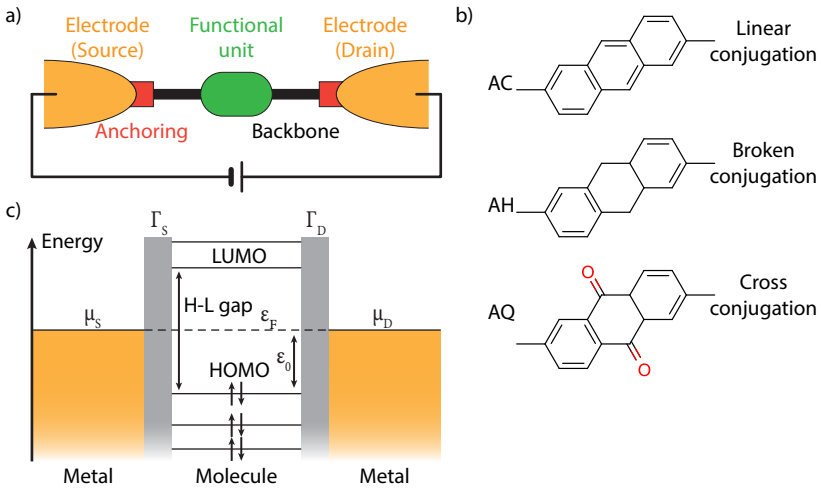

Figure 1.1: a) Schematics of a single-molecule junction. b) Energy level diagram of a single-molecule junction. c) Chemical structure of anthracene (AC), anthraquinone (AQ), dihydroanthracene (AH).

the energy of the MOs is renormalized and the HOMO-LUMO gap is reduced. When the molecule and metal are close enough for their wave-functions to overlap, they can, according to chemical specificity, form a chemical bond (*chemisorption*). The hybridization of the MOs with the metal means that electrons can escape from the molecule into the metal, *i.e.* that their lifetime in the MOs is finite. According to Heisenberg's uncertainty principle (Eq. (1.1)), the finite lifetime on the molecule results in a broadening of the MOs density of states:

$$\Delta E \, \Delta t \geq \frac{\hbar}{2} \, . \tag{1.1}$$

When the MOs are on discrete levels, $\Delta E \to 0$ and their lifetime $\Delta t \to \infty$; however, when a level is broadened its energy spread ΔE is finite, therefore its lifetime Δt must also be finite.

When a bond is formed, differences in electronegativity can induce the formation of a dipole, or charge transfer between the metal and the anchoring groups of the molecule can change the electrostatic environment of the molecule. This brings the MOs to rigidly shift to higher (lower) energies therefore aligning the HOMO (LUMO) towards the Fermi energy of the metal (see the right panel in Fig. 1.2). For example, when binding to gold, thiol ($-$SH) and amino ($-NH_2$) groups tend to transfer charges from the electrodes to the molecule, thus shifting the levels upwards in energy.Pyridine ($-$Pyr) and cyano ($-$CN) groups, on the contrary, shift the levels to lower energies because charge transfer occurs in the opposite direction.

Charge transport is facilitated by the hybridization between the MOs and the wavefunction of the electrodes. This means that highly delocalized MOs, like π-orbitals, can transport charge more efficiently than more localized orbitals. Additionally, if inversion through the center of symmetry in a molecule results in the same phases for the MO, then the MO is said to have gerade symmetry. Conversely, if the inversion results in a phase change, then the MO is said to have ungerade symmetry. This character of MOs determines whether they

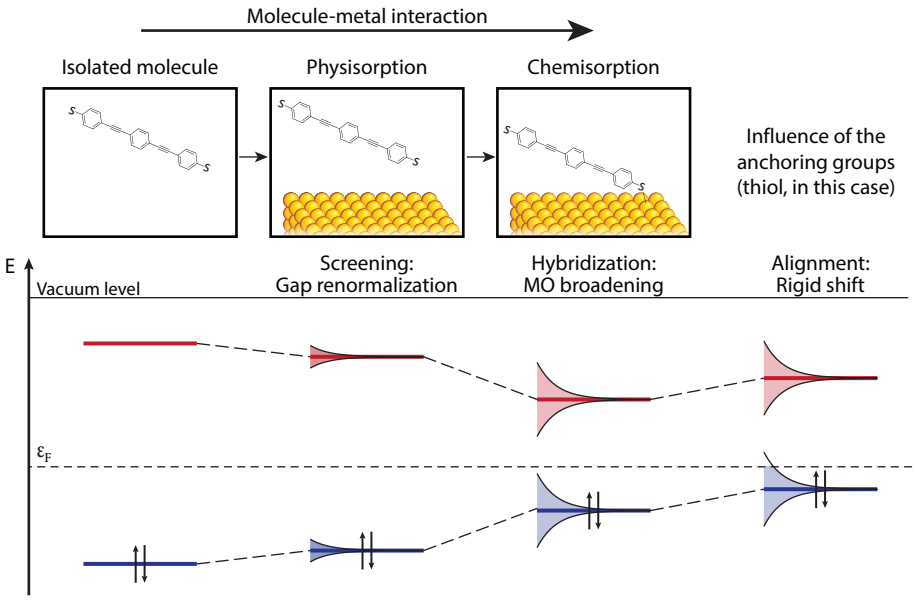

Figure 1.2: Schematic drawing of the effect of the interaction between a molecule and a metal on the frontier molecular orbitals in respect to the Fermi energy (ε_F) of the metallic surface. The isolated molecule (left) initially interacts with the metal surface only via long-range interactions (middle, physisorption) and subsequently also with a chemical bonds (right, chemisorption). The screening of the metal surface causes the energy gap to reduce, the formation of the chemical bond induces the broadening of the MOs and their hybridization with the wavefunction of the metal. The formation of a surface dipole causes the levels to rigidly shift towards higher or lower energies, depending on the electronegativity of the anchoring groups.

interfere constructively or destructively when participating to a transport channel [71, 72].

ELECTRONIC COUPLING

The electron transfer rate from the source to the molecule (Γ_S) and from the molecule to the drain (Γ_D) depends on the overlap of the wavefunction of the molecule and those of the electrodes, and defines the level broadening. The total coupling ($\Gamma = \Gamma_S + \Gamma_D$) is a measure for the overall hybridization, and determines the amount of current that can flow through the junction.

The electron coupling Γ is related to the time ($\tau_{el} \approx \hbar/\Gamma$) a conduction electron spends on the molecule when going from source to drain and, depending on its ratio with the other energy scales Δ, E_C and k_BT, determines the transport regime [73–76]. If $\tau_{el} \ll \tau_{e-e} \approx \hbar/E_C$, the tunneling event is completed before electron-electron interactions can take place: electrons preserve their phase information and transport is coherent. The system is in the *strong coupling* regime, the condition for which is usually defined as $\Gamma \gg E_C,\ \Delta$.

On the other hand, in the *weak coupling* regime ($\Gamma \ll E_C,\ \Delta,\ k_BT$), the electrons dwell on the molecule long enough to lose the information on their phase. The system is in the regime of *incoherent transport*: the level broadening can be neglected, the MOs can be described by discrete energy levels represented by Dirac delta functions.The transport

process happens by charges sequentially hopping on and off the molecule, therefore only integer charges are allowed to tunnel.

A system can also be in a regime that cannot be defined as strong or weak; in this case we talk about *intermediate coupling* regime. Typical values for the coupling of molecules to the electrodes are in the tens of meV [77, 78], which corresponds to strong coupling for measurements at cryogenic temperatures, and intermediate coupling at room temperature.

1.3.4. MOLECULAR DESIGN

The molecules utilized for break junction experiments usually follow a certain design that can be decomposed in different units Fig. 1.1a. Molecules are generally built around a backbone that can host a functional unit and is terminated with groups which have high affinity to the material of the electrodes.Occasionally, bulky side groups are also present with the purpose of reducing the possible configurations of the molecular junctions.

Depending on the character of their p orbitals, molecules can have different degrees of *conjugation*. In its original definition, conjugation is the interaction between two p-orbitals across a σ-bond, but the term has now been extended to the analogous interaction involving a p-orbital containing an unshared electron pair [79]. A simple way to determine the nature of the conjugation of a molecule comes from looking at its structure. If the molecule presents alternating single and double bonds along consecutive atoms, then it is *linearly conjugated*; on the other hand, if the alternating sequence is interrupted at some point, then the molecule has *broken conjugation*. Alternatively, if a molecule contains three subunits, two of which are conjugated to the third but are not conjugated to each other, it is said to have *cross conjugation* [80]. An example of these three conjugation characters can be found in Fig. 1.1b.

As we will see later, transport through a molecular junction depends strongly on the level alignment and coupling. These two parameters are regulated by the choice of material used for the electrodes (which determines the Fermi energy) and the anchoring groups.

ELECTRODES

In BJ devices, different metals, such as Au, Ag, Pd, and Pt, and non-metal, like carbon and indium tin oxide, are employed to fabricate the electrodes [41, 52, 81, 82]. For the metals mentioned above, the Fermi level decreases in the order Ag > Au > Pd > Pt [83] and this affects the conductance of the molecular junction: *e.g.*, HOMO-dominated molecules will have a higher conductance when Au electrodes are used instead of Ag, because the lower ε_F of Au will result in reduction of the level alignment [82]. Apart from the change in Fermi energy, different materials can also have different binding character. For example, Au has a predominant σ-character binding, whereas Pt and Pd electrodes have a π-character binding deriving from the d-orbitals. In some cases, this difference can result in a significantly increased coupling strength and broadening of the energy levels and thus be responsible for a higher conductance compared to Au electrodes when Pt or Pd leads are used [84].

ANCHORING GROUPS

Systematic studies comparing different anchoring groups have been carried out in the last years, focusing on the most widely used moieties: thiol (−SH), amine ($-NH_2$), pyridine (−Pyr), cyano (−CN), nitro ($-NO_2$), methyl sulfide (−SMe), dimethyl phosphines $-PMe_2$,

dihydro benzothiophene (−BT), carboxyl (−COOH), and many others [85, 86, 86–90]. It is important to realize that there is a difference between electronic coupling, anchoring strength, and junction stability. For example, when the anchoring groups −SH, $-NH_2$, and −COOH are compared for the same molecule, the conductance measured follows the same ordering of the electric coupling efficiencies between the anchoring groups and the gold electrodes (−SH (1.7 eV) > $-NH_2$ (0.35 eV) > −COOH (87 meV)) [91–93]. However, the strong binding interaction between the thiol group and gold can cause the deformation of the electrodes, which results in junctions that are worse defined than, *e.g.* when amino anchoring groups are used [94]. Despite the difference in anchoring strength, however, thiol and amino anchoring groups show similar junction lifetimes, indicating comparable mechanical stability of the junctions. Moreover, Pyr groups show a higher mechanical stability than thiol groups even though their electronic coupling to gold (and thus the measured conductance) is lower [77]. Recently there have also been attempts to form molecular junctions via direct carbon-gold covalent bond. This has been achieved both by spontaneous [95] and adventitious [96] cleavage of a protecting group, or even with unprotected carbon-terminated groups [97]. If the interaction of the anchoring groups with the gold electrodes is very strong, it can bring to the formation organometallic chains mediated by the incorporation of gold atoms provided by the electrodes, as has been reported when using isocyano anchoring groups [98].

1.3.5. Single level model

Let us now give a more quantitative description of the current that flows through a molecule bridging two metallic contacts. The electrodes (or leads) are electron reservoirs, *i.e.* bulk-like regions where the electrons are in equilibrium. The electrons in the leads can be described as an ideal Fermi gas, characterized by the Fermi-Dirac distribution:

$$f(E,\mu) = \frac{1}{1+\exp\left(\frac{E-\mu}{k_B T}\right)}\,, \tag{1.2}$$

where μ is the chemical potential of each lead. At $T = 0$, the electrons in the metal fill up the available quasi-continuum set of levels up to an energy ε_F. When a bias voltage V_b is symmetrically applied to the leads, the chemical potential of the electrodes is shifted accordingly:

$$\begin{aligned} \mu_S &= \varepsilon_F + eV_b/2, \\ \mu_D &= \varepsilon_F - eV_b/2. \end{aligned} \tag{1.3}$$

The source and drain contacts thus have different Fermi functions and each seeks to bring the molecule into equilibrium with itself, one by adding electrons, the other by removing them.

For simplicity, let us assume that only one level ε is available for this electron flow. The current flowing from source to drain can then be estimated by balancing the kinetic equations [61]:

$$I = \frac{2e}{\hbar}\int_{-\infty}^{+\infty} D(E)\frac{\Gamma_S\Gamma_D}{\Gamma_S+\Gamma_D}[f(E,\mu_S) - f(E,\mu_D)]\,\mathrm{d}E\,, \tag{1.4}$$

where $D(E)$ is the density of states of the molecule, *i.e.* the number of states available to be occupied at each energy level. This equation shows that no current will flow if $f(E,\mu_S) = f(E,\mu_D)$. This can happen if the two leads have the same chemical potential ($\mu_S = \mu_D$), which is the trivial case in which the leads are in equilibrium. However, since at $T = 0$ the Fermi functions become sharp steps, transport is also blocked if the molecular level is above the chemical potential of the source or below that of the drain. In the former case we have $f(E,\mu_S) = f(E,\mu_D) = 0$ and in the latter $f(E,\mu_S) = f(E,\mu_D) = 1$. This yields an important result: no current can flow unless the level lies in the energy range between the chemical potentials of the source and the drain, which is usually called *bias window*, because only in this case $f(E,\mu_S) \neq f(E,\mu_D)$. In particular, at $T = 0$, $f(E,\mu_S) = 1$ and $f(E,\mu_D) = 0$, so the current is at its maximum.

The model we obtain is called *single-level model* and describes particularly well the case of small molecules, where the energy spacing is typically much larger than the bias voltage which can be applied in experiments. Transport is therefore dominated by the level that is closest to the Fermi energy, while the others can be neglected.

A popular theoretical formalism to describe the coherent transport in nanodevices is the scattering approach. The main idea of this approach is that transport can be viewed as a scattering problem and inelastic interactions can be ignored. The consequence of these assumptions is that transport properties like the electrical conductance can be derived by the transmission probability for an electron to cross the system. One of the conlcusions of this approach is that the conductance of a nano contact can be written as:

$$G = \frac{2e^2}{h} \sum_{n=1} N\mathcal{T}_n \,, \tag{1.5}$$

where the summation is performed over all the current-carrying channels and $\mathcal{T}_n$ are their transmissions.

Continuing along this approach we reach the Landauer-Büttiker formula for the total current flowing through the junction [61, 63]:

$$I = \frac{2e}{h} \int_{-\infty}^{+\infty} \mathcal{T}(E)\,[f(E,\mu_S) - f(E,\mu_D)]\,\mathrm{d}E \,. \tag{1.6}$$

By comparing Eq. (1.4) and Eq. (1.6), we notice that they have the same form and it is thus possible to define the transmission of the molecule from its density of states as:

$$\mathcal{T}(E) = 2\pi\, D(E)\, \frac{\Gamma_S \Gamma_D}{\Gamma_S + \Gamma_D}. \tag{1.7}$$

Since at $T = 0$ only the energy levels inside the bias window matter, we can restrict the intergral to obtain:

$$I = \frac{2e}{\hbar} \int_{\mu_D}^{\mu_S} \frac{\Gamma_S \Gamma_D}{\Gamma_S + \Gamma_D}\, D(E)\, \mathrm{d}E \,. \tag{1.8}$$

Due to the hybridization of the MOs with the electrodes, the density of states of a level can be approximated by a broadened Lorentzian centered around ε:

$$D(E) = \frac{1}{2\pi} \frac{\Gamma}{(E-\varepsilon)^2 + (\Gamma/2)^2} \,. \tag{1.9}$$

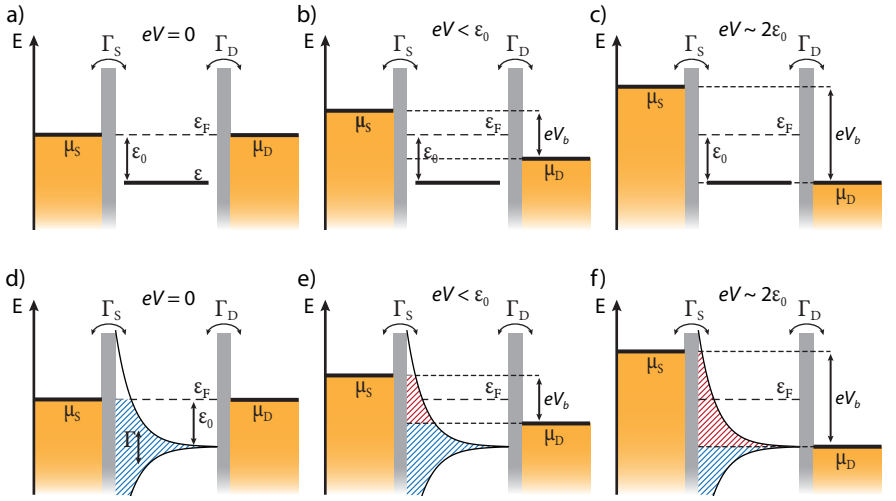

Figure 1.3: Schematic representation of a molecular junction consisting of a single-level (HOMO) with level alignment ε_0 and symmetrically coupled to the electrodes, ($\Gamma_S = \Gamma_D$). When the leads are in equilibrium no current can flow (a). In the presence of a bias, the chemical potential of the leads are different (b), but current can only flow once the level lies inside the bias window (c). When the MO hybridizes with the electrodes, it can be represented by a boradened Lorentzian of half-width at half-maximum Γ. The blue shaded area corresponds to the occupation of the orbital. As in the previous case, no current can flow when no bias voltage is applied (d). However, in this case some current can flow even for a small voltage difference (e). The red shaded area feels competing pulls from the two electrodes: the source tries to pump electrons into it, while the drain tries to empty it. When the bias window is large enough to include the peak, the system is in resonance and a large current flows (f).

The coupling represents the half-width at half-maximum, which means that a stronger coupling 'spreads' the Lorentian across a wider energy region. The portion of the Lorentzian that falls within the bias window contributes to charge transport (Fig. 1.3). This means that orbitals which would lie outside the bias window in the gas phase can participate to transport after their broadening. This is relevant when the HOMO-LUMO gap is small (large molecules), or when HOMO and HOMO-1, or LUMO and LUMO+1 are close in energy and thus both contribute to transport. This latter case is particularly interesting when orbitals close in energy interfere either destructively or constructively, drastically affecting the transmission (and hence the conductance) (Chapter 4). It is worth mentioning that other effects, *e.g.* thermal excitations, can also contribute to level broadening. The initial delta function can be obtained from the Lorentzian in the limit where the coupling goes to zero: $\Gamma \to 0$.

In the weak to intermediate coupling regime at low bias voltages, the first accessible molecular level is typically located far from the chemical potential of the leads, therefore the current flowing through the molecular junction is small. Transport in this regime is usually referred to as *off-resonant*. As the voltage increases and the first molecular level enters the bias window, the current increases rapidly as trasnport enters the *resonant* tunneling regime.

In the above derivation, we have assumed that $E_C = 0$, but it is important to mention that charging effects may significantly change the transport behaviour. Fractional charging

is possible in the strong coupling regime and may lead to a pinning of the molecular level at either of the chemical potentials of the leads when the bias voltage is increased. Further details about this can be found in Ref. [61].

In molecular electronics it is common to express the conductance in units of G_0, which is the quantum of conductance and can be obtained from Eq. (1.8) if we assume that:

i the bias window is small enough that the density of states (and hence the transmission) remains constant over it,
ii the energy level ε is exactly at the Fermi energy ε_F,
iii the coupling to the leads is symmetrical ($\Gamma_D = \Gamma_S$).

Under these assumptions, we find that the conductance maximum is:

$$G_0 = \frac{I_{\max}}{V_b} = \frac{2e^2}{h} = 77.8\,\mu S\ . \tag{1.10}$$

1.3.6. SIMULATION OF CURRENT-VOLTAGE CURVES

In the case of a single Lorentzian density of states (Eq. 1.7) and zero temperature, Eq. 1.8 becomes:

$$I = \frac{2e}{h}\int_{\mu_D}^{\mu_S} \frac{\Gamma_S + \Gamma_D}{(E-\varepsilon)^2 + (\frac{\Gamma_S+\Gamma_D}{2})^2}\,\mathrm{d}E\ , \tag{1.11}$$

which can be solved analytically yielding:

$$I(V) = 2\frac{G_0}{e}\frac{\Gamma_S\Gamma_D}{\Gamma_S+\Gamma_D}\left[\arctan\left(\frac{\varepsilon_0 + \frac{eV_b}{2}}{\Gamma_S+\Gamma_D}\right) - \arctan\left(\frac{\varepsilon_0 - \frac{eV_b}{2}}{\Gamma_S+\Gamma_D}\right)\right], \tag{1.12}$$

where $\varepsilon_0 = \varepsilon_F - \varepsilon$ is the *level alignment*, *i.e.* the energy difference between the single level and the Fermi energy.

A simple Matlab code can be used to numerically solve the integral in 1.8 and simulate current-voltage (IV) curves varying the transport parameters. Figure 1.4 presents plots of the current-voltage (IV) and the differential conductance $\mathrm{d}I/\mathrm{d}V$ across a single Lorentzian-broadened level. In Fig. 1.4a it can be seen how shifting the level alignment changes the position of the resonance, whereas Fig. 1.4b shows how increasing the coupling spreads the Lorentian peak and washes out the blockade and resonance features. For symmetric couplings $\Gamma_S = \Gamma_D$, the differential conductance shows two peaks of equal height at $V_b = \pm 2\varepsilon_0/e$, which corresponds to resonant transport. The characteristic conductance gap between the peaks marks the regime of off-resonant transport.

With the same code it is also possible to probe more exotic transmission landscapes. For example we can investigate how the IV curve would look like if both HOMO and LUMO are relevant for the conductance of the junction. This is just a toy-model, since it neglects many effects (*e.g.* the level shift due to charging or image charge effects) that become relevant in more complex situations. Nonetheless, it can give a rough description of a system for which the behaviour is not immediately intuitive. An example of such system could be one that features an antiresonance in the transmission landscape. This can be modelled by including three Lorentzian peaks in the spectrum, one of which is 'flipped' and thus reduces the transmission. In this case the current does not show blockade and only small kinks are observed when one of the levels is on resonance. More insightful are instead the curves of

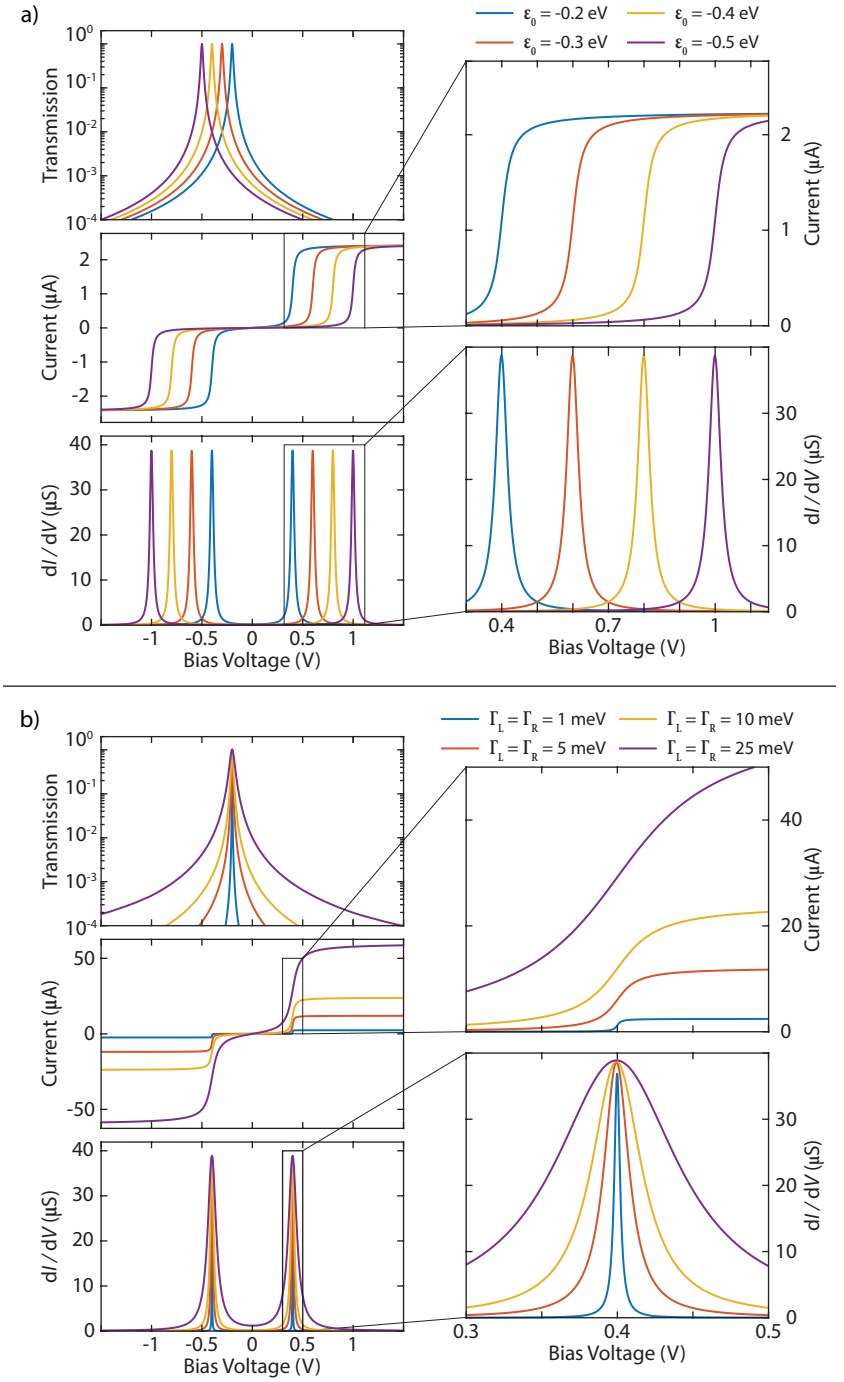

Figure 1.4: a) Current-voltage and differential conductance curves for various values of ε_0 and a fixed symmetric coupling $\Gamma_S = \Gamma_D = 5$ meV. b) Current-voltage and differential conductance curves for various values of Γ and a fixed ε_0 of -0.2 eV.

the differential conductance $\mathrm{d}I/\mathrm{d}V$, which show a dip when the antiresonance is crossed. The $\mathrm{d}I/\mathrm{d}V$ curves for a single-level model system only show peaks at the resonance, which also appear in the more complex scenario that was just described.

1.4. Mechanically Controlled Break Junction

The mechanically controlled break junction (MCBJ) technique was initially developed to study electron tunneling in point-contacts [99, 100] and has since been developed [101–103] and adapted for single-molecule experiments [104]. The versatility of the platform allows for measurements to be carried out in the most diverse conditions with only small adaptations or limitations: in air, in vacuum, or in solution, and at room or cryogenic temperature. All the experiments presented in this dissertation have been performed using this technique.

In this technique, a thin gold wire is deposited on a flexible substrate. The center of the wire consists of a 100 nm wide constriction that is suspended after etching the supporting polyimide with an O_2 plasma. The flexible substrate is clamped between two lateral supports in a three-point bending mechanism and deformed by driving a pushing rod connected to a cantilever into it (Fig. 1.6). Upon bending of the substrate, the gold wire is stretched until a single gold atom connects the two extremities. Further bending results in the breaking of the wire, thus forming two sharp electrodes whose separation can be adjusted mechanically. The geometrical design of the samples is such that the ratio between the vertical displacement of the cantilever and the horizontal electrode displacement is around $5 \cdot 10^{-5}$, which results in a sub-nanometer control over the electrodes separation. The two broken extremities can be fused again to reform the wire by unbending the substrate. This process can be repeated tens of thousands of times without a noticeable aging of the wire, making the technique ideal for statistical studies.

1.4.1. Experimental set-up

A detailed description of the mechanics and the electronics of the MCBJ set-up can be found in the PhD dissertations of C. Martin [105], M. Perrin [106] and R. Frisenda [107].

Mechanical

The heart of the set-up is represented by the three-point bending mechanism. The bending of the sample can be controlled either by a brushless servo motor (Faulhaber) or by a piezoelectric element (Physik Instrumente). The stepper motor is slow, but has a high-dynamic range and is therefore used for the initial breaking of the wire. The piezoelectric element, on the other hand, is fast and responsive and is therefore used during the conductance measurement of molecular junctions, since only a limited displacement range is required at this stage. Because of the strong thermal dependence of its properties, the piezoelectric element is only used for experiments at room temperature.

The set-up can be closed with a conical vacuum-tight seal and evacuated to high vacuum ($\approx 1 \cdot 10^{-6}$ mbar. Once closed, the vacuum seal also acts as a shield that protects the measured signal from electromagnetic interference coming from the outside.

The bending mechanism can be placed in a dipstick or in a table-top mechanical support. The former allows for the set-up to be inserted in liquid nitrogen or liquid helium vessels for experiments at cryogenic temperatures. The latter allows not only for an easier access

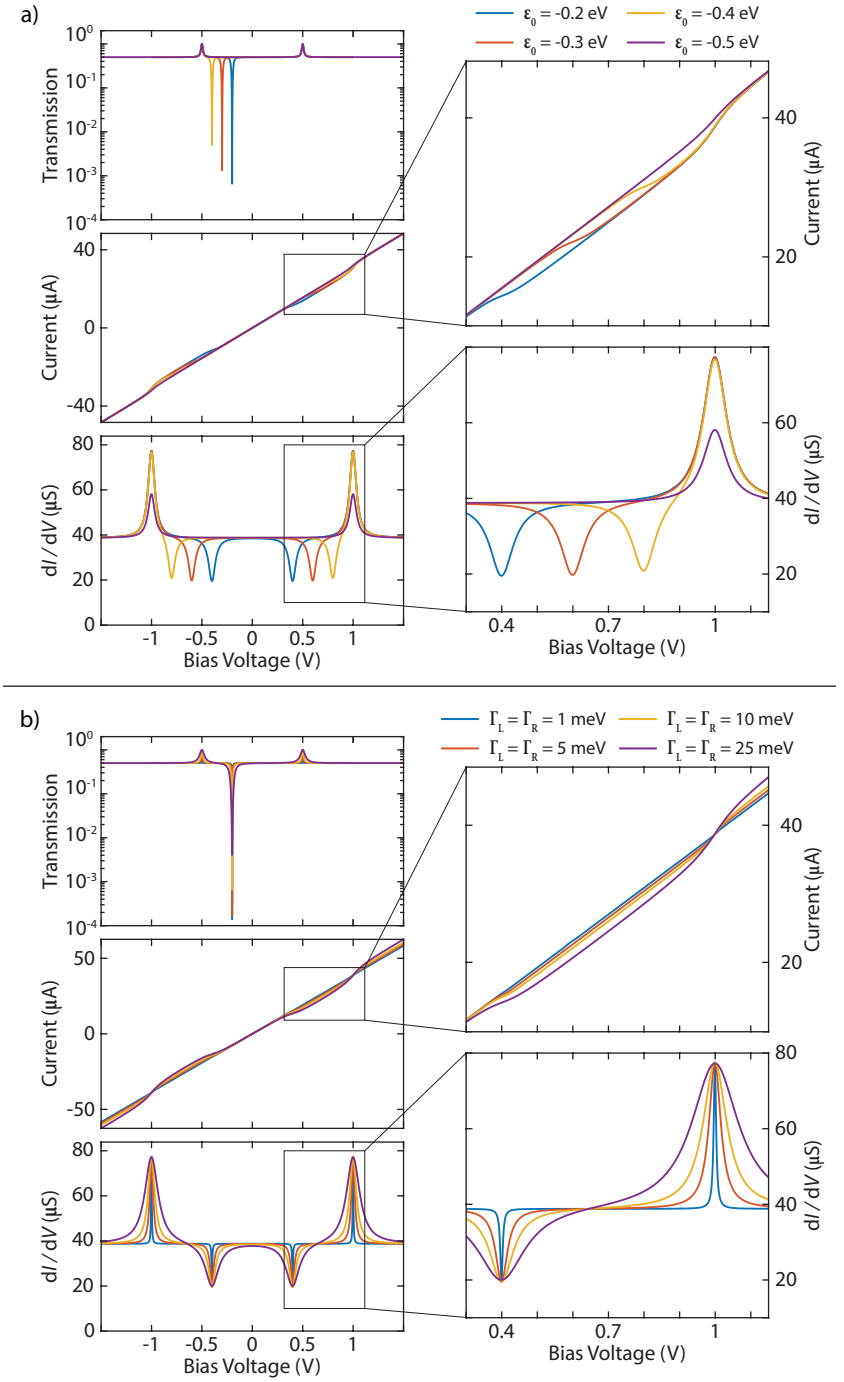

Figure 1.5: a) Current-voltage and differential conductance curves for a potential landscape of two levels at $\varepsilon_{1,2}$ of ±0.5 eV, an antiresonance level at varying position ε_0, and fixed symmetric coupling $\Gamma_S = \Gamma_D = 5$ meV. b) Current-voltage and differential conductance curves for a potential landscape of two levels at $\varepsilon_{1,2}$ of ±0.5 eV, an antiresonance level at $\varepsilon_0 = -0.2$ eV, and varying symmetric coupling.

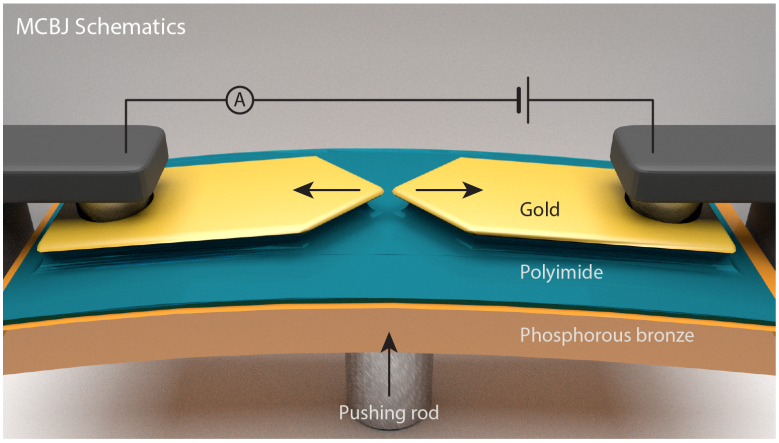

Figure 1.6: Schematic illustration of the MCBJ setup.

of the set-up, but the reduced distance to the amplifiers also means that the capacitance of the wires is reduced, opening the door to faster acquisition speeds.

Electronics

The electronic components used for the measurements were developed by Raymond Schouten (TU Delft) and are powered by two batteries in order to avoid interferences that a normal power line experiences. A voltage source is used to supply a bias voltage across the two-terminal MCBJ sample, while the current flowing through it is measured via a logarithmic or a linear amplifier. The logarithmic amplifier can measure currents as small as $\approx$10 pA) with a response time of hundreds of milliseconds, but its greatest advantage is its large dynamic range of about ten orders of magnitude. The linear amplifier has a more limited range but can, on the other hand, measure currents with a noise floor of 5 fA/$\sqrt{\text{Hz}}$ at the highest gain setting. It is therefore usually employed when performing current-voltage (IV) measurements at cryogenic temperatures. The home-made modules are connected to a shielded IVVI rack via optically coupled isolation amplifiers, which make them ideal for low-noise measurements of small currents (documentation available at [108]). An ADwin Gold (Jäger Messtechnik GmbH) unit is utilized to access and read out the measurement electronics, and is controlled via home-made Python and ADbasic scripts. One of the newer set-ups is operated with an ADwin Gold II unit, which most notably features analog-to-digital converters with 18 bits, contrary to the 16 bits of the previous model.

1.4.2. MCBJ Samples

The device fabrication process has been extensively detailed in the PhD dissertations of C. Martin [105] and M. Perrin [106] and will only briefly described.

The devices are fabricated in the Kavli NanoLab in Delft on a substrate of polished phosphorus bronze wafer for its high flexibility. Wafers of 50×50×0.5 mm are generally utilized for the fabrication of 10 individual samples with 4 junctions each (Fig. 1.7a). An adhesion promoter (VM651, HD Microsystems) and a polyimide precursor (PI2610, HD

Microsystems) are spin-coated on the wafers, which are then cured in a vacuum oven at up to 300 °C. This results in a 6 µm thick polyimide layer that ensures the electrical isolation of the junctions from the metallic substrate. A double layer of resist (methylmethacrylate-methacrylic acid (MMA(8.5)MAA) 8% in ethyl-L-lactate layer, followed by polymethylmethacrylate (PMMA) 950k 4% in anisole (Microchem) for a combined thickness of 400 nm) is then spin-coated and cured on the wafers so that the device layout can be lithographically defined with a Leica electron-beam pattern generator. The smallest sections in the design are exposed with a beam size of 3 nm, a beam step-size of 2 nm and a dose of 850 µC/cm^2, resulting in ≈100 nm wide junctions in their narrowest part (Fig. 1.7b,c). The patterns are developed in a mixture of methyl-isobutyl-ketone (MIBK) and isopropanol (IPA) (volume ratio 1:3) and then rinsed in IPA for 20 s. Subsequently, electron-beam evaporation (Temescal FC-2000) is used to deposit a 3 nm sticking layer of titanium (0.5 Å/s) and a 80 nm of gold (1.0 Å/s) for the electrodes. For this process, the base pressure of the evaporation chamber should be below $2 \cdot 10^{-6}$ mbar. The lift-off process is done in hot acetone and the wafers are then rinsed with acetone and isopropanol.

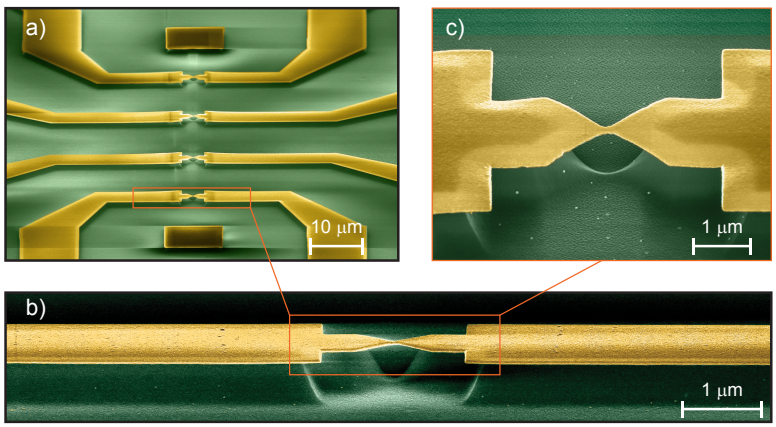

Figure 1.7: a) Scanning electron microscopy images of four parallel wires of a MCBJ sample and b,c) of the central constriction of one of the wires. Images by R. Frisenda.

The individual break junction devices are separated from the wafer using laser-cutting. This step is performed at ILT Fineworks BV (Enschede), therefore the fully processed wafers are coated with a 500 nm thick layer of PMMA 350k 3% in anisole (Microchem) to protect them during the handling and cutting procedure. The underetching of the electrodes that suspends the gold wire is carried out on the individual devices not more than a week prior to each experiment. This process starts by removing the protective layer by submerging the devices in a hot acetone bath and then rinsing them with acetone and IPA. The samples are then placed in a reactive ion etcher (Leybold Heraeus) and plasma etched with a gas flow of 50 sccm of O_2 gas and 8.5 sccm of CF_4, at a pressure of 0.2 mbar and with an RF power of 30 W. Alternatively, a 50 sccm gas flow of O_2 only can be used, which will result in a slighlty lower etching rate. During the process, a laser interferometer is used to monitor the thickness of the polyimide layer in order to obtain an underetch of ≈ 1 µm. Finally, the devices are dipped into fresh ethanol immediately after etching to

reduce the possible formation of gold oxide on the surface, which is expected to reduce the reproducibility of self-assembly processes [109, 110]. Before the measurements start, the samples are cleaned one last time with an ozone cleaner for 10 minutes. This procedure has resulted in sharper breaking of the junction and a cleaner tunneling behaviour observed during the characterization of the bare devices that preceeds the deposition of the molecular solution.

Alumina-coated Devices

When experiments are performed in a polar solution, parasitic currents arise due to the flow of ions in the solution [111]. To reduce this contribution, we slightly modify the fabrication steps of the samples that are used for this kind of measurements. We coat the samples with a 15 nm thick layer of aluminium oxide by means of atomic layer deposition (ALD). This is done after the suspension of the gold constriction; this way, the suspended wire is coated all around and not just on top. As the wire is stretched, gold and alumina rupture at different moments because of their different ductility. The more brittle alumina breaks first, whereas the gold is stretched further before it breaks. This means that only a minute portion of the gold electrodes sticks out of the insulating coating and is exposed to the liquid environment, thus minimizing parasitic effects. These changes produce slightly more delicate junctions, but by increasing the bridge size to 200 nm and the gold thickness to 160 nm it is possible to obtain devices capable of undergoing tens of thousands of breaking traces without significant degradation.

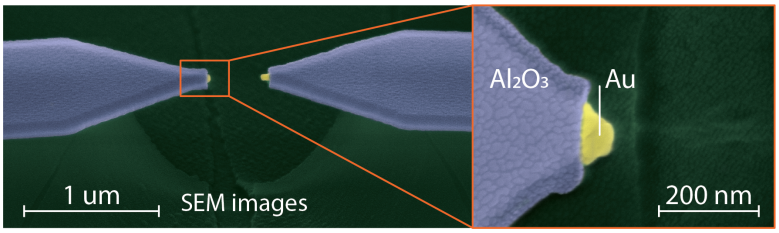

Figure 1.8: Scanning electrode microscope images (colorized) of a typical device with alumina-coated gold electrodes. Only a minute portion of the gold electrodes protrudes out of the insulating coating, thus minimizing the flow of parasitic currents. Images by M. Perrin

1.5. Dissertation outline

This dissertation concerns transport measurements in single-molecule junctions using the mechanically controlled break junction (MCBJ) technique. Chapter 2 introduces the basics of MCBJ experiments on a simple rod-like molecule and gives an idea of the amount of information that can be extracted from a relatively simple systems.

Chapter 3 shows the role of the anchoring configurations in single-molecule junctions. The conductance histogram of a C_{60} molecule is dominated by effects that can be traced to the anchoring groups.

Chapter 4 reports the detailed study of quantum interference effects in a mechanosensitive molecule. Conductance variations up to two orders of magnitude are observed and can be controlled by mechanically deforming the molecule.

Chapter 5 presents a first characterization of the role of water and other solvents on the single-molecule conductance. Density functional theory calculations show that the effects of the water environment cannot be explained with the intuitive description of water as a dielectric continuum.
Chapter 6 contains a study on peptides of different lengths and various amino-acid compositions. The role of the secondary structure on the molecular conductance is investigated with a clustering analysis method.
Chapter 7 displays projects that are currently being developed. The molecule presented in chapter 4 shows great potential for thermopower and cryogenic measurements in the presence of a back gate. A preliminary study of such measurements is shown in this chapter. Afterwards, the role of bulky groups is investigated on the OPE3 family of molecules. The influence of anchoring and bulky groups on the electronic paths is studied on a family of porphyrins. Finally, the topic of molecular machines is touched upon with a section on pseudo-rotaxane molecules. In the appendix, more details are given on the clustering technique that has been employed in some of the chapters and the limitations of the technique are also discussed.

2

OPE3 MOLECULES, A MODEL SYSTEM FOR MOLECULAR-SCALE ELECTRONICS

This chapter provides an overview of our recent efforts to unravel charge transport characteristics of a metal-molecule-metal junction containing an individual π-conjugated molecule. By combining room- and low-temperature data, we estimate the level alignment and the electronic couplings to the leads using the single level model and show that the dominant transport mechanism for electrons through the OPE3 molecule is off-resonant tunneling.

Parts of this chapter have been published in Accounts of Chemical Research (51), 1359–1367 (2018).
Part of the experimental measurements and analysis in this chapter have been performed by R. Frisenda (TU Delft).

2.1. INTRODUCTION

In this chapter, we discuss MCBJ experiments on a rigid and π-conjugated oligo(phenelyne-ethynylene) derivative with three benzene rings, OPE3 in short. At either end, acetyl protected thiol groups provide the anchoring to the electrodes (Fig. 2.1a). OPE3 has a relatively high conductance and forms stable and well-distinguishable molecular features in MCBJ experiments [8, 77, 78, 112–121]. These characteristics make it a 'fruit fly' molecule for detailed single-molecule transport studies and for statistical analysis of single-molecule traces. Special attention will be paid to those experimental approaches that exploit the stability and the control over the electrodes separation of the MCBJ technique. Importantly, the technique also allows measurements at different temperatures, and here we discuss a comparison between room-temperature and low-temperature experiments at 6 K [78].

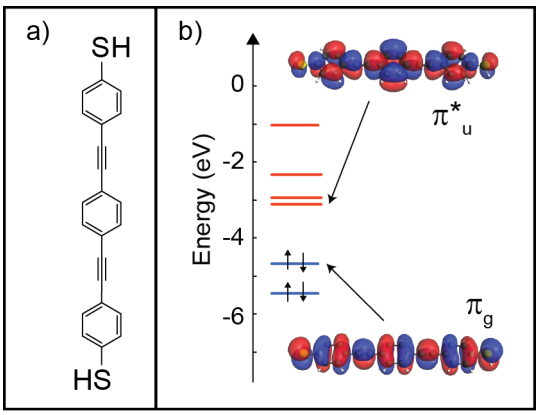

Figure 2.1: a) Chemical drawing of an OPE3 molecule. b) Electronic structure in gas phase calculated with DFT B3LYP//TZ2P.

2.2. ROOM-TEMPERATURE MEASUREMENTS

At room temperature, an MCBJ experiment starts with the characterization of the clean gold electrodes by measuring the low-bias (0.1 V) conductance while breaking and reforming the wire. During the breaking event, a transition occurs from ballistic conduction through few-atom gold contacts (conductance $\leq 1\,G_0 \approx 77\,\mu S, G_0 = 2e^2/h$) to a tunnelling regime across the broken wire (conductance $\ll 1\,G_0$) either in air or vacuum. The quantum of conductance G_0 defines the conductance of a quantum channel for a unitary transmission probability of electrons passing through it and corresponds also to the largest conductance that can be reached in a quantum object (such as a single molecule).

The distance dependence of the current in the ballistic and tunneling regimes is very different, showing steps and flat plateaus in the former case and an exponential decay in the latter. If instead a molecule bridges the two electrodes and hybridizes with both of them, electrons can tunnel through the molecular orbitals and the distance dependence of the conductance typically shows plateaus and steps. In the case of OPE3, the conductance is dominated by the frontier orbitals depicted in Fig. 2.1b. On the bare junction, we measure

typically a few thousand conductance-displacement traces to check for the presence of contaminants in the device and to extract the calibration factor of the electrode displacement by using the length of single-gold atom plateaus in these traces [122, 123].

Deposition of OPE3 molecules is done by pipetting onto the MCBJ device a 1 µL droplet of a 1 mM solution in dichloromethane with the addition of two equivalents of tetrabutylammonium hydroxide, which deprotects the thiol groups favoring the formation of gold-sulfur bonds [116, 124]. During the deposition of the molecular solution, we monitor the conductance while breaking and reforming the electrodes. In the case of OPE3, the formation of single-molecule contacts starts as soon as the molecular solution is deposited onto the electrodes and plateaus in the conductance versus electrode spacing traces are a sign of their formation. Figure 2.2a displays such a conductance trace with a clear plateau that is 1 nm long and centered around $1 \cdot 10^{-4}\,G_0$.

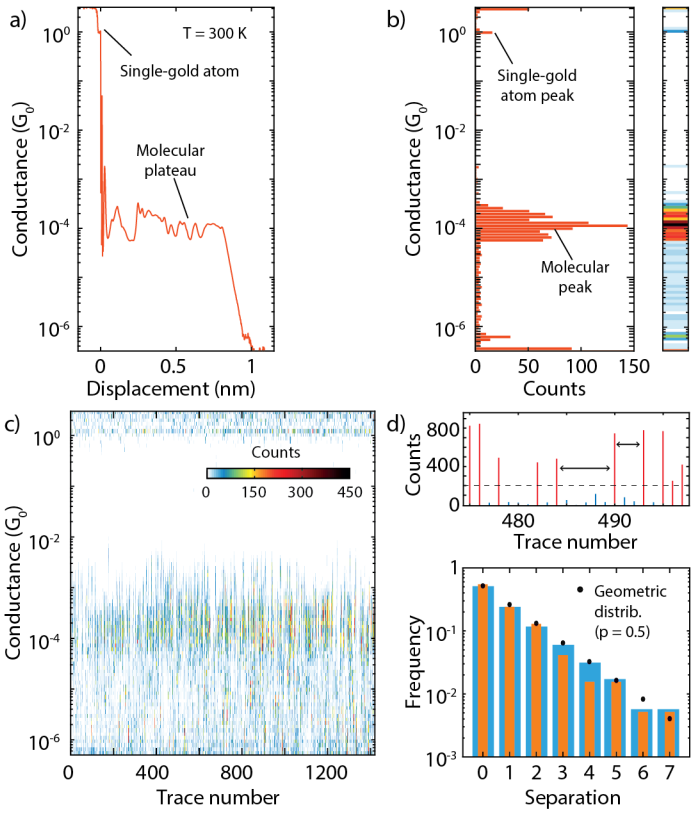

Figure 2.2: a) Conductance-displacement trace measured in the presence of OPE3 at room temperature, bias 0.1 V, and speed 5 nm/s. b) Histogram built from the trace in a) by logarithmically binning the conductance. Right: histogram represented as a color map. c) Two-dimensional color map built from 1.450 breaking traces of OPE3 color-coded like in b). d) Histograms built from trace number 25 to 725 (blue) and from 725 to 1.425 (orange) by counting the number of empty junctions traces separating two subsequent molecular junctions (bottom). The black dots represent a geometric distribution with probability $p = 0.5$.

A conductance histogram built from the trace in panel a) is shown in Fig. 2.2b. The peak in the histogram centered around $1 \cdot 10^{-4}\,G_0$ corresponds to the conductance of the molecular junction and the peak width reflects the variability in the conformations and/or in the local environment felt by the molecule [125, 126]. A different representation of the same histogram is also shown in where the counts of the histogram are represented as colors. Figure 2.2c represents a full data-set built up from 1450 consecutive breaking traces measured as a function of time starting from the deposition of the molecular solution. With an electrode displacement speed of 5 nm/s, each breaking trace takes between 3 to 6 seconds. The 2D histogram reveals that the measurements are homogeneous in time apart for the first 100 traces in which mostly empty junctions appear. However, the diagram shows that even after the initial 100 traces, not all traces contain molecular features.

A junction formation yield as high as possible is not desirable in single-molecule experiments. In fact, the larger the yield the larger the probability that more than one molecule bridges the gap between the electrodes, either in series (dimerization) or in parallel (clusterization). In these cases, it is more difficult to disentangle single-molecule properties from the measurements; for example in the conductance histograms additional structures may appear connected with the formation of junctions with two molecules in parallel [127]. Yield rates of 10 – 30% are usual and yield rates of 90% or more are not advisable. We further note that yield variations occur when comparing different MCBJ samples and/or molecules despite keeping the experimental conditions the same. One important aspect in the junction formation is that molecules have to diffuse inside the gap; temperature, density of molecules adsorbed, gold-molecule interactions and contact geometry are key aspects in determining this process and thus the junction-formation yield.

A final comment concerns the use of breaking traces and the disregard of making traces. While in the breaking, atomically sharp tips are formed that face each other as evidenced in 1D and 2D conductance histograms by a clear feature at $1\,G_0$; in the making of the junction, one cannot be sure that this is the case since the contacts may reconfigure and the two closest points may not face each other, further complicating the analysis of the data. Moreover, the electrode snap-back effect happening at the jump-out-of-contact, which separates the metallic ballistic region from the tunneling one setting the origin of the displacement scale, is only clearly present during the breaking. The electrodes, right after the breaking, are spaced apart by a certain distance that in previous studies was estimated to be about 0.5 nm [122].

Functions commonly used for statistical analysis of single-molecule datasets assume stochasticity of the data, *i.e.*, each single-molecule junction is independent from the other ones meaning that each open-close cycle can be considered as a separate experiment. This can be achieved experimentally by forming a new electrode configuration for every cycle. To enforce that, at the end of every breaking trace we push the electrodes back to a state in which a continuous wire with substantial thickness has been recreated by imposing that it has a conductance of $30 - 40\,G_0$, corresponding to a diameter of few nanometres.

To check that this intuitive picture indeed leads to independent rupture events, we analyse the separation between the successful formation of molecular junctions. This problem can be modelled by picturing the junction opening as the flip of a (biased) coin, the capturing of a molecule as a head (win) and an empty junction as a tail (loss). In other words, the process is a series of Bernoulli trials. This means that the distribution of the separation

between two consecutive molecular junctions should follow the geometric distribution:

$$P(n) = (1 - p)^{n-1} \cdot p \,, \tag{2.1}$$

where n is the number of breaking traces recorded after trapping of a molecule and p is the overall yield rate of the experiment. If capturing a molecule is a random event, the experimental separation between molecular junctions follows this geometric distribution. As illustrated in Fig. 2.2d, this is indeed the case for the conditions used in our experiment.

Individual conductance versus length traces are typically collected in 1D and 2D histograms. To determine the molecular-junction formation yield one has to distinguish between molecular and empty junctions. With recent technical advances, the acquisition of data sets exceeding tens of thousands of breaking traces is common and we developed a simple method for selecting molecular junctions.

The conductance of breaking traces of empty junctions shows an exponential decay with increasing displacement, but if a molecule is trapped the conductance remains higher at larger electrode displacements. Exploiting this fact we sum all counts recorded between $1 \cdot 10^{-2}\,G_0$ and $1 \cdot 10^{-5}\,G_0$ and label as molecular ones those that have more counts in that region than the average; 1D and 2D histograms are then built (Fig. 2.3). This procedure can help uncover features due to molecular configurations that would otherwise be hidden by other more probable configurations. For example, in Fig. 2.3b a short region of higher counts is visible above the main high-count conductance region. This higher conductance feature is present in other devices as well.

In this chapter, we discuss in detail the results of two devices measured at room temperature and two at cryogenic temperatures. Samples measured at low temperatures are typically not used for room-temperature measurements and vice versa since the technical requirements of the measuring setups are different. The results obtained from five additional room-temperature devices are also presented in Table 2.1. The measurements of – done over the course of several years – were performed with the same molecular concentration and with the same experimental settings. Table 2.1 summarizes some of the important parameters obtained from the histograms: the most probable conductance (G_M) as determined from a fit to the peak representing the molecules in the full data set and in the filtered 1D histogram, the full-width at half maximum (FWHM) of this peak, the average plateau length and the junction yield.

As the table shows, variations in the parameters are observed. The most probable conductance value ranges from 1 to $2.4 \cdot 10^{-4}\,G_0$, about a factor two of difference. The FWHM is about one order of magnitude in conductance for all cases. The average plateau length ranges from 0.9 to 1.5 nm. Finally, the sample yield at room temperature changes by an order of magnitude from 7% to 75% among the seven samples. The junction yield thus seems to be determined by geometrical and concentration differences in the region close to the separated electrodes as the other parameters that may influence it are held the same.

To access the stability of the molecule-electrode interfaces and how the mechanical stability depends on the anchoring groups, we have recorded conductance-time traces with the self-breaking technique [77]. In this experiment the gold wire is stretched until the low-bias conductance reaches a value of $10\,G_0$. Subsequently, a bias voltage of 0.1 V is applied and the current flowing through the wire is measured. Due to the built-up strain, the Au wire spontaneously breaks (self-breaking) while the conductance is measured as a function

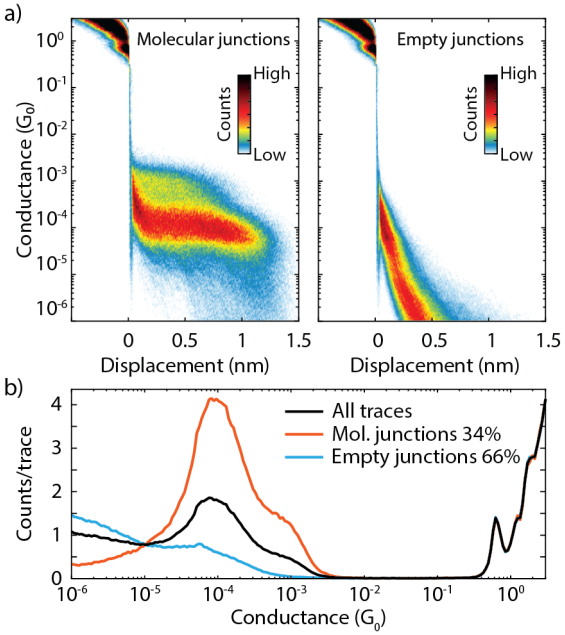

Figure 2.3: a) 2D conductance-displacement histograms of OPE3 built from 10.000 breaking traces (bias 0.1 V and speed 4.5 nm/s. The curves in each histogram have been automatically filtered as described in the main text and correspond to molecular junctions (left) and empty tunnel traces (right). b) Conductance histograms built from all traces (black thick line) and from the two automatically selected groups (thin lines).

of time. Once the conductance falls below $2 \cdot 10^{-7}\,G_0$ the electrodes are fused again until the conductance reaches $40\,G_0$. The sequence is then repeated and hundreds of traces can be collected.

Figure 2.4 shows examples of conductance-time traces measured on OPE3 in a fast-breaking experiment (Fig. 2.4a) and in the self-breaking regime with the electrodes stopped as described above (Fig. 2.4b). Remarkably, we find that the lifetime of the molecular junctions formed with the self-breaking method can reach thousands of seconds (the lifetime of empty junctions is a few seconds at most). Figure 2.4c shows the conductance histograms of OPE3 built from self-breaking traces (thick line) and from fast breaking traces (thin line). The self-breaking histogram displays a sharp peak centered around $1 \cdot 10^{-3}\,G_0$, which is a value comparable to the high-conductance shoulder observed in the fast breaking histogram of OPE3. This configuration appears to be more stable than the one with a conductance around $1 \cdot 10^{-4}\,G_0$ which is the one observed more often in the fast breaking experiments and probably involves the overlap of the outer phenyl rings with the gold electrodes, providing an additional mechanical anchor.

The stability of the MCBJ technique allows one to measure current (I) versus bias voltage (V) characteristics (IV) at different electrode separations. A simplified model can be used to extract the level alignment and the electronic metal-molecule coupling from the data [89, 128, 129]. Since thousands of IVs can be recorded during different breaking traces, a statistical analysis can be adopted to analyze the results.

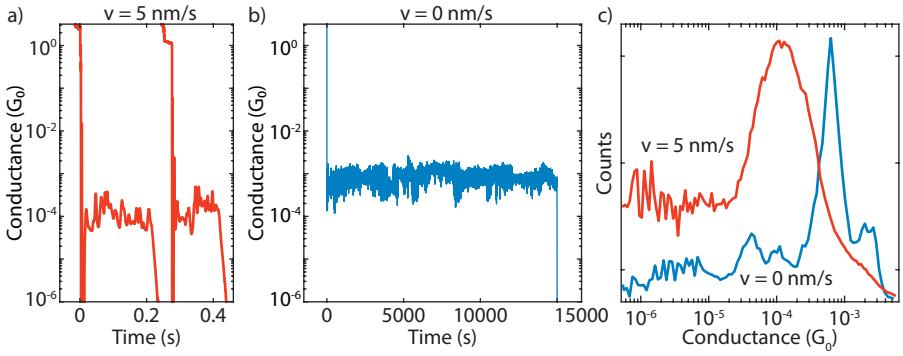

Figure 2.4: a) Individual breaking traces measured in the presence of OPE3 molecules (bias 0.1 V and speed 5 nm/s). The traces are offset along the x-axis for clarity. b) Same as a) with the electrodes stopped. c) Conductance histograms built from the conductance traces recorded in the presence of the molecule. The red thick curve is the histogram built from 1.450 fast breaking traces (v = 5 nm/s), and the blue thin line is built from 275 self-breaking traces (v = 0 nm/s). Adapted with permission from [77]. Copyright Beilstein-Institut.

To measure current-voltage characteristics of molecular junctions we separate the electrodes at a lower speed than during the acquisition of the conductance traces discussed above, typically at a speed of 0.01 nm/s. While the gold wire is still intact, the bias is swept between −0.1 V and 0.1 V until the low-bias conductance reaches a value smaller than 0.1 G_0. After this, we continuously sweep the voltage between −0.7 V and 0.7 V at a rate of 0.05 V/s. At room temperature the voltage applied to a single-molecule junction cannot be too high and empirically the value of 0.8 V appears to be the maximum. On the other hand, at low temperatures higher voltages up to a few Volts can be applied. Once the low-bias conductance drops below $1 \cdot 10^{-6}$ G_0, the gold contact is reformed until the conductance reaches 30-40 G_0 and a new breaking trace starts. In this way hundreds of individual IV breaking traces are recorded yielding thousands of individual IVs.

The asymmetric Breit-Wigner model [130, 131] can be used to extract quantitative information from the IVs yielding three parameters: the electronic coupling between molecule and left and right electrode, respectively Γ_L and Γ_R, and the injection barrier ε_0, defined as the misalignment between the Fermi energy of the electrodes (E_F) and the energy of the closest frontier orbital $\varepsilon_0 = |E_F - \varepsilon|$, where ε is the energy of the closest frontier molecular orbital. In the Landauer transport formalism [132], the current is given by:

$$I(V) = \int_{E_F - \frac{eV}{2}}^{E_F + \frac{eV}{2}} T(E)\,\mathrm{d}E\ , \tag{2.2}$$

where $T(E)$ is the transmission, which in the single-level model is a Lorentzian peak centered at ε_0 and broadened by the electronic coupling $\Gamma = \Gamma_L + \Gamma_R$. An asymmetry in the IV can be modelled by introducing a voltage dependence in the Lorentzian peak position, that is replacing ε_0 with $\varepsilon_0(V) = \varepsilon_0 + \eta\frac{V}{2}$ where η is a dimensionless parameter between −1 and 1 ($\eta = 0$ gives symmetric IVs). Often the approximation $\eta = (\Gamma_L - \Gamma_R)/(\Gamma_L + \Gamma_R)$ is used, but one should keep in mind that η depends on the capacitive coupling, which in principle is independent from the asymmetry in the resistance coupling. In Fig. 2.5a the drawn red line

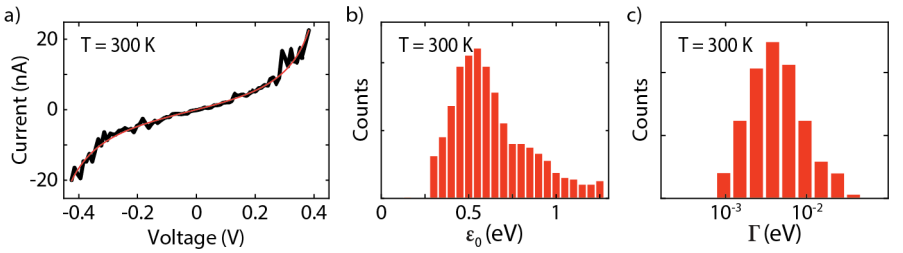

Figure 2.5: a) Example of a room temperature IV of OPE3. The black thick line represents the experimental data while the red thin curve is a fit to the single-level model. b,c) Parameters extracted from the fit of 985 room temperature IVs.

is a fit of a measured IV characteristic to the single-level model. Good agreement is found with $\varepsilon_0 = 0.49\,\text{eV}$ and $\Gamma = 9\,\text{meV}$. Note, that in this case a symmetric bias was chosen so that $\eta = 0$. The fitting has been performed on 985 IVs obtained from 40 different molecular junctions. Figure 2.5b,c shows the histograms of the fit parameters: the level alignment peaks around 0.5 eV with a long tail towards energies up to 1.5 eV. The electronic coupling ranges from 1 to 20 meV; the average value is 8 meV. It is important to realize that these numbers are anchoring group dependent, which indicates the importance of charge redistributions near the interface that affect the electrostatic environment of the molecule and thereby its level alignment.

2.3. LOW-TEMPERATURE MEASUREMENTS

When carrying out MCBJ measurements at cryogenic temperatures a stepper motor connected to a differential screw is used instead of a piezo. The electrode speed is limited to 0.2 nm/s and thus a longer measurement time is needed to complete each breaking event. Moreover, due to the reduced atomic and molecular mobility at low temperature, the molecular junction-formation yield is strongly reduced, going from approximately $10 - 70\%$ at room temperature to $2 - 5\%$ at low temperatures. The combination of a longer measuring time and lower junction-formation yield implies that a smaller number of molecular junctions can be probed as compared to room-temperature studies. The main advantages at low temperature, on the other hand, are the reduced thermal noise, which allows for more precise electrical measurements, and the increased electrode and molecule-electrode stability, that permits larger bias voltages to be applied.

Figure 2.6a displays three conductance versus displacement traces measured on OPE3 at a temperature of 10 K. In the region below $1\,G_0$, the conductance traces show plateaus, typically at around $1 \cdot 10^{-4}\,G_0$, a value similar to the room-temperature one. The plateaus extend for a length of about 1.5 nm after which the conductance drops to the noise level of the setup. The three plateaus present regions in which the conductance evolves gradually and regions with abrupt conductance changes. We have measured more than 1000 breaking traces and built a conductance histogram, shown in Fig. 2.6b, by selecting the 38 traces that show a conductance plateau in the region between $1 \cdot 10^{-2}\,G_0$ and $1 \cdot 10^{-5}\,G_0$ with the filter procedure discussed earlier (junction formation probability of 3.5%). The low-temperature conductance histogram can be compared to the room-temperature one. Apart from the

better signal-to-noise ratio in the latter histogram, the distribution of conductance values is similar; at both temperatures the conductance peak has a width of approximately one order of magnitude and is centered respectively around $1.8 \cdot 10^{-4}\,G_0$ (10 K) and $1.2 \cdot 10^{-4}\,G_0$ (300 K). These observations support coherent tunneling as the main transport mechanism in single-OPE3 junctions.

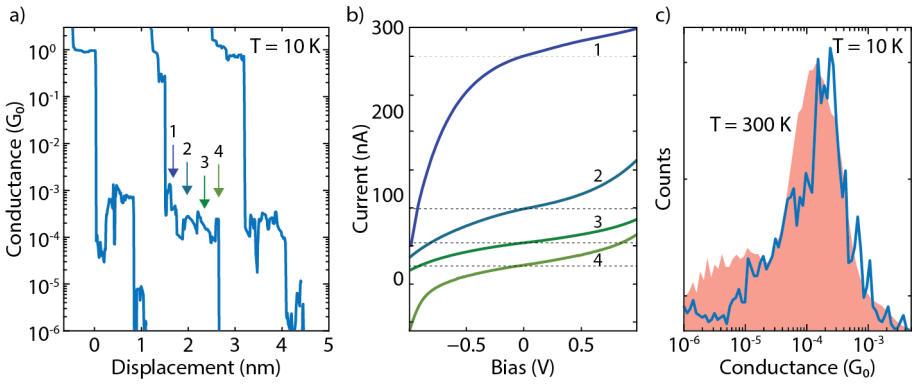

Figure 2.6: a) Breaking traces recorded in the presence of OPE3 (sample 3) at a temperature of 10 K (0.1 V). The traces have been offset along the x-axis for clarity. b) Current-voltage characteristics measured during the central breaking trace shown in a), shifted along the y-axis for clarity. c) Conductance histogram built from molecular low temperature and room temperature conductance traces. Adapted with permission from [78]. Copyright American Physical Society.

During a low-temperature breaking trace one can also record IVs at each electrode position (with minimum separation being approximately 10 pm). Figure 2.6c shows four IVs measured at four different positions in the central breaking trace displayed in Fig. 2.6a. The current can be asymmetric in voltage (IVs 1, 4) or symmetric (IVs 2, 3) and conductance switches -either gradually or abruptly- occur while stretching. Configurational noise, which at room temperature manifests itself in a large width of molecular conductance peaks, translates at low temperature into clear jumps. Interestingly, IVs recorded just after molecular-junction formation typically present a large asymmetry; the coupling to the electrodes being is in this case very asymmetric. A possible scenario involves the interaction of only one phenyl ring with one electrode, while on the other side a sulfur-gold connection provides the coupling.

Figure 2.7a shows one IV characteristic of a molecular junction recorded in the central breaking trace of Fig. 2.6a (plateau region). The IV is symmetric and it can be well fitted to the Breit-Wigner model with parameters $\Gamma_L = \Gamma_R = 0.3$ meV and $\varepsilon_0 = 0.64$ eV. We fitted 297 IVs recorded from 13 breaking traces showing molecular plateaus and collect the fit parameters in the histograms of Fig. 2.7b-c. Similar to the room temperature case, a parameter spread is observed as evidenced in the histogram widths. The level alignment is shifted to slightly larger values compared to the room temperature case, whereas the electronic coupling covers the range from 1 to 10 meV.

The high junction stability at low temperature allows following the evolution of the fit parameters upon separating the electrodes. Figure 2.8a-b displays two conductance plateaus with a conductance that fluctuates around $5 \cdot 10^{-5}\,G_0$ and around $2 \cdot 10^{-4}\,G_0$ respectively,

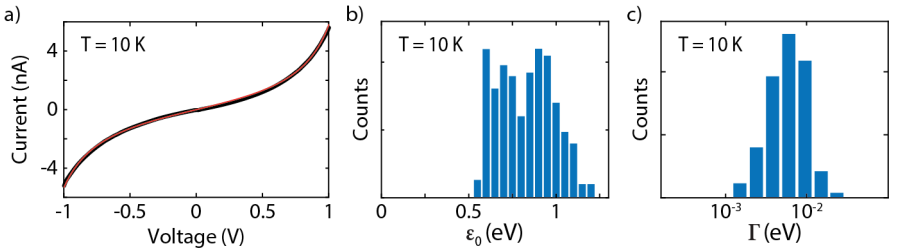

Figure 2.7: a) Example of a low-temperature *IV* of OPE3. The black thick line represents the experimental data, while the red thin curve is a fit to the single-level model. b,c) Parameters extracted from the fit of 297 low temperature *IV*s.

with continuous regions (in which the conductance gradually increases or decreases) separated by abrupt jumps. Figure 2.8c-d shows the level alignment at each position for the two junctions, while Fig. 2.8e-f shows the electronic coupling. In the continuous regions the parameters ε_0, Γ_L and Γ_R gradually change value. In contrast, conductance jumps induce abrupt changes either in the coupling or in the level alignment or in both parameters at the same time. In junction 2 in Fig. 2.8b, one can see that in the first part of the stretching both the conductance and the electronic coupling show three jumps while the level alignment evolves gradually from 0.7 eV to 0.95 eV at 0.8 eV/nm. The measurements thus confirm the intuitive picture that the jumps are connected to abrupt changes in the junction conformation at the atomic level.

We have also investigated the *IV*s when exposed to bias voltages up to 3.7 V at cryogenic temperature ($\approx$ 6 K). The measurements initially follow the standard procedure of stretching the gold wire until it ruptures, forming the electrodes. The conductance is measured continuously during this process, until the drop in conductance signals the opening of the junction. At this point the electrodes are displaced further by 0.4 nm and then an *IV* curve is recorded. In the first *IV* the voltage is swept in the range of $\pm$0.1 V. After this displacement of 0.4 nm, empty junctions have a conductance lower than the noise level ($1 \cdot 10^{-7}$ G_0), while for molecular junctions the conductance remains well above this level and in this case another *IV* is taken with a voltage sweep that is larger by a value of 0.3 V. The process is repeated until the zero-bias conductance falls below $1 \cdot 10^{-7}$ G_0 or until a voltage limit of $\pm$3.7 V is reached.

Figure 2.9a shows the distribution of the zero-bias conductance values obtained from the *IV*s versus the maximum voltage applied before losing the molecule. Blue areas represent low counts, while red areas indicate high counts. The inset shows the corresponding 1D conductance histogram which indicates that more than one conductance value can be found. The most probable conductance at room temperature ($1.5 \cdot 10^{-4}$ G_0) is one of the values, but not the most likely one in this type of measurement. A large percentage of *IV*s has conductance values centered around $1 \cdot 10^{-3}$ G_0 and $1 \cdot 10^{-5}$ G_0. The presence of different conductance values is due to the different junction configurations which are stable at low temperature.

Figure 2.9b shows the conductance histogram for *IV*s with the same voltage limit. Go-

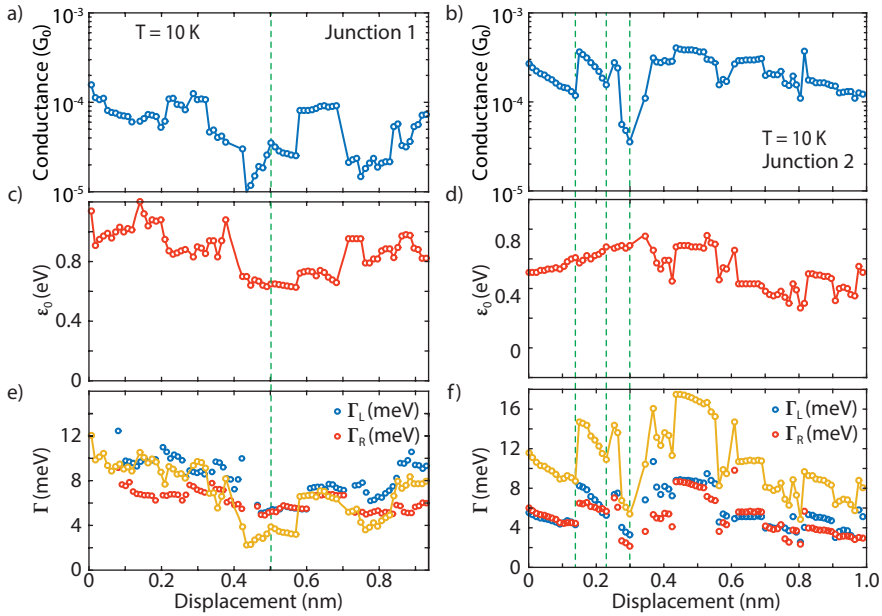

Figure 2.8: a,b) Low-temperature conductance traces obtained from a low-bias fit of *IV*s. c,d) Corresponding level alignment and e,f) electronic coupling during electrode separation as determined from fits to the Breit-Wigner model.

ing from ±0.4 V (blue histogram) to ±1.0 V (green) and ±2.1 V (red), an overall decrease of counts at high conductance values is observed while peaks at lower conductance become more relevant. The counts around $1 \cdot 10^{-3}$ G_0 are prominent at ±0.4 V, but decrease considerably at ±1.0 V and are absent for junctions to which more than ±2.1 V has been applied. Something similar happens to the *IV*s with a conductance of $1 \cdot 10^{-4}$ G_0, which make up the majority of conductance values up to ±1.0 V but decrease sharply in numbers for larger voltages allowing the conductance values around $1 \cdot 10^{-5}$ G_0 to become the most probable ones in that region. The choice of the bias voltage range can thus change dramatically the single-molecule conductance distribution.

2.4. CONCLUDING REMARKS

We presented a detailed study of the transport properties of single OPE3 molecules anchored to gold electrodes. The measurements show that a single molecule can be contacted by two metal electrodes, but the atomistic configuration of each single junction is not known. Variations in the level alignment and electronic coupling, give a broad distribution (one order of magnitude) in the observed conductance values indicating that at the microscopic level both the hybridization with the metallic electrodes and the molecular electronic configuration can fluctuate. The low-temperature data show that these variations are due to abrupt changes in the configuration of the molecule in the junction leading to abrupt changes in either one of these parameters or both at the same time. The comple-

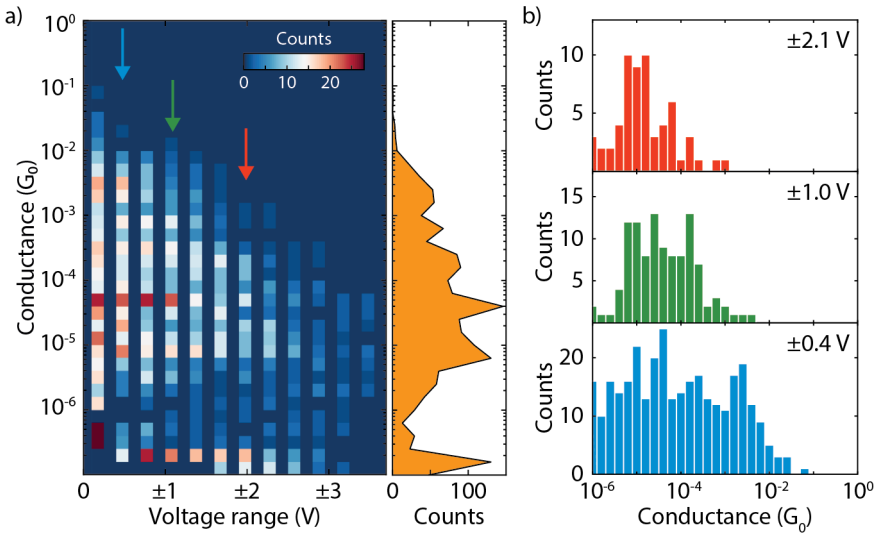

Figure 2.9: a) Histogram of the zero-bias conductance versus the voltage limit of the *IV* (at cryogenics temperature of ≈ 6 K). Red points have high counts, while blue ones have low counts. The inset shows the conductance distribution obtained by integrating over the voltage range. b) Low-bias conductance distribution of an *IV* recorded to a given voltage limit. The histograms are built from *IV*s with ±0.4 V voltage sweep (blue), ±0.1 V (green), and ±2.1 V (red).

mentary information gained from different experiments is needed to build up a consistent and extended picture of the variability of molecular configurations, omnipresent in single-molecule studies. Statistics helps to understand the overall behavior from which a clear picture of the average configuration emerges. Knowledge of this variability can help to better understand the behavior of molecules at the atomic level and at the metal-molecule interface in particular.

Sample	Bias voltage (mV)	Bending speed (μm/s)	G_M ($10^{-4}G_0$)	FWHM ($\log_{10}(G_0)$)	Avg. trace length (nm)	Molecular yield
1	100	150	1.5	1.0	0.9	60%
2a	100	60	1.0	0.9	1.2	35%
2b	100	100	1.3	1.0	1.4	75%
5a	100	15	1.1	1.0	1.0	15%
5b	100	15	1.3	1.0	1.1	7%
6	100	30	1.1	0.9	1.3	43%
7a	50	30	1.5	1.0	1.1	42%
7b	100	30	2.3	1.3	1.2	71%
7c	150	30	1.8	1.0	1.2	40%
7d	200	30	2.2	1.1	1.3	57%
7e	250	30	2.2	1.0	1.4	43%
7f	300	30	1.9	1.1	1.1	33%
8a	100	7.5	1.4	1.1	1.0	49%
8b	100	15	1.1	1.0	1.1	40%
8c	100	30	1.1	0.9	1.1	32%
8d	100	60	1.0	0.9	1.2	37%
9a	50	30	1.4	0.7	1.6	32%
9b	100	30	1.5	1.1	1.3	41%
9c	150	30	1.7	1.1	1.4	35%
9d	200	30	2.0	1.1	1.5	45%
9e	250	30	2.0	1.1	1.5	57%
9f	300	30	2.4	1.0	1.4	67%

Table 2.1: Transport parameters from fast breaking conductance-displacement experiments on seven different MCBJ samples at room temperature (indicated by numbers) in presence of OPE3 done at different breaking speed and bias voltage. Measurements performed on the same sample under different conditions are labelled with letters.

3

Role of anchoring groups

Fullerenes have attracted interest for their possible applications in various electronic, biological, and optoelectronic devices. However, for efficient use in such devices, a suitable anchoring group has to be employed that forms well-defined and stable contacts with the electrodes. In this work, we propose a novel fullerene tetramalonate derivate functionalized with trans-1 4,5-diazafluorene anchoring groups. The conductance of single-molecule junctions, investigated in two different setups with the mechanically controlled break junction technique, reveals the formation of molecular junctions at three conductance levels. We attribute the conductance peaks to three binding modes of the anchoring groups to the gold electrodes. Density functional theory calculations confirm the existence of multiple binding configurations and calculated transmission functions are consistent with experimentally determined conductance values.

Parts of this chapter have been published in Chemistry of Materials **29** (17), 7305–7312 (2017)
Part of the experimental measurements and analysis in this chapter have been performed by A. Gutierréz-Cerron and J. Labra-Muñoz (University of Chile, Chile) The chemical synthesis has been performed by C. Suarez, S. Liu, and L. Echegoyen (University of Texas, U.S.A.), the theoretical calculations have been performed by D. Aravena (University of Santiago de Chile, Chile).

3.1. INTRODUCTION

For many years a wide variety of fullerene derivatives has been reported and their potential applications as electronic, magnetic, catalytic, biological and optical materials have been explored [133–139]. In particular, C_{60} and its derivatives are ideal candidates for molecular-based devices because of their interesting and unique electronic properties [140, 141]. One of the long-standing challenges in obtaining functional molecular electronic devices is the transport of electrons through single molecules [24, 142]; *i.e.* it is necessary to guarantee molecular conduction through a single molecule rather than through a group of molecules [143]. The electron transport properties of single molecules can then be controlled electrically, magnetically, optically, mechanically or chemically to obtain the desired functionality [144]. However, in the case of fullerene derivatives, the groups used to functionalize the carbon cage may also modify the electronic properties of the molecule [145]. In addition, the molecule needs to possess anchoring groups that will form well defined and stable molecular junctions with the electrodes [89, 146, 147]. Therefore, the orientation and nature of the anchoring groups will affect the charge transport properties of the molecule. Finding a suitable anchoring group to connect C_{60} electrically would be an important step towards more interesting derivatives in the future.

Charge transport in pristine C_{60} has been studied for a long time using both scanning tunnelling microscope break junction (STM-BJ) [148, 149] and mechanically controlled break junction (MCBJ) [150, 151] techniques and conductance values around 0.1 G_0 have been reported; here G_0 is the quantum of conductance equaling $2e^2/h = 77.48$ μS [152, 153]. Taking advantage of its affinity for metals, C. Martin *et al.* [154] studied a 'dumbbell' benzene-difullerene (BDC60) derivate in which C_{60}, at both ends of the molecule, acts as the anchoring group. The single peak of conductance found at $3 \cdot 10^{-4}$ G_0 for this derivative was attributed to a transport-limiting barrier created by the nitrogen atoms of the pyrrolidine rings that are connected to the benzene backbone [155]. An analogous work with a dumbbell fullerene molecule reported a conductance peak around $1 \cdot 10^{-4}$ G_0 confirming the low conductance values for functionalized fullerenes [156]. Additionally, a more recent study of a dumbbell fullerene derivative shows two different electronic transport configurations, one assigned to the transport through the molecular bridge and the second, at higher conductance values, ascribed to a single C_{60} anchoring group trapped between the two adjacent electrodes [157]. These two peaks differ by two orders of magnitude (10^{-1} G_0 and 10^{-3} G_0), which is relatively consistent with the previous reported values for pristine C_{60} fullerenes [148–151] and dumbbell C_{60} fullerene derivatives [154–156, 158]. We can also find theoretical studies that support these results [159, 160] and experimental studies of other C_{60} fullerene derivatives, *i.e.* amino-terminated derivatives [161].

In this work, we study the molecular conductance through single-molecule junctions of a C_{60} fullerene all-equatorial tetramalonate derivate functionalized with *trans*-1 4,5-diazofluorene anchoring groups [162] (see structure in Fig. 3.1b and hereafter denoted as C_{60}-daf for convenience). The diazafluorene anchoring groups are perfectly perpendicularly oriented with respect to the fullerene surface, and linearly disposed with respect to each other. Four equatorial diethyl malonate groups were added to the C_{60} to avoid direct interactions between the gold electrodes and the fullerene cage. The ethyl esters in these groups have high contact resistance and low binding energy to gold, which effectively renders them bulky groups that block access to the C_{60} cage [91]. This aspect and the evidence

of direct coordination between the diazafluorene groups and many metal ions [162, 163] suggest that the formation of a molecular junction occurs only through a linear arrangement of diazafluorene groups and the gold electrodes. Such a junction structure allows the study of charge transport through the carbon cage of the fullerene derivative. The computational simulations performed indeed show preferential binding of the nitrogen atoms to the gold leads and that the highest occupied molecular orbital (HOMO) is sufficiently well communicated to allow the electronic transfer.

Because one of the biggest challenges in molecular electronics field is to have comparable and reproducible results between different techniques, instruments, or data sets, we have performed our experiments in two identical MCBJ setups located in two different laboratories in Delft and Santiago de Chile.

To the best of our knowledge, the diazafluorene group has never been tested as an anchoring group before [85, 164]. In addition, charge-transport studies using a C_{60} derivative with *trans*-1 terminal groups to form molecular junctions with gold electrodes have not been reported.

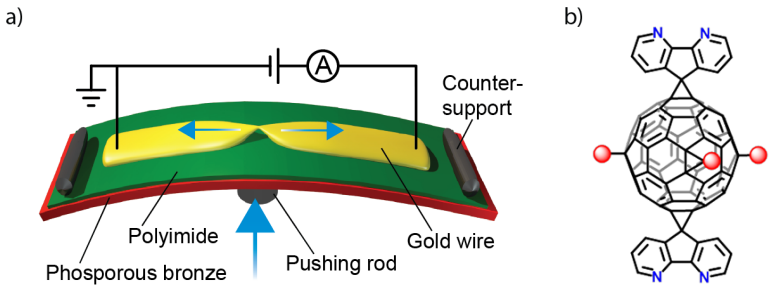

Figure 3.1: a) Schematics of the MCBJ devices used in the experiment [165]. b) Chemical structure of the *trans*-1-bis-diazofluorene adduct of C_{60}-tetramalonate (C_{60}-daf). Malonates are designated with red balls representing the $C(COOC_2H_5)_2$ groups.

3.2. Results and discussion

The conductance of C_{60}-daf (Fig. 3.1b) was measured in air at room temperature. Both MCBJ setups (the setups are copies and made in Delft/Leiden) and the measuring technique have been extensively described elsewhere [165, 166]. To fabricate the MCBJ devices (Fig. 3.1a), e-beam lithography is used to deposit a gold wire with a thin (<100 nm wide) constriction on a bendable substrate. The substrate is then bent by driving a pushing rod onto its middle part while keeping its edges clamped. This causes the gold wire to stretch until a single gold atom connects the two extremities. Further bending results in a breaking of the wire forming two sharp electrodes. The single-gold atom termination can be observed in a conductance vs. electrode displacement trace (breaking trace) as the formation of a plateau around 1 G_0. A sudden drop in conductance to about 10^{-3} G_0 signals the rupture of the gold wire. This point is defined as the zero displacement ($d = 0$) in a breaking trace. After the initial opening of the junction, the electrodes are moved apart and the conductance is recorded until the noise level is reached. When this sequence is finished, the electrodes are fused back together until the conductance is above 30 G_0 and the whole process is

repeated.

We start each experiment by characterizing the bare device. We apply a bias voltage of 0.1 V to the gold wire and measure the current passing through it while repeatedly opening and closing the junction. A device is used for molecule measurements only if it shows just vacuum tunneling and a clear single-gold atom, 1 G_0 plateau [118]. An $\approx$ 30 µM solution with the molecules under investigation is prepared by dissolving the starting compound in dichloromethane. Two 2 µl droplets of the solution are subsequently drop-cast on the freshly characterized device.

A data set is composed of thousands of consecutive breaking traces from individual junctions recorded with the same settings and is used to construct a 2D conductance histogram (conductance vs. electrode displacement) [118]. By integrating over the displacement, a one-dimensional histogram is obtained, from which the most probable junction conductance is usually estimated. To facilitate the identification of molecular traces, a homemade MatLab program is used to select traces that have high counts in the conductance region of interest. The filtering method is based on the fact that if a molecule is not trapped in the junction the conductance decreases exponentially; the corresponding breaking trace therefore does not display many counts in the high-conductance region. The filtering procedure can also be used to estimate the percentage of junctions that contain a molecule. To construct the 2D histogram in Fig. 3.2a, we used the following criterion: traces that have 1.2 times the average amount of counts in the $1 \cdot 10^{-4}$ to $1 \cdot 10^{-6}$ G_0 region are selected. The inset in the same figure displays the traces that did not satisfy the requirements and were therefore excluded from the selection. The sum of these two histograms thus constitutes the complete data set.We have furthermore verified that when adjusting the filtering criteria the main conclusions of the paper do not change.

The 2D histogram in Fig. 3.2a shows a high-count region around 10^{-5} G_0, which extends up to 1.5-2 nm. The counts are concentrated mostly around two values and a log-normal fit of the one-dimensional histogram (Fig. 3.2c) indicates that the corresponding most probable conductance values are $2.3 \cdot 10^{-5}$ (peak A) and $7.9 \cdot 10^{-6}$ G_0 (peak B). The individual breaking traces show that the plateaus can (traces i-ii in Fig. 3.2b) but do not always appear together (trace iii). Some breaking traces also show a third plateau around $2 \cdot 10^{-6}$ G_0 (traces iv-v in Fig. 3.2b), but their appearance is not as frequent. Including this third peak in the fitting increases the accuracy of the fit and yields a conductance value of $1.8 \cdot 10^{-6}$ for peak C.

The experiment has been repeated in Santiago de Chile by the group of D. Dulić. Fig. 3.3a shows the two-dimensional histogram obtained from a selection of the 5.000 traces collected (same criterion as used in Fig. 3.2a; a histogram made from the rest of the traces is shown in the inset). The same bias voltage of 0.1 V as in Delft was used, but the electrode speed was one and a half times higher in this case. The plot confirms the same high-count region near 10^{-5} G_0, displaying a striking resemblance with the one measured in Delft. In addition, the histogram measured at Santiago de Chile more clearly shows the high counts in the low-conductance region, centred around $2 \cdot 10^{-6}$ G_0 and extending to lengths of 1.5 nm. The one-dimensional histogram (Fig. 3.3b) highlights this area with a peak in conductance, from which the most probable conductance value of $1.7 \cdot 10^{-6}$ G_0 (peak C) is obtained. The log-normal fit of the higher conductance region yields $3.1 \cdot 10^{-5}$ (peak A) and $7.7 \cdot 10^{-6}$ G_0 (peak B), values which are close to those found in the measurements

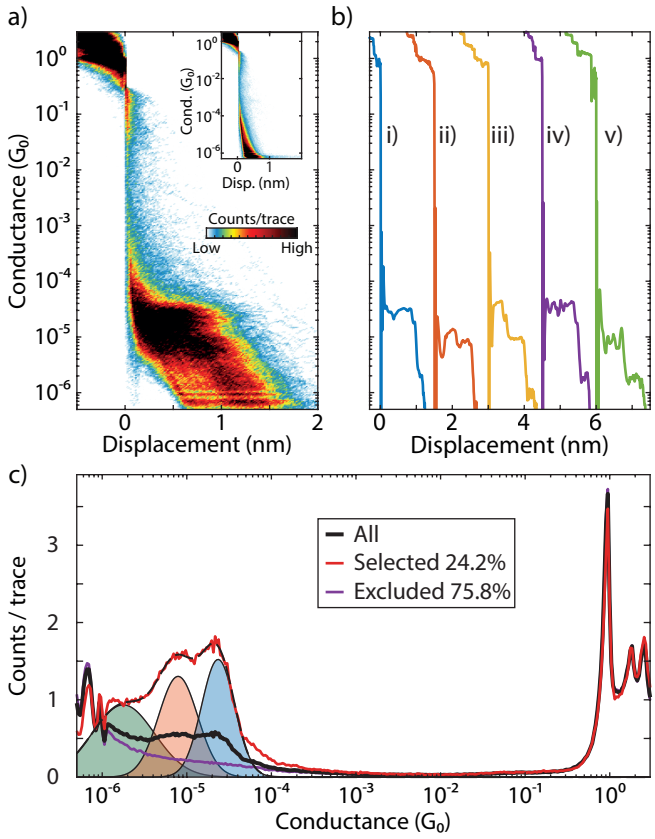

Figure 3.2: a) Two-dimensional conductance histogram built from a selection of the 10.000 consecutive breaking traces recorded after drop-casting the solution containing C_{60}-daf. Traces that had 1.2 times the average amount of counts between $1 \cdot 10^{-4}$ and $1 \cdot 10^{-6}$ G_0 were selected (24.2% of the total). The inset shows the traces that were not selected (*i.e.*, that have less than 1.2 times the average count in the region under consideration, 75.8%). The breaking traces have been logarithmically binned in the conductance axis with 49 bins/decade and with 58.4 bins/nm in the displacement axis. The applied bias voltage is 0.1 V and the electrode speed is 4.0 nm/s. b) Individual breaking traces in the presence of a C_{60}-daf molecule. Traces are offset along the x-axis by 1.5 nm for clarity. c) Normalized one-dimensional histograms obtained by integrating the breaking traces along the displacement axis. The red line represents the histogram obtained for the selected traces, the purple line from the excluded traces, and the thick black line shows the histogram of the whole data set. The dashed black line represents the log-normal fit to the selected histogram (red line). Experiment conducted in Delft, The Netherlands.

performed in Delft.

From the conductance histograms in Fig. 3.2-Fig. 3.3 it is evident that peak A represents the most probable formation of molecular junctions in both measurements. The measurements obtained in Delft show the presence of peak B more clearly, whereas peak C is more pronounced in the measurements from Santiago de Chile. A comparison between the fit results obtained from fitting the data set acquired in Delft and in Santiago de Chile can be seen in Tab. Table 3.1. The values obtained from two other samples are also included within parenthesis.The conductance values for the three peaks obtained in Delft and in Santiago

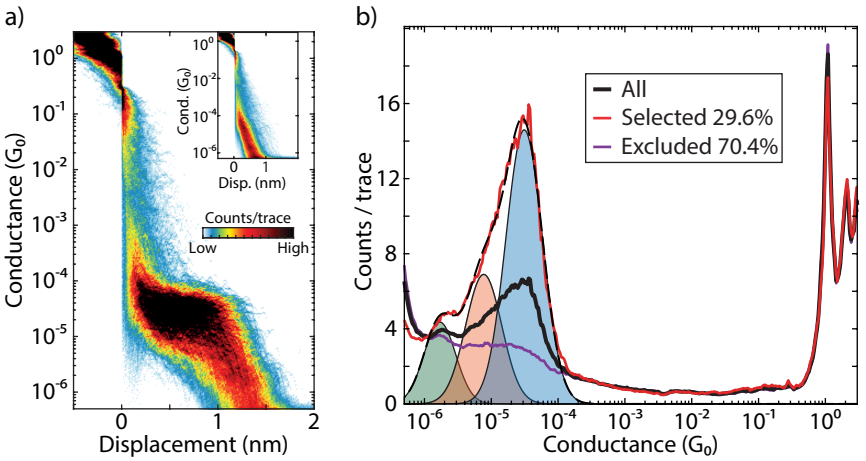

Figure 3.3: a) Two-dimensional conductance histogram built from a selection of the 5.000 consecutive breaking traces recorded after drop-casting the solution containing C_{60}-daf. Traces that had 1.2 times the average amount of counts between $1 \cdot 10^{-4}$ and $1 \cdot 10^{-6}$ G_0 were selected (29.6% of the total). The inset shows the traces that were not selected (*i.e.* that have less than 1.2 times the average count in said region, 70.4%). The breaking traces have been logarithmically binned in the conductance axis with 49 bins/decade and with 88.4 bins/nm in the displacement axis. The applied bias voltage is 0.1 V and the electrode speed is 6.0 nm/s. b) Normalized one-dimensional histograms obtained by integrating the breaking traces along the displacement axis. The red line represents the histogram obtained for the selected traces, the purple line from the excluded traces, and the thick black line shows the histogram of the whole data set. The dashed black line represents the log-normal fit to the selected histogram (red line). Experiment conducted in Santiago de Chile, Chile.

de Chile match very well. The width (w) of peaks A and B is very similar in both cases, whereas that of peak C is different. We attribute this difference to the difficulty of fitting peak C in the sample obtained in Delft. Furthermore, peak A is more prominent in the measurements from Santiago de Chile, while its importance is less striking in those from Delft (this is true for all samples except one). Peak C is the smallest one in all measurements.

Recently, Seth *et al.* [167] studied the conductance through a bis-terpyridine derivate with the MCBJ technique, finding that multiple configurations that display short plateaus are accessible for charge-transport with the conductance spanning several orders of magnitude. Although we could expect a similar behaviour from the diazafluorene group, the number of accessible conductance configurations should be less because of the reduced number of nitrogen atoms. Moreover, the C_{60} and malonate groups contribute to the rigidity of the molecule, resulting in more stable conductance plateaus, as clearly shown in the data presented in Fig. 3.2-Fig. 3.3. We tested the behaviour of this molecule in our setup and to be able to do a more accurate comparison with these previous result we measured its single molecule conductance. In this case we did not observe well defined conductance values , again suggesting that the presence of the C_{60} molecular bridge plays an important role in obtaining well defined molecular junctions. Moreover, the additional nitrogen binding site could provide configurations with more similar conductance to each other, thus hindering their identification.

Although the measurements cannot directly discard the involvement of the aromatic

	Delft			Santiago de Chile		
Peak	μ (10^{-5} G_0)	p	w	μ (10^{-5} G_0)	p	w
A	2.3 (2.3)	-4.7 (-4.6)	0.6 (0.5)	3.1 (2.8)	-4.5 (-4.6)	0.6 (0.6)
B	0.79 (0.87)	-5.2 (-5.1)	0.5 (0.7)	0.77 (0.82)	-5.1 (-5.1)	0.6 (1.3)
C	0.18 (0.12)	-5.8 (-5.9)	0.9 (1.7)	0.17 (0.16)	-5.8 (-5.8)	0.6 (0.4)

Table 3.1: Comparison of the fitting parameters obtained from the measurements in Delft and Santiago de Chile.

The $\log_{10}$ of the peaks found in the one-dimensional conductance histogram after data filtering were fitted to a triple-log normal ($y = h\, e^{-\left(\frac{\log_{10}(G/G_0)\, p}{w}\right)^2}$), where p is the peak maximum expressed in $\log_{10}(G/G_0)$, μ is the corresponding conductance in G_0, w is the full-width-half-maximum of the peak expressed in $\log_{10}(G/G_0)$, and h is the peak height (not displayed in the table). The results obtained from two other samples are included within parenthesis.

rings in the diazafluorene units in the charge transport, we would expect a more continuous decrease in conductance if they were involved, instead of the step-like plateaus observed in the breaking traces. The more continuous decay would in turn result in a broader distribution of the conductance values instead of the agglomeration around only three separate values, each with a variance comparable to that of other experiments that employ amino anchoring groups [77, 96].

To gain additional insight on the binding configurations of C_{60}-daf, *ab-initio* density functional theory calculations have been performed. The transmission function $T(E)$ at zero bias was calculated using the B3LYP functional (see Computational Details section for a detailed description of the computational methodology). To consider the different binding modes of the diazafluorene group, a geometry optimization of this anchoring group and a Au_{20} cluster was performed. The lowest energy conformation corresponds to a geometry in which the Au_{20} cluster is coordinated to the two N-donor atoms with a distance of ca. 2.45 Å. A relaxed surface scan was then run, elongating the distance between the top Au atom and the central C atom of the diazafluorene moiety (position 9 of the fluorene moiety, see Fig. 3.4). As the distance constraint is not defined with respect to the Au–N distance, the nitrogen atoms are free to accommodate their position with respect to the gold tip during the scan.

A clear rupture of one of the Au–N bonds occurs at a Au–C(9) distance of 5.35 Å, when one of the Au–N bonds remains short (blue line) while the other is markedly longer (red line) (Fig. 3.4a). Considering the orientation change of the diazafluorene group during the breaking of the Au–N contacts, it is also convenient to explore the possibility of a van der Waals contact between the Au and the H atoms in the diazafluorene. Such interactions can yield additional low-conductance peaks and have been identified in molecular junctions with thiophene anchoring groups [168]. In this way, a second surface scan was performed; this time by elongating the Au–H distance (Fig. 3.4b). A clear minimum is observed at 2.18 Å when using a dispersion corrected density functional (D3 correction and BP86 functional). The corresponding Au–C(9) distance is 7.49 Å in this conformation.

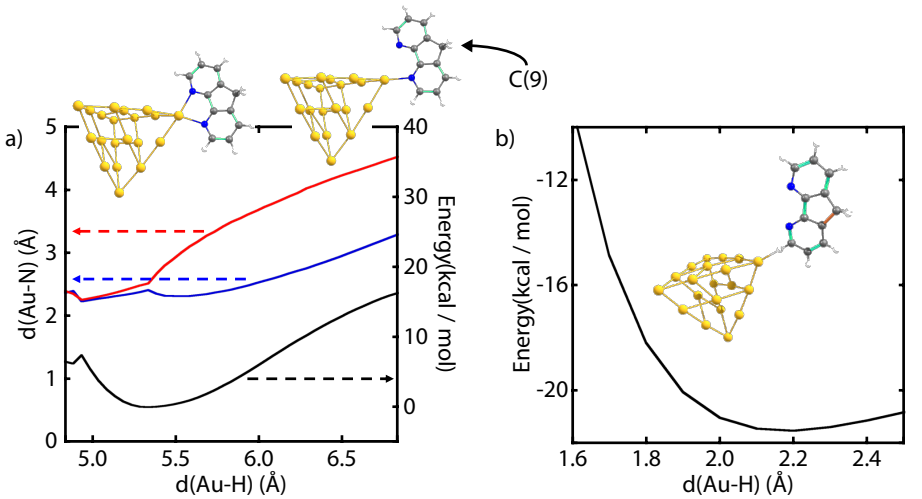

Figure 3.4: a) Au–N distance (blue and red lines) and total energy (black line) at each step of the surface scan of the diazafluorene-Au_{20} model. Snapshots of a two- and one- N coordinated geometry are depicted in the graphic. b) Potential energy surface for the Au–H interaction.

The three binding motifs can be combined to yield nine different anchoring patterns to the gold tips: ranging from a strongly bonded geometry where both diazafluorene groups are bonded through their two N atoms, to a weakly bonded case with two Au–H interactions. Regardless of the specific binding mode, all calculations show a relatively large band gap (>3 eV), where the LUMO orbital tends to be closer to the Fermi level (between 1 and 1.5 eV above E_F) and should therefore dominate electron transport. Despite the relatively large extension of the molecule, pronounced conductance peaks can be observed. In Fig. 3.5, broad maxima are present at –2.5 eV, 1 eV and 2-3 eV, where the Fermi level is set to 0 eV. This is due to the delocalized nature of the conducting orbitals, associated with the π-systems of the fullerene and the diazafluorene moieties. In this way, chemical modifications altering the frontier orbital energies should be efficient in tuning electron transport in this system, as these orbitals appear as efficient conduction channels due to their extensive delocalization.

It is interesting to consider how the transmission function at the Fermi level is affected by the different coordination modes of the diazafluorene ligands (Fig. 3.5). As expected, the model considering both diazafluorene groups coordinated by two N atoms (2N–2N binding) presents the highest conductance (blue line in Fig. 3.5a). If one of the four N atoms is uncoordinated, one side will have two Au–N bonds and the opposite electrode will present only one bond (2N–1N binding). This situation is represented with a dark orange line in Fig. 3.5b and is characterized with a significantly lower conductance than the completely coordinated model. As a result, both coordination modes should correspond to different conductance peaks (A and B). If another Au–N bond is broken to yield a 1N–1N bonding geometry (light orange line), we observe a similar conductance to the 2N–1N motif. The conductance of both situations is remarkably similar and should be indistinguishable in

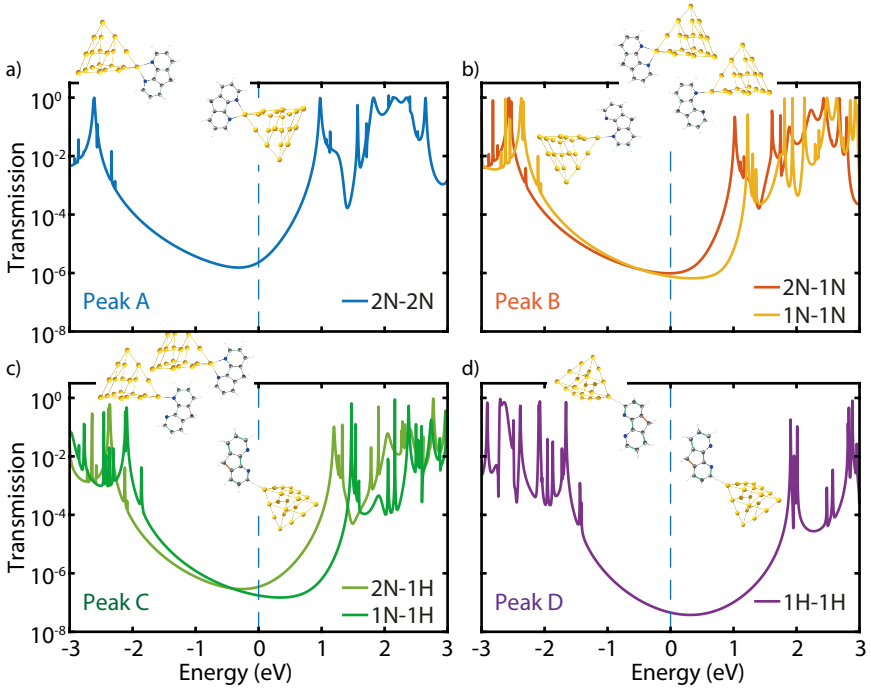

Figure 3.5: Transmission function for the different binding models. The line colour represents the number of Au–N bonds at each gold tip. The blue line indicates binding by two N atoms at each side. The two orange lines indicate binding by one N atom at one side and one or two N bindings on the opposite side. The two green lines indicate binding by a Au–H van der Waals contact at one side and one or two N bindings on the opposite side. The purple line indicates binding by two H atoms at each side. The Fermi level is located at 0 eV and is indicated by a vertical dashed line.

break-junction experiments (both are assigned to peak B). For the 1N–1N bonding geometry, we also verified the effect of the relative orientation of the binding N atoms, calculating the 'cis'-like conformation (considering the light orange line geometry as '*trans*' because the Au–N bond is placed at opposite sides in each anchoring group). Again, the change in conductance is negligible. Calculations considering weak Au–H contacts are depicted in green and purple (Fig. 3.5c,d). We observe two clear groups, with the one combining Au–H contacts and Au–N bonds (light and dark green) at a markedly larger conductance than the geometry considering only Au–H interactions (purple line).

To summarize, we relate peak A with the highest conductance curve in which both diazafluorene groups are coordinated by two N atoms (blue line), and peak B with the binding motifs which include only Au–N bonds, where at least one of the binding modes is by only one N atom (orange lines). Peak C is consistent with the presence of one Au–H interaction (green lines) and explains the lower yield for this junction geometry, as it involves weak interactions. The presence of a fourth peak originating from Au–H interactions at both contacts is not observed in the measurements.

The comparison of the relative values of the calculated transmission functions at the

Fermi level and the experimental conductance reinforces this assignment. In log units, the difference between the position of peak A and B ranges from 0.5 to 0.6, while the calculated values for $T(E)$ between blue and orange lines ranges from 0.37 to 0.46. In the experiment, peaks A and C are separated by 1.1-1.3 log units, comparing favourably with the difference between the blue and green curves (0.82-1.18). The lowest curve (purple line) is 1.7 log units less conductive than the most conductive mode, and is unlikely to be detected in the experiment. Furthermore, having weak contacts at both golds tips simultaneously leads to a weak binding mode, for which it may be difficult to obtain well-defined conductance plateaus.

The fact that peak B and C each incorporate two different binding arrangements can also explain why they are generally broader than peak A, which only includes one: they comprise different configurations which have slightly different conductance values. This can result in a broadening of the conductance peaks when enough statistics is acquired.

3.3. CONCLUSIONS

We measured C_{60}-daf with the MCBJ technique in two different laboratories (Delft and Santiago de Chile). The measurements from both locations agree in identifying three most probable conductance values that we attribute to different configurations between the diazafluorene anchoring groups and the electrodes. Through DFT calculations using the B3LYP density functional, we relate the most conductive peak A with the configurations where both Au–N bonds are present at each side, the middle peak B with the Au–N bonds where at least one of the binding modes is through only one N atom, and the lowest conductance peak C with the presence of one Au–H interaction. The presence of multiple stable arrangements and the relatively low conductance values make this derivative as-is not appealing for employment in single-molecule devices. However, these results show that this geometry is promising and, with some modifications, could open the way to further studies in which the C_{60} backbone can be modified with different functional groups.

4

Conductance variations in a mechanosensitive molecular spring

An appealing feature of molecular electronics is the possibility of inducing changes in the orbital structure through external stimuli. This can provide functionality on the single-molecule level that can be employed for sensing or switching purposes if the associated conductance changes are sizable upon application of the stimuli. Here, we show that the room-temperature conductance of a spring-like molecule can be mechanically controlled up to an order of magnitude by compressing or elongating it.

Parts of this chapter have been published in Nano Letters **18** (9), 5981–5988 (2018).
Part of the experimental measurements have been performed by C. Hsu (TU Delft). The chemical synthesis has been performed by K. Weiland and M. Mayor (University of Basel, Switzerland), the theoretical calculations have been performed by M. Skripnik and F. Pauly (University of Konstanz, Germany).

4.1. Introduction

The combination of the structural diversity accessible by synthetic chemistry with the continuously improving skills of experimental and theoretical physics enabled the exploration of individual molecules as the tiniest functional building blocks for electronic circuits and sensors [24, 169]. The steady refinement of the break-junction technique also allowed to study correlations between mechanical manipulations and transport features at the single-molecule level in a systematic way [170]. Some examples are binary switching through mechanical control of the metal-molecule contact geometry [171] or stereoelectronic effects [172], mechanical stress sensitive redox chromophores [173] or coordination compounds that show spin-state switching under mechanical stress [174]. Furthermore, the sensitivity of the technique makes it possible to observe intermolecular behaviours like π-stacking [114, 175], and more recently, the interdependence of conductance and frontier orbitals involved in the π-stacking [176, 177] could be directly demonstrated [121].

Particularly interesting are destructive quantum interference effects leading to a strong suppression of electron transmission at specific energies, which make them an ideal feature for applications in, *e.g.*, thermo- [178] or voltage-dependent switching [179]. Their manipulation has been reported by external means including solid state [9] or electrochemical gating [180], humidity [181], and sliding of π-stacked molecules relatively to each other [121]. Deliberate manipulation of the latter, however, remains elusive as it requires strict temperature conditions and is based on intermolecular interactions. In particular, the intermolecular character requires the coincidental presence of two molecules inside the junction. For this reason, approaches that intramolecularly imitate intermolecular π-stacking move into the focus of interest. Along these lines, the [2.2]paracyclophane (PC) compound is highly appealing [182]. First described by Farthing *et al.* in 1949, it consists of two stacked benzene rings which are mechanically stabilised by two non-conjugated linkers [183]. Integrated as central unit of an oligo-phenylene-ethynylene (OPE) rod with terminal binding groups to gold electrodes (Fig. 1), we show here that using a mechanically controlled break junction (MCBJ) the π-stacking (and therefore the conductance) can be modulated by exerting a mechanical shear force to it. Simulations based on density functional theory (DFT) reveal a sensitive correlation between electrode displacement and molecular conductance, which is interpreted in terms of quantum interference effects between the frontier orbitals.

4.2. Results

The employed molecule and the conceptual idea behind the mechanical conductance manipulation are displayed in Fig. 4.1. The molecule comprises a motif where two ethynylphenylthiols are bound to PC in such a way that the connection resembles a para-substitution in benzene [184, 185]. The thiol groups are connected in the para position of the outer benzene rings with respect to the PC building block, directing the current path through the PC, and offering considerable mechanical stability between gold electrodes [186]. The molecular motif and substitution pattern allow for flexibility by stretching of the PC; the ethynylphenylthiol building block, on the other hand, only offers limited movement upon application of a pulling force on the molecule (Fig. 4.1c). Precedence for mechanical flexibility of PC derivatives exists, as high-pressure solid state absorption experiments show

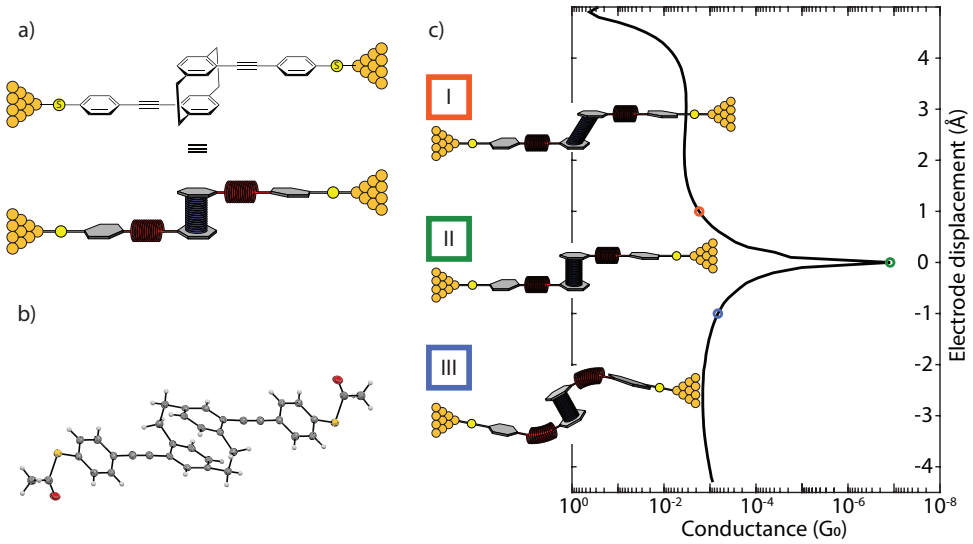

Figure 4.1: a) Schematic illustration of the break junction experiment of the OPE-linked PC molecule trapped between nanoelectrodes (top panel), together with a presentation displaying, as springs, the combinations of mechanosensitive structures in the molecular design (bottom drawing in this panel). b) Solid state molecular structure determined by single crystal X-ray analysis. c) Possible behaviour of the molecule under applied force: I) elongation of the molecule under pulling force of the electrodes; II) junction with the molecule in its relaxed configuration; III) compression results in a shortening of the overall junction length. The simulated conductance (in units of the conductance quantum $G_0 = 2e^2/h$) as a function of the applied mechanical stress is displayed as the drawn line; the three cases I-III are indicated by the coloured circles.

shortened distances of its benzene rings [187]. When the thiol groups are moved apart, the applied tensile force is relayed to the central PC unit along the axis connecting the anchoring groups. Our DFT calculations show that the alkynes are more susceptible to compressive motions, whereas the PC subunit only stretches after these are fully extended. It is noteworthy that electrical transport studies through monolayers consisting of the proposed molecular rods and similar PC-containing subunits have been reported [185, 188]. However, the limited control over the number of molecules inside the junction made the interpretation of the results challenging.

4.2.1. SINGLE-MOLECULE EXPERIMENTS

The target molecule was synthesised by adapting literature-known procedures [189, 190]; its structure was unambiguously verified by single-crystal X-ray analysis (Fig. 4.1b). The analytical data corroborating the identity of the molecule is in agreement with the data already reported [185]. The molecular conductance was investigated using the MCBJ technique under ambient conditions. In this technique, atomically sharp electrodes are formed in a lithographically defined gold wire and repeatedly opened and closed with sub-nanometre accuracy. The measurement of the conductance as the electrodes are continuously moved further apart constitutes a so-called breaking trace. Further details about the MCBJ setup and the measuring technique have been described elsewhere [165, 166].

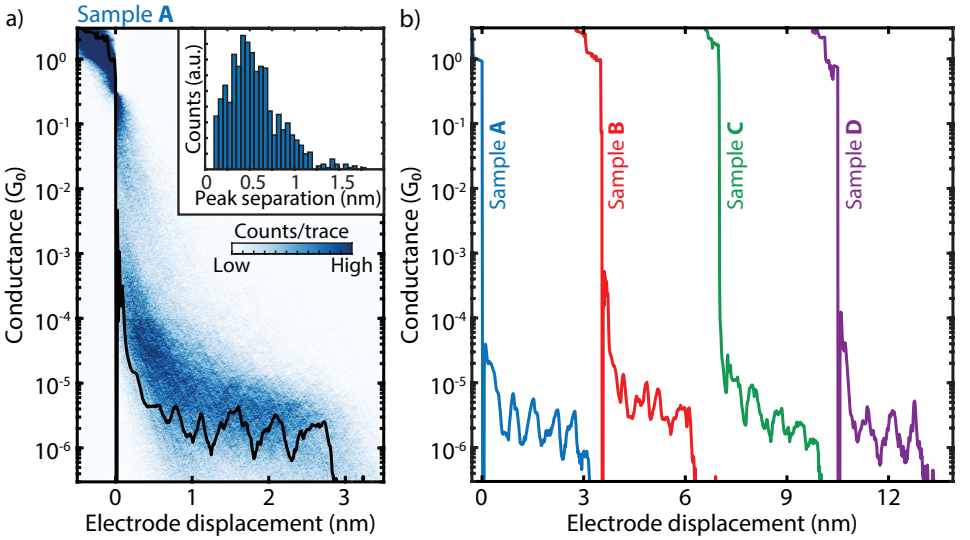

Figure 4.2: a) Two-dimensional histogram built from 3.000 consecutive breaking traces collected after deposition of the solution containing the molecule displayed in Fig. 4.1. The applied bias is 100 mV, and the electrode speed is 4.0 nm/s. A single breaking trace (black line) has been overlaid as an example. The inset shows the peak-separation distribution. b) Examples of breaking traces, showing oscillations in conductance as a function of displacement. The traces are taken from four different samples and are offset in the x-axis for clarity. The first trace comes from sample **A**, shown in panel a; samples **B**-**D** are presented in Fig. 4.8 alongside more examples of breaking traces.

Fast-breaking measurements were performed to characterise the conductance of the OPE-linked PC molecules [118]. The two-dimensional histogram in Fig. 4.2 a shows the distribution of conductance versus electrode displacement. Fitting a log-normal distribution to the one-dimensional histogram constructed from the same data (Fig. 4.7a) reveals that the most probable conductance value is $3.7 \cdot 10^{-6}\,G_0$, where $G_0 = 2e^2/h$ is the quantum of conductance. Interestingly, inspection of individual traces shows the appearance of pronounced oscillations in the conductance as the electrodes are pulled from one another, as illustrated in Fig. 4.2b for four different samples. These oscillations are found in a large fraction of the molecular traces (40%) and have an amplitude up to an order of magnitude. The inset of Fig. 4.2a presents a histogram of the spacing of the individual peaks, showing a periodicity of about 0.5 nm (Section 4.B.1 for more details). Note that such oscillations are absent in the control measurements without the molecule (Fig. 4.9).

To investigate in more detail the dependence of the molecular conductance on the electrode displacement, we performed conductance measurements with a modulated electrode spacing [191]. In this experiment, the MCBJ was initially stretched to a few-atom width (about $3\,G_0$) and allowed to self-break by its surface tension to form atomically sharp electrodes [192]. Then, the electrodes were separated by a distance equal to the length of the molecule to recognise, by evaluating the conductance, whether the trapping of a molecule occurred: if the conductance is found to be larger than $1 \cdot 10^{-6}\,G_0$, a molecule is presumably

connected between the two electrodes, and a triangular wave is applied to the piezoelectric stack that controls the electrode positions (Fig. 4.3a). Note, that a higher voltage on the piezoelectric stack corresponds to a larger electrode separation. Hundreds of such so-called distance-modulation traces are collected and from them a conductance histogram is built, similarly to that obtained for fast-breaking measurements. Fitting a log-normal distribution to this histogram yields a peak at $2.7 \cdot 10^{-6}\,G_0$, a value close to that found for fast-breaking measurements (Fig. 4.7b). Thus, molecular traces in this measurement appear at approximately the same conductance values as found for the fast-breaking measurements and have a long lifetime, consistently surviving for the entire modulation time of 120 s.
As illustrated in Figs. 4.3a, 4.11 and 4.12a,b, as the gap size increases the conductance can either increase or decrease. In the former case we define the conductance changes to be in-phase with the gap size modulation (orange curve in Fig. 4.3a). In the latter it is the other way around: the conductance change is in antiphase with the gap size modulation (blue curve in Fig. 4.3a). About 32% of the molecular traces show in-phase conductance variations, 28% appear to respond in antiphase, and about 40% show a mixture of both or a more complex response (Figs. 4.12c, 4.13 and 4.14). Most of the conductance traces show these conductance variations at the same frequency as the driving modulation (Fig. 4.16); however, surprisingly, many (31%) respond at double the driving frequency. The green curve in Fig. 4.3a is an example of this.

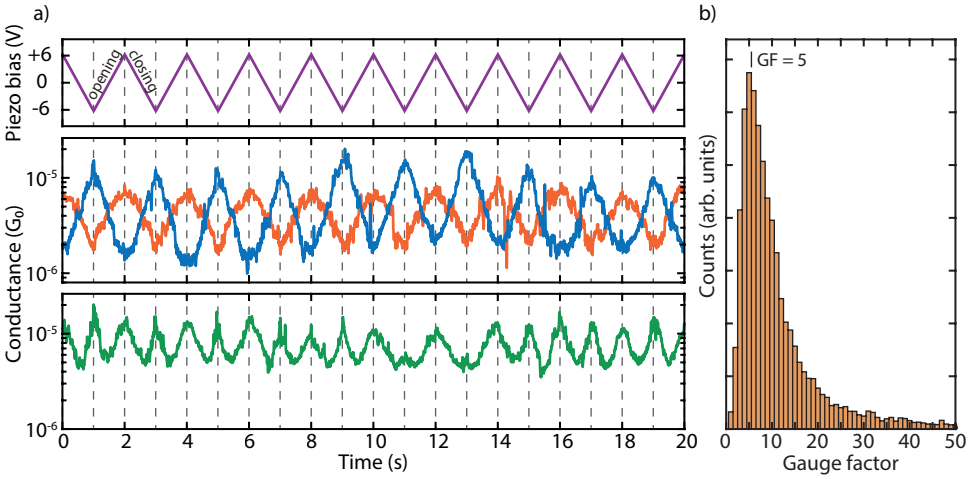

Figure 4.3: a) Examples of distance-modulation traces (sample **B**). The blue, orange and green lines (middle and bottom panel) represent three different conductance measurements, whereas the purple line (top panel) represents the voltage applied to the piezoelectric stack. The applied piezo voltage translates into a peak-to-peak distance of 5.0 Å and a positive voltage corresponds to a larger electrode distance. The total modulation time is 120 s at a frequency of 0.5 Hz. The conductance responds to the electrode-separation modulation either in-phase (orange), in antiphase (blue), or with double the modulation frequency (green). An example of a full measurement, extending over 120 s, is shown in Fig. 4.14 and Fig. 4.15. b) Distribution of absolute values of gauge factors obtained from 123 selected traces of the distance-modulation measurements performed on sample **B**. The number in the figure corresponds to the peak value of the distribution.

4.2.2. Theoretical calculations

To shed more light on these experimental observations, DFT-based calculations were carried out. For the evaluation of the conductance we used a proprietary framework [193]. To start, we place the molecule between two pyramidal gold leads, as shown in Fig. 4.4b. The upper electrode exhibits an atomically sharp tip, while the tip atom is removed for the lower one. By placing a terminal sulfur atom of the molecule at the hollow site of the lower pyramid, it binds to three gold atoms. Compared to the sulfur-gold bonding at the top lead, the stronger bonding of the sulfur atom to the hollow site ensures a stable mechanical connection, and the sulfur atom at the upper electrode starts sliding down the gold facets, as the contact is being stretched.

The total energy and conductance of this system show pronounced jumps at certain displacements during the gap opening. The snapshots at these displacements are shown in Fig. 4.4b and reveal the expected movement of the sulfur atom. The displacement between snapshots iii and v (just after the sulfur atom jumped to the next gold atom) amounts to 2.8 Å, which is close to the gold-gold binding length of 2.89 Å in the simulated leads. The molecule in snapshots i, iii and v is close to its relaxed gas phase configuration (discussed below) and exhibits a low conductance. Upon further stretching, the conductance rises until it eventually levels off and reaches a local maximum at snapshots ii and iv. At this point, the sulfur anchor slips onto the next gold atom, thus releasing the mechanical tension in the molecule and restoring the conductance to a low value (iii, v). After the sulfur atom has reached the last gold atom of the upper lead, it finally loses its connection: the junction breaks, and the molecule snaps back, as shown in snapshot vi. Thus, distancing of the electrodes leads to a stick-slip like motion of the molecule along the surface of one of the electrodes.

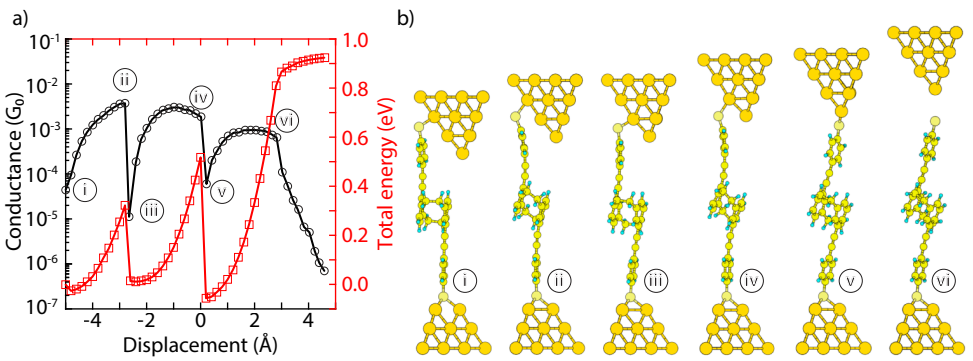

Figure 4.4: a) Calculated conductance and total energy of the system during gap opening. b) Selection of snapshots illustrating the stick-slip motion. A video of the simulated stick-slip motion can be found in the SI

In a detailed analysis of the displacement-dependent conductance, we study the molecule between two hollow leads, where each sulfur binds to three gold atoms of the respective lead. This allows us to concentrate on the deformations of the actual molecule: the rigid bonding of the hollow-hollow configuration ensures that the lead displacement is directly passed to the molecule, minimizing deformations of the lead-molecule bonds. Starting from the configuration with minimal energy, corresponding to a molecule close to its relaxed

state in the gas phase, the leads are either separated farther apart (positive displacement) or brought closer together (negative displacement), thereby stretching or compressing the molecule. The resulting conductance shows a pronounced dip at a well-determined displacement, which we define here as zero (Fig. 4.5b). The conductance rapidly increases when the molecule is either stretched or compressed from this position. The deformation in the stretched molecule is mainly identified with the shifting of the stacked benzene rings. By evaluating the transmission in an energy range between −2 eV and 3 eV around the Fermi energy E_F for each displacement step, we obtain the transmission map in Fig. 4.5c. It reveals a transmission valley (purple diagonal line) between the traces related to the molecular frontier orbitals (yellow horizontal lines). The conductance dip in Fig. 4.5b can be traced back to the intersection of the transmission valley and the Fermi energy. In other words, the energy position of the dip can be tuned by the lead separation. In the following, we present the underlying mechanism based on quantum interference of the molecular frontier orbitals.

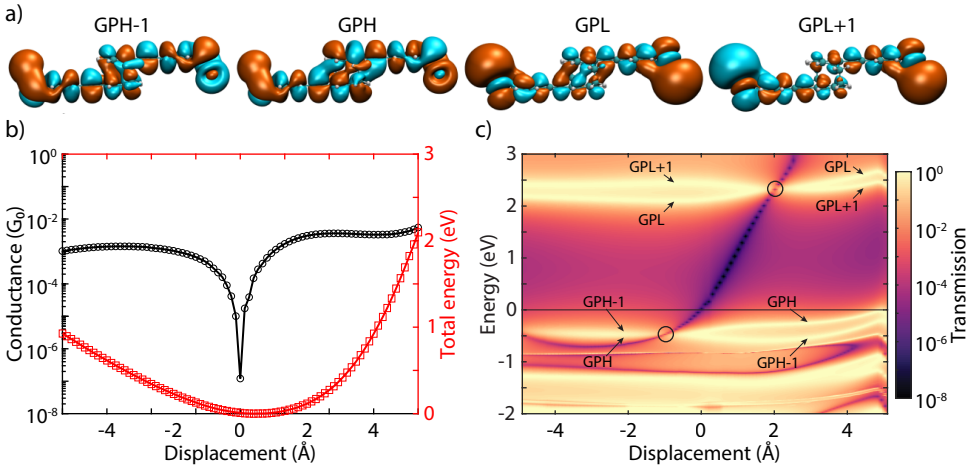

Figure 4.5: a) Frontier orbitals of the molecule. The orbitals are either symmetric (GPH, GPL) or antisymmetric (GPH-1, GPL+1) with respect to the centre of the molecule. They are shown in gas phase for clarity (with the sulfur atoms "terminated" with one gold atom each, as they do not change significantly when the gold leads are attached to the molecule). b) Conductance (horizontal black line in panel c) and total energy. c) Transmission map of the molecule between two leads from DFT calculations. The horizontal yellow traces in the map arise from orbitals which can be related to the gas phase frontier orbitals. An antiresonance is observed between the frontier orbital traces. It shifts in energy as the displacement is varied. The positions at which the pairs GPH-1, GPH and GPL, GPL+1 degenerate are marked with circles.

A closer look at Fig. 4.5 reveals HOMO and LUMO pairs that arise from the HOMO and LUMO states of the OPE units and are typically slightly split by the weak coupling through the PC core. To distinguish the character of the HOMO-1, HOMO, LUMO and LUMO+1, we relate them to the frontier orbitals in the gas phase. For this purpose, we introduce the abbreviations GPH-1 to GPL+1, where GPH/L denotes the gas phase HOMO/LUMO. The orbitals are either symmetric (GPH, GPL) or antisymmetric (GPH-1, GPL+1) with respect to the centre of the molecule. The crucial aspect is now that the energy of the frontier orbitals depends on the displacement. The states within HOMO and LUMO pairs, GPH-1 and

GPH as well as GPL and GPL+1, eventually change their energetic order in the studied displacement window between around −4 to 4 Å. The displacements of the degeneracy points, at which these reversals take place, differ for the occupied and unoccupied states. They are located at $d = -1.0$ Å and $d = 2.0$ Å, respectively, as marked by circles in Fig. 4.5c. According to the theory of quantum interference [176, 194] the orbital symmetry leads to a pronounced destructive interference feature in the HOMO-LUMO gap between displacements from −1.0 to 2.0 Å, when the HOMO and LUMO pairs are ordered as in the gas phase. Outside of this displacement window, the molecular orbital pairs GPH-1, GPH or GPL, GPL+1 rearrange in energy, thereby lifting the condition for destructive interference. Indeed, we can reproduce the main features of the conductance map by considering the displacement-dependent energies of the four frontier orbitals and their symmetries, as corroborated further in the appendix.

4.3. Discussion and concluding remarks

With the insights provided by the DFT calculations, the pronounced conductance oscillations can be explained through quantum interference of frontier orbitals in combination with the molecule acting as a spring when subject to mechanical deformations. Its relaxed conformation corresponds to the situation in which the antiresonance originating from destructive interference of the HOMO and LUMO is in the vicinity of the Fermi energy, yielding a low-conductance state. By stretching or compressing the molecule, the antiresonance is moved away from the Fermi energy, which leads to an increase of the conductance. The experimentally observed oscillations in conductance during continuous opening of the junction (Fig. 4.2b) can then be associated to the stick-slip motion of the anchoring sulfur atoms on the gold surface, as this process releases the built-up mechanical strain in a semi-periodic fashion. Ab-initio molecular dynamics calculations at room temperature predict that Au-Au bonds should break instead of the Au-S bonds [195]. However, if a gold adatom attached to a sulfur anchor was dragged along the gold electrode instead of the S itself, this would not lead to a qualitative change of the stick-slip picture.

The different behaviours (in-phase, antiphase, frequency doubling) observed in the distance-modulation measurements (simulation: second panel in Fig. 4.6a; experiment: bottom two panels in Fig. 4.6a) can be attributed to variations in the initial molecular configuration at the beginning of the modulation. Traces which are in phase with the gap modulation are related to molecules which are prestreched in the starting configuration (orange panel in Fig. 4.6c). The starting point is at positive displacement and the oscillation takes place at the right lobe of the conductance curve (orange area in Fig. 4.6b): an increase in electrode displacement corresponds to a higher conductance (and a decrease to a lower conductance). Along a similar line, traces in antiphase with the gap modulation can be related to molecules which are pre-compressed in the starting configuration (blue panel in Fig. 4.6c) and therefore correspond to oscillations at the left lobe of the conductance curve (blue area in Fig. 4.6b). Traces with a doubled frequency (such as the green trace in Fig. 4.6a) are related to molecules which are close to the relaxed gas phase geometry, in which the Fermi energy of the leads is aligned with the position of the interference dip (green panel, Fig. 4.6c). In this case the conductance dip is crossed two times during each piezo modulation period, therefore doubling the frequency of the measured conductance, as can be seen by following the purple steps in Fig. 4.6b. The appearance of the doubled

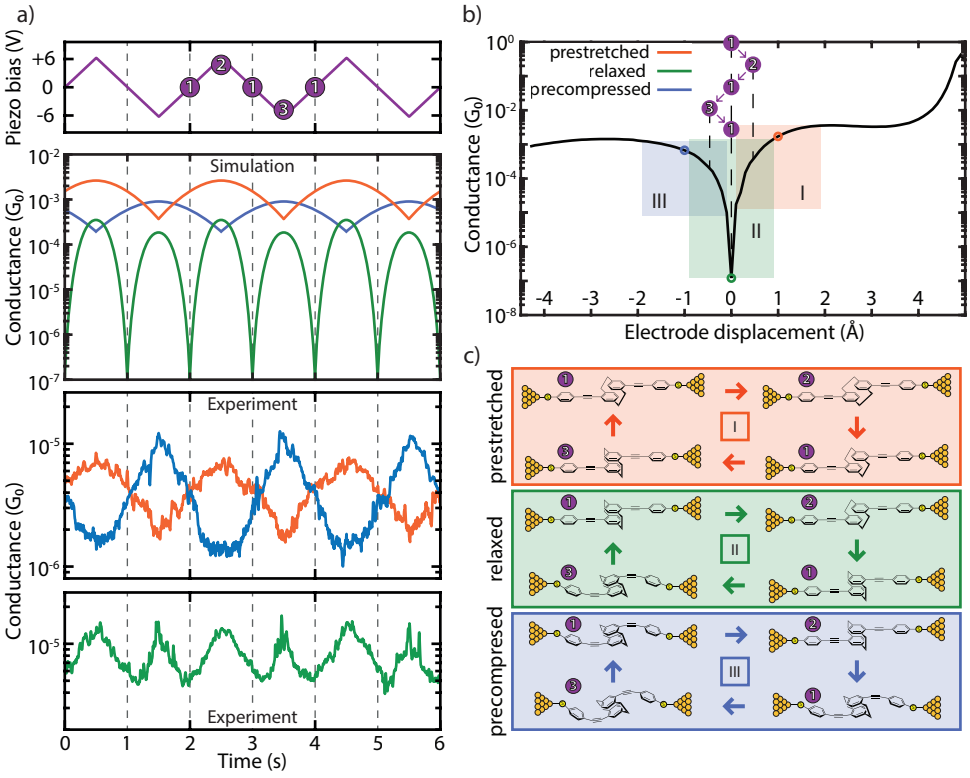

Figure 4.6: a, top panels) Simulation of conductance traces (second panel) when the electrode displacement is periodically modulated (top panel) for three different trapping configurations: prestretched (orange), relaxed (green) and precompressed (blue). Centres of oscillation at $+1,0$ and -1.0 Å respectively; amplitude: 0.5 Å. a, bottom panels) Zoom-in of the experimental distance-modulation traces presented in Fig. 4.3. b) Calculated conductance vs. electrode displacement. The blue, green and orange areas (I, II and III, respectively) show the portion of the curve spanned in the case of different starting positions (precompressed, relaxed and prestretched, represented by circles in the same colours). The numbers in purple circles represent the position of the electrodes along the oscillation period in the case of a relaxed trapping configuration. c) Schematics of the molecular configurations along a period of electrode distance-modulation. Different starting configurations are represented with different colours: prestretched in orange, relaxed in green and precompressed in blue. White numbers in purple circles represent the position of the electrodes along the oscillation period. Note, that the molecular compression/elongation in the simulation is 0.5 Å, a value smaller than the gap size variation in the experiment. This can be rationalised by the elastic response of the sulfur-gold connections and of the gold atoms in the electrodes themselves.

frequency is thus a direct proof for the existence of the destructive interference dip. Importantly, the ability to mechanically tune the position of this dip to be located at the Fermi energy can be exploited in future studies and applications of quantum interference effects.

We note that the conductance variations as a function of displacement can be used to estimate the gauge factor, characterizing the piezoresistive response of the molecular spring. The gauge factor is defined as the relative conductance change divided by displacement normalized to the molecular length (Fig. 4.3b and Section 4.B.4 for more details). We find

gauge factors exhibiting a wide distribution with a peak located at $GF = 5$ and a tail at higher values, reaching up to 40 orders of magnitude larger than those that have been reported on single DNA molecules [196]. We expect that thermally occupied ring rotations of the OPE rods at room temperature will reduce the electronic coupling in the molecule, the electron delocalization and hence the conductance. Besides known shortcomings of DFT with regard to the description of level alignments [197], this could explain part of the overestimation of the theoretically predicted conductance values in our static DFT geometries. In addition, longitudinal vibrations, as well as thermal fluctuations, will lead to gap-size modulations and an effective averaging over a range of junction configurations. Such vibrationally induced decoherence effects will wash out the interference-induced conductance minimum [198]. Therefore a precise control of the temperature may turn out to be crucial in the optimization of gauge factors, and the molecule studied here appears to be an ideal candidate to investigate quantum interference effects at lower temperatures and to quantify if decoherence limits the room-temperature performance [198–200]. In order to achieve even higher gauge factors, it would also be interesting to explore different chemical designs based on the mechanical manipulation principle of quantum interference.

4.A. Appendix - Methods

MCBJ experiments

The molecule was dissolved in dichloromethane and the solution was drop casted on the MCBJ sample after the characterisation of the bare device (Fig. 4.9). All measurements were performed in air at room temperature after the evaporation of the solvent. Concentrations of 9 µM (sample **A**, **B**), 90 µM (sample **C**) and 900 µM (sample **D**) have been used, but no significant dependence on the concentration has been observed.

Fast-breaking measurements

Fast-breaking measurements were performed by applying a bias of 100 mV and using a constant pulling speed of the electrodes of 4.0 nm/s. The conductance is recorded until it falls below the noise level, which is about $5 \cdot 10^{-7}\,G_0$ in our setup. At this point the electrodes are fused back and a new trace is recorded. 3.000 such traces were recorded for samples A, B and C; 5.000 for sample **D**. Further information on the technique can be found in Frisenda et al [118].

Distance-modulation measurements

In these measurements, the electrode spacing was modulated to periodically increase and decrease [191]. The MCBJ was initially stretched to a few-atom width ($3\,G_0$) and allowed to self-break by its surface tension to form atomically sharp electrodes. Then, the electrodes were separated by 1.75 nm, which is approximately the estimated length of the unstretched molecule. At this point, a 0.5 Hz triangular wave was applied to the piezoelectric stack that controls the electrode positions with a peak-to-peak gap size variation of 5.0 Å (Fig. 4.3) or 2.5 Å (Fig. 4.11), depending on the amplitude of the applied piezo voltage. Note, that a higher voltage on the piezoelectric corresponds to a larger electrode separation.

The initial opening of the junction allows to recognise if trapping of a molecule occurs, since for a displacement of 1.75 nm the tunnelling conductance in the absence of a molecule is below the noise level of our set-up. The modulation was kept for 120 s, after which the junction was stretched until the noise level was reached and fused back again to start a new cycle. It should be noted that the initial configuration in a distance-modulation experiment cannot be controlled.

Simulations

DFT calculations were carried out with TURBOMOLE [201]. We used the def-SVP basis set and the PBE functional [202, 203]. During structural relaxations the total energy was converged to $1 \cdot 10^{-6}$ au and the maximum norm of the Cartesian gradient to $1 \cdot 10^{-3}$ au The electronic transmission was evaluated with a proprietary cluster-based framework. The procedure includes the separation of the system into semi-infinite leads and a central part, which contains the molecule and parts of the electrodes. The energy-dependent transmission function is expressed in terms of non-equilibrium Green's functions (NEGF) of the leads and the central part. The bulk parameters of the leads were extracted from a cluster of 1415 gold atoms. Further details on the method can be found in Pauly et al [193].

4.B. Appendix - Transport Measurements

4.B.1. Fast-breaking measurements

The conductance histograms for fast-breaking and distance-modulation measurements are displayed in Fig. 4.7. The most probable conductance values ($3.7 \cdot 10^{-6}\,G_0$ and $2.7 \cdot 10^{-6}\,G_0$, respectively) match well despite the measurement being performed on different samples and with different techniques. Distance-modulation measurements were recorded for a maximum time of 120 s, and therefore the histogram highlights the most stable configurations, as opposed to the fast-breaking measurements, where metastable ones have a bigger impact on the conductance histogram.

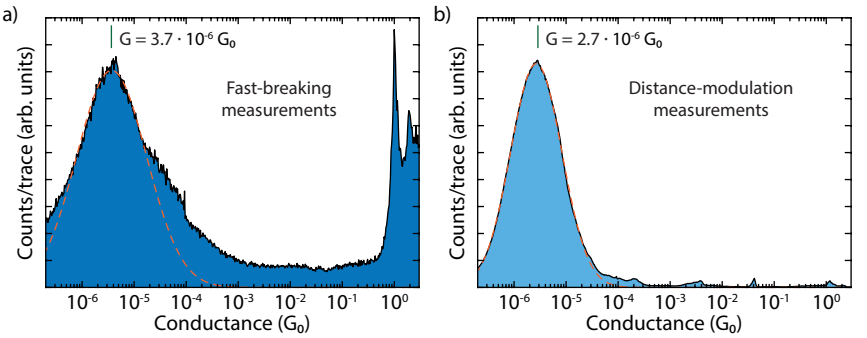

Figure 4.7: One-dimensional histogram a) of a fast-breaking measurement of sample **A** and b) of a distance-modulation measurement of sample **B**. The applied bias is 100 mV in both cases, fast-breaking measurements were recorded at 4 nm/s. The dashed orange line shows the fit result.

Figure 4.8 shows the two-dimensional histograms of samples **A**-**D**. The concentrations of the molecular solution dropcasted were 9 µM for sample **A** and **B**, 90 µM for sample **C**, and 900 µM for sample **D**. As can be seen from the histograms, no significant dependence on the concentration is observed and all samples show similar conductance oscillations.

For each measurement we perform a thorough characterisation of the bare device before dropcasting the molecular solution to ensure that the electrodes are clean and well aligned. The characterisation of the bare device used for sample **A** is shown in Fig. 4.9.

Estimation of the oscillation periodicity

To estimate the periodicity of the conductance variations, we selected 315 breaking traces from the 3.000 of sample **A** that showed particularly clear oscillations. For each trace we then identified the position of peaks with a prominence of at least 30% and calculated the distance between consecutive peaks. We fit a Gaussian to the histogram and find the parameters shown in the inset of Fig. 4.10.

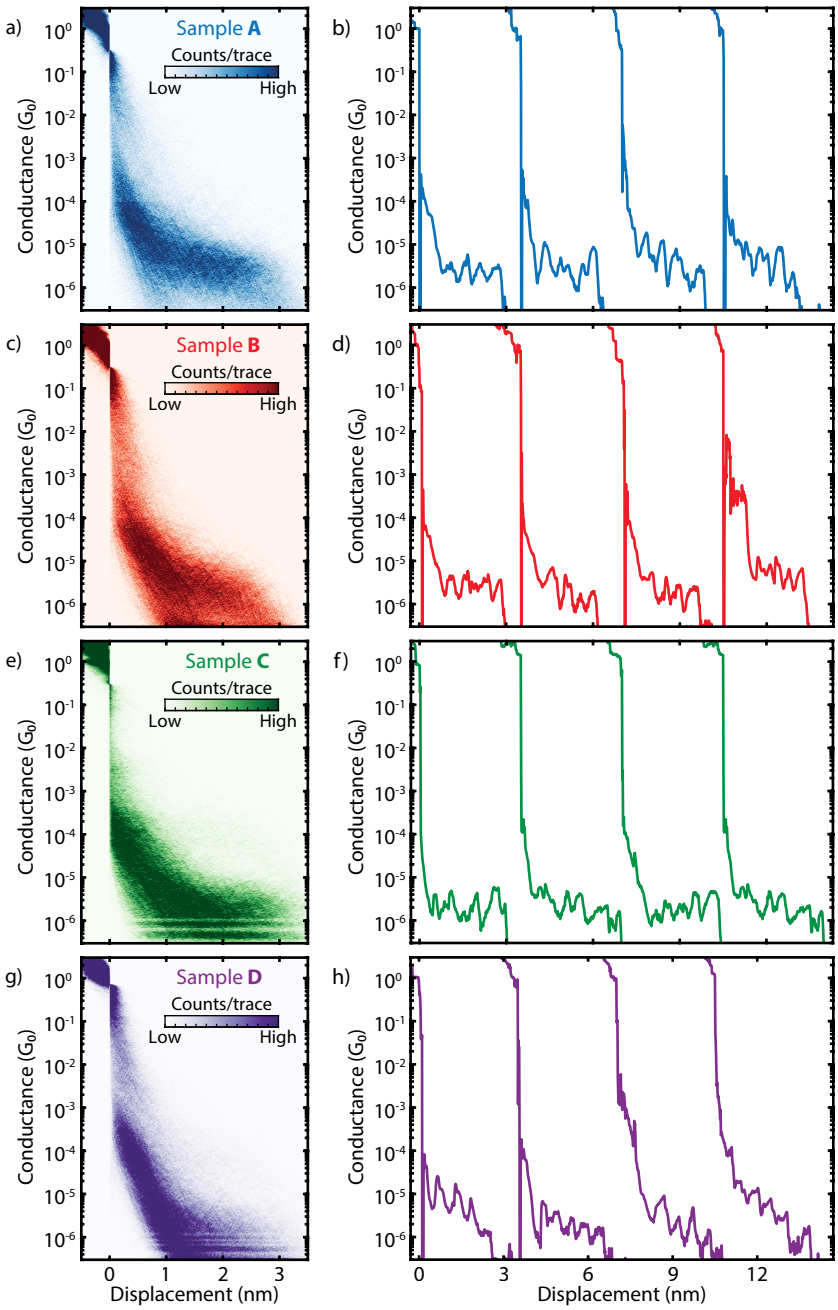

Figure 4.8: a,c,e,g) Two-dimensional conductance histogram of sample **A** (a), **B** (c), **C** (e) and **D** (g) with no data selection. b,d,f,h) Examples of the 3.000 (b,d,f) and 5.000 (h) consecutive breaking traces. The applied bias is 100 mV and the electrode speed is 4 nm/s for all measurements.

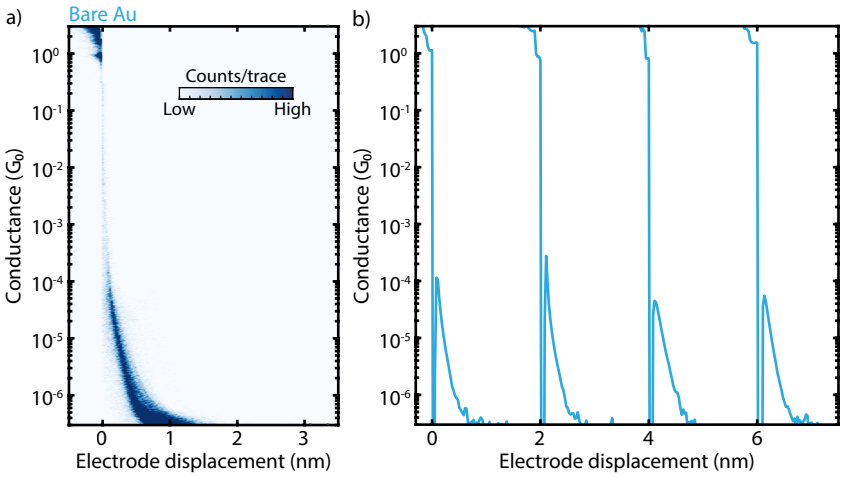

Figure 4.9: a) Two-dimensional conductance histogram and b) examples of conductance traces from the characterisation of the pristine sample used for measurements **A**. The applied bias is 100 mV and the electrode speed is 8 nm/s.

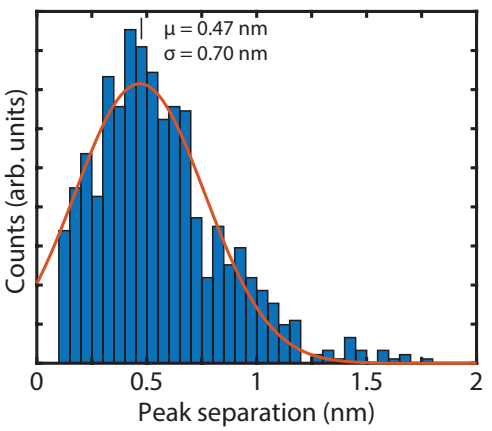

Figure 4.10: Distribution of the separation between consecutive peaks found in the selected breaking traces from sample **A**. The Gaussian fitted to it is represented as an orange line.

4.B.2. Distance-modulation measurements

Additional measurements of sample **B** are shown in Fig. 4.11. These measurements were taken with a peak-to-peak amplitude of 2.5 Å, smaller than those presented in the main text and in the following figures. Also in this case, both traces in-phase and in antiphase are observed. More examples of traces in-phase (Fig. 4.12a), in antiphase (Fig. 4.12b) and with doubled frequency (Fig. 4.12c and Fig. 4.13) are reported here. Figure 4.14 shows a trace for which the behaviour changes from antiphase to in-phase. The inset shows the moment of the transition. Figure 4.15 shows another full distance-modulation trace with the initial opening of the gap, the gap size modulation, and the final breaking to the noise level.

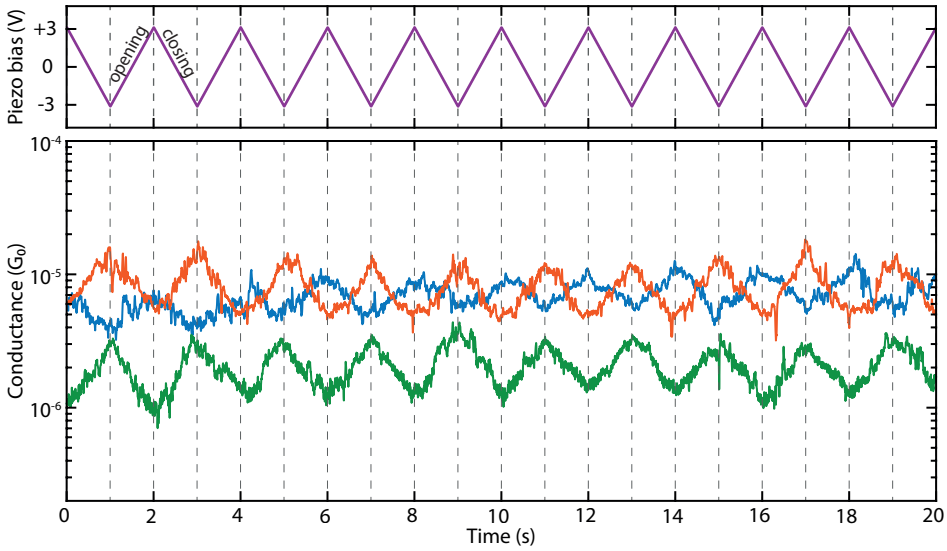

Figure 4.11: Examples of distance-modulation traces. The total modulation time is 120 s at a frequency of 0.5 Hz. The blue, green and orange lines (bottom panel) represent three different conductance measurements, whereas the purple line (top panel) represents the voltage applied to the piezoelectric stack. The applied piezo voltage translates into a **peak-to-peak distance of** 2.5 Å and a higher voltage corresponds to a larger electrode distance. The conductance responds to the electrode-separation modulation either in-phase (blue curve) or in antiphase (orange and green curves).

Figure 4.16 presents the Fourier Transform of the distance-modulation traces showing that it is mainly at the same frequency of the driving modulation.

4.B.3. Statistical analysis

The junction-formation statistics and percentage of molecular junctions showing conductance oscillations for fast-breaking measurements is shown in Fig. 4.17a, whereas the junction-formation statistics and percentage of phase response behaviours of the conductance oscillations in triangular modulation measurements are presented in Fig. 4.17b. The percentage of molecular traces is remarkably similar despite the measurements being performed on different samples and with different techniques.

4.B.4. Estimation of the gauge factor

The gauge factor of a strain gauge GF is defined as the ratio between the change in relative electrical conductance $\Delta G/G$ and the mechanical strain ε. From the distance modulation experiment it is possible to estimate the gauge factor of the molecule. To do so, we selected 123 traces from the 806 of sample **B** that showed particularly clear and stable oscillations. We then split each trace into semi-periods of the piezo modulation, i.e., portions in which the electrodes move in the same direction. For each of these portions we then identified the maxima and minima in conductance and their respective positions. From the former two, $\Delta G/G$ is extracted by dividing the change in conductance with the average conductance

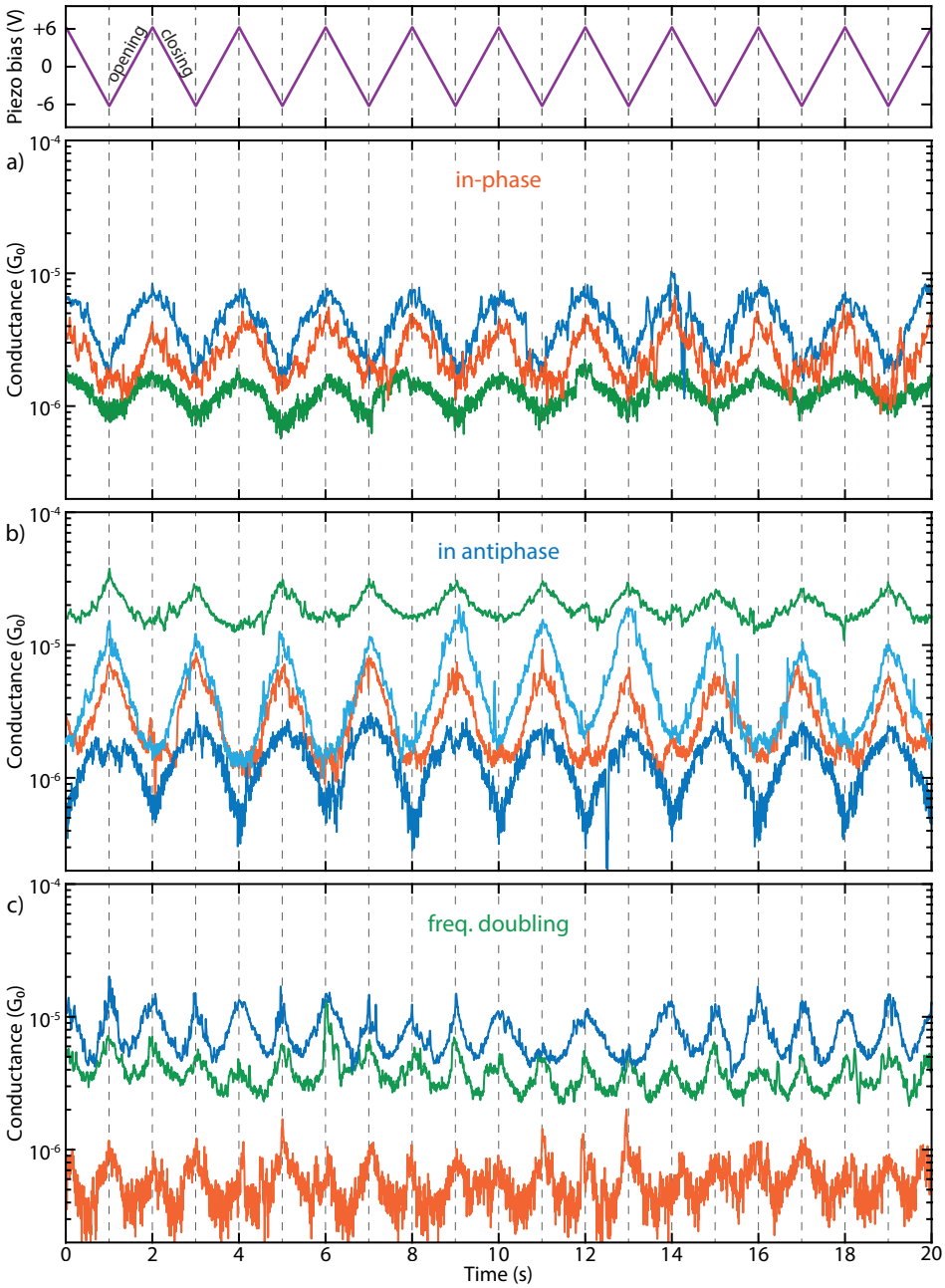

Figure 4.12: Examples of distance-modulation traces. The total modulation time is 120 s at a frequency of 0.5 Hz. The blue, green and orange lines (bottom panel) represent three different conductance measurements, whereas the purple line (top panel) represents the voltage applied to the piezoelectric stack. The applied piezo voltage translates into a peak-to-peak distance of 5.0 Å and a higher voltage corresponds to a larger electrode distance. In these cases, the conductance responds **in-phase** (a) or **in antiphase** (b) with the gap-size variation, whereas (c) contains traces with **double the frequency** of the driving modulation.

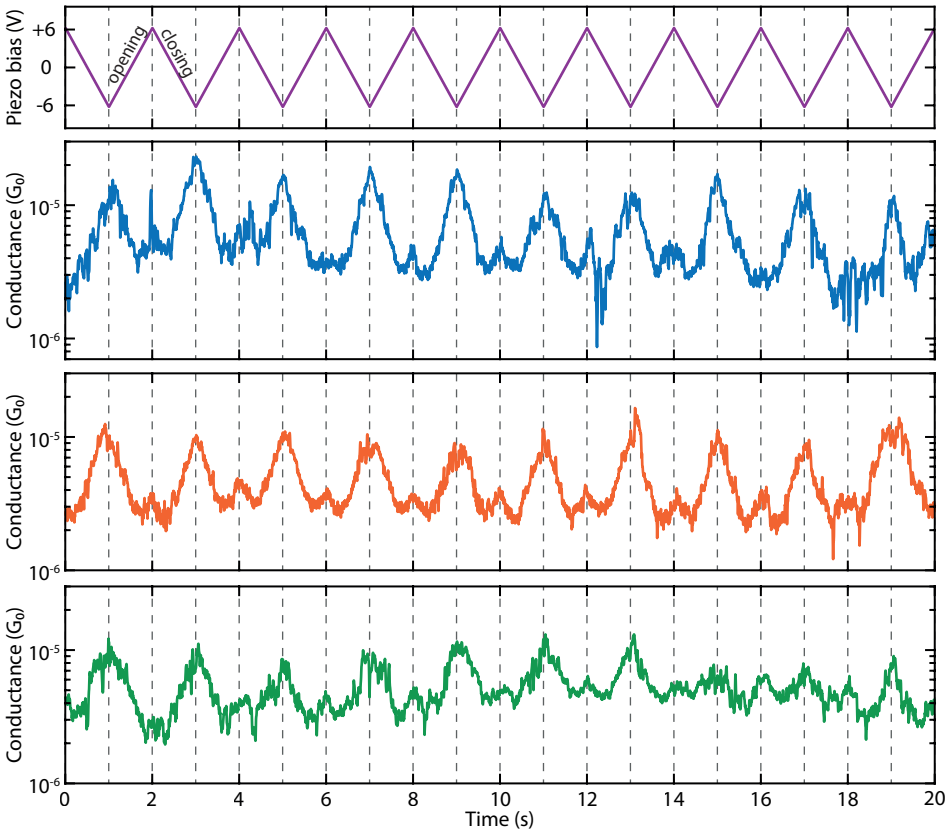

Figure 4.13: Examples of distance-modulation traces. The total modulation time is 120 s at a frequency of 0.5 Hz. The blue, green and orange lines (bottom panels) represent three different conductance measurements, whereas the purple line (top panel) represents the voltage applied to the piezoelectric stack. The applied piezo voltage translates into a peak-to-peak distance of 5.0 Å and a higher voltage corresponds to a larger electrode distance. In these cases the conductance responds with **double the frequency** of the driving modulation, with subsequent peaks having different heights.

for the portion of trace considered; from the latter, ε is obtained by dividing the electrode displacement (ΔL) by the size of the relaxed molecule ($L = 1.75$ nm). The GF is thus given by:

$$GF = \frac{\frac{\Delta G}{G}}{\varepsilon} = \frac{\frac{\Delta G}{G}}{\frac{\Delta L}{L}} \tag{4.1}$$

Since the frequency of the modulation was 0.5 Hz for a maximum time of 120 s, each trace can provide up to 120 gauge factor values.
The GF distribution is shown in Fig. 4.18. Both in-phase and antiphase traces were among the selected traces, which means that both positive and negative values in the gauge factor can be obtained: negative gauge factor values are obtained from antiphase traces. The peaks in the distribution are found at $GF = +5$ and $GF = -7$. The distribution of the absolute

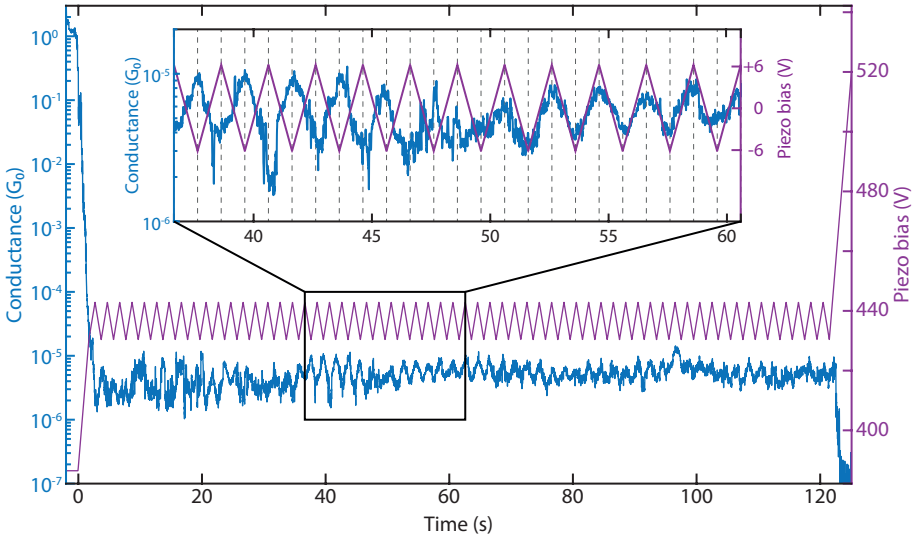

Figure 4.14: Example of a distance-modulation trace. The total modulation time is 120 s at a frequency of 0.5 Hz. The blue line represents the conductance measurement, whereas the purple line the voltage applied to the piezoelectric stack. The applied piezo voltage translates into a peak-to-peak distance of 5.0 Å, and a higher voltage corresponds to a larger electrode distance. The inset shows a portion of the trace in which a shift from antiphase to in-phase occurs.

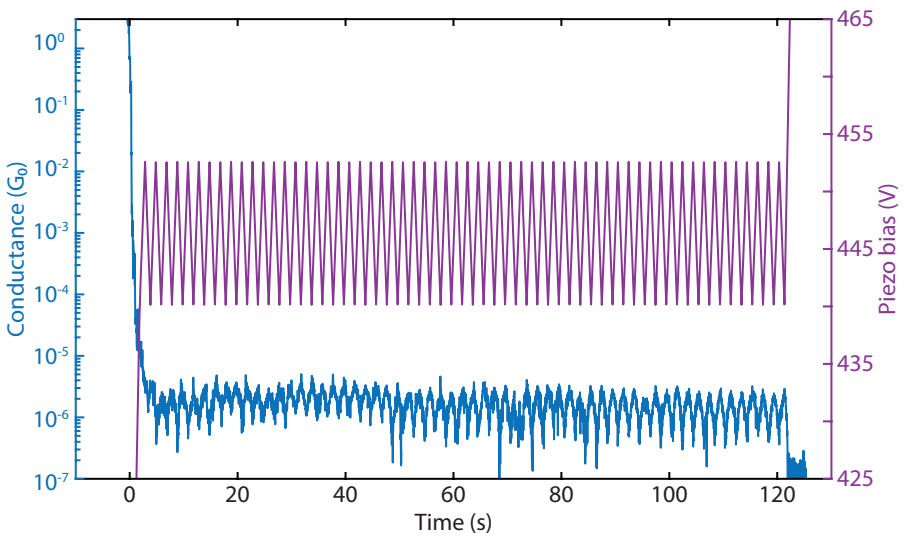

Figure 4.15: Example of a distance-modulation trace. The full trace is shown here with the initial opening of the gap, the gap size modulation at 0.5 Hz for 120 s, and the final breaking to the noise level. The blue line represents the conductance measurement, whereas the purple line represents the voltage applied to the piezoelectric stack. The applied piezo voltage translates into a peak-to-peak distance of 5.0 Å and a higher voltage corresponds to a larger electrode distance.

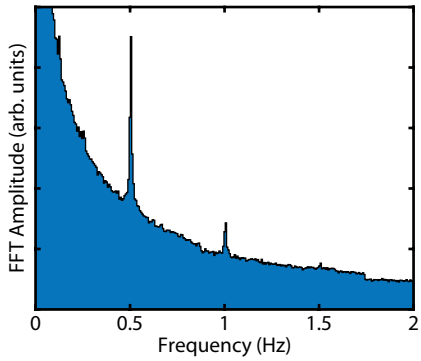

Figure 4.16: Fourier Transform of the conductance traces measured with a displacement modulation at 0.5 Hz. A pronounced peak is found at the driving frequency of the piezoelectric stack and a smaller one at the second harmonic.

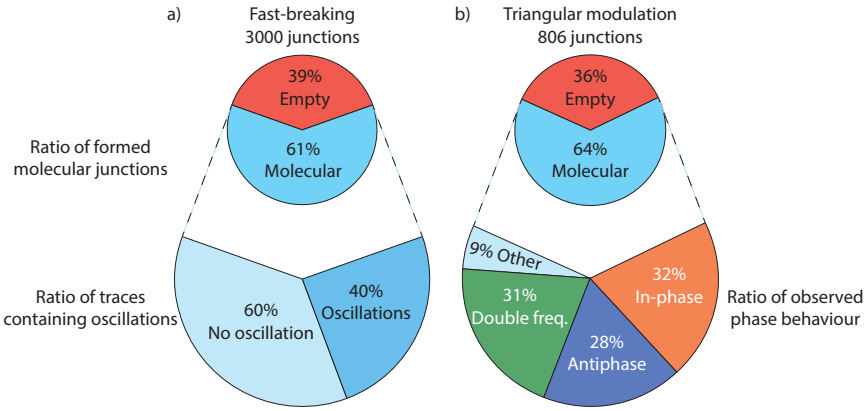

Figure 4.17: a) Junction-formation statistics and percentage of molecular junctions showing conductance oscillations for fast-breaking measurements (sample **A**). b) Junction-formation statistics and percentage of phase response behaviours of the conductance oscillations in triangular modulation measurements (sample **B**).

values is plotted in the main text (Fig. 4.3b).

This simple method for estimating the *GF* yielded the same qualitative result as others with more restrictive constraints in the peak selection or with preliminary smoothing of the curves, showing that noise spikes do not play an important role in the average result.

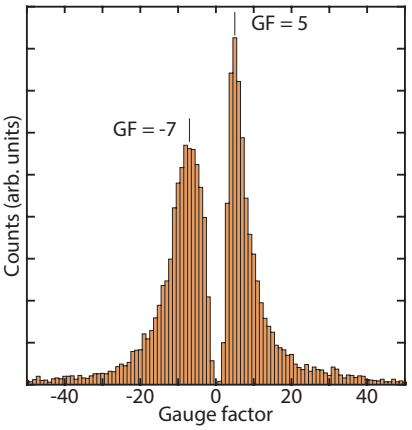

Figure 4.18: Distribution of gauge factor values obtained from 123 selected traces of the distance-modulation measurements performed on sample **B**.

4.C. Appendix - Transport Calculations

4.C.1. Quantum interference effects

The source of the transmission valley in Fig. 4.5 lies in the quantum mechanical interference of frontier orbital contributions to the transmission. Its presence can be explained solely by the gas-phase HOMO (GPH) and gas-phase LUMO (GPL). However, the shift in energy of the conductance dip as a function of the displacement can only be explained, if one also takes the GPH-1 and GPL+1 into account.

The position of the antiresonance depends on the relative energy distances $\Delta_H := \varepsilon_{\mathrm{GPH}} - \varepsilon_{\mathrm{GPH-1}}$ and $\Delta_L := \varepsilon_{\mathrm{GPL+1}} - \varepsilon_{\mathrm{GPL}}$. At $d = -1.5\,\text{Å}$ GPH-1 and GPH degenerate and $\Delta_H = 0$. Since GPH and GPH-1 energies are equal and their coefficients are of opposite sign ($c_{\mathrm{GPH-1}} = -1$ and $c_{\mathrm{GPH}} = +1$) their contributions cancel out. Therefore, at $d = -1.5\,\text{Å}$ the orbitals GPH-1 and GPH do not contribute to the total conductance. For $d < -1.5\,\text{Å}$ GPH-1 and GPH change their order so that $\Delta_H < 0$. Now the HOMO-1 is attributed to the GPH and the HOMO to the GPH-1. This means that HOMO and LUMO are of different symmetries, which, according to the argument above, leads to summands of the same sign and the resulting contributions to the conductance add up in a constructive manner. In this case there is no antiresonance between the HOMO and the LUMO anymore. An analogous explanation for the vanishing of the destructive interference can be given for $d > 1.8\,\text{Å}$, where GPL and GPL+1 change their energetic order ($\Delta L < 0$).

4.C.2. Displacement dependence of molecular orbital energies

As stated above, the displacement dependence of the orbital energies is crucial for the theoretical explanation of the displacement-dependent transmission. The isovalue plots of the four frontier orbitals are shown in Fig. 4.5a. These are sufficient to understand the displacement dependence of the orbital energies. First, we consider the GPH and GPL: starting from $d = 0\,\text{Å}$ (near the total energy minimum at 0.2 Å, where the molecule is closest to its

gas-phase configuration) their energies increase, if the molecule is stretched (see Fig. 4.5c). The reason for this is the shifting of the stacked benzene rings.

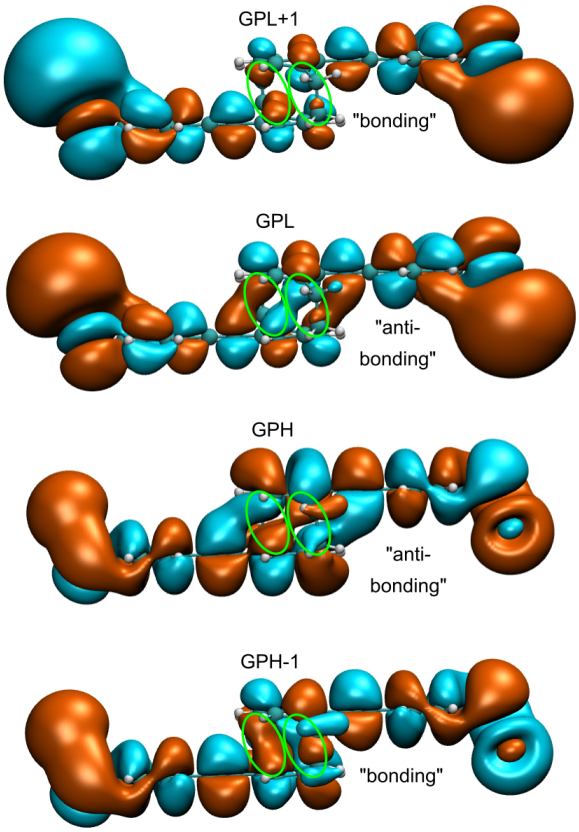

Figure 4.19: Molecular orbitals of the gas phase configuration. The sulfur atoms are terminated with one gold atom each. Green circles mark the parts of the wave function which arise from the π-orbitals of the stacked benzene rings. These parts show a sign change for GPH and GPL and no sign change for GPH-1 and GPL+1.

The wave function at the opposing stacked rings shows a sign change for GPH and GPL, marked with green circles in Fig. 4.19, which corresponds to an antibonding configuration. Upon stretching these π-orbitals are brought closer together, thereby increasing the energy. Additionally, the π-orbitals of each OPE unit are moved away from the orbitals arising from the ethynyl atoms of the other unit, which have the same sign and therefore correspond to a bonding configuration, which as well increases the orbital energy. We can use an analogous argumentation to justify the decrease of the orbital energy of the two other frontier orbitals, GPH-1 and GPL+1. Here, the opposing π-orbitals have the same sign and are in a bonding configuration. If the molecule is stretched, these π-orbitals are brought closer to each other and are removed from the energetically unfavourable ethynyl-chain orbitals, which reduces the orbital energy.

If the benzene rings are shifted too far, the energy change can even be reversed. This is observed, e.g., for the trace caused by GPL+1 in Fig. 4.5c. Starting from $d = 0$ Å at first, it moves to lower energies and from $d = 3$ Å back to higher ones. This happens because the benzene rings are shifted far enough that the π-orbitals start to feel the presence of the next neighbour orbitals of the other OPE unit, which are again of opposite sign. This corresponds to a transition from a bonding to an antibonding configuration, which results in an increase of orbital energy.

5

Influence of a water environment on single-molecule conductance

This chapter contains a study of the influence of the environment on the molecular junction, i.e.*, what happens when we measure molecules in solution. Knowing the effects of an aqueous environment is important in the prospect of studying molecules that are involved in biological processes, which are naturally found in solution In this chapter, we will give a first characterization of the role of water and other solvents on the single-molecule conductance. Density functional theory calculations show that the effects of the water environment cannot be explained with the intuitive description of water as a dielectric continuum.*

Part of the experimental measurements have been performed by M. Doelman (TU Delft). The chemical synthesis has been performed by E. Galan and F. Grozema (TU Delft), the theoretical calculations have been performed by N. Kavadias and J. M. Thijssen (TU Delft).

5.1. Introduction

It is well known that solvents can have a variety of effects on molecular transport, [58, 204] but while for non-polar solvents the effect may be limited to a shift in the local electrostatic potential at the junction [205], the situation is less clear for polar solvents. These can affect the molecular junction formation [206], or the anchoring dynamic [207], or form solvation-shells around the molecular wire, thereby shifting the transmission peaks [208]. The strength and result of this 'gating effect' strongly depends on the polarity of the solvent [204, 209]. Nevertheless, a more complete description of the effects of polar solvents will extend the possibilities for environmental control and gating [39, 41, 210], for sensing applications, and also to help the recent efforts to use single-molecule technique to detect and decode genetic material [211].

While single-molecule measurements in non-polar solvents have been reported both in scanning tunneling microscope-based break junction (STM-BJ) [144, 212] and mechanically controlled break junction (MCBJ) [115, 213–215], experiments in polar solvents need special care to avoid faradaic leakage currents. This is more easily done in STM-BJ [35, 216], and has only recently been achieved in MCBJ [217, 218]. In this work, using an MCBJ-in solution technique, we determine and compare the conductance of oligo(phenylene-ethynylene) molecules in air and in water. Our findings show that the conductance measured in water is a factor 4 lower than in air. This contradicts the intuitive picture that the effect of water can solely be understood as arising from a continuum, effective electrostatic medium. Density functional theory with non-equilibrium Green's function (DFT+NEGF) calculations corroborate the experimental observation: although the gap between the the highest occupied and lowest unoccupied molecular orbitals (HOMO or LUMO, respectively) decreases in the presence of water, the molecule-electrode coupling is weaker and constitutes the dominant contribution in determining the conduction change.

5.2. Results and discussion

5.2.1. Experimental results

When experiments are performed in a polar solution, parasitic currents arise due to the flow of ions in the solution [111]. To reduce this contribution, we coat the samples with a 15 nm thick layer of aluminium oxide by means of atomic layer deposition (ALD). For details about the fabrication process please see 1.4.2.

The molecule under investigation is a member of the oligo(phenylene-ethynylene) family, a class of rigid and fully-conjugated molecules. The derivative used in this study has amino groups as anchoring moieties to help its solubility in water [219]. A 0.2 mM solution containing the OPE3 molecules is prepared with dichloromethane (for measurements in air) or Sigma-Aldrich W3500 sterile-filtered water. In the latter case, a *liquid cell* made of Polychlorotrifluoroethylene (PTCFE) is filled with the solution and sealed to minimize evaporation of the solvent, thus preserving the initial concentration throughout the whole duration of the experiments.

Thousands of breaking traces are consecutively collected and combined without data selection to build a two-dimensional histograms (Fig. 5.2) showing the distribution of the conductance versus electrode displacement. A log-normal fit of the conductance histogram constructed from the same data is then used to determine the most probable conductance

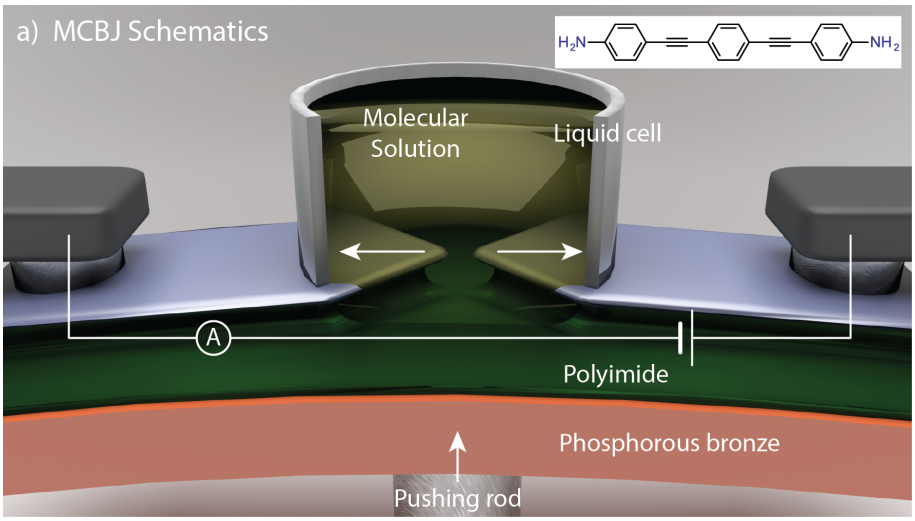

Figure 5.1: a) Schematic representation of the MCBJ setup with liquid cell mounted on top. Chemical structures of the studied molecule in the inset. b) Scanning electrode microscope images (colorized) of a typical device with alumina-coated gold electrodes. Only a minute portion of the gold electrodes protrudes out of the insulating coating, thus minimizing the flow of parasitic currents.

value of the molecule and the corresponding full-width half maximum (FWHM). Further information on the technique can be found in Frisenda *et al* [220].

Figure 5.2 compares two measurements on the OPE3 molecule performed with the same experimental parameters in different environments: in air, after drop-casting the molecular solution, and in an aqueous environment, with the solution contained in the liquid cell. The molecular signature is clear in both conditions, but in water the plateau is more slanted and spreads over a larger conductance range. The most probable conductance is $4.4 \cdot 10^{-5}\,G_0$ in air and $1.6 \cdot 10^{-5}\,G_0$ in water, while the FWHM is 1.0 orders of magnitude in air and 1.4 in water. We then quantify the steepness of the plateau by extracting the conductance with the highest probability for each displacement, thus obtaining a *master trace* that can be used as a representative of the whole histogram. From this trace, an average slope of $-0.14\,\mathrm{dec/nm^{-1}}$ is extracted for measurements in air and $-0.88\,\mathrm{dec/nm^{-1}}$ for measurements in water. The average plateau length does not change significantly when measurements are performed in solution, however a larger number of traces reaches larger displacements, with 19.8% of the traces surpassing 2 nm in water, whereas only 2.6% do in air.

The measurements have been repeated with different parameters and in different samples, consolidating the finding that measurements on the same molecule in water show a lower conductance ($(1.2 \pm 0.4) \cdot 10^{-5}\,G_0$ on average), higher dispersion ($(1.3 \pm 0.2) \cdot 10^{-5}$ decades) and a plateau with a more pronounced dependence of conductance on displacement ($-0.70\,\mathrm{dec/nm^{-1}}$) compared to those in air ($(4.4 \pm 0.5) \cdot 10^{-5}\,G_0$, (1.1 ± 0.1) decades and $-0.19\,\mathrm{dec/nm^{-1}}$ respectively on average). The full results are reported in Section 5.A. Preliminary measurements in other polar solvents show a similar behavior (Table 5.1) to what is observed in water.

If we follow the intuitive picture and imagine the water as a dielectric continuum we

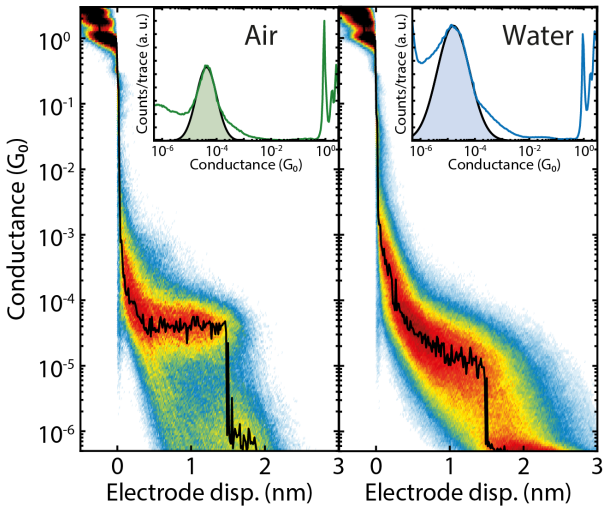

Figure 5.2: a) Two-dimensional histogram built from 3.500 and 10.000 consecutive breaking traces without data selection. The applied bias is 100 mV, and the electrode speed is 4.0 nm/s. The measurements were performed in ambient conditions after drop-casting the solution containing the molecule in air (left) or in aqueous environment in the liquid cell (right). The black line highlights the master trace (most probable conductance-displacement combination) of the measurements. The insets show the corresponding one-dimensional histograms and their log-normal fits.

would expect that the electrostatic interactions would give rise to an increase in conductance. This is due to the additional screening caused by the liquid, resulting in a reduction of the HOMO-LUMO gap [208]. The measurements, however, show and opposite trend, and therefore suggest that this picture is not correct and water cannot be modelled as a continuum electrostatic medium. Starting from this change in perspective, we will now turn to DFT+NEGF calculations to shed more light on the role of water.

5.2.2. Theoretical calculations

We present transmission curves of the Au-OPE3-Au system calculated within the DFT+NEGF formalism [221] together with a self-consistently applied scissors operator procedure [197], using our NEGF implementation [222] within the quantum chemistry package ADF by Software for Chemistry and Materials (SCM), [223] version 2017.108. The water was modelled by taking explicit water molecules into account during both the geometry optimization stage and transport calculation stage. The water molecules were placed around the molecular backbone and near the anchoring points. In addition, the COSMO model [224–226] was applied to take the bulk water effects into account.

The main mechanisms influencing the transport properties are the dielectric properties of the water, which affect the electronic structure on the molecule, and microscopic effects, which influence the electrons in the gold contact and the conformation and dipole moment of the anchoring groups.

These result into three different effects caused by the presence of water: (i) a rigid shift

of the transmission curve, (ii) a renormalization of the transport gap and (iii) a reduction of the electronic coupling between leads and molecule. These effects will be discussed separately in the subsequent paragraphs. Figure 5.3 visualizes effects (i) to (iii), whereas Figure 5.4 illustrates several mechanisms responsible for them.

Immersing a molecular junction in a solvent environment induces a rigid shift of the transmission function in the direction of negative gate voltage compared to the ambient case ('gating effect' [205]). In the case of an OPE3 molecule bridging two gold contacts surrounded by water, our DFT calculations predict a shift of −0.6 eV. As a result of this, the LUMO becomes dominant in electronic transport through the junction, in contrast to the case of an ambient environment, in which the HOMO dominates. A conductor like screening model such as COSMO is able to capture the electrostatic gating effect (effect (i)) to a large extent. In addition to this, electrostatic effects act on a microscopic scale: in the lead surface, the electron density changes due to the presence of water molecules. Also, the lead-molecule contact will adopt a different conformation due to the water molecules, altering the coupling. These microscopic effects require water molecules to be taken into account explicitly in the calculation: we have surrounded the OPE3 molecule by 92 water molecule, the exact position and orientation of which were optimised in a quantum mechanics/molecular mechanics (QM/MM) calculation [227].

The width of the transport gap (effect (ii)) is the difference in chemical potential of the ionization potential (IP) and electron addition (EA) peaks, as observed in the transmission. Adding water as an environment influences the transport gap in two ways. First, as the water is a dielectric, it effectively reduces akk Coulomb interactions. Therefore, the energy needed to add (remove) a charge to (from) the existing charge distribution on the molecule is smaller, leading to a reduction in the IP and EA, and hence a reduction of the transport gap. Second, the electrostatic screening reduces the image charge effect (ICE), leading to an increase in the transport gap (as the ICE reduces the transport gap [228]). The net effect of these two opposing mechanisms is that the transport gap is reduced in the case of a water environment. This indicates that the direct electrostatic influence of the water environment on the IP and EA is more significant than the reduction of the image charge effect.

The next effect (iii) to consider is the influence of water on the electronic coupling, which is determined by the hybridization of the molecular orbitals with the electrode wave functions [63]. Various coupling regimes can be classified by comparing the coupling strength to the charging energy and thermal energy. In the current experiment we observe off-resonant transport corresponding to the weak coupling regime. The coupling strength is directly related to the widths of the transmission peaks in a transmission plot. As the transmission curves can be described as a series of Lorentzian peaks with a width given by the coupling strength Γ [63], an estimate of the most relevant coupling strength can be made by fitting a Lorentzian to the transmission peak closest to the Fermi energy of the electrodes. In the ambient case, a Lorentzian curve is fitted to the HOMO, whereas in the presence of water a Lorentzian curve is fitted to the LUMO, as these molecular orbitals dominate the conductance at zero bias. A visual inspection of both transmission curves directly shows that the coupling is reduced upon addition of water (*i.e.*, the peaks in transmission graph have smaller width). Results from the fitted Lorentzian curves confirm this and indicate a reduction in coupling strength by a factor 9.

Inspection of the MOs with energies close to the transmission peaks in Fig. 5.4 shows

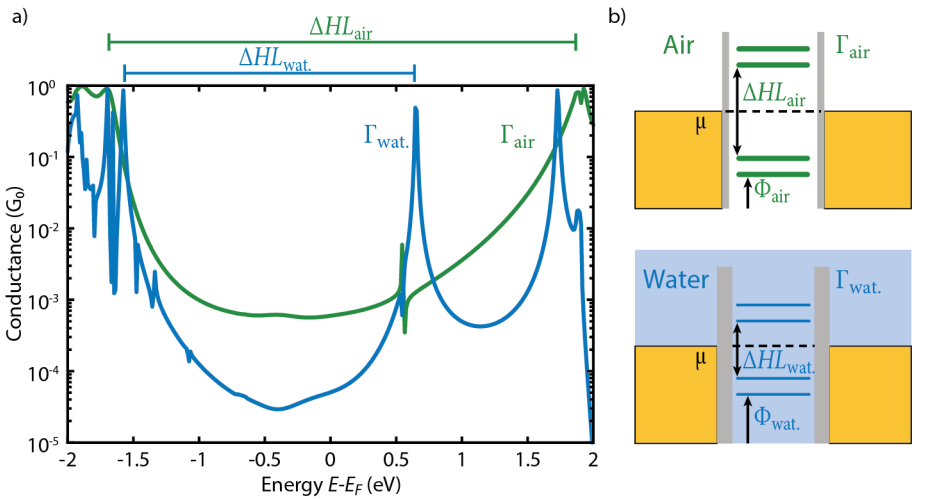

Figure 5.3: a) Transmission curves of OPE3 between two gold contacts in air (green) or a water environment (blue). From the transmission curves we can extract the lead coupling Γ, the transport gap ΔHL, and the rigid shift of the transmission curve Φ. b) Schematic representation of the influence of a water environment on a molecular junction. The yellow blocks represent the gold contacts characterized by their chemical potential μ (dashed line). The horizontal lines represent the molecular levels, the lead coupling is denoted by the vertical black barriers.

that a water environment localizes the molecular orbitals on one of the phenyl sites (Fig. 5.4b). This is contrast to the ambient case, in which the molecular orbital resembles to a good extent the structure of the gas phase LUMO, and is well hybridized with the gold contact (Fig. 5.4a). The tendency of the molecular orbital to localize when surrounded by a water environment can be understood from a reduced Coulomb repulsion between the molecular orbitals due to the screening of the charges.

Finally, a water environment severely reduces the opportunities for an amine anchoring group to form a bond with the gold electrode. The chemisorption-induced surface dipole between the gold and the anchoring group increases upon the addition of a solvent environment (units Debye): 2.13 (ambient) < 2.68 (methanol) < 3.10 (water). This leads to an increase in the gold work function and contributes to the explanation of the experimentally observed trend in conductance (units $1 \cdot 10^{-5}$ G_0): 5 (ambient) > 3 (methanol) > 1 (water).

5.3. Conclusion

An intuitive picture arising from adding a dielectric continuum to an electrode-molecule-electrode system suggests that the electrostatic interactions decrease the HOMO-LUMO gap, resulting in an increase in conductance. However, measurements of single OPE3 molecules show a lower conductance, higher dispersion and steeper plateau when performed in water rather than in air. Preliminary measurements in other polar solvents show a similar behavior (Table 5.1). DFT+NEGF calculations explain this by revealing that the role of water is not limited to electrostatic interactions, but also includes competing effects on the coupling to the leads, the molecular orbitals, the anchoring dynamic, and the molecular geometry. Overall, the theoretical calculations are in good agreement with the experimental

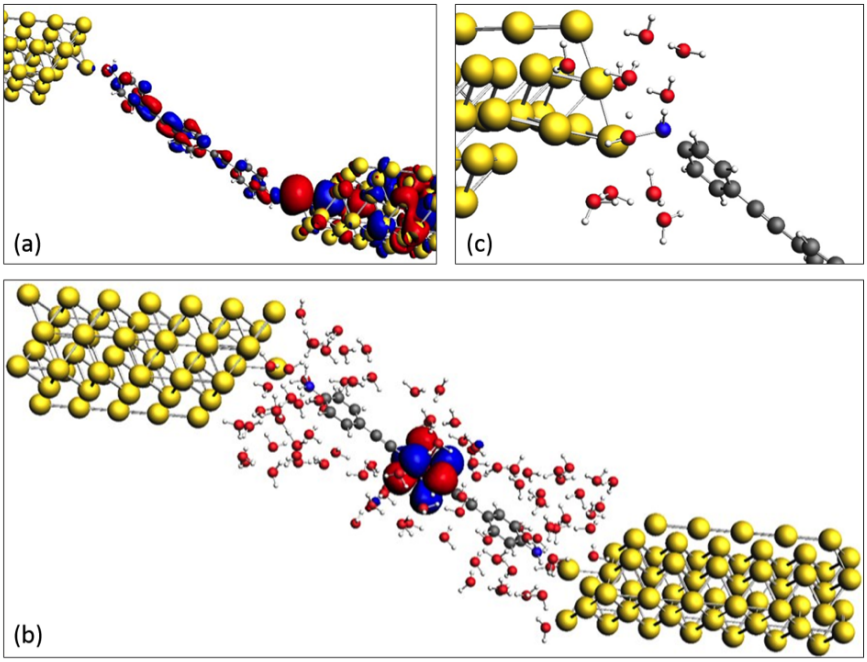

Figure 5.4: a,b) LUMO-like orbitals in the ambient and water case respectively. Without surrounding water molecules, the MO is spread out over the whole molecular backbone and one of the gold leads; with surrounding water molecules the MO is confined to a single phenyl ring. c) Visual representation of the result of a geometry optimization in a water environment. The geometry optimization procedure was performed for various contact type geometries, serving both as input for transport calculations as well as providing insight in anchoring characteristics (*e.g.*, strength of the surface dipole).

findings and give a detailed picture of the mechanisms at play. This study shows that polar solvents cannot be accurately described by a simply electrostatic model, and that a careful evaluation of the conflicting effects can predict the net effect of a polar environment on the molecular conductance.

5.A. Appendix

5.A.1. Additional measurements in air, water and other solvents

Table 5.1 reports the transport parameters obtained from five conductance measurements in air and seven in water. The averages obtained from them are compared against two measurements performed in solution of OPE3 dissolved in ethanol and methanol. All solutions were prepared with the same concentration of 0.1 mM except for W3-7, for which a concentration of 1 mM was used. This difference does not significantly affect the transport parameters.

Figure 5.5 shows the one- and two-dimensional histograms of measurements on A2, W2, E1 and M1. Figure 5.6 compares conductance, full-width-half-maximum, and slope and length of the molecular plateau in the four solvents. The measurements in methanol resemble those taken in water, yielding similar values for the slope, whereas the measurements in ethanol show a faster decay. The average conductance values obtained for the three solvents are not significantly different from one another.

Sample	Solvent	Bias (mV)	Speed (nm/s)	Traces	Molecular yield	G ($10^{-5}G_0$)	FWHM ($\log_{10}(G_0)$)	Avg. trace length (nm)	Slope (dec/nm^{-1})
A_{avg}	Air	-	-	30.340	-	4.4	1.1	1.6	-0.20
W_{avg}	Water	-	-	57.583	-	1.2	1.3	1.7	-0.65
E1	Ethanol	100	4	8.550	34.8%	1.6	1.9	1.2	-1.43
M1	Methanol	100	4	2.214	75.0%	1.6	1.6	1.6	-0.87
A1	Air	100	4	3.500	74.4%	4.4	1.0	1.5	-0.14
A2	Air	100	2	11.039	69.2%	4.3	1.0	1.4	-0.12
A3	Air	200	2	3.004	72.3%	3.7	1.1	1.6	-0.13
A4	Air	50	2	6.250	90.3%	5.0	1.0	2.1	-0.18
A5	Air	200	4	6.547	67.4%	4.7	1.3	1.7	-0.40
W1	Water	100	4	10.000	89.3%	1.6	1.4	1.6	-0.88
W2	Water	100	4	10.000	76.5%	1.0	1.6	1.5	-0.65
W3	Water	100	2	10.000	97.5%	2.0	1.2	1.4	-0.55
W4	Water	100	2	4.242	81.0%	1.2	1.7	1.5	-1.02
W5	Water	200	2	4.094	46.1%	0.9	1.4	1.3	-0.95
W6	Water	250	2	11.847	31.2%	0.8	1.0	1.8	-0.48
W7	Water	200	2	7.400	65.4%	1.0	1.2	2.4	-0.35

Table 5.1: Transport parameters from conductance measurements in different solvents at room temperature performed with different breaking speed and bias voltage. The averages obtained for experiments in air and water are calculated from the five and seven measurements (respectively) in air and water reported below.

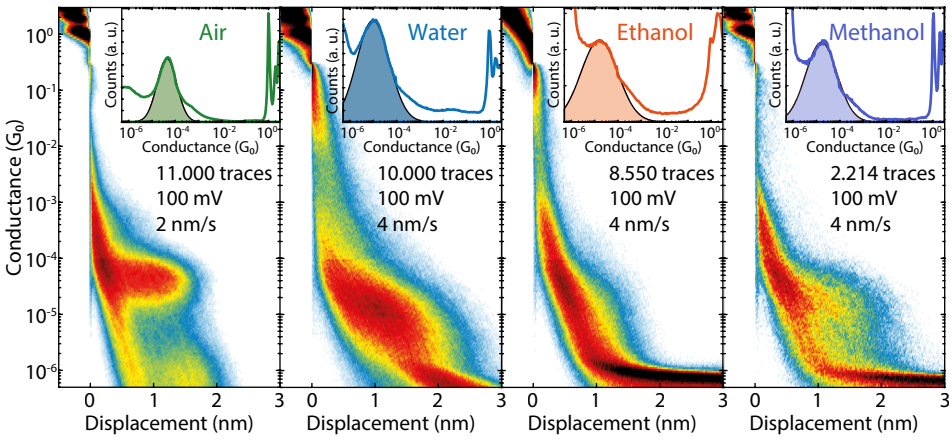

Figure 5.5: Two-dimensional histograms obtained without any data selection from measurements of OPE3 in ambient conditions, and dissolved in water, ethanol and methanol. The number of traces included in each histogram is reported in each panel, together with the applied bias and electrode speed. The insets show the corresponding one-dimensional histogram and their log-normal fit.

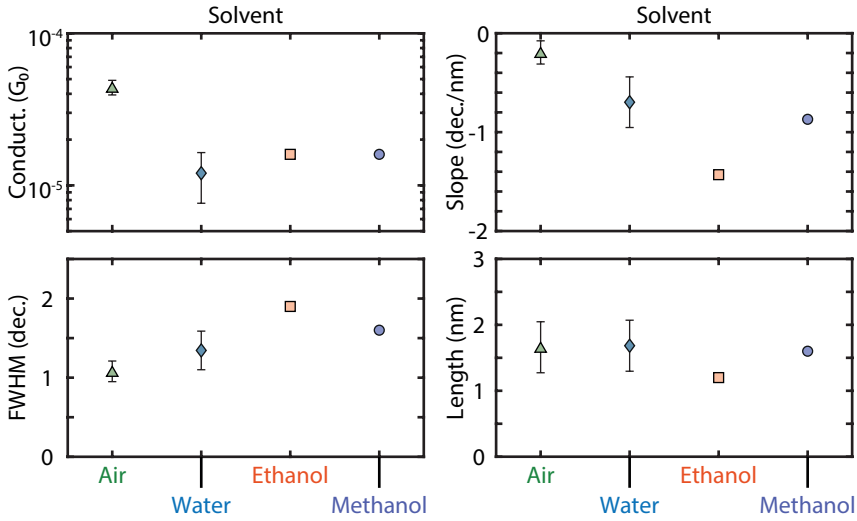

Figure 5.6: Comparison of conductance, full-width-half-maximum, and slope and length of the molecular plateau of OPE3 in air and different solvents. The parameters for air and water are averaged from 5 and 7 different measurements respectively.

6

IMPORTANCE OF PEPTIDE LENGTH AND COMPOSITION ON CHARGE TRANSPORT

Peptides are commmon building blocks of biomolecules and their ability to transport charge plays a key role in many biological functions. Because of their interesting properties, they are promising candidates for applications in molecular devices. This chapter presents a study on the length and amino acid composition of peptides and their role on their ability to transport charge. Many different conductance values are found, which can be related to different metastable configurations of the molecular junction.

The chemical synthesis of the peptides has been performed by C. Guo and D. Cahen (Weizmann institute of Science, Israel). The cluster analysis in this chapter has been performed by D. Cabosart (TU Delft).

6.1. Introduction

Charge transport through a peptide matrix is crucial for proteins to perform their function in processes such as respiration, photosynthesis, and cellular signaling [229]. The unexpected conductance, diverse and programmable structure, and unique bio-recognition of biomolecules make them promising candidates for applications in electronic devices [230]. Peptides are commmon building blocks of biomolecules, but in order to implement them in solid state devices, the relation between electron transport and peptide structure and amino acid composition needs to be better understood.

Amino acid composition, *i.e.*, the peptide side chain, influences the electronic structure of the peptide, impacting their energy levels and their coupling to the electrodes [231–233]. Tunneling is the dominant charge transport mechanism found for monolayers of short and linear peptides, with the conductance exponentially decreasing with peptide length [233, 234]. However, the electronic properties of peptides significantly change once they form secondary structures, generally resulting in an increase in conductance and variable length-conductance dependence for helical peptides [233]. Electron transport occurs through hopping or a mixture of hopping and tunneling under different experimental conditions [235–238]. Changes on the conformation of the secondary structure also affect electron transport: even slightly bending the α-helix can dramatically decrease electron transfer of peptides in solution [239]. Besides the composition and secondary structure of the peptides, many functional groups found in the amino acid components (like thiol and indole) are highly likely to interact with the electrodes [240, 241]. All these variables multiply the possibile behaviours of peptide molecular junctions, the information of which are usually masked by measurements in bulk or in orientated self-assembled monolayers. However, this information is crucial in order to understand the details of electron transport via peptide junctions and to design and improve peptide-based molecular electronic devices. For this reason, it is needed to study peptides at the single-molecule level in order to separate intrinsic properties from those arising from cooperative effects.

In this chapter, we used the mechanically controlled break junction (MCBJ) technique (Fig. 6.1) to study the electron transport propeprties of single-peptide molecular junctions. We studied a series of linear peptides composed of typical amino acids: alanine (Ala), tryptophan (Trp), and cysteine (Cys). Mercaptopropionic acid (MPA) is added to the N-terminus of the peptides to introduce a thiol group that acts as an anchoring unit to one of the gold electrodes of the MCBJ device. The dependence of electron transport on chain length is studied with poly-Ala peptides (Fig. 6.1a), whereas the importance of chain composition is investigated in a series of 4-amino-acid long peptides with different amino acid combinations. The roles of different electrode anchoring groups at the C-terminus (−COOH and −SH) are discussed by introducing a terminal Cys element (Fig. 6.1b). Because of the important role that aromatic groups play on the molecular conductance [114, 121, 175–177], Trp, an aromatic amino acid, is introduced in the peptide to investigate its effect on electron transport. Trp has low ionization potential (IP) in natural amino acids and its indole ring provides delocalized electrons that can contribute to tranport [242]. In the following, the peptides will be mentioned without the MPA and using the abbreviations for the amino acids (Ala, Cys and Trp or A, C, W).

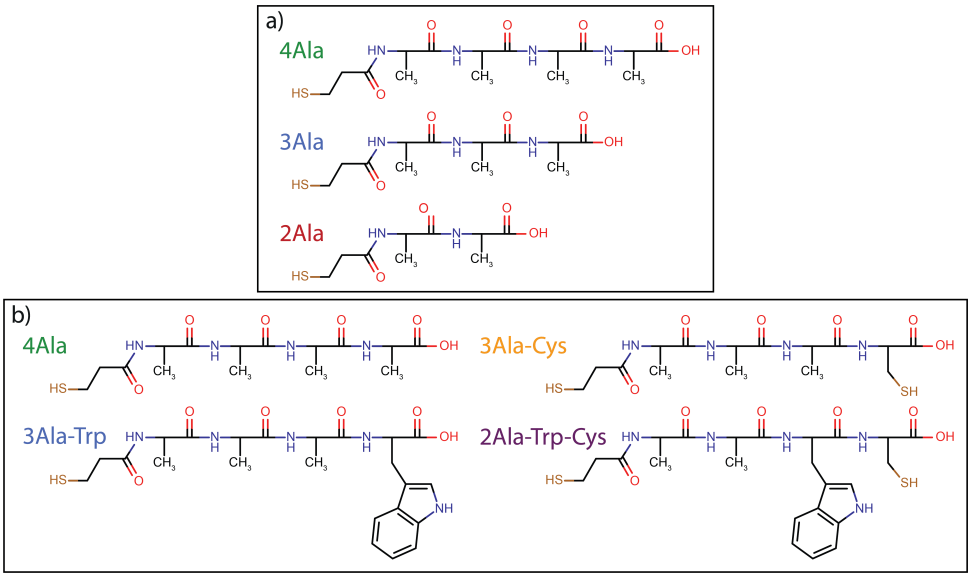

Figure 6.1: a) Structure of the (*n*)Ala (n = 2, 3, 4) peptides utilized for the length study in this work. b) Structure of the peptides utilized in the 4-amino-acid peptide study. MPA is attached at the N-terminus of each peptide.

6.2. EXPERIMENTAL RESULTS

The target peptide was dissolved in a 1 : 3 solution of acetonitrile (ACN) and deionized water and then dropcasted on the MCBJ sample. Thousands of consecutive breaking traces are collected in vacuum and combined into one- and two-dimensional conductance histograms (Fig. 6.2a and Figs. 6.6 and 6.7). One-dimensional histograms (right panel of Fig. 6.2a) are usually employed to extract the most probable conductance of the molecule. However, for all peptides, a clear unique conductance peak is not found in these histograms. When comparing the 2D histograms to the bare gold sample characterized before the dropcasting of the molecular solution (Fig. 6.5), on the other hand, longer traces and counts at higher conductance value reveal a signature of the molecule. Specifically, short plateaus are observed in the breaking traces as the molecule is stretched across the junction (Fig. 6.2b). These plateaus indicate the formation of a (meta)stable molecular junction at different conductance values and electrode separation.

To gain more insight on the appearance of the plateaus, we utilize a reference-free classification algorithm based on clustering of the data with the K-means++ method (Fig. 6.2c). The algorithm groups traces that have similar one- and two-dimensional histogram, thus highlighting their most prominent features. Briefly, the algorithm works as follows. From each trace, a 28-by-28 two-dimensional histogram and a 100-bin one-dimensional histogram are extracted. These are then combined to form the feature space over which the clustering algorithm operates. For the creation of the one-dimensional histogram, the trace is interpolated to have 1.000 points between 0 and 1.5 nm. This gives more weight to the plateaus in the traces and thus helps with their classification. The K-means++ algorithm is then run 100 times with randomly initialized conditions and the result that yields the small-

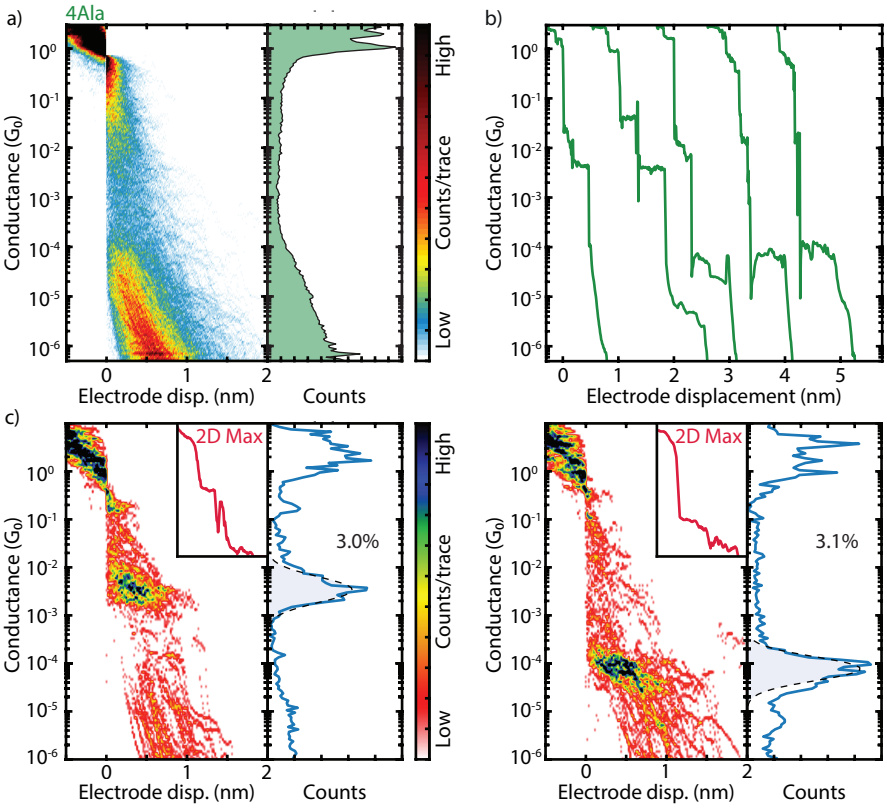

Figure 6.2: a) Two-dimensional (left panel) and one-dimensional (right panel) conductance histogram built from 2.000 consecutive breaking traces collected after deposition of 4Ala and displayed without data selection. The measurements are performed in vacuum with an applied bias of 100 mV, and an electrode speed of 3.0 nm/s. b) Example of breaking traces of 4Ala with molecular signature. The traces are offset by 1 nm in the *x*-direction for clarity. c) Example of clusters obtained with the K-means++ method from the measurement of 4Ala shown in panel a). The inset shows the *master trace* of the cluster, *i.e.* the conductance with the highest probability for each displacement. The one-dimensional histogram of the cluster is shown in the right panel, together with a log-normal fit to the conductance peak (shaded area under the dashed line).

est cost function value is used. A more detailed description of the clustering method can be found in Section 6.A.4 and in Appendix A.

The conductance value, position, and length of the plateaus are extracted for each cluster and compared between the different peptide series. The three parameters are obtained in the following way. The log-normal fit of the one-dimensional histogram of each cluster yields the conductance value associated to that cluster. We define the master trace associated to a cluster from its two-dimensional histogram by highlighting the conductance with the highest counts for each displacement (insets of Fig. 6.2c). The length of the plateau associated to the cluster is determined from the portion of the master trace that falls within ± half an order of magnitude of the cluster peak. Finally, the plateau position is defined as the center of the displacement range defined above. The set of log-normal fits to the clus-

ters obtained for each molecule represents a simplified one-dimensional histogram in which only the signal of conductance plateaus is taken into account (Fig. 6.3b and Fig. 6.4b). This helps to compare the results for the different peptides. The width of the peaks is proportional to the FWHM of the log-normal fit, and their height is related to the number of traces belonging to the corresponding class. With the conductance values and position of the clusters defined above we can also construct an analogous of the two-dimensional histogram, which shows where the various clusters are most likely to appear in the breaking traces (Fig. 6.3a and Fig. 6.4a).

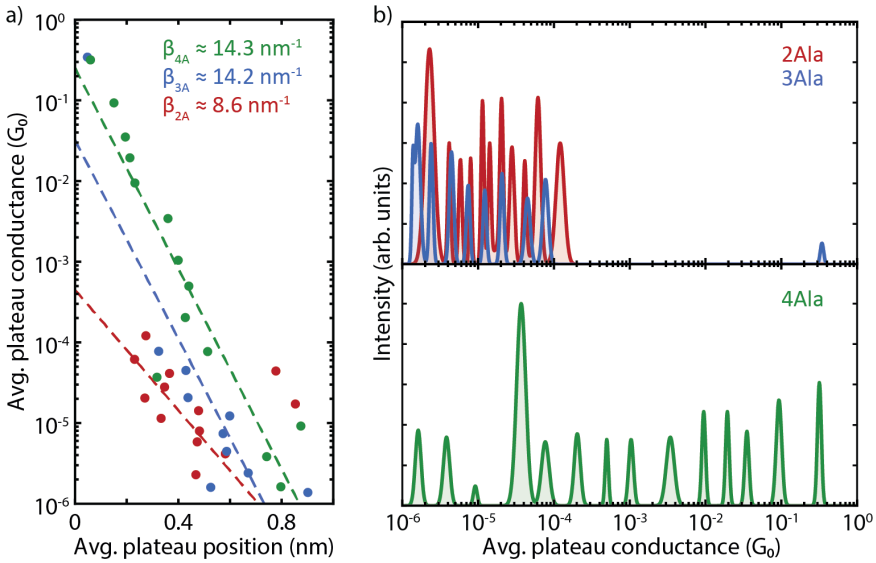

Figure 6.3: a) Extracted conductance value versus plateau position of the (*n*)Ala peptides shown on a semilog scale. The shorter peptides do not show conductance peaks at high conductance values. A linear fit to the data of 3Ala and 4Ala is used to extract the decay rate β. The red dots and line represent 2Ala, the blue 3Ala, and the green 4Ala. b) Conductance peak distribution of the (*n*)Ala-peptides.

For 4Ala, the extracted conductance peaks are found across the whole conductance range accessible in our setup and at displacement values ranging from < 0.05 to 1.0 nm, with an average plateau length between 0.2 and 0.7 nm (Fig. 6.8a). The conductance peaks follow an exponential decay with displacement over six orders of magnitude, so it is possible to fit the data in order to extract the decay rate parameter β ($G = Ae^{-\beta L}$). We obtain $\beta = (-14.3 \pm 1.2)\,\mathrm{nm}^{-1}$, a value larger than the previously reported $\beta = (8.7 \pm 7.0)\,\mathrm{nm}^{-1}$ in the case of cysteamine-(*n*)glycine-cysteine chains [243], $\beta = 9.3\,\mathrm{nm}^{-1}$ for trialanine and $\beta = 9.7\,\mathrm{nm}^{-1}$ for triglycine [244]. The β values from literature are measured with the STM break junction method in high concentration solution (1 mM) and are binding to the electrodes by a Au–S bond in the former case, but not in the latter two. The β value found in our case is larger than both, indicating that electron transport is not solely determined by the peptide-electrode binding mechanism. The low tunneling efficiency, inferior even to other non-conjugated molecules like alkanes ($\beta \approx 7.5 - 10.0\,\mathrm{nm}^{-1}$) [35, 58, 86, 91], indicates that peptides are not particularly good conductors.

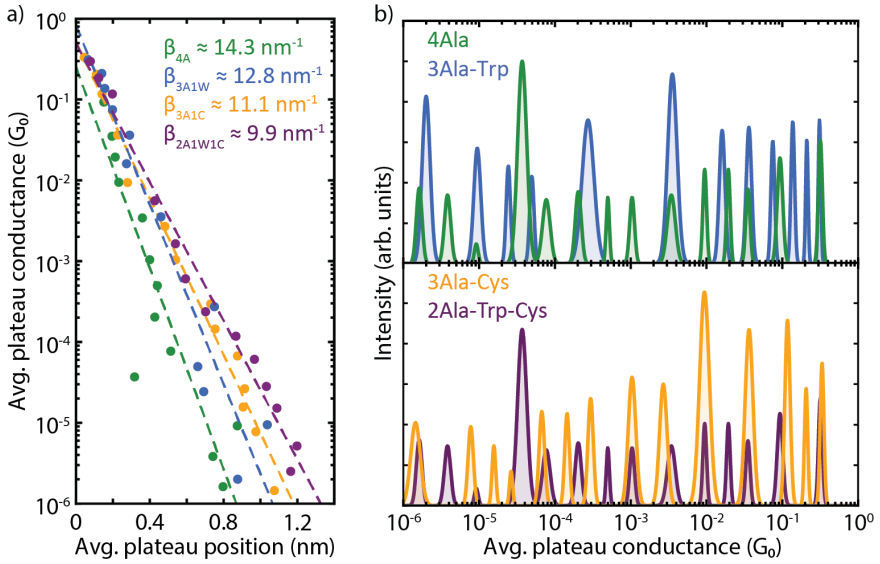

Figure 6.4: a) Extracted conductance value versus plateau position of the 4-amino-acid peptides shown on a semilog scale. A linear fit to the data is used to extract the decay rate β. The green dots and line represent 4Ala, the blue represent 3Ala-Trp, the yellow 3Ala-Cys and the purple 2Ala-Trp-Cys. b) Conductance peak distribution of the 4-amino-acid peptides.

The conductance peaks for the shorter peptides 2Ala and 3Ala are found in the 0.1 – 0.8 nm displacement range at lower conductance values ($< 10^{-4}\,G_0$) than those of 4Ala (Fig. 6.3a). We performed the same linear fit for these molecules, obtaining a β for 3Ala that is similar to that of 4Ala, while β is higher for 2Ala. However, the intercepts for these three peptides are 4Ala > 3Ala > 2Ala.

The role of peptide composition on its electron transport is discussed by comparing the clustering results of 4Ala, 3Ala-Trp, 3Ala-Cys, and 2Ala-Trp-cys (Fig. 6.4). The extracted conductance peaks are found across the whole conductance range and at displacement values ranging from 0.05 to 1.2 nm. This matches well with the estimated length of the 4-amino-acid peptides of 1.7 nm after we take into account the ≈0.5 nm snap back of the electrodes that happens when the last gold atom connection is broken [123, 245]. The average plateau length is found between 0.2 and 0.7 nm for all peptides, and it increases with decreasing plateau conductance (Fig. 6.8a). The conductance peaks of these four peptides all show exponential decays with displacement. The β values obtained from the fit are 4Ala > 3Ala-Trp > 3Ala-Cys > 2Ala-Trp-Cys, and the intercepts are in the sequence 3Ala-Trp > 3Ala-Cys > 2Ala-Trp-Cys > 4Ala, albeit with similar values. Moreover, peptides with Trp give longer plateaus at higher conductance than their Ala counterparts (Fig. 6.8). The full fit results are found in Table 6.1.

Molecule	β (nm^{-1})	A (G_0)
3Ala	-14.2 ± 1.8	$3.2 \cdot 10^{-2}$
4Ala	-14.3 ± 1.2	$2.5 \cdot 10^{-1}$
3Ala-Trp	-12.8 ± 0.7	$8.3 \cdot 10^{-1}$
3Ala-Cys	-11.2 ± 0.3	$5.2 \cdot 10^{-1}$
2Ala-Trp-Cys	-9.9 ± 0.3	$5.0 \cdot 10^{-1}$

Table 6.1: The function $G = Ae^{-\beta L}$ is fitted to the conductance vs. displacement histogram in semilog scale, in order to obtain a linear fit. The results of the linear fit for the various peptides are reported here.

6.3. Discussion

The plateau-like features observed in the measurements are likely associated with various metastable configurations involving different binding configurations probed during the breaking process. Each conductance peak is then related to a certain junction configuration, which can in turn vary depending on the binding sites involved, on the local geometries of the Au atoms on the electrode surface and on the conformation of the binding group. The most stable binding groups in the peptides are the thiol (−SH), amide (−CONH-) carboxyl/carboxylic (−COOH / −COO−), and indole groups [240, 241]; the binding configurations related to the peaks observed in the measurements are therefore expected to involve these groups. Similar combinations of these binding sites can be found in the different peptides, which suggests that there should be some similarity between the conductance values and positions of the peaks for different peptides. Indeed there are similarities between the extracted conductance peak distributions for different peptides (peaks overlay for different peptides in Fig. 6.3 and Fig. 6.4). However, it is not straightforward to associate each conductance peak with a specific electron path because of the complexity of the peak distribution.

The presence in 4Ala of conductance plateaus above $10^{-4}\,G_0$, compared to the shorter 2Ala and 3Ala, may be related to the flexibility of the peptides. When a polymer is shorter than the persistence length, it behaves like a relatively rigid rod. The persistence length of unfold peptides is around 0.4 nm [246–249], a value close to the distance of two adjacent α-carbon (approximately the length of an amide group). Therefore, it is possible to imagine a peptide as composed of rigid rods (the amide groups) that can rotate around their connection points (the α-carbons). Its flexibility thus increases with the number of amino acids it is composed of. Since the length of the stretched peptides (2Ala, 3Ala, 4Ala) are approximately 2, 3, 4 times the persistence length, the flexibility of the peptides should follow 4Ala > 3Ala > 2Ala. Based on this information, it is possible that 4Ala has the ability to fold and form a molecular junction with non-linear configurations which result in high conductance values at short displacement, whereas these plateaus are not observed for 2Ala and 3Ala because the associated configurations are not available to them. Moreover, since all of the 4-amino-acid peptides have a similar length, they are also expected to have a flexibility similar to 4Ala. This is consistent with the experiments, which show that all of them exhibit conductance plateaus above $10^{-4}\,G_0$ at short displacement. Finally we note that at large electrode spacings the peptides are extended in the junction: they have a linear structure and the conductances are low in this regime. On the other hand, peptides that can fold

into more compact non-linear configurations can support shorter charge pathways, resulting in high conductances. These configurations are probed only in the initial stage of the breaking sequence, and are only observed if the pepetides that are pulled across the gap are long and flexible enough to be able to bridge the gap while preserving a non-linear structure.

The estimation of the β decay rate is commonly used to study the conductance of molecules which present a repeating subunit. The measurements of all the 4-amino acid peptides, nonetheless, show an exponential decay of the extracted conductance peaks versus displacement. Determining the decay rate helps to compare the overall conductivity of the different peptides. The β values for the -Cys peptides are lower than their non-Cys counterparts (3Ala-Cys < 4Ala and 2Ala-Trp-Cys < 3Ala-Trp); and the –Trp peptides have lower beta values than the –Ala counterparts (3Ala-Trp < 4Ala and 3Ala-Cys < 2Ala-Trp-Cys). Normally, the electronic transport of peptides with a secondary structure is mainly due to the secondary structure [235] and not affected by amino acid compositions. However, our measurements suggests that the thiol group in the Cys and the indole ring in the Trp play a significant role in the electronic transport, and thus that peptide composition directly affects electron transport, provided that they can assume non-linear conformations. These four peptides also display similar values for the intercepts, indicating similar peptide-electrode binding conditions at the interfaces for the four peptide junctions [250], or that electron transport through peptides is not sensitive to interface interactions.

6.4. Conclusions

In conclusion, we have measured the conductance of six different peptides, investigating the influence of the chain length and composition on the electronic transport. The low tunneling efficiency found for these peptides suggest that peptides are not good conductors. However, short plateaus at high conductance values are found for peptides composed of 4 amino acids, indicating that the ability to fold into non-linear configurations might be beneficial to electron transport. Finally, we have shown that the peptide transport efficiency is improved by the presence of Trp and Cys in the chain composition.

6.A. Appendix

6.A.1. Characterization of the bare gold device

Before each measurement, we perform a thorough characterisation of the bare device before dropcasting the molecular solution, in order to ensure that the electrodes are clean and well aligned. This is done by recording 2.000 consecutive breaking traces in ambient conditions. The characterisation of the bare device used for the measurements of 4Ala is shown in Fig. 6.5. The traces show a clear plateau at a conductance of 1 G_0, a sudden drop in conductance due to the snapback of the electrodes, and finally an exponential decay in conductance with the electrode displacement.

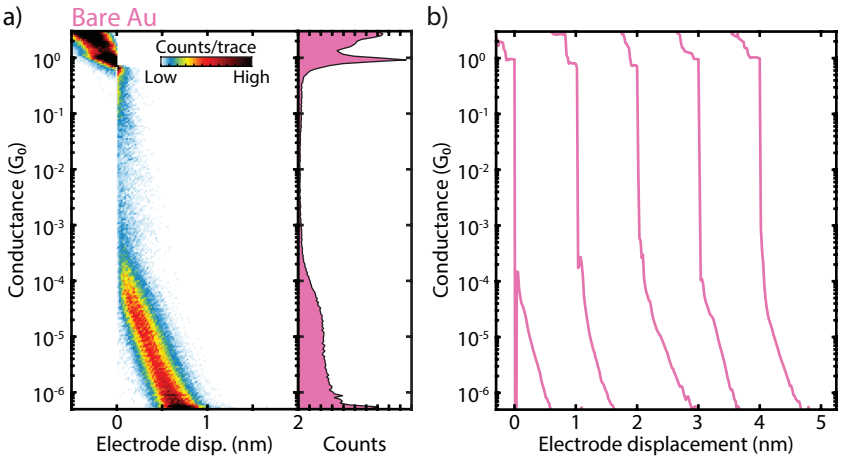

Figure 6.5: a) Two-dimensional (left panel) and one-dimensional (right panel) conductance histogram built from 2.000 consecutive breaking traces collected on the bare device before deposition of the molecular solution and displayed without data selection (same device used for the measurements of 4Ala shown in Fig. 6.2). The applied bias is 100 mV, and the electrode speed is 6.0 nm/s. b) Examples of breaking traces recorded on the bare device.

6.A.2. Measurements of (*n*)Ala series

Figure 6.6a,c shows the two-dimensional histograms of the peptides 2Ala and 3Ala, whereas Fig. 6.6e shows an additional measurement of 4Ala performed on a different sample than the one shown in the main text. The concentration of the molecular solutions dropcasted was 2 μM in all cases.

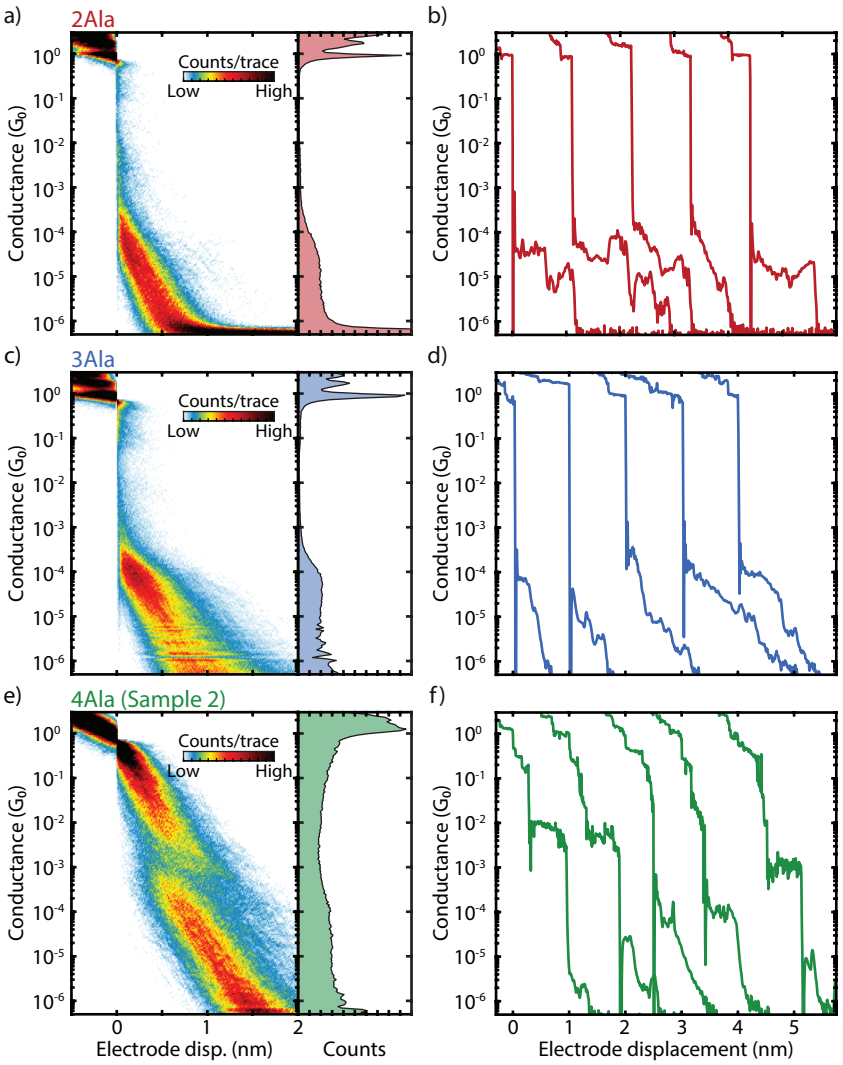

Figure 6.6: a,c,e) Two-dimensional (left panel) and one-dimensional (right panel) conductance histograms with no data selection of 2Ala (a), 3Ala (c) and 4Ala (e). b,d,f) Examples of the 2.000 consecutive breaking traces collected for each molecule. The applied bias is 100 mV and the electrode speed is 2 nm/s for 2Ala, 3 nm/s for 3Ala and 3 nm/s for 4Ala.

6.A.3. Measurements of 4-amino-acid series

Figure 6.7 shows the two-dimensional histograms of 3Ala-Trp, 3Ala-Cys and 2Ala-Trp-Cys. The concentration of the molecular solutions dropcasted was 2 μM in all cases.

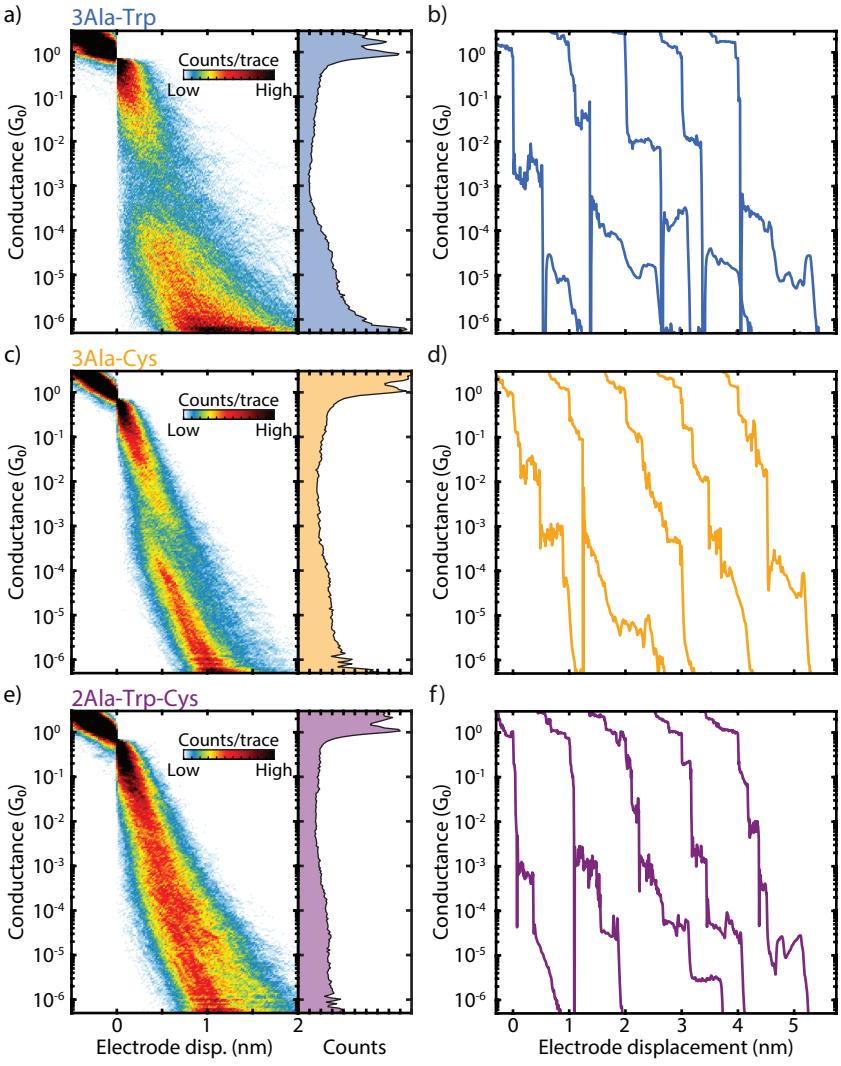

Figure 6.7: a,c,e) Two-dimensional (left panel) and one-dimensional (right panel) conductance histograms with no data selection of 3Ala-Trp (a), 3Ala-Cys (c) and 2Ala-Trp-Cys (d). b,d,f) Examples of the 2.000 consecutive breaking traces collected for each molecule. The applied bias is 100 mV and the electrode speed is 4 nm/s for 3Ala-Trp, 3 nm/s for 3Ala-Cys and 2 nm/s for 2Ala-Trp-Cys.

6.A.4. Clustering parameters

Since the algorithm groups traces that have similar one- and two-dimensional histogram, it highlights their most characteristic features, thus focussing on the most stable configuration probed during that breaking event. The clusters do not show strong correlations between plateaus, which means that there is no preferred transition from one configuration to another.

The number of clusters is chosen to be 15. This number is somewhat arbitrary: for instance, clustering with a lower number of classes is also possible and would result in similar conclusions to those presented here. In particular, a smaller number of cluster would most likely result in clusters with a similar conductance to be merged into one. Nonetheless, since the lengths of plateaus with similar conductance are also similar, the plateaus will display the same overall behaviour.

6.A.5. Plateau length distribution

As mentioned in the main part of the chapter, the length of the plateau associated to a cluster is determined from the portion of the master trace that falls within ± half an order of magnitude of the cluster peak. The distribution of plateau length versus conductance for the 4-amino-acid is reported in Fig. 6.8.

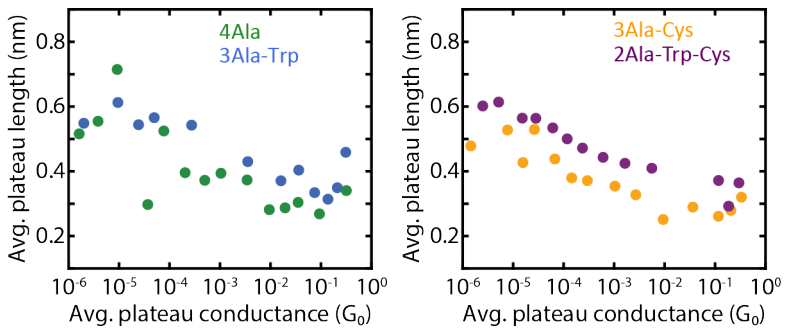

Figure 6.8: Plateau length versus conductance value shown on a semilog scale of the clusters found for the peptides in the 4-amino-acid series.

6.A.6. Analysis of the conductance steps

The initial approach we followed to analyze the distribution of the peaks in the breaking traces did not involve the clustering method described above. Given that it is not infrequent to observe multiple plateaus in a single trace, we tried to extract information from all of them. The results of this analysis lead to similar conclusions as those obtained with the clustering method, but with less evidence. In the following, the analysis procedure and results will be presented.

The data sets obtained for each peptide of the 4-amino-acid series is run through a filter that selects traces that have short plateaus. A plateau is defined as a portion of the trace that has a decrease in conductance of less than 0.2 dec/nm over a distance of at least 0.2 nm. This is done by fitting the breaking trace over limited portions of the trace until the conditions set above are met. After a plateau has been identified, the search continues on

the same trace until the conductance falls below the noise level, which means that if a trace contains multiple plateaus, all of them will be considered. We then extract the position (defined as the centre of the plateau) and conductance (the average of the conductance values which constitute the plateau) of these plateaus and build one- and two-dimensional histograms with them (Fig. 6.9). Plateaus centred at less than 0.3 nm displacement are discarded to avoid false positives. The algorithm is the most sensitive to the requirements on the plateau length, but small changes to the parameters do not affect the overall conclusions presented here.

The conductance distribution of the plateaus for the various peptides shows peaks at different conductance values. In particular, plateaus are found at low conductance in 4Ala, whereas when Ala moieties are substituted with Trp ones, new peaks appear at higher conductance values of 10^{-4}, 10^{-3} and up to 10^{-2} G_0 for 3Ala-Trp. When Ala is substituted with Cys instead, the distribution is centred around 10^{-4} G_0, although peaks at 10^{-6} G_0 can still be found. The multitude of conductance plateaus found hints that multiple binding configurations can be available and are explored in a single breaking event [243]. In this regard, the presence of the thiol moiety in the Cys group gives more stability to the junction configuration than the carboxyl group found in Ala or the indole ring in Trp and for this reason the distribution is more strongly polarized around a single conductance value. On the other hand, the increased number of peaks in amino acids containing Trp suggests that the indole ring plays a significant role in electronic transport through peptides. No clear clustering of the plateaus is found in the two-dimensional histograms, as shown in Fig. 6.9.

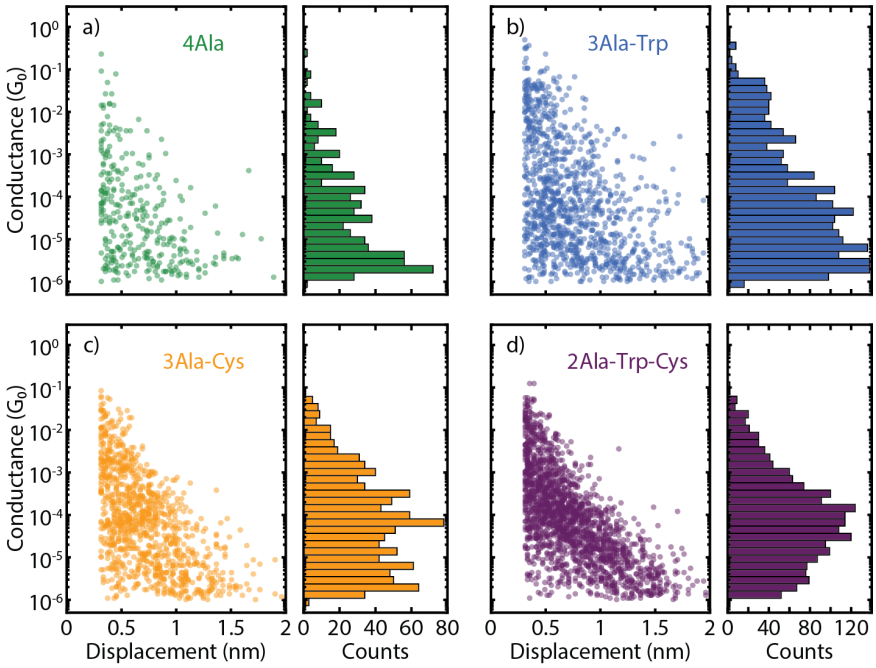

Figure 6.9: Conductance and conductance vs. displacement distributions of the plateaus found in the peptides of the 4-amino-acid series.

7

OUTLOOK

This chapter presents preliminary results on four ongoing projects. The first is an initial approach to characterize the transmission dip of the molecule presented in Chapter 4. In the second, the role of bulky side groups is investigated on the OPE3 family of molecules. Additionally, the influence of anchoring and bulky side groups in the electronic paths is studied on a family of porphyrins. Finally, the topic of molecular switches is touched upon in the work on pseudo-rotaxane molecules.

Part of the experimental measurements and the cluster analysis in this chapter have been performed by M. El Abbassi and A. Rates (TU Delft). The chemical synthesis of the PCP3 molecule has been performed by K. Weiland and M. Mayor; that of the porphyrin molecules by P. Zwick and M. Mayor; that of the bulky OPE3 molecules by T. Brandl and M. Mayor (University of Basel, Switzerland). The rotaxanes were synthesised by S. Tatay, E. Miguel and E. Coronado (University of Valencia, Spain).

7.1. Mechanical tuning of quantum interference

In order to better understand how mechanical deformations affect the transmission of the molecules presented in Chapter 4 (here named PCP3 for convenience), measurements were performed at cryogenic temperature ($\approx$ 6 K). The reduced thermal agitations present at low temperature further increase the stability of the molecular junctions, allowing to measure the electronic properties while deforming the molecule. By collecting current-voltage (IV) curves, one can directly compare the results of the measurements with the predictions coming from the theoretical calculations.

From the transmission map obtained from density functional theory (DFT) calculations (Fig. 7.1a), the transmission curves for different values of deformation (Fig. 7.1b) can be extracted and, from these, it is possible to simulate the current-voltage and differential conductance ($\mathrm{d}I/\mathrm{d}V$) curves of PCP3. The $\mathrm{d}I/\mathrm{d}V$ curves so obtained exhibit distinctly different behaviours that are related to the deformation of the molecule. In Fig. 7.1, positive values of displacement correspond to a stretching of the molecule, whereas negative values indicate its compression. When the molecule is compressed (negative displacements, blue curves in Fig. 7.1), the differential conductance presents a Fano resonance-like feature at symmetric voltage values between 0 and 1.3 V (Fig. 7.1c). As the compression decreases and the molecule approaches its relaxed configuration, the Fano resonance is smeared out and eventually disappears when the molecule is relaxed (purple curve). Instead, a pronounced transmission dip appears as a consequence of the destructive interference taking place in this configuration. As the molecule is stretched (red curves) the dip becomes more and more shallow, and resonance features can be found at smaller and smaller bias values.

It is important to mention that the displacement at which the transmission valley intersects the Fermi energy has been chosen as the zero displacement, since only relative displacements are physically meaningful in this scenario. Further details can be found in Stefani *et. al.* [251].

The IV measurements are performed at cryogenic temperature ($\approx$ 6 K) and explore a symmetric voltage range of $\pm$0.7 V. The junction is stretched by bending the substrate with a brushless servomotor and, after the opening of the junction and the formation of a gap, IVs are collected at increasing electrode displacements. When the maximum current recorded during the bias sweep falls below 100 pA, the junction is fused back.

Examples of IVs and their corresponding $\mathrm{d}I/\mathrm{d}V$s are presented in Fig. 7.2. The IVs and $\mathrm{d}I/\mathrm{d}V$s have been normalized and offset in the y-axis for clarity. The $\mathrm{d}I/\mathrm{d}V$s are also displayed in log-scale for clarity. All three behaviours expected from the DFT calculations are observed in the experiments: (i) small peaks found symmetrically around zero bias are shown in Fig. 7.2a, (ii) a sharp and narrow conductance dip at zero bias is seen in Fig. 7.2b and a broad and shallow one instead in Fig. 7.2c, (iii) together with a resonance-like feature just below 0.4 V.

The first kind of curves (i) is expected for configurations in which the molecule is compressed. The fact that the molecule is compressed while the motion of the electrodes is only expected to stretch it is somewhat surprising, yet these features are observed consistently. Since they are associated to a compressed molecule, these resonances are expected to be found at progressively lower voltage values in the measurement sequence (see how they approach zero as the displacement increases in the blue curves in Fig. 7.1c), as the IV curves are measured at increasing displacement (and therefore stretching of the molecule). This

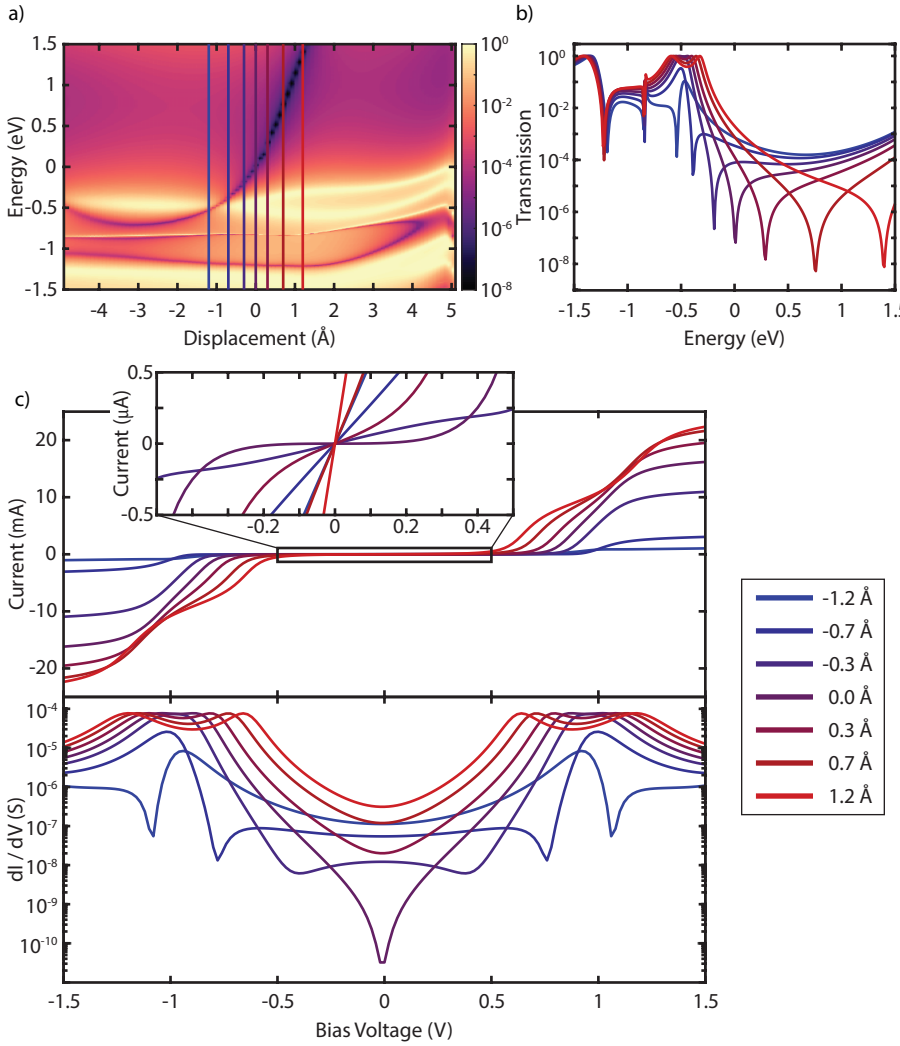

Figure 7.1: a) Transmission map of PCP3 between two leads obtained from DFT calculations. b) Transmission curves for various degrees of deformation of the PCP3 molecule. c) Current-voltage (IV) and differential conductance ($\mathrm{d}I/\mathrm{d}V$) curves for different deformations obtained from the transmission map in a and b. The IV curve at a determined deformation is calculated by integrating the corresponding transmission according to Eq. (1.6) and the $\mathrm{d}I/\mathrm{d}V$ curve is obtained from its derivative.

is indeed observed (Fig. 7.3a), but also the opposite behaviour is observed, or even no correspondence between spacing and electrode displacement (Fig. 7.3b). The spacing could instead be related to the low-bias conductance value associated to the IV curve. However, while in Fig. 7.4a the spacing is smaller for larger conductance values, the opposite trend is observed in Fig. 7.4b.

The second kind of $\mathrm{d}I/\mathrm{d}V$s (ii) show a dip at zero bias that is the sharpest when the

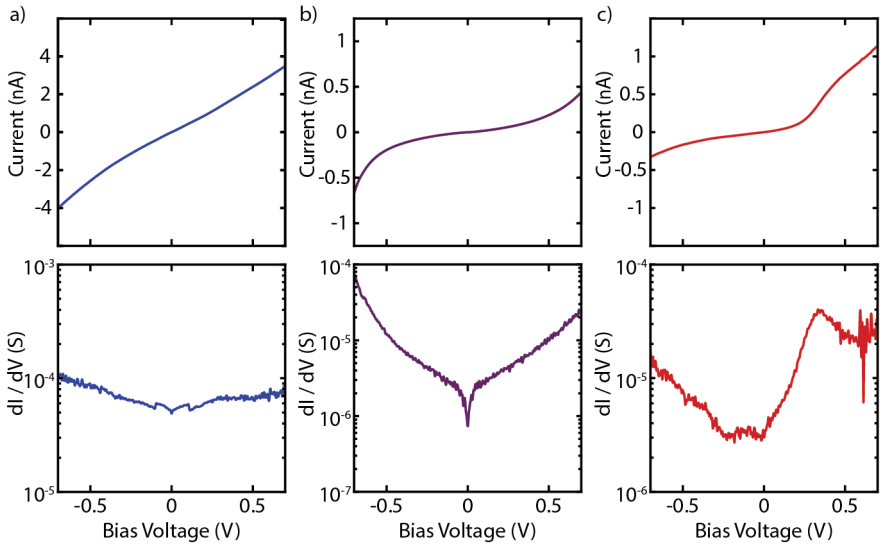

Figure 7.2: a-c) Examples of IV and dI/dV curves displaying Fano resonance-like peaks expected for a compressed molecule (a), a sharp and narrow conductance dip at zero bias expected for at the antiresonance (b), and a resonance-like feature expected for a stretched molecule (c).

conductance is the lowest (*i.e.* at the antiresonance) (Fig. 7.3b) and is often accompanied by two Fano-like peaks like the ones expected for a compressed molecule. The exact position of the dip is also expected to depend on the Fermi energy. If this does not coincide with zero bias voltage, the dip should be found at different voltage values. This is, however, not observed, as the dip is always found at zero bias. Compared to the dip predicted from the theoretical calculations, the observed dip is much sharper and narrower. Since the dip is due to quantum interference, the jumping up of the conductance dip at low voltages needs to be a "dephasing" effect, possibly caused by zero-point vibrational motion. Moreover, the dip could be further smeared by the excitation of vibrations (perhaps vibrations in the gold electrodes rather than in the molecule). If this is the case, the frequency of the mode might provide useful information to identify its origin.

Finally, the kind of curves (iii) presenting a shallow dip and resonance-like features are most commonly found in measurement sequences with constantly decreasing conductance. Since resonances are only expected within the investigated bias range for significant stretchings, it is possible that once the molecule is stretched that far, the junction stability is compromised.

The whole succession of curves presenting Fano-like peaks, dip and resonance has not been found in a single breaking sequence.

To conlcude, the strong entanglement between the electrical and mechanical properties of the PCP3 molecules makes this chemical architecture very promising to study the dephasing mechanism that are suspected to cause the transmission dip to be so sharp. A systematic study of the voltage at which the various features are observed will be conducted to help identify the dephasing mechanism. The use of a setup fitted with a piezoelectric el-

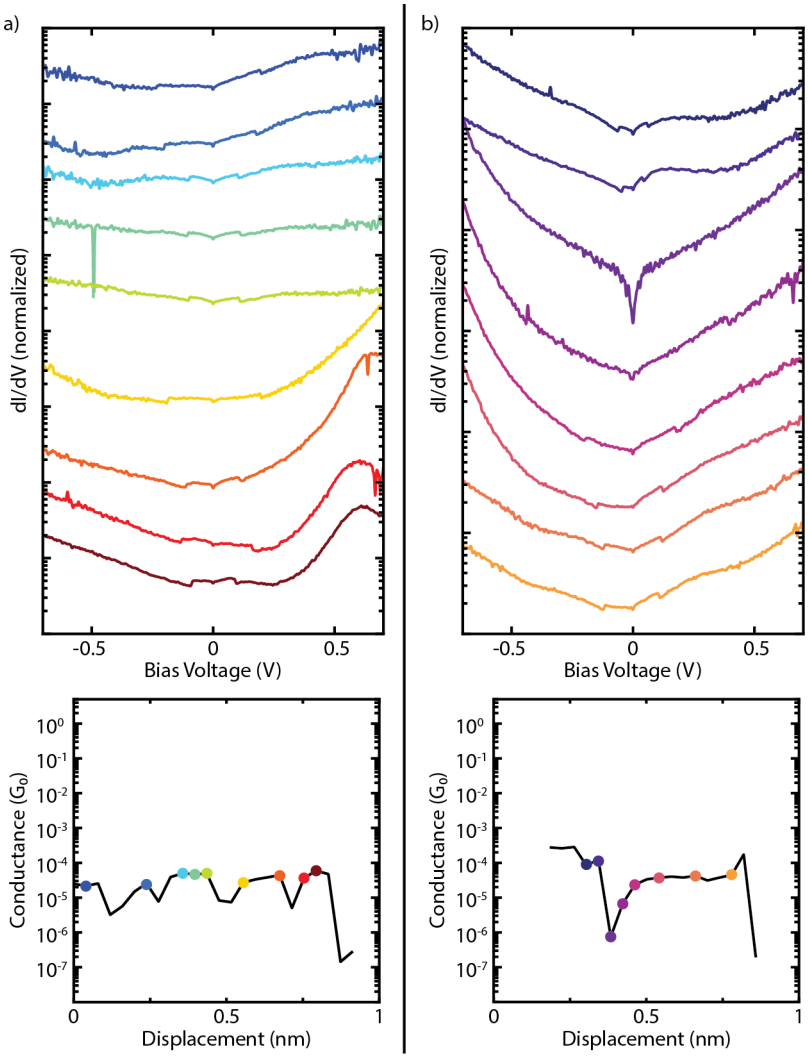

Figure 7.3: a-b) Examples of dI/dV curves extracted from the same measurement sequence. The conductance corresponding to each curve is shown as a dot of the same colour in the conductance vs. displacement trace.

ement suitable for cryogenic temperatures could further expand the possibility of reliably manipulating the molecule, thus allowing for an innovative spectroscopy study based on mechanical gating.

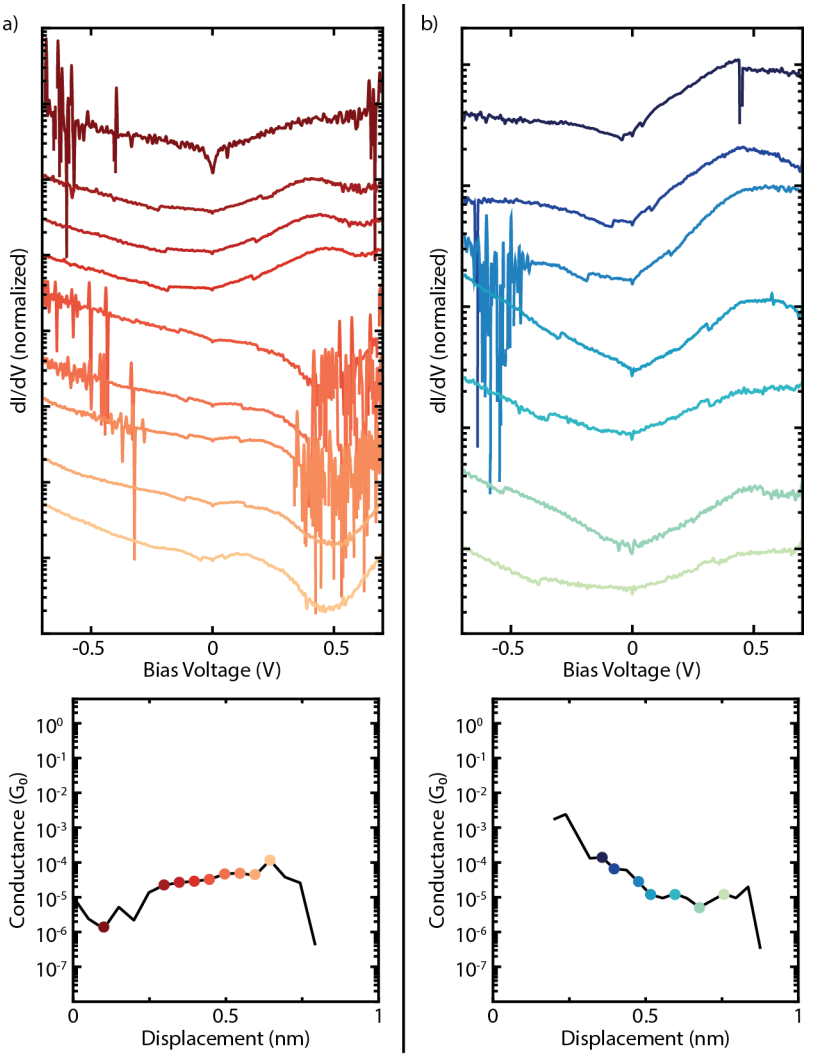

Figure 7.4: a-b) Examples of dI/dV curves extracted from the same measurement sequence. The conductance corresponding to each curve is shown as a dot of the same colour in the conductance vs. displacement trace.

7.2. INFLUENCE OF BULKY SIDE GROUPS IN OPE3 TRANSPORT

Side groups can be added to molecules in order to limit possible interactions and cooperative effects between them. We can intuitively think that adding side groups to aromatic molecules may prevent them from π-stacking [114, 175, 176]. This project investigates the role of such groups (usually referred to as *bulky side groups*) on derivatives of the well-studied OPE3 with dimethyl groups added in the meta position (with respect to the anchoring thiol group) of the outer phenyl rings (inset of Fig. 7.5b) (OPE3-B) and alkane chains on the central phenyl ring (inset of Fig. 7.5b) (OPE3-C). This placement of bulky side groups does not affect the conjugation of the backbone.

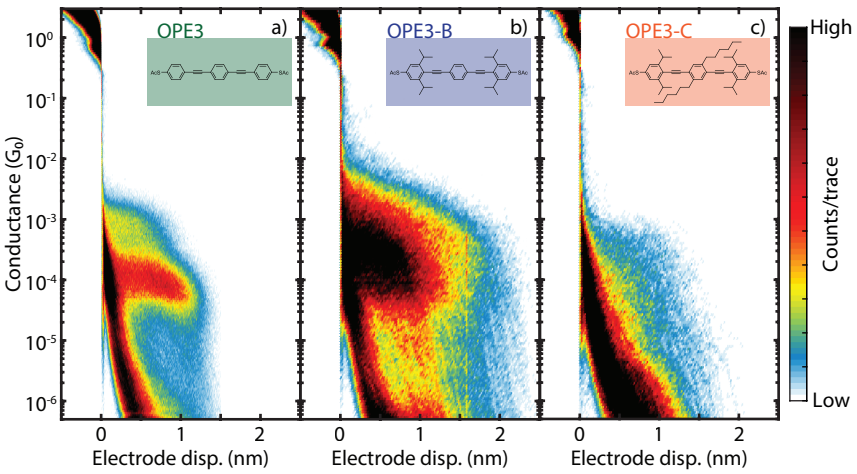

Figure 7.5: Comparison of the two-dimensional conductance histograms of OPE3 and derivatives with added bulky side groups. The histogram of bare OPE3 is comprised of 10.000 consecutive traces, that of OPE3-B of 5.000, that of OPE3-C of 2.461. The chemical structures are presented in the inset.

The measurements of OPE3-B with only bulky side groups show a very broad plateau that extends for about 1.5 nm (Fig. 7.5b). The position and length of the plateau is comparable to that found in bare OPE3 (Fig. 7.5a), but the spread is considerably larger. When the alkane chains are added to the central phenyl ring, the conductance histogram changes significantly in overall shape (Fig. 7.5c), as no clear plateu can be identified, but a broad conductance distribution is found from $1 \cdot 10^{-3}$ to $5 \cdot 10^{-7}$ G_0.

To characterize them in more detail, the measurements have been analysed with the clustering technique presented in Appendix A. Three clusters have been used in the case of OPE3-B: two classes can be associated to the signature of the molecule (46% of the total traces), while the third one can be associated to tunnelling (54% of the total traces). Class A presents a plateau around $2.1 \cdot 10^{-4}$ G_0 typical of OPE3 (see Fig. 7.5a). This peak is usually associated to the conductance of a single OPE3 molecule attached to the electrodes by the two S atoms, and the bulky side groups do not seem to have an effect on this value. The presence of a longer high conductance plateau at $9.1 \cdot 10^{-4}$ G_0 (Class B, see Fig. 7.6b), on the other hand, is not observed in bare OPE3. It could be related to either cooperative effects in a few-molecule cluster, possibly favoured by the mechanical interactions between

the bulky side groups, since they extend for a displacement larger than the length of a single molecule (≈ 2 nm). Alternatively, the curves in class B could arise from the interaction between the bulky side groups and the gold electrodes. To account for the longer displacement, this interacion would have to pull a Au atom (or a small cluster of them) alongside while stretching the molecule. Preliminary molecular dynamics calculations indeed present this possibility in certain junction configurations. We notice that for this particular cluster, the 1 G_0 plateau is shorter and not as well defined as the one in class A.

In the case of OPE3-C, four clusters were needed to split the data, with 40% of the traces belonging to the tunnelling class. The two most representative molecular-like classes are presented in Fig. 7.6c and d. Class A presents a high conductance plateau at $1.3 \cdot 10^{-4}$ G_0 (Fig. 7.6c) which has similar length and width to the one representitve of class A for OPE3-B. Since the length of the corresponding plateaus is closer to the length of the molecule and because of the similarities between these traces and those found in OPE3 and OPE3-B, this class could be associated to the single-molecule conductance. Class B and C present traces that are about 1 nm long and are centered around at $2 \cdot 10^{-6}$ G_0 (class B) and $3.7 \cdot 10^{-5}$ G_0 (class C, Fig. 7.6d). Preliminary molecular dynamics calculations suggest that the presence of the arms prevents the molecules from π-stacking, thus making this a less plausible explanation for the occurrence of the low conductance plateaus.

The measurements show that the bulky side groups do not reduce the zoo of conductance traces observed for standard OPE3, which suggests that they do not reduce the number of possible junction configurations. Contrary to bare OPE3, plateaus longer than the molecule itself with high conductance were found for OPE3-B. Moreover, the plateaus found for these molecules are slanted, unlike in the OPE3 case. We can also note that the 1 G_0 position and length seems to change after the deposition of the molecules and fluctuate between the different clusters. This may indicate that the interaction between the molecules and the gold is influenced by the presence of the bulky group. The occurrence of molecular traces belonging to class A drops from 70% to 15% when introducing the arms, suggesting that these reuduce the likelihood of trapping a single molecule in the junction. The lower conductance observed in the case of the molecule with arms still needs to be understood. However, the analysis of these data is still ongoing and we are running molecular dynamics calculations to shed a light on the effect of the bulky side groups on the junction configurations. The role of bulky side groups will be further investigated in the next section.

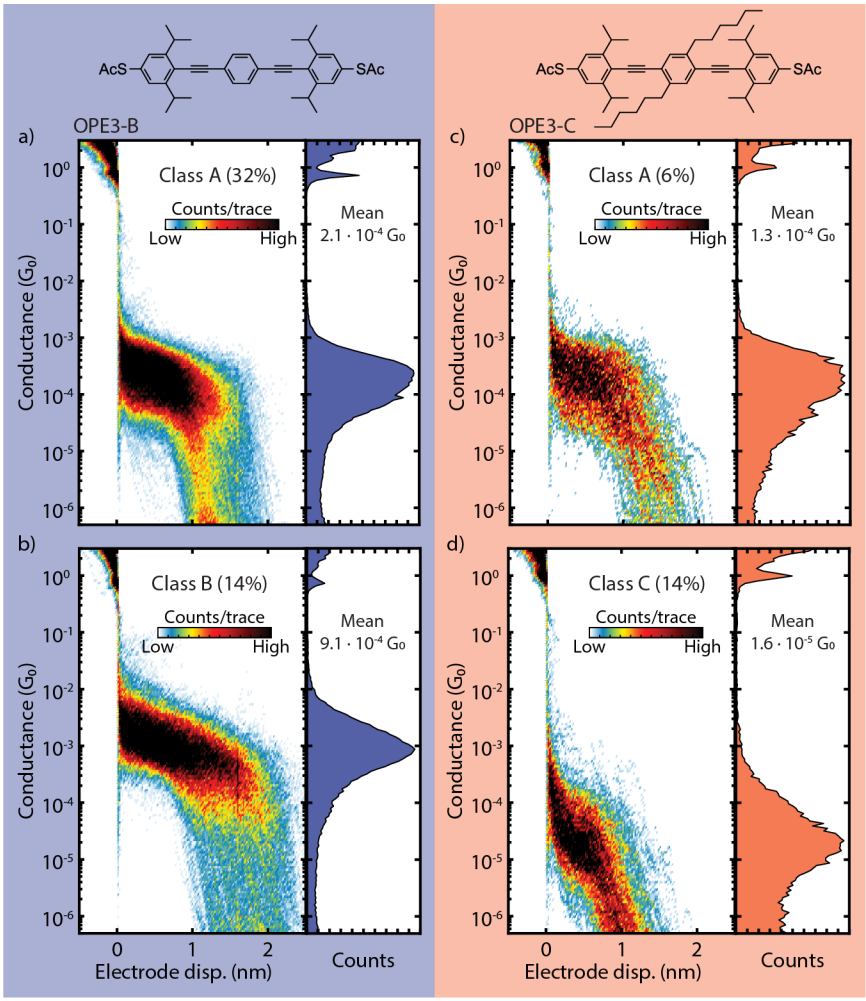

Figure 7.6: Comparison between the clusters obtained from the cluster analysis of OPE3-B (a,b) and OPE3-C (c,d). The percentages indicate the proportion of the traces belonging to the class, compared to the number of molecular traces.

7.3. Identifying electronic pathways in porphyrin derivatives

Porphyrins are a family of molecules that finds applications in nature, for example in the heme group in hemoglobin or in chlorophyll. They have rich optical properties and can be functionalized with different metal ions, obtaining properties that can be modified by external means, such as light, chemical reaction, mechanical changes, magnetic or electric fields [252–256]. Because of their great versatility and since the chemical processes required to synthesize them are well known, they can be viewed as ideal candidates for fundamental transport studies at the single-molecule level [257]. Side groups can be added to porphyrins in a modular way, allowing to methodically test various chemical designs with different anchoring, bulky and a spacer groups. Additionally, the porphyrin backbone can also be easily modified to add some built-in functionality [258]. However, the potential for applications at the single-molecule level is still limited by relatively low conductance values of the order of $1 \cdot 10^{-5}\,G_0$, with only a few works reporting higher conductance ($\approx 1 \cdot 10^{-4}\,G_0$) [259, 260]. Moreover, the presence of multiple different transport pathways makes it important to have a well-defined junction configuration when designing a functional device based on these molecules, in order to reduce the possibility that the intrinsic properties of the molecule are washed out by the changes due to different configurations.

This project aims to identify the transport pathways across porphyrins, and to understand the role of bulky and anchoring groups in order to design a porphyrin backbone that has a high conductance and forms well-defined molecular junctions. To achieve this, we synthesized and measured seven different compounds based around a similar geometry and employed an unsupervised clustering algorithm to identify common behaviours in the breaking traces.

The chemical design of the molecules included in this study can be found in Fig. 7.7. Compound **P1**, **P2** and **P3** share the same backbone, comprised of the porphyrin core, phenylene-acetylene spacers and thiol anchoring groups, but differ in the bulky side groups. A variant of **P1** which includes a Zn atom at the center of the porphyrin core is also part of the study. The role of the anchoring groups and of the spacers is investigated by comparing the results of **P1**, with those obtained from three derivatives that possess the same bulky side groups, but have different combinations of side groups: **R1** only has one spacer and anchoring group on one side, **R2** has neither spacers nor anchoring groups, whereas **R3** has acetylene spacers on opposite sides, but no anchoring groups.

All the measurements presented in this section have been performed at room temperature with a bias voltage of 100 mV and a bending speed of 60 µm/s. A clear plateau above $1 \cdot 10^{-4}\,G_0$ that extends for about 2 nm is found in the conductance histogram of **P1** (Fig. 7.8a). A similar plateau is also found in the other molecules containing two thiol groups (Fig. 7.8b-d): **P2**, **P3** and **ZnP1**. When the thiol groups are not present, the plateau is absent; instead a wide conductance decay is observed in the conductance histograms of **R2** and **R3** (Fig. 7.9b-c). If the thiol group is present only on one side, the spread of the conductance histogram is reduced, yet no plateau is observed (Fig. 7.9d).

To further investigate the nature of the traces measured, a clustering method has been used to subdivide the different datasets in four different classes. Classes A-C are associated to the presence of a molecule inside the junction, whereas class D contains the traces in which no molecular junction has been formed and only show the exponential decay typical of single-barrier tunneling. The results obtained for **P1** are reported in Fig. 7.10, as an

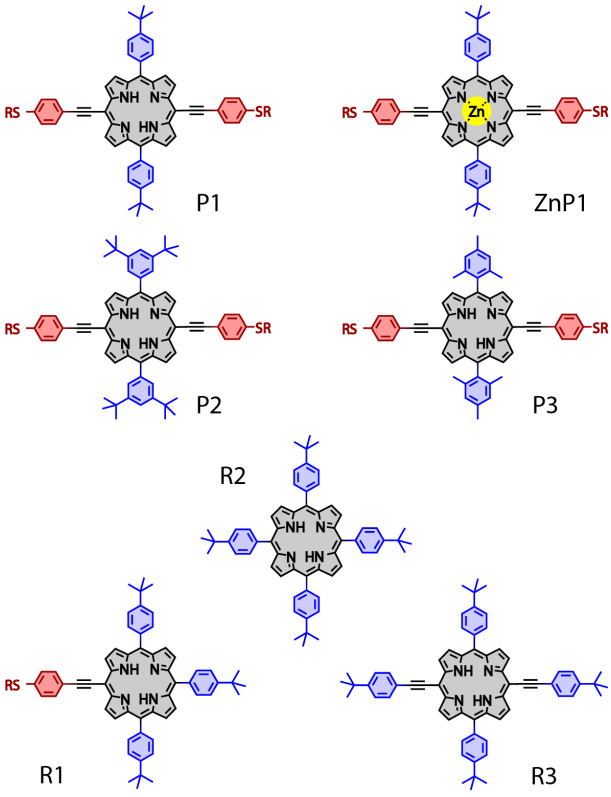

Figure 7.7: Chemical structure of the molecules included in the study.

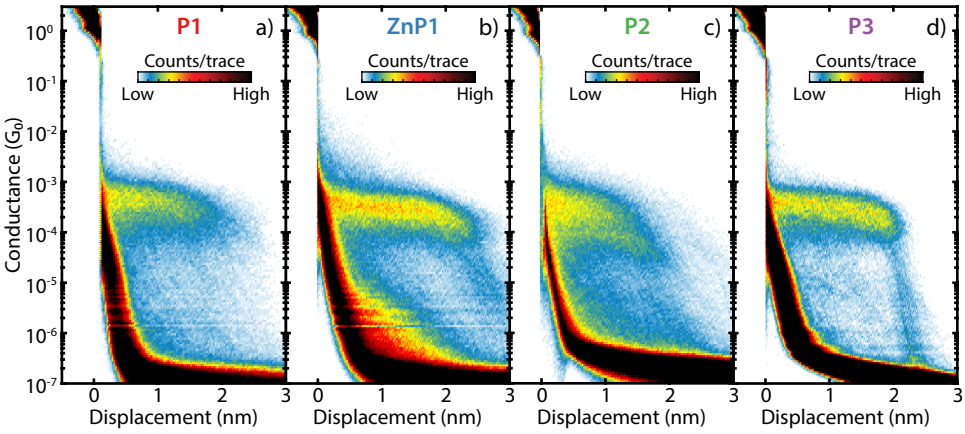

Figure 7.8: Two-dimensional histograms built from 10.000 consecutive breaking traces of **P1** (a), **ZnP1** (b), **P2** (c) and **P3** (d) without data selection.

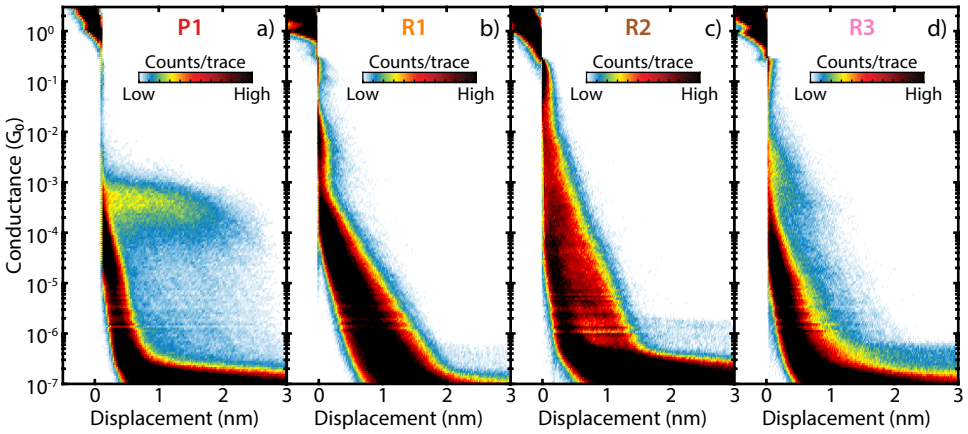

Figure 7.9: Two-dimensional histograms built from 10.000 consecutive breaking traces of **P1** (a), **R1** (b), **R2** (c) and **R3** (d) without data selection.

example. Class A constitutes 62.7% of the molecular junctions and contains the traces that exhibit a plateau about 2.2 nm long, which a log-normal fits reveals being centered around $2 \cdot 10^{-4}$ G_0. The traces grouped in class B (15.9%) form a slightly shorter and wider plateau, centered at $3 \cdot 10^{-5}$ G_0. In some of the traces of classes A and B, the conductance initially decays exponentially as it would do for vacuum tunneling, only to jump up at an electrode displacement of approximately 0.5-1 nm. Finally, class C (21.4%) shows a peak centered at $2 \cdot 10^{-6}$ G_0. Apart from tunneling traces (class D), only class C is found for **R1**, whereas for **R3** both class B and C are present. None of the classes found in **R2** exhibits a clear molecular signature and all traces are included in class D.

The differences in conductance or length of the plateau characterizing class A (Fig. 7.8) are well within the variations typically found in MCBJ experiments even when performed on the same molecule. For this reason, we relate the breaking traces in class A to the junction configuration in which the molecule is bound to both electrodes via the thiols and transport occurs from sulfur to sulfur. Noticeably, the presence of the Zn atom does not affect this plateau, indicating that the electron paths involved in tranport are not localized on the center of the porhpyrin [261]. The small variations in length and slope of the plateau may be attributed to the influence of the bulky group on the configuration of the molecular junction.

Compared to the plateau of class A, that in class B has lower conductance, is shorter, more spread out and observed less frequently. All these traits hint at the fact that it originates from a junction configurations that is both mechanically and electronically less favourable. The corresponding charge conduction pathway could involve the acetylene spacer or the phenyl ring at both sides of the molecule, as it is not observed in molecules that do not contain these groups.

Class C can be related to the path that sees injection in the π-system of the acetylene group and ends at one of the phenyl rings found in the bulky side groups. This is suggested by the fact that this class is observed also in molecules that do not have sulfur atoms in their structure. In this case, however, the plateau is more slanted, suggesting that the sulfur,

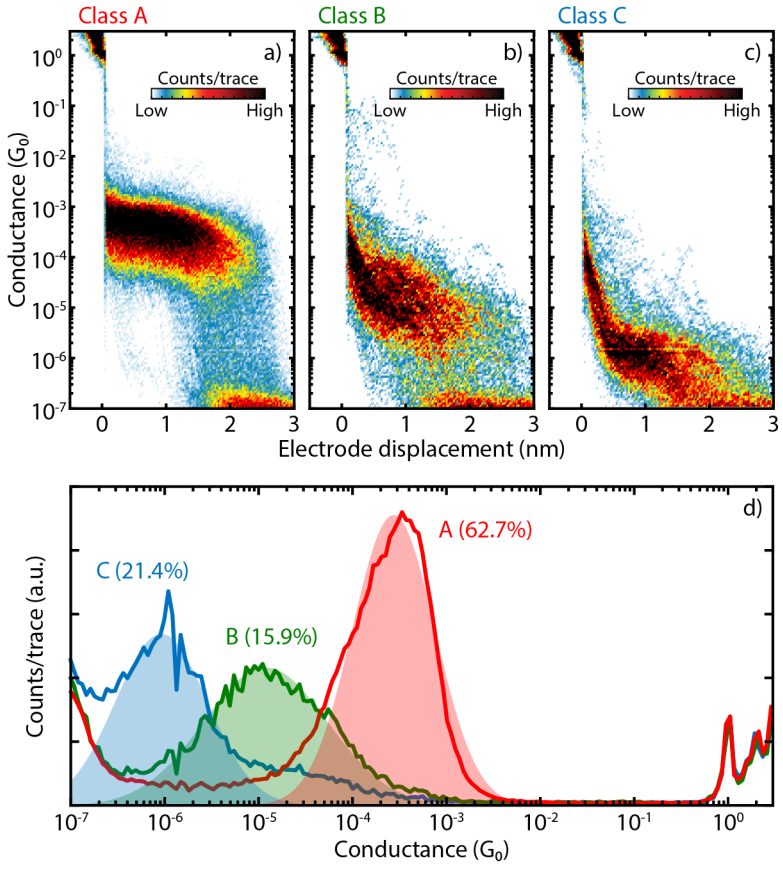

Figure 7.10: a-c) Two-dimensional histograms of the three different categories of breaking traces obtained from the reference-free cluster analysis applied to **P1**. d) One-dimensional conductance histograms corresponding to class A (62.7% of the molecular junctions), B (15.9%) and C (21.4%). The log-normal fits (colored shaded areas) to the one-dimensional histograms have peak positions at $2 \cdot 10^{-4}$ G_0 for class A, $3 \cdot 10^{-5}$ G_0 for class B and $2 \cdot 10^{-6}$ G_0 for class C.

although not participating to the conductance, still plays a role in the stability of the junction configuration, leading to flatter plateaus. The role of the sulfur in mechanically stabilizing the junction configuration is also corroborated by the reduced conductance spread in **R1**, which contains a single anchoring group, compared to **R2** and **R3**, which do not. Both class B and C are not observed in the porhpyrin without the acetylene spacers (**R3**), indicating that their presence is needed to establish a charge pathway through the molecule. The pathways attributed to class A and C can be compared to the 'para' and 'orto' paths found by Li *et al.* in the case of porhpyrins without acetylene spacers and with pyridne anchoring groups [260]. While in their experiments the two pathways resulted in a conductances that differed by a factor of 1.4, in our case the difference is two orders of magnitude. The properties of all classes can be found in Table 7.1.

In this project, we identified the transport pathways across a series of porphyrin mole-

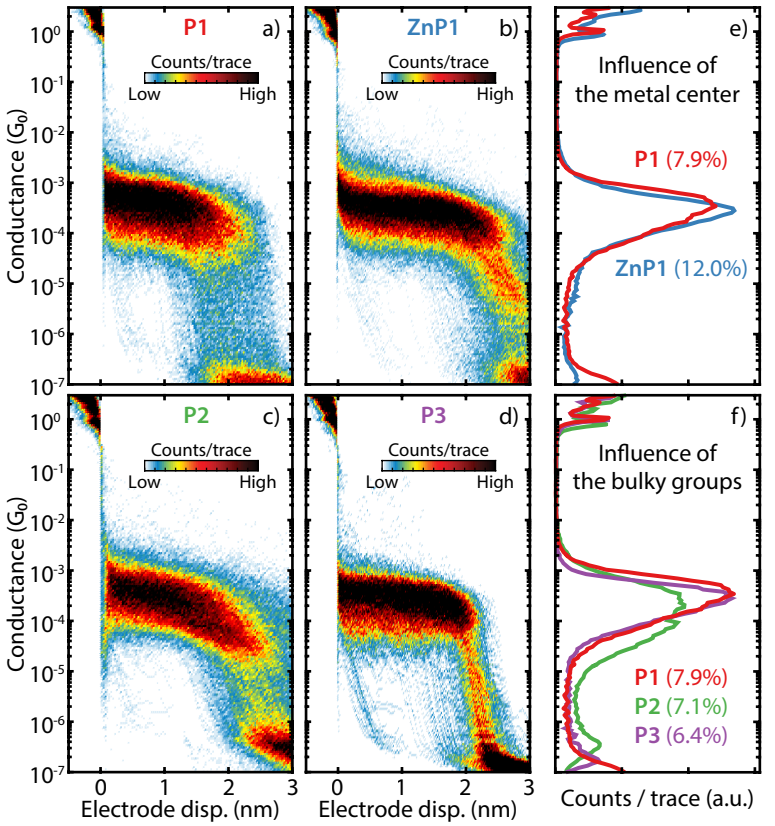

Figure 7.11: a-d) Two-dimensional histograms of class A obtained from (a) **P1**, (b) **ZnP1**, (c) **P2** and (d) **P3**. e-f) Comparison between the conductance histograms of class A from (e) **P1** and **ZnP1**, showing the influence of the metal center, and from (f) **P1**, **P2** and **P3**, showing the influence of the bulky side groups.

cules by methodically and purposefully modifying their chemical design and by applying an unbiased algorithm for the analysis of the breaking traces. A well-defined, high-conductance plateau with high stability at room temperature was related to the thiol-to-thiol conduction path. Both bulky groups and Zn atom as a metal center did not have a significant influence on the junction properties, suggesting the frontier molecular orbitals are mainly localized on the porphyrin core.

	Class A				Class B			
Molecule	G_M (G_0)	FWHM	Yield	l (nm)	G_M (G_0)	FWHM	Yield	l (nm)
P1	$2.8 \cdot 10^{-4}$	1.1	7.9%	1.9	$1.1 \cdot 10^{-5}$	1.5	2.0%	1.8
ZnP1	$2.4 \cdot 10^{-4}$	1.8	12.0%	2.0	$2.1 \cdot 10^{-5}$	1.7	4.1%	1.5
P2	$1.9 \cdot 10^{-4}$	1.2	7.1%	1.8	$4.0 \cdot 10^{-5}$	1.2	7.1%	1.8
P3	$2.3 \cdot 10^{-4}$	0.8	6.4%	2.2	$8.3 \cdot 10^{-6}$	0.9	1.0%	2.0
R1	-	-	-	-	-	-	-	-
R2	-	-	-	-	-	-	-	-
R3	-	-	-	-	$5.1 \cdot 10^{-5}$	2.4	19.0%	1.0

	Class C			
Molecule	G_M (G_0)	FWHM	Yield	l (nm)
P1	$1.0 \cdot 10^{-6}$	1.0	2.7%	2.0
ZnP1	$4.1 \cdot 10^{-6}$	1.9	16.2%	1.1
P2	$1.7 \cdot 10^{-6}$	1.7	4.7%	1.8
P3	$1.0 \cdot 10^{-6}$	0.6	0.3%	2.3
R1	$1.2 \cdot 10^{-6}$	2.0	7.0%	1.5
R2	-	-	-	-
R3	$2.8 \cdot 10^{-6}$	1.6	14.0%	1.0

Table 7.1: Properties of the classes obtained for the molecules measured: position G_M and full-width-at-half-maximum (FWHM) of the fitted peak, yield and average trace length l. The yield is expressed with respect to the total number of traces.

7.4. ROTAXANE MOLECULAR SWITCH

While in porhpyrins the orbital localization along the backbone results in the metal center not being directly involved in tranport, this is not the case for rotaxanes. Rotaxanes are molecules which consist of a molecular ring threaded onto a dumbbell shaped backbone. The ring can rotate around the backbone (pirouetting rotaxane) or move up and down along it (shuttle rotaxane), thus allowing to be employed in molecular machines [262–265], for which they have been the subject of the Nobel Prize in Chemistry in 2016. In particular, the electronic changes associated to the different conformations of the rotaxane system can be employed to create molecular switches. The switching mechanism can be driven optically, electrochemically/photochemically, or with the fluorescence techinque, and has been studied extensively in thin films, liquid crystals, membranes, photoinduced electron and energy transfer switching systems [266]. However, reports regarding the transport properties of rotaxanes at the single-molecule level are very scarce [267].

The molecules involved in this project are pseudo-rotaxanes (since they lack the stopper moieties at the extremities of the backbone typical of rotaxanes) that comprise the same backbone, but differ in the macrocycle that encompasses it (Fig. 7.12a-c). The backbone consists of a copper complex connected via acetylene rods to the pyridine anchoring groups. The macrocycles of R2 and R3 present structures with 2 or 3 nitrogen atoms (respectively) which connect to the copper complex and keep the ring in place. The ring of R23, on the other hand, contains both the structures found in the rings of R2 and R3, and can thus bind

to the complex in the backbone in two different configurations depending on the oxidation state of the copper atom. When this is in the Cu(I) oxidation state, the ring in R23 is bound to the copper atom in the same configuration as the ring of R2, whereas the ring binding is similar to that of R3 for the Cu(II) oxidation state. R23 is therefore a bistable system and the switching mechanism is shown in Fig. 7.12d.

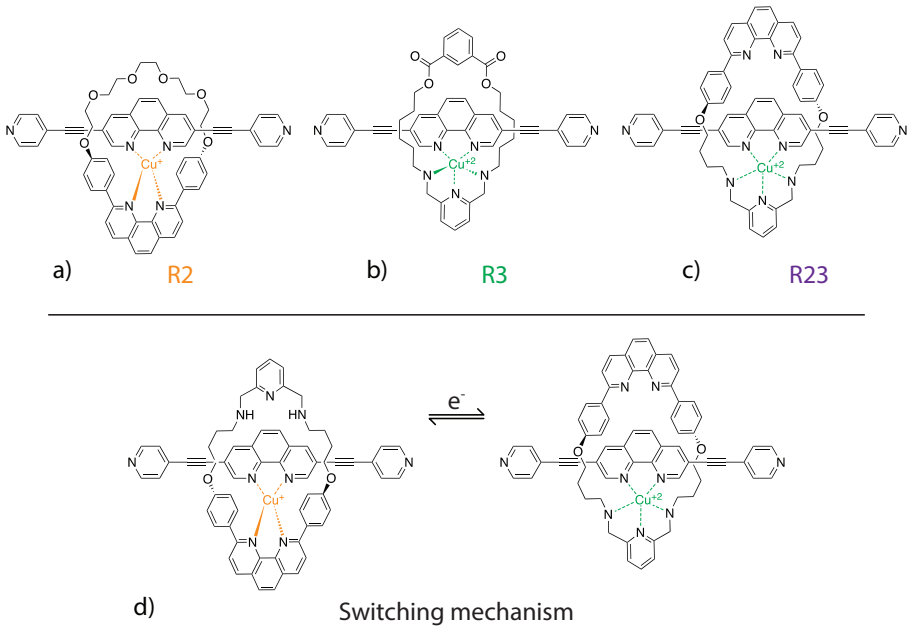

Figure 7.12: a-c) Chemical structure of the rotaxanes R2, R3 and R23. d) Switching mechanism of R23.

The molecules were dissolved in acentonitrile to obtain a 0.02 mM solution that was dropcasted immediately before the measurements. Since the R2 molecule is particularly unstable if exposed to air, all measurements were performed in high vacuum condition, with a bias voltage of 300 mV and a bending speed of 60 µm/s.

The two-dimensional histograms obtained from the measurements of R2 and R3 show counts across the whole conductance range, with no clear plateau (not shown here). A cluster analysis, however, reveals the presence of traces up to 2 nm long with slanted plateaus centered around $1.7 \cdot 10^{-3}\,G_0$ (R2, Fig. 7.13b), and $3.1 \cdot 10^{-5}\,G_0$ (R3, Fig. 7.13d). Charge transport is expected to occur along the backbone and to be influenced only by the Cu oxidation state and corresponding ring configuration. These measurements indicate that the ring configuration found in R2 is related to a conductance one order of magnitude higher than that of R3.

The conductance histogram obtained from the measurements of R23 presents a wider distribution, but the cluster analysis identifies classes centered at $7.9 \cdot 10^{-4}\,G_0$ and $1.0 \cdot 10^{-5}\,G_0$ (Fig. 7.13a, c). These clusters are similar to those observed for R2 and R3 (respectively), thus suggesting that the configurations which originate them correspond to the ring positions found in R2 and R3. The conductance peaks found through the clustering

	Class A		Class B	
Molecule	G_M	Yield	G_M	Yield
R2	$1.7 \cdot 10^{-3}$ G_0	5%	-	-
R3	-	-	$3.1 \cdot 10^{-5}$ G_0	5%
R23	$7.9 \cdot 10^{-4}$ G_0	4%	$1.0 \cdot 10^{-5}$ G_0	7%

Table 7.2: Conductance peak of the classes obtained for the molecules measured and occurrence of the classes on the total number of traces.

method are reported in Table 7.2.

Since no significant switching between the two conductance values has been observed in individual fast-breaking traces, self-breaking time-trace measurement have also been performed with a measuring time surpassing two minutes, following the protocol described in Chapter 2. Switching beheaviour is observed in a handful of traces for molecule R23, but it cannot be easily related to a switch in ring configuration, since the conductance values do not correspond to those found in breaking traces. The observed jumps in conductance may thus have a different origin. The time traces also suggest that the ring configurations are stable on the timescale of the measurements (hundreds of seconds).

Future work towards a functional device involve finding a knob that can be used to reliably trigger the state switch. One option for this is an electrochemical gate that could induce the change in oxidation state of the copper complex.

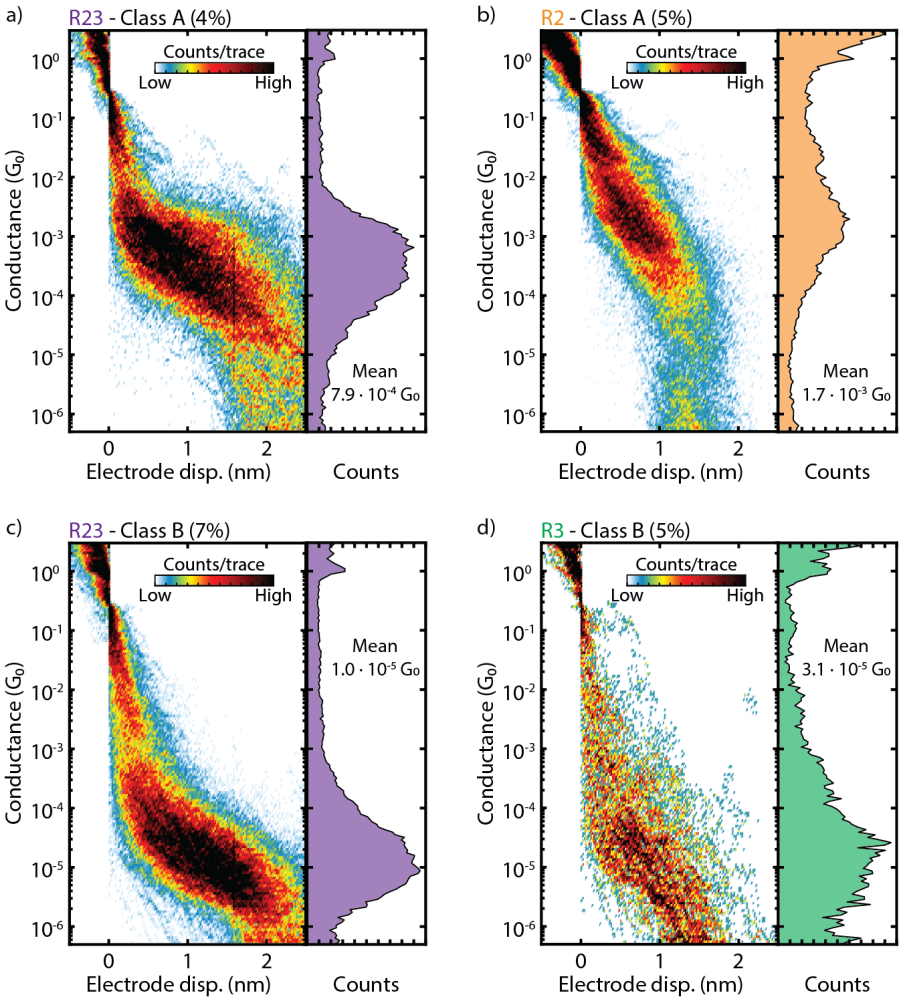

Figure 7.13: Comparison of the one- and two-dimensional histograms of the classes obtained from the cluster analysis of R23 (a, b) R2 (c) and R3 (d).

A

A REFERENCE-FREE CLUSTERING METHOD FOR THE ANALYSIS OF MOLECULAR BREAK-JUNCTION MEASUREMENTS

Single-molecule break-junction measurements are intrinsically stochastic in nature, requiring the acquisition of large datasets of "breaking traces" to gain insight into the underlying electronic properties of the molecule under study. For example, the most-probable conductance value of the molecule is often extracted from the conductance histogram built from these traces. In this section, we present an unsupervised and reference-free machine learning tool to improve the determination of the conductance of oligo(phenylene ethynylene)dithiol (OPE3) from mechanically controlled break-junction (MCBJ) measurements. Our method allows to classify individual breaking traces based on an image recognition technique. Moreover, applying this technique to multiple merged datasets makes it possible to identify common breaking behaviours present across different samples, and therefore to recognize global trends. In particular, we find that the variation in the extracted molecular conductance can be significantly reduced resulting in a more reliable estimation of molecular conductance values from MCBJ datasets.

The development of experimental tools for the collection of large datasets plays a key role in molecular electronics [35, 214, 268, 269]. In particular, recent technological advancements in break-junction techniques such as the scanning tunneling microscopy one (STM-BJ) [35, 269] or the mechanically controlled one (MCBJ) [270] have made it possible to acquire statistically relevant datasets. Their measurement principle consists of repeatedly forming a quantum point contact in the presence of molecules while at the same time measuring the current flowing through it. Each breaking trace provides information about the conformation and configuration of the junction [271]. However, it is only through the statistical analysis of thousands of such traces, that an in-depth mapping of the breaking

dynamics [78, 172, 251] and a meaningful interpretation of the molecular junction behavior can be obtained [47, 267, 272].

In break-junction measurements, molecules are usually identified by the presence of plateau-like features after the breaking point of the last gold-gold atom connection, which has a conductance equal to the conductance quantum ($G_0 = 2e^2/h$). Since the behavior of the molecules in the junction can vary from one breaking trace to another (*e.g.*, due to different injection points, number of molecules, electrode shapes, anchoring configuration, electronic coupling, level alignments, etc. ...), the recorded breaking traces may exhibit diverse features. A common way to process these traces and obtain statistical information about the most probable conductance value of the molecule (G_M) is by building a conductance histogram and fitting the prominent peak with a log-normal distribution [214].

In the following, we illustrate why this approach may lead to inaccurate data interpretation and conclusions. For this purpose, we use a portion of the dataset recorded on the oligo(phenylene ethynylene)dithiol (OPE3) molecule presented in Chapter 2, which consists of more than 50.000 breaking curves. These curves are obtained from six MCBJ samples and recorded at different breaking speeds and bias voltages (see details in Table A.1), forming in total 16 datasets, all carried out at room temperature and in ambient conditions. The samples have been chosen based on relabelled in this work for convenience. Figure A.1 shows two examples of conductance histograms built from these 16 datasets of breaking curves recorded at 100 mV. Although both datasets are recorded with the same experimental settings, they exhibit different molecular yields [220]. From this comparison plot, two main observations can be made: (i) the peak shapes and relative amplitudes are different for the two datasets, even though the same molecule is measured, and (ii) the extracted values of G_M are not the same and differ by a factor 4.

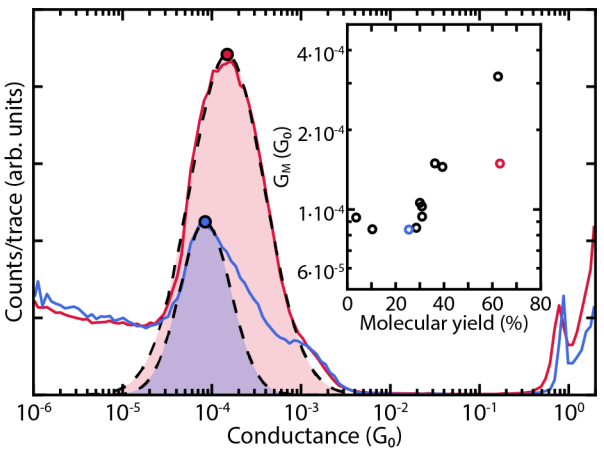

Figure A.1: Two unfiltered one-dimensional conductance histograms of the OPE3 molecule. The red and blue curves are built from breaking traces of the datasets related to samples 1b and 5a (see Table A.1), respectively. The black dashed lines and the red/blue shaded regions correspond to log-normal distribution fits to the red/blue curves. The red/blue dots highlight the maximum of the log-normal distribution fits allowing to extract G_M. The inset shows G_M for all samples as a function of the molecular yield. The red/blue circles highlight the extracted G_M values using the red/blue histograms.

In total, 11 different datasets have been recorded with a bias voltage of 100 mV, each exhibiting different molecular yields, varying from 3% to 63% [220]. The inset of Fig. A.1 presents the extracted value of G_M for all of them. The graph shows a considerable spread of about half an order of magnitude in conductance, and an apparent increase in G_M for increasing molecular yield. The dependence of G_M on the molecular yield raises an important point about the correct interpretation of the extracted G_M values. This is particularly important for datasets exhibiting various types of breaking curves in which the most probable conductance value obtained from the raw histogram cannot be attributed to a unique molecular conformation, and more importantly, cannot be considered as a universal conductance value associated with that of a single and fully stretched molecule.

The problem of classification of breaking traces has recently been tackled using machine learning (ML) tools [273, 274]. Generally speaking, ML algorithms can be subdivided into two main categories: supervised and unsupervised learning [275, 276]. Supervised learning is used when the nature of the desired ML model output is known. The ML model is then trained to learn a function that describes the input-output relationship based on a given set of input-output pairs, also called labeled dataset. This ML method is often employed to make output predictions of the model for input values which were not present during the training step. For example, recently, supervised learning was used to train an artificial neural network for classifying experimental breaking curves of gold break junction based on labeled traces obtained by molecular dynamics simulations [277]. Moreover, 'deep' neural network has recently been applied to single-molecule measurements for DNA sequencing applications [278].

Supervised learning is in contrast to unsupervised learning, in which the outcome of the ML model is not predefined and the ML algorithms are used to detect the underlying structures of a given dataset. This approach allows, *e.g.*, to classify the data according to specific characteristic features. Unsupervised learning has successfully been applied to breaking curves classification [273, 279, 280], highlighting the importance of using more sophisticated tools to identify different types of breaking behavior in a given set of traces. However, the classification algorithm applied in those studies needed a reference vector, the choice of which may affect the clustering outcome. Recently, an unsupervised clustering approach to identify the hierarchical data structure has been reported [281], but in this case the clustering required several parameters, and was performed on the 2D conductance-displacement histograms, not on the individual breaking traces.

Our approach, schematically depicted in Fig. A.2a, aims to identify features in the experimental breaking traces and group the traces accordingly. The general workflow for the unsupervised ML classification can be summarized as follows: (i) construction of the *feature space* containing the relevant information about the shape of every breaking curve; (ii) application of a ML clustering algorithm in the constructed feature space that groups feature vectors into clusters. In the following, the workflow is explained in detail. The starting point of the method is the set of individual breaking traces, of which several examples are presented in Fig. A.2b. Each trace exhibits a specific shape and corresponds to a different breaking scenario of the junction. The blue trace, for example, shows a sharp conductance drop below 1 G_0 followed by an exponential conductance decrease as a function of the electrode displacement. This behavior is indicative of tunneling across a barrier when no molecule is bridging the electrodes. On the other hand, the green and red traces

exhibit a step-like behavior below 1 G_0, which is associated with at least one OPE3 molecule trapped between the electrodes. However, the two curves do not have the same shape. The green trace has a conductance plateau around $1 \cdot 10^{-3}\,G_0$ while the red one exhibits a longer plateau at lower conductance ($\approx 1 \cdot 10^{-4}\,G_0$). These two traces exemplify the variability of molecular junctions during breaking and illustrate how MCBJ measurements allow to stochastically probe different molecular conformations/behaviors.

The creation of the applied feature space is partly inspired by the well-known MNIST data set for handwritten digits, in which the image of the digits are reduced to 28×28 pixel images [275]. In this method, supervised learning is employed to train a ML model to identify handwritten digit images. During the learning process, the ML model identifies relevant features related to each digit in the training set using a discretized image. We employ the same principle to construct the feature space for our breaking-trace classification approach, even though it is an unsupervised learning problem. As any image constitutes a two-dimensional (2D) representation of the shape of an object, one can naturally think of transforming every breaking curve into an individual 2D image. In our case, the created images are individual 2D histograms. Figure A.2c illustrates how a breaking curve is transformed into an image by defining a region of interest (ROI), *i.e.*, the boundaries of the final image. In the case of the OPE3 dataset, the ROI is defined in a conductance range between $1 \cdot 10^{-6}$ and 1 G_0 and an electrode displacement range of $[0-2]$ nm. The conductance range excludes the behavior of the metallic contact and of the measurement noise-floor, while focusing purely on the behavior after the breaking of the junction. In addition to the ROI, the number of bins along the conductance and displacement axes is defined, *i.e.*, the resolution of the individual 2D histograms. For instance, the breaking curve shown in Fig. A.2c is transformed into a $M \times N$ pixels image. To construct the feature space, every 2D histogram is converted into a feature vector associated with a specific breaking curve. Each component of the obtained vectors represents one dimension in the feature space, meaning that one has to deal with a high-dimensional space. For example, in the case of 28×28 pixels images (Fig. A.2c), the resulting feature space has 784 dimensions.

The last step of the classification task is to choose an appropriate clustering algorithm for the created feature space. For this work, we use the K-means++ method (from the Scikit-Learn Python library), which is one of the more popular clustering techniques (see Ref. [276, 282] for details about the algorithm principle). Its popularity is mainly due to its conceptual simplicity, low computational cost and scalability, unlike more advanced clustering techniques. Another important advantage of the K-means++ algorithm is its abiliy to deal with high-dimensional spaces, which is a necessary requirement for our feature space. We note that other more advanced algorithms (DBSCAN [283], HDBSCAN [284], Gaussian mixture [285], fuzzy [286] and MAP-DP [287]) which, *e.g.*, take into account non-isotropic cluster shapes, have been tested but fail in the case of such a high-dimensional feature space.

A commonly used approach to get insight into the feature vector distribution, as well as the classification result is to use a two- or three-dimensional scattering plot. However, this is only feasible when the number of feature space dimensions is at most three, which is not the case for our feature space. Nevertheless to obtain a reduced representation of the high-dimensional space while preserving the maximum data variance, we employ a method called principal component analysis (PCA). This technique consists in projecting every

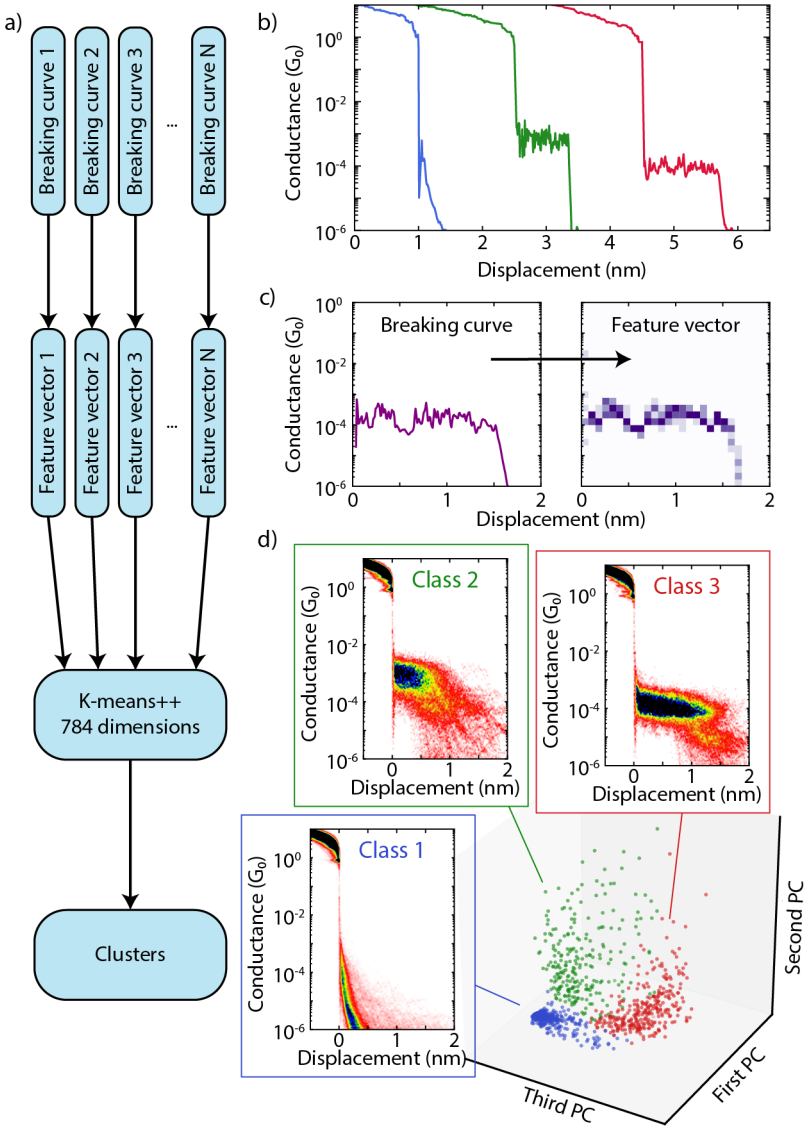

Figure A.2: a) Schematic of the clustering algorithm. b) Examples of breaking curves from the OPE3 dataset. c) From left to right, transformation of a breaking trace into an individual 2D histogram. The number of bins along the conductance and electrode displacement axes is 28 for both. The region of interest is defined in the conductance range $[10^{-6} - 1]$ G_0 and in the electrode displacement range $[0 - 2]$ nm. d) Reduced feature space obtained using the principle component analysis in the case of the OPE3 dataset of sample 5a (see Table A.1). The blue, green and red points correspond to the reduced feature vectors related to the three different classes formed after using the K-means++ method. The 2D histograms built from the breaking curves of each class are displayed according to the cluster color.

feature vector onto the first three eigenvectors of the covariance matrix of the analyzed data. Figure A.2d displays the reduced feature vector distribution, as well as the classification results obtained for one of the OPE3 datasets (sample 5a). We note that the PCA is not used in the clustering algorithm but only to reduce the 784 dimensional feature vector to three dimensions for visualization purposes. The three clusters obtained from the high-dimensional clustering algorithm are plotted in different colors. It is important to realize that each point in the scatter plot corresponds to a single breaking trace. The clusters can subsequently be used to construct the 2D histograms belonging to the different classes, as shown in Fig. A.2d. The plot shows that the blue cluster (class 1) mainly contains breaking traces without any molecular signatures, while the green (class 2) and red (class 3) clusters are related to curves with plateau-like features. The fraction of breaking curves belonging to classes 2 and 3 is defined as the molecular yield. Since the method utilized to calculate the molecular yield in Chapter 2 did not involve this clustering techinque, some differences may arise. The green cluster contains breaking traces with conductance plateaus around $1 \cdot 10^{-3}\,G_0$, while for the red class longer plateaus are observed at lower conductance values ($\approx 1 \cdot 10^{-4}\,G_0$).

We now apply this approach to investigate the influence of the molecular yield on the most probable conductance value. For this purpose, we group all the datasets recorded at a fixed bias voltage (V) of 100 mV, *i.e.* in 11 sets with a cumulative amount of traces exceeding 40.000 curves. The conductance and 2D histograms for the full dataset are shown in Fig. A.3a, alongside the histograms of the three classes identified using our clustering method (Fig. A.3b-d). The obtained classes are similar to those previously obtained with a single OPE3 dataset (Fig. A.2d). Class 1 contains curves without distinct molecular signatures (Fig. A.3b), class 2 exhibits slanted plateaus starting around $1 \cdot 10^{-3}\,G_0$, while the histograms of class 3 shows flat and long plateau-like features around $1 \cdot 10^{-4}\,G_0$ (Fig. A.3d). In the following, we focus on class 2 and class 3.

As the clustering algorithm has been applied to the full dataset and all the classes were found in all the datasets, the three identified clusters are universal, allowing for tracking of these classes and their respective occurrence across them. The extracted values of G_M for classes 2 and 3 as a function of the molecular yield are shown in Fig. A.4a. For both classes, G_M remains largely unaffected by the molecular yield, with extracted values of $5.0 \pm 1.1 \cdot 10^{-4}\,G_0$ and $1.1 \pm 0.1 \cdot 10^{-4}\,G_0$ for class 2 and class 3, respectively. The horizontal red dashed line indicates the most probable conductance value obtained by considering all curves belonging to class 3, while the shaded area corresponds to the standard deviation of the red data points in Fig. A.4a. The plot also shows that the most probable conductance value of the unfiltered histogram is dominated by class 3, consisting of long traces up to 1.5 nm around $1 \cdot 10^{-4}\,G_0$ (note that when adding a snap-back distance of 0.5 nm [117, 123], the length is close to that of the molecule). Such traces are commonly considered to originate from a single and fully-stretched molecule bridging the two electrodes. However, the plot also demonstrates that it is only after the removal of class 1 and class 2 that the molecular conductance of these 'ideal' molecular junctions is unraveled.

In contrast to the unfiltered data, the systematic dependence of G_M on the molecular yield is now absent for classes 2 and 3. In addition, the standard deviation in G_M for class 3 is about 5 times smaller than for the unfiltered dataset, allowing for a more accurate determination of the molecular conductance of the fully-stretched molecule. Moreover, a

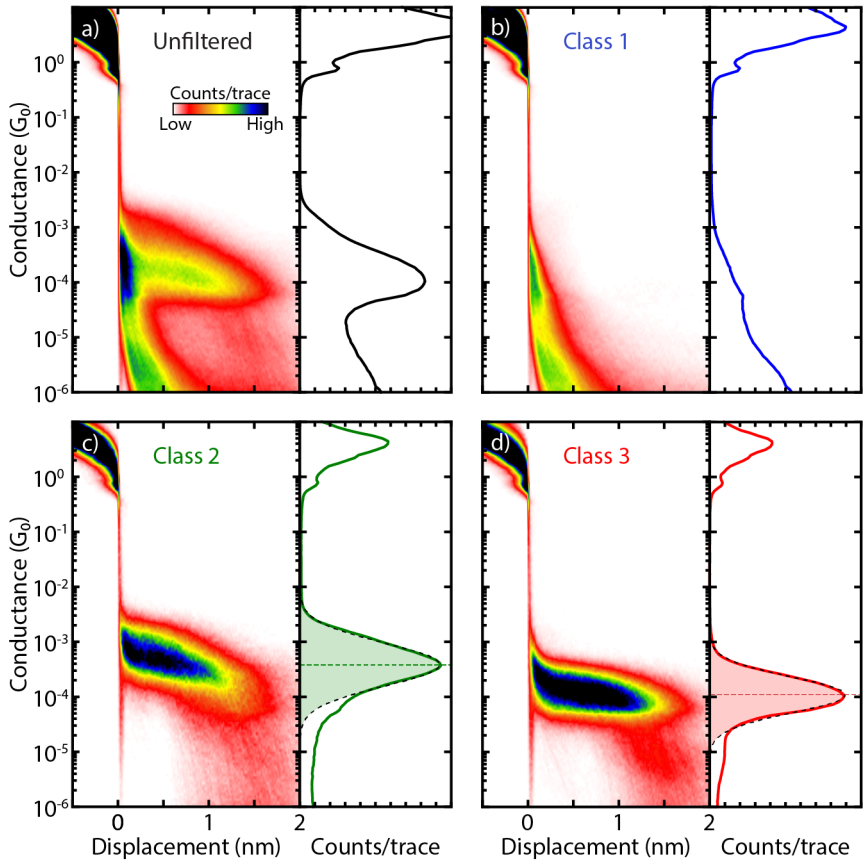

Figure A.3: a) 2D (right panel) and 1D (left panel) conductance histograms built from all the breaking curves recorded at $V = 100\,\text{mV}$, corresponding to 41.916 traces. b-d) 2D (right panel) and 1D (left panel) conductance histograms built from the breaking curves of classes 1, 2 and 3, respectively, obtained with the clustering method. The black dashed lines and shaded regions in d) show log-normal distribution fits to the prominent peak in the histograms. The horizontal dashed lines correspond to the mean of the log-normal distribution fit.

large portion of the unfiltered conductance values lies outside the standard deviation of the conductance of class 3. The high occurence of class 3 in determining the molecular conductance arises its higher occurrence, as shown in Fig. A.4b. However, the plot also shows that the yield of both classes scales close to linearly with the total molecular yield. These observations highlight the importance of data classification methods in break-junction measurements.

Finally, we also apply our method to a second dataset series with the aim to investigate the influence of the bias voltage on the determination of G_M. For this study, to avoid sample-to-sample variations, six OPE3 datasets successively recorded on the same sample for different bias voltages (V = 50, 100, 150, 200, 250 and 300 mV) are merged to obtain a dataset containing more than 10.000 curves. The three resulting classes strongly resemble those obtained in Fig. A.2d and Fig. A.3b-d). The extracted G_M values versus bias volt-

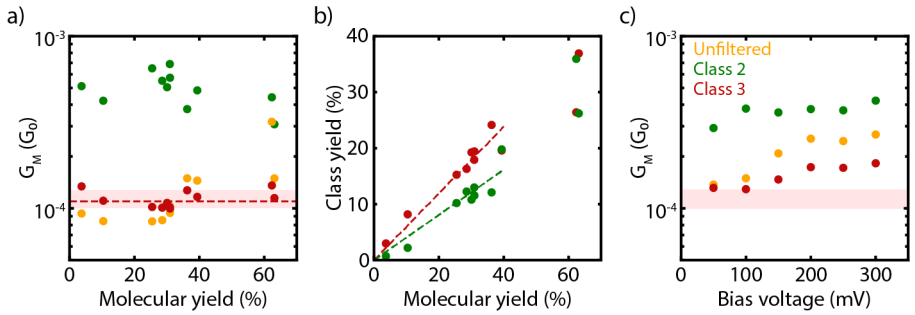

Figure A.4: a) Most probable conductance G_M as a function of molecular yield. The orange, green and red points are the extracted G_M in the case of the unfiltered data, class 2 and class 3, respectively. The horizontal red dashed line indicates the mean of the log-normal distribution fit obtained in Fig. A.3d and the shaded area to the standard deviation of the red data points in a). b) Class yield as a function of the overall molecular yield. The green and red dashed lines are linear fits to the data related to classes 2 and 3, respectively. The linear fits were performed in a molecular yield range of [0-40]%. c) G_M as a function of bias voltage. The orange, green and red points are the extracted G_M in the case of the unfiltered data and classes 2 and 3, respectively. The red shaded region corresponds to the same conductance range of class 3 depicted in a).

age are shown in Fig. A.4c. When considering the unfiltered data, a pronounced increase of G_M is observed for increasing bias voltage. Classes 2 and 3, on the other hand, exhibit a smaller dependence. As a comparison, the graph highlights the extracted conductance range of class 3 for the yield dependence. While the most probable conductance of class 3 recorded at 50 mV and 100 mV lies at the edge of the conductance range, the extracted G_M in a bias voltage range of 150-300 mV lies outside. This observation suggests that the bias voltage indeed has the effect of increasing the conductance, as expected in the case of electron tunneling through a single, broadened level.

In our analysis, similarly to previous studies [273], the number of clusters is a free parameter and needs to be defined empirically. For the analysis of this dataset, we have used three clusters. Nevertheless, this choice can be rationalized as follows: one can assume that each cluster corresponds to one particular molecular configuration with a distinct conductance. However, each cluster still includes local conformational and configurational changes which may lead to conductance fluctuations. Such fluctuations have been reported to be as high as one order of magnitude [271]. This puts a lower bound on how often clusters can be subdivided. The clusters obtained with the method presented here can be further utilized for a more in-depth analysis of the molecular junctions configurations.

In our case, class 1 corresponds to the formation of junction in which only single-barrier tunneling is observed, without any molecule bridging the gap. On the other hand, classes 2 and 3 show molecular signatures such as the formation of well-defined plateaus. Even though both classes have a molecular origin, clear differences between the two are observed. Class 2 is characterized by a slanted plateau with a higher conductance, whereas class 3 exhibits flat plateaus at lower conductance values. A possible explanation of this behavior may be related to variations in the anchoring of the molecule to the electrodes and the resulting changes in the injection point of the charges into the molecules. The long and flat plateaus present in class 3 are commonly believed to originate from a single molecule bound to the two electrodes. In this scenario, charge transport occurs via the covalent bonds

Au−S. For class 2, on the other hand, charges may also be injected through-space into the benzene rings via the overlap between its π-orbitals and the gold electrode wavefunctions. In this case, the sliding of the molecule on top of the electrodes and the resulting change in orbital overlap may explain the gradual decay in conductance and the shorter plateaus. To gain more insight into the junction formation, density functional theory and/or molecular dynamics calculations would be required.

To summarize, we demonstrated that unsupervised ML methods applied to MCBJ measurements allow for significant improvements in the extraction of the molecular conductance. Using our reference-free approach, we identify different molecular classes, which we track across several datasets. As such, we find that the two identified molecular classes are largely independent on the molecular yield, in contrast to the unfiltered data. Moreover, we find that the standard deviation of the extracted molecular conductance of the fully stretched molecule can be reduced by a factor 5. Finally, by applying our approach on datasets with varying bias voltages, we observe a small dependence on the molecular conductance. The obtained results highlight the importance of using advanced and appropriate tools, such as ML algorithms, to efficiently analyze break junction data and extract meaningful statistical molecular information.

Sample	Bias voltage (mV)	Bending speed (μm/s)	Molecular yield	# Traces
1a	100	60	31.0%	10.000
1b	100	100	63.1%	6.346
2a	100	15	10.4%	3.180
2b	100	15	3.7%	10.000
3	100	30	30.9%	1.440
4	100	30	62.5%	2.000
5a	100	30	25.5%	2.000
5b	100	15	30.1%	2.000
5c	100	60	28.6%	2.000
5d	100	7.5	39.4%	950
6a	100	30	36.3%	2.000
6b	150	30	28.5%	2.000
6c	200	30	36.9%	2.000
6d	250	30	45.3%	2.000
6e	300	30	52.0%	2.000
6f	50	30	29.8%	1.124

Table A.1: Details about the OPE3 datasets used for this work.

REFERENCES

[1] B. Mann and H. Kuhn, *Tunneling through fatty acid salt monolayers,* Journal of Applied Physics **42**, 4398 (1971).

[2] A. Aviram and M. A. Ratner, *Molecular rectifiers,* Chemical Physics Letters **29**, 277 (1974).

[3] N. Agraıt, A. L. Yeyati, and J. M. Van Ruitenbeek, *Quantum properties of atomic-sized conductors,* Physics Reports **377**, 81 (2003).

[4] M. Fujihira, K. Nishiyama, and H. Yamada, *Photoelectrochemical responses of optically transparent electrodes modified with langmuir-blodgett films consisting of surfactant derivatives of electron donor, acceptor and sensitizer molecules,* Thin Solid Films **132**, 77 (1985).

[5] C. Zhou, M. R. Deshpande, M. Reed, L. Jones, and J. Tour, *Nanoscale metal/self-assembled monolayer/metal heterostructures,* Applied Physics Letters **71**, 611 (1997).

[6] J. Chen, M. Reed, A. Rawlett, and J. Tour, *Large on-off ratios and negative differential resistance in a molecular electronic device,* Science **286**, 1550 (1999).

[7] H. Park, J. Park, A. K. Lim, E. H. Anderson, A. P. Alivisatos, and P. L. McEuen, *Nanomechanical oscillations in a single-c 60 transistor,* Nature **407**, 57 (2000).

[8] S. Kubatkin, A. Danilov, M. Hjort, J. Cornil, J.-L. Brédas, N. Stuhr-Hansen, P. Hedegård, and T. Bjørnholm, *Single electron transistor with a single conjugated molecule,* Current Applied Physics **4**, 554 (2004).

[9] M. Koole, J. M. Thijssen, H. Valkenier, J. C. Hummelen, and H. S. van der Zant, *Electric-field control of interfering transport pathways in a single-molecule anthraquinone transistor,* Nano Letters **15**, 5569 (2015).

[10] C. Collier, E. Wong, M. Belohradskỳ, F. Raymo, J. Stoddart, P. Kuekes, R. Williams, and J. Heath, *Electronically configurable molecular-based logic gates,* Science **285**, 391 (1999).

[11] C. P. Collier, G. Mattersteig, E. W. Wong, Y. Luo, K. Beverly, J. Sampaio, F. M. Raymo, J. F. Stoddart, and J. R. Heath, *A [2] catenane-based solid state electronically reconfigurable switch,* Science **289**, 1172 (2000).

[12] Rick Merritt, EE Times, *TSMC to start 5 nm production in april (2019),* https://www.eetasia.com/news/article/18100502-tsmc-to-start-5nm-production-in-april (2018), accessed on 4 January 2019.

[13] T. Online, *5 nm technology,* https://www.tsmc.com/english/dedicatedFoundry/technology/5nm.htm (2018), accessed on 4 January 2019.

[14] P. Reddy, S.-Y. Jang, R. A. Segalman, and A. Majumdar, *Thermoelectricity in molecular junctions,* Science **315**, 1568 (2007).

[15] N. Xin, J. Guan, C. Zhou, X. Chen, C. Gu, Y. Li, M. A. Ratner, A. Nitzan, J. F. Stoddart, and X. Guo, *Concepts in the design and engineering of single-molecule electronic devices,* Nature Reviews Physics , 1 (2019).

[16] J. R. Heath and M. A. Ratner, *Molecular electronics,* (2003).

[17] J. C. Love, L. A. Estroff, J. K. Kriebel, R. G. Nuzzo, and G. M. Whitesides, *Self-assembled monolayers of thiolates on metals as a form of nanotechnology,* Chemical reviews **105**, 1103 (2005).

[18] Y. Selzer, L. Cai, M. A. Cabassi, Y. Yao, J. M. Tour, T. S. Mayer, and D. L. Allara, *Effect of local environment on molecular conduction: Isolated molecule versus self-assembled monolayer,* Nano Letters **5**, 61 (2005).

[19] C. A. Nijhuis, W. F. Reus, and G. M. Whitesides, *Molecular rectification in metal- sam- metal oxide- metal junctions,* Journal of the American Chemical Society **131**, 17814 (2009).

[20] C. A. Nijhuis, W. F. Reus, J. R. Barber, M. D. Dickey, and G. M. Whitesides, *Charge transport and rectification in arrays of sam-based tunneling junctions,* Nano Letters **10**, 3611 (2010).

[21] W. F. Reus, C. A. Nijhuis, J. R. Barber, M. M. Thuo, S. Tricard, and G. M. Whitesides, *Statistical tools for analyzing measurements of charge transport,* The Journal of Physical Chemistry C **116**, 6714 (2012).

[22] E. Scheer, *Visions for a molecular future,* Nature Nanotechnology **8**, 386 (2013).

[23] S. V. Aradhya and L. Venkataraman, *Single-molecule junctions beyond electronic transport,* Nature Nanotechnology **8**, 399 (2013).

[24] D. Xiang, X. Wang, C. Jia, T. Lee, and X. Guo, *Molecular-scale electronics: from concept to function,* Chemical reviews **116**, 4318 (2016).

[25] H. Park, A. K. Lim, A. P. Alivisatos, J. Park, and P. L. McEuen, *Fabrication of metallic electrodes with nanometer separation by electromigration,* Applied Physics Letters **75**, 301 (1999).

[26] P. S. Ho and T. Kwok, *Electromigration in metals,* Reports on Progress in Physics **52**, 301 (1989).

[27] D. Strachan, D. Smith, D. Johnston, T.-H. Park, M. J. Therien, D. Bonnell, and A. Johnson, *Controlled fabrication of nanogaps in ambient environment for molecular electronics,* Applied Physics Letters **86**, 043109 (2005).

[28] J. Park, A. N. Pasupathy, J. I. Goldsmith, C. Chang, Y. Yaish, J. R. Petta, M. Rinkoski, J. P. Sethna, H. D. Abruña, P. L. McEuen, *et al.*, *Coulomb blockade and the kondo effect in single-atom transistors,* Nature **417**, 722 (2002).

[29] W. Liang, M. P. Shores, M. Bockrath, J. R. Long, and H. Park, *Kondo resonance in a single-molecule transistor,* Nature **417**, 725 (2002).

[30] E. Burzurí, Y. Yamamoto, M. Warnock, X. Zhong, K. Park, A. Cornia, and H. S. van der Zant, *Franck–condon blockade in a single-molecule transistor,* Nano Letters **14**, 3191 (2014).

[31] L. Yu, Z. K. Keane, J. W. Ciszek, L. Cheng, M. Stewart, J. Tour, and D. Natelson, *Inelastic electron tunneling via molecular vibrations in single-molecule transistors,* Physical Review Letters **93**, 266802 (2004).

[32] E. A. Osorio, K. O'Neill, N. Stuhr-Hansen, O. F. Nielsen, T. Bjørnholm, and H. S. van der Zant, *Addition energies and vibrational fine structure measured in electromigrated single-molecule junctions based on an oligophenylenevinylene derivative,* Advanced Materials **19**, 281 (2007).

[33] R. Gaudenzi, J. de Bruijckere, D. Reta, I. d. P. Moreira, C. Rovira, J. Veciana, H. S. van der Zant, and E. Burzurí, *Redox-induced gating of the exchange interactions in a single organic diradical,* ACS Nano **11**, 5879 (2017).

[34] E. A. Osorio, K. O'Neill, M. Wegewijs, N. Stuhr-Hansen, J. Paaske, T. Bjørnholm, and H. S. Van der Zant, *Electronic excitations of a single molecule contacted in a three-terminal configuration,* Nano Letters **7**, 3336 (2007).

[35] B. Xu and N. J. Tao, *Measurement of single-molecule resistance by repeated formation of molecular junctions,* Science **301**, 1221 (2003).

[36] J. R. Widawsky, P. Darancet, J. B. Neaton, and L. Venkataraman, *Simultaneous determination of conductance and thermopower of single molecule junctions,* Nano Letters **12**, 354 (2011).

[37] A. V. Rudnev, V. Kaliginedi, A. Droghetti, H. Ozawa, A. Kuzume, M.-a. Haga, P. Broekmann, and I. Rungger, *Stable anchoring chemistry for room temperature charge transport through graphite-molecule contacts,* Science advances **3**, e1602297 (2017).

[38] C. Li, A. Mishchenko, I. Pobelov, and T. Wandlowski, *Charge transport with single molecules–an electrochemical approach,* CHIMIA International Journal for Chemistry **64**, 383 (2010).

[39] V. Fatemi, M. Kamenetska, J. Neaton, and L. Venkataraman, *Environmental control of single-molecule junction transport,* Nano Letters **11**, 1988 (2011).

[40] M. Baghernejad, D. Z. Manrique, C. Li, T. Pope, U. Zhumaev, I. Pobelov, P. Moreno-García, V. Kaliginedi, C. Huang, W. Hong, *et al.*, *Highly-effective gating of single-molecule junctions: an electrochemical approach,* Chemical communications **50**, 15975 (2014).

[41] C. Huang, A. V. Rudnev, W. Hong, and T. Wandlowski, *Break junction under electrochemical gating: testbed for single-molecule electronics,* Chemical Society Reviews **44**, 889 (2015).

[42] J. Bai, A. Daaoub, S. Sangtarash, X. Li, Y. Tang, Q. Zou, H. Sadeghi, S. Liu, X. Huang, Z. Tan, *et al.*, *Anti-resonance features of destructive quantum interference in single-molecule thiophene junctions achieved by electrochemical gating,* Nature Materials , 1 (2019).

[43] J. Zhang, A. M. Kuznetsov, I. G. Medvedev, Q. Chi, T. Albrecht, P. S. Jensen, and J. Ulstrup, *Single-molecule electron transfer in electrochemical environments,* Chemical reviews **108**, 2737 (2008).

[44] Y. G. Naidyuk, J. G. Najdjuk, and I. Yanson, *Point-contact spectroscopy*, Vol. 145 (Springer Science & Business Media, 2005).

[45] R. Waitz, O. Schecker, and E. Scheer, *Nanofabricated adjustable multicontact devices on membranes,* Review of Scientific Instruments **79**, 093901 (2008).

[46] C. A. Martin, R. H. Smit, H. S. van der Zant, and J. M. van Ruitenbeek, *A nanoelectromechanical single-atom switch,* Nano Letters **9**, 2940 (2009).

[47] M. L. Perrin, C. J. Verzijl, C. A. Martin, A. J. Shaikh, R. Eelkema, J. H. Van Esch, J. M. Van Ruitenbeek, J. M. Thijssen, H. S. Van Der Zant, and D. Dulić, *Large tunable image-charge effects in single-molecule junctions,* Nature Nanotechnology **8**, 282 (2013).

[48] M. L. Perrin, E. Galan, R. Eelkema, F. Grozema, J. M. Thijssen, and H. S. van der Zant, *Single-molecule resonant tunneling diode,* The Journal of Physical Chemistry C **119**, 5697 (2015).

[49] D. Xiang, H. Jeong, D. Kim, T. Lee, Y. Cheng, Q. Wang, and D. Mayer, *Three-terminal single-molecule junctions formed by mechanically controllable break junctions with side gating,* Nano Letters **13**, 2809 (2013).

[50] J.-H. Tian, Y. Yang, X.-S. Zhou, B. Schöllhorn, E. Maisonhaute, Z.-B. Chen, F.-Z. Yang, Y. Chen, C. Amatore, B.-W. Mao, *et al.*, *Electrochemically assisted fabrication of metal atomic wires and molecular junctions by mcbj and stm-bj methods,* ChemPhysChem **11**, 2745 (2010).

[51] T. Konishi, M. Kiguchi, M. Takase, F. Nagasawa, H. Nabika, K. Ikeda, K. Uosaki, K. Ueno, H. Misawa, and K. Murakoshi, *Single molecule dynamics at a mechanically controllable break junction in solution at room temperature,* Journal of the American Chemical Society **135**, 1009 (2012).

[52] F. Prins, A. Barreiro, J. W. Ruitenberg, J. S. Seldenthuis, N. Aliaga-Alcalde, L. M. Vandersypen, and H. S. van der Zant, *Room-temperature gating of molecular junctions using few-layer graphene nanogap electrodes,* Nano Letters **11**, 4607 (2011).

[53] K. Thodkar, M. El Abbassi, F. Lüönd, F. Overney, C. Schönenberger, B. Jeanneret, and M. Calame, *Comparative study of single and multi domain cvd graphene using large-area raman mapping and electrical transport characterization,* physica status solidi (RRL)–Rapid Research Letters **10**, 807 (2016).

[54] P. Gehring, A. Harzheim, J. Spiece, Y. Sheng, G. Rogers, C. Evangeli, A. Mishra, B. J. Robinson, K. Porfyrakis, J. H. Warner, *et al.*, *Field-effect control of graphene–fullerene thermoelectric nanodevices,* Nano Letters **17**, 7055 (2017).

[55] V. M. García-Suárez, A. García-Fuente, D. J. Carrascal, E. Burzurí, M. Koole, H. S. van der Zant, M. El Abbassi, M. Calame, and J. Ferrer, *Spin signatures in the electrical response of graphene nanogaps,* Nanoscale (2018).

[56] G. F. Schneider and C. Dekker, *Dna sequencing with nanopores,* Nature Biotechnology **30**, 326 (2012).

[57] S. J. Heerema and C. Dekker, *Graphene nanodevices for dna sequencing,* Nature Nanotechnology **11**, 127 (2016).

[58] A. Salomon, D. Cahen, S. Lindsay, J. Tomfohr, V. B. Engelkes, and C. D. Frisbie, *Comparison of electronic transport measurements on organic molecules,* Advanced Materials **15**, 1881 (2003).

[59] Y. Chen, G.-Y. Jung, D. A. Ohlberg, X. Li, D. R. Stewart, J. O. Jeppesen, K. A. Nielsen, J. F. Stoddart, and R. S. Williams, *Nanoscale molecular-switch crossbar circuits,* Nanotechnology **14**, 462 (2003).

[60] D. Stewart, D. Ohlberg, P. Beck, Y. Chen, R. S. Williams, J. O. Jeppesen, K. Nielsen, and J. F. Stoddart, *Molecule-independent electrical switching in Pt/organic monolayer/Ti devices,* Nano Letters **4**, 133 (2004).

[61] M. Paulsson, F. Zahid, and S. Datta, *Resistance of a molecule,* arXiv preprint cond-mat/0208183 (2002).

[62] S. Datta, *Electrical resistance: an atomistic view,* Nanotechnology **15**, S433 (2004).

[63] J. M. Thijssen and H. S. Van der Zant, *Charge transport and single-electron effects in nanoscale systems,* physica status solidi (b) **245**, 1455 (2008).

[64] G. Bergmann, *Weak localization in thin films: a time-of-flight experiment with conduction electrons,* Physics Reports **107**, 1 (1984).

[65] G. Dumpich and A. Carl, *Anomalous temperature dependence of the phase-coherence length for inhomogeneous gold films,* Physical Review B **43**, 12074 (1991).

[66] B. Van Wees, H. Van Houten, C. Beenakker, J. G. Williamson, L. Kouwenhoven, D. Van der Marel, and C. Foxon, *Quantized conductance of point contacts in a two-dimensional electron gas,* Physical Review Letters **60**, 848 (1988).

[67] M. Peshkin and A. Tonomura, *The aharonov-bohm effect,* (1989).

[68] R. A. Webb, S. Washburn, C. Umbach, and R. Laibowitz, *Observation of h/e aharonov-bohm oscillations in normal-metal rings,* Physical Review Letters **54**, 2696 (1985).

[69] T. Koopmans, *Über die zuordnung von wellenfunktionen und eigenwerten zu den einzelnen elektronen eines atoms,* Physica **1**, 104 (1934).

[70] W. Richards, *The use of koopmans' theorem in the interpretation of photoelectron spectra,* International Journal of Mass Spectrometry and Ion Physics **2**, 419 (1969).

[71] K. P. C. Vollhardt and N. E. Schore, *Organic Chemistry* (Macmillan International Higher Education, 2014).

[72] C. Housecroft and S. A. G, *Inorganic Chemistry* (Prentice Hall, 2004).

[73] S. Datta, *Quantum transport: atom to transistor* (Cambridge university press, 2005).

[74] S. Elke and C. J. Carlos, *Molecular electronics: an introduction to theory and experiment*, Vol. 15 (World Scientific, 2017).

[75] F. Zahid, M. Paulsson, and S. Datta, *Electrical conduction through molecules,* in *Advanced Semiconductor and Organic Nano-Techniques* (Elsevier, 2003) pp. 1–41.

[76] W. A. Goddard III, D. Brenner, S. E. Lyshevski, and G. J. Iafrate, *Handbook of Nanoscience, Engineering, and Technology* (CRC Press, 2012).

[77] R. Frisenda, S. Tarkuç, E. Galán, M. L. Perrin, R. Eelkema, F. C. Grozema, and H. S. van der Zant, *Electrical properties and mechanical stability of anchoring groups for single-molecule electronics,* Beilstein journal of nanotechnology **6**, 1558 (2015).

[78] R. Frisenda and H. van der Zant, *Transition from strong to weak electronic coupling in a single-molecule junction,* Physical Review Letters **117**, 126804 (2016).

[79] A. D. McNaught and A. D. McNaught, *Compendium of chemical terminology*, Vol. 1669 (Blackwell Science Oxford, 1997).

[80] N. F. Phelan and M. Orchin, *Cross conjugation,* Journal of Chemical Education **45**, 633 (1968).

[81] F. Chen, Z. Huang, and N. Tao, *Forming single molecular junctions between indium tin oxide electrodes,* Applied Physics Letters **91**, 162106 (2007).

[82] T. Kim, H. Vázquez, M. S. Hybertsen, and L. Venkataraman, *Conductance of molecular junctions formed with silver electrodes,* Nano Letters **13**, 3358 (2013).

[83] D. Xiang, H. Jeong, T. Lee, and D. Mayer, *Mechanically controllable break junctions for molecular electronics,* Advanced Materials **25**, 4845 (2013).

[84] C.-H. Ko, M.-J. Huang, M.-D. Fu, and C.-h. Chen, *Superior contact for single-molecule conductance: electronic coupling of thiolate and isothiocyanate on pt, pd, and au,* Journal of the American Chemical Society **132**, 756 (2009).

[85] E. Leary, A. La Rosa, M. T. González, G. Rubio-Bollinger, N. Agraït, and N. Martín, *Incorporating single molecules into electrical circuits. the role of the chemical anchoring group,* Chemical Society Reviews **44**, 920 (2015).

[86] Y. S. Park, A. C. Whalley, M. Kamenetska, M. L. Steigerwald, M. S. Hybertsen, C. Nuckolls, and L. Venkataraman, *Contact chemistry and single-molecule conductance: a comparison of phosphines, methyl sulfides, and amines,* Journal of the American Chemical Society **129**, 15768 (2007).

[87] A. Mishchenko, L. A. Zotti, D. Vonlanthen, M. Bürkle, F. Pauly, J. C. Cuevas, M. Mayor, and T. Wandlowski, *Single-molecule junctions based on nitrile-terminated biphenyls: a promising new anchoring group,* Journal of the American Chemical Society **133**, 184 (2010).

[88] P. Moreno-García, M. Gulcur, D. Z. Manrique, T. Pope, W. Hong, V. Kaliginedi, C. Huang, A. S. Batsanov, M. R. Bryce, C. Lambert, *et al.*, *Single-molecule conductance of functionalized oligoynes: Length dependence and junction evolution,* Journal of the American Chemical Society **135**, 12228 (2013).

[89] L. A. Zotti, T. Kirchner, J.-C. Cuevas, F. Pauly, T. Huhn, E. Scheer, and A. Erbe, *Revealing the role of anchoring groups in the electrical conduction through single-molecule junctions,* Small **6**, 1529 (2010).

[90] Z. Li, M. Smeu, M. A. Ratner, and E. Borguet, *Effect of anchoring groups on single molecule charge transport through porphyrins,* The Journal of Physical Chemistry C **117**, 14890 (2013).

[91] F. Chen, X. Li, J. Hihath, Z. Huang, and N. Tao, *Effect of anchoring groups on single-molecule conductance: comparative study of thiol-, amine-, and carboxylic-acid-terminated molecules,* Journal of the American Chemical Society **128**, 15874 (2006).

[92] A. Ulman, *Formation and structure of self-assembled monolayers,* Chemical reviews **96**, 1533 (1996).

[93] F. Tarazona-Vasquez and P. B. Balbuena, *Complexation of the lowest generation poly (amidoamine)-nh2 dendrimers with metal ions, metal atoms, and cu (ii) hydrates: An ab initio study,* The Journal of Physical Chemistry B **108**, 15992 (2004).

[94] C. R. Arroyo, E. Leary, A. Castellanos-Gómez, G. Rubio-Bollinger, M. T. Gonzalez, and N. Agraït, *Influence of binding groups on molecular junction formation,* Journal of the American Chemical Society **133**, 14313 (2011).

[95] Z.-L. Cheng, R. Skouta, H. Vazquez, J. Widawsky, S. Schneebeli, W. Chen, M. Hybertsen, R. Breslow, and L. Venkataraman, *In situ formation of highly conducting covalent au–c contacts for single-molecule junctions,* Nature Nanotechnology **6**, 353 (2011).

[96] W. Hong, D. Z. Manrique, P. Moreno-Garcia, M. Gulcur, A. Mishchenko, C. J. Lambert, M. R. Bryce, and T. Wandlowski, *Single molecular conductance of tolanes: experimental and theoretical study on the junction evolution dependent on the anchoring group,* Journal of the American Chemical Society **134**, 2292 (2012).

[97] I. J. Olavarria-Contreras, M. L. Perrin, Z. Chen, S. Klyatskaya, M. Ruben, and H. S. van der Zant, *C–au covalently bonded molecular junctions using nonprotected alkynyl anchoring groups,* Journal of the American Chemical Society **138**, 8465 (2016).

[98] A. Vladyka, M. L. Perrin, J. Overbeck, R. R. Ferradás, V. García-Suárez, M. Gantenbein, J. Brunner, M. Mayor, J. Ferrer, and M. Calame, *In-situ formation of one-dimensional coordination polymers in molecular junctions,* Nature Communications **10**, 262 (2019).

[99] J. Moreland and P. Hansma, *Electromagnetic squeezer for compressing squeezable electron tunneling junctions,* Review of scientific instruments **55**, 399 (1984).

[100] J. Moreland and J. Ekin, *Electron tunneling experiments using nb-sn "break"junctions,* Journal of Applied Physics **58**, 3888 (1985).

[101] C. Muller, J. Van Ruitenbeek, and L. De Jongh, *Experimental observation of the transition from weak link to tunnel junction,* Physica C: Superconductivity **191**, 485 (1992).

[102] C. Zhou, C. Muller, M. Deshpande, J. Sleight, and M. Reed, *Microfabrication of a mechanically controllable break junction in silicon,* Applied Physics Letters **67**, 1160 (1995).

[103] J. Van Ruitenbeek, A. Alvarez, I. Pineyro, C. Grahmann, P. Joyez, M. Devoret, D. Esteve, and C. Urbina, *Adjustable nanofabricated atomic size contacts,* Review of Scientific Instruments **67**, 108 (1996).

[104] M. A. Reed, C. Zhou, C. Muller, T. Burgin, and J. Tour, *Conductance of a molecular junction,* Science **278**, 252 (1997).

[105] C. A. Martin, *Charge transport through single molecules in two-and three-terminal mechanical break junctions*, Ph.D. thesis, TU Delft, Delft University of Technology (2010).

[106] M. Perrin, *Charge Transport Through Single-Molecule Junctions: Experiments and Theory*, Ph.D. thesis, TU Delft, Delft University of Technology (2015).

[107] R. Frisenda, *OPE3: A Model System For Single-Molecule Transport*, Ph.D. thesis, TU Delft, Delft University of Technology (2016).

[108] R. Schouten, *QT designed instrumentation,* `http://homepage.tudelft.nl/8q71q/`, accessed on 18 February 2019.

[109] H. Ron, S. Matlis, and I. Rubinstein, *Self-assembled monolayers on oxidized metals. 2. gold surface oxidative pretreatment, monolayer properties, and depression formation,* Langmuir **14**, 1116 (1998).

[110] H. Ron and I. Rubinstein, *Alkanethiol monolayers on preoxidized gold. encapsulation of gold oxide under an organic monolayer,* Langmuir **10**, 4566 (1994).

[111] L. Nagahara, T. Thundat, and S. Lindsay, *Preparation and characterization of STM tips for electrochemical studies,* Review of scientific instruments **60**, 3128 (1989).

[112] Z. Donhauser, B. Mantooth, K. Kelly, L. Bumm, J. Monnell, J. Stapleton, D. Price, A. Rawlett, D. Allara, J. Tour, *et al.*, *Conductance switching in single molecules through conformational changes,* Science **292**, 2303 (2001).

[113] M. Mayor, H. B. Weber, J. Reichert, M. Elbing, C. von Hänisch, D. Beckmann, and M. Fischer, *Electric current through a molecular rod - relevance of the position of the anchor groups,* Angewandte Chemie International Edition **42**, 5834 (2003).

[114] S. Wu, M. T. González, R. Huber, S. Grunder, M. Mayor, C. Schönenberger, and M. Calame, *Molecular junctions based on aromatic coupling,* Nature Nanotechnology **3**, 569 (2008).

[115] R. Huber, M. T. González, S. Wu, M. Langer, S. Grunder, V. Horhoiu, M. Mayor, M. R. Bryce, C. Wang, R. Jitchati, *et al.*, *Electrical conductance of conjugated oligomers at the single molecule level,* Journal of the American Chemical Society **130**, 1080 (2008).

[116] M. T. Gonzalez, E. Leary, R. García, P. Verma, M. A. Herranz, G. Rubio-Bollinger, N. Martín, and N. Agraït, *Break-junction experiments on acetyl-protected conjugated dithiols under different environmental conditions,* The Journal of Physical Chemistry C **115**, 17973 (2011).

[117] V. Kaliginedi, P. Moreno-García, H. Valkenier, W. Hong, V. M. García-Suárez, P. Buiter, J. L. Otten, J. C. Hummelen, C. J. Lambert, and T. Wandlowski, *Correlations between molecular structure and single-junction conductance: a case study with oligo (phenylene-ethynylene)-type wires,* Journal of the American Chemical Society **134**, 5262 (2012).

[118] R. Frisenda, M. L. Perrin, H. Valkenier, J. C. Hummelen, and H. S. van der Zant, *Statistical analysis of single-molecule breaking traces,* physica status solidi (b) **250**, 2431 (2013).

[119] C. R. Parker, E. Leary, R. Frisenda, Z. Wei, K. S. Jennum, E. Glibstrup, P. B. Abrahamsen, M. Santella, M. A. Christensen, E. A. Della Pia, *et al.*, *A comprehensive study of extended tetrathiafulvalene cruciform molecules for molecular electronics: synthesis and electrical transport measurements,* Journal of the American Chemical Society **136**, 16497 (2014).

[120] R. Frisenda, M. L. Perrin, and H. S. van der Zant, *Probing the local environment of a single ope3 molecule using inelastic tunneling electron spectroscopy,* Beilstein journal of nanotechnology **6**, 2477 (2015).

[121] R. Frisenda, V. A. Janssen, F. C. Grozema, H. S. van der Zant, and N. Renaud, *Mechanically controlled quantum interference in individual π-stacked dimers,* Nature Chemistry **8**, 1099 (2016).

[122] C. Untiedt, A. Yanson, R. Grande, G. Rubio-Bollinger, N. Agraït, S. Vieira, and J. Van Ruitenbeek, *Calibration of the length of a chain of single gold atoms,* Physical Review B **66**, 085418 (2002).

[123] A. Yanson, G. R. Bollinger, H. Van den Brom, N. Agrait, and J. Van Ruitenbeek, *Formation and manipulation of a metallic wire of single gold atoms,* Nature **395**, 783 (1998).

[124] H. Valkenier, E. H. Huisman, P. A. van Hal, D. M. de Leeuw, R. C. Chiechi, and J. C. Hummelen, *Formation of high-quality self-assembled monolayers of conjugated dithiols on gold: base matters,* Journal of the American Chemical Society **133**, 4930 (2011).

[125] S. Guo, J. Hihath, I. Díez-Pérez, and N. Tao, *Measurement and statistical analysis of single-molecule current-voltage characteristics, transition voltage spectroscopy, and tunneling barrier height,* Journal of the American Chemical Society **133**, 19189 (2011).

[126] P. D. Williams and M. G. Reuter, *Level alignments and coupling strengths in conductance histograms: The information content of a single channel peak,* The Journal of Physical Chemistry C **117**, 5937 (2013).

[127] M. G. Reuter, M. C. Hersam, T. Seideman, and M. A. Ratner, *Signatures of cooperative effects and transport mechanisms in conductance histograms,* Nano Letters **12**, 2243 (2012).

[128] Z. Xie, I. Bâldea, C. E. Smith, Y. Wu, and C. D. Frisbie, *Experimental and theoretical analysis of nanotransport in oligophenylene dithiol junctions as a function of molecular length and contact work function,* ACS Nano **9**, 8022 (2015).

[129] Y. Kim, T. J. Hellmuth, D. Sysoiev, F. Pauly, T. Pietsch, J. Wolf, A. Erbe, T. Huhn, U. Groth, U. E. Steiner, *et al.*, *Charge transport characteristics of diarylethene photoswitching single-molecule junctions,* Nano Letters **12**, 3736 (2012).

[130] Y. Xue, S. Datta, and M. A. Ratner, *First-principles based matrix green's function approach to molecular electronic devices: general formalism,* Chemical Physics **281**, 151 (2002).

[131] J. C. Cuevas and E. Scheer, *Molecular electronics: an introduction to theory and experiment*, World scientific series in nanoscience and nanotechnology (World Scientific, 2010).

[132] Y. Imry and R. Landauer, *Conductance viewed as transmission,* Reviews of Modern Physics **71**, S306 (1999).

[133] A. L. Balch and M. M. Olmstead, *Reactions of transition metal complexes with fullerenes (C60, C70, etc.) and related materials,* Chemical Reviews **98**, 2123 (1998).

[134] Y. Matsuo and E. Nakamura, *Selective multiaddition of organocopper reagents to fullerenes,* Chemical Reviews **108**, 3016 (2008).

[135] C.-Z. Li, Y. Matsuo, and E. Nakamura, *Octupole-like supramolecular aggregates of conical iron fullerene complexes into a three-dimensional liquid crystalline lattice,* Journal of the American Chemical Society **132**, 15514 (2010).

[136] B. Ballesteros, G. de la Torre, A. Shearer, A. Hausmann, M. o. Herranz, D. M. Guldi, and T. Torres, *Lanthanide(III) bis(phthalocyaninato)-[60]fullerene dyads: Synthesis, characterization, and photophysical properties,* Chemistry - A European Journal **16**, 114 (2010).

[137] M. Halim, R. D. Kennedy, S. I. Khan, and Y. Rubin, *Gold(I) triphenylphosphine complexes incorporating pentaarylfulleride ligands,* Inorganic Chemistry **49**, 3974 (2010).

[138] S. Zhang, T. L. Brown, Y. Du, and J. R. Shapley, *Metalation of fullerene (C60) with pentacarbonylrhenium radicals. reversible formation of C60{Re(CO)5}2,* Journal of the American Chemical Society **115**, 6705 (1993).

[139] C.-H. Andersson, L. Nyholm, and H. Grennberg, *Synthesis and characterization of a ferrocene-linked bis-fullerene[60] dumbbell,* Dalton Transactions **41**, 2374 (2012).

[140] L. Grüter, F. Cheng, T. T. Heikkilä, M. T. González, F. Diederich, C. Schönenberger, and M. Calame, *Resonant Tunnelling Through a C60 Molecular Junction in a Liquid Environment,* Nanotechnology **16**, 2143 (2005).

[141] A. Hirsch, *The Era of Carbon Allotropes,* Nature Materials **9**, 868 (2010).

[142] H. Jeong, D. Kim, D. Xiang, and T. Lee, *High-yield functional molecular electronic devices,* ACS Nano **11**, 6511 (2017).

[143] D. M. Guldi, B. M. Illescas, C. M. Atienza, M. Wielopolski, and N. Martin, *Fullerene for organic electronics,* Chemical Society Reviews **38**, 1587 (2009).

[144] N. J. Tao, *Electron Transport in Molecular Junctions,* Nature Nanotechnology **1**, 173 (2006).

[145] A. A. Peyghan, H. Soleymanabadi, and M. Moradi, *Structural and electronic properties of pyrrolidine-functionalized [60]fullerenes,* Journal of Physics and Chemistry of Solids **74**, 1594 (2013).

[146] I. S. Kristensen, D. J. Mowbray, K. S. Thygesen, and K. W. Jacobsen, *Comparative study of anchoring groups for molecular electronics: structure and conductance of Au-S-Au and Au-NH_2-Au junctions,* Journal of Physics: Condensed Matter **20**, 374101 (2008).

[147] V. Kaliginedi, A. V. Rudnev, P. Moreno-García, M. Baghernejad, C. Huang, W. Hong, and T. Wandlowski, *Promising anchoring groups for single-molecule conductance measurements,* Physical Chemistry Chemical Physics **16**, 23529 (2014).

[148] C. Joachim, J. K. Gimzewski, R. R. Schlittler, and C. Chavy, *Electronic transparence of a single C60 molecule,* Physical Review Letters **74**, 2102 (1995).

[149] T. Böhler, A. Edtbauer, and E. Scheer, *Conductance of individual C60 molecules measured with controllable gold electrodes,* Physical Review B **76**, 125432 (2007).

[150] J. Parks, A. Champagne, G. Hutchison, S. Flores-Torres, H. Abruna, and D. Ralph, *Tuning the kondo effect with a mechanically controllable break junction,* Physical Review Letters **99**, 026601 (2007).

[151] M. Kiguchi and K. Murakoshi, *Conductance of single C60 molecule bridging metal electrodes,* The Journal of Physical Chemistry C **112**, 8140 (2008).

[152] H. Ohnishi, Y. Kondo, and K. Takayanagi, *Quantized conductance through individual rows of suspended gold atoms,* Nature **395**, 780 (1998).

[153] R. Landauer, *Electrical resistance of disordered one-dimensional lattices,* Philosophical magazine **21**, 863 (1970).

[154] C. A. Martin, D. Ding, J. K. Sørensen, T. Bjørnholm, J. M. van Ruitenbeek, and H. S. van der Zant, *Fullerene-based anchoring groups for molecular electronics,* Journal of the American Chemical Society **130**, 13198 (2008).

[155] E. Lörtscher, V. Geskin, B. Gotsmann, J. Fock, J. Sørensen, T. Bjørnholm, J. Cornil, H. van der Zant, and H. Riel, *Bonding and electronic transport properties of fullerene and fullerene derivatives in break-junction geometries,* Small **9**, 209 (2013).

[156] E. Leary, M. T. Gonzalez, C. Van Der Pol, M. R. Bryce, S. Filippone, N. Martín, G. Rubio-Bollinger, and N. Agraït, *Unambiguous one-molecule conductance measurements under ambient conditions,* Nano Letters **11**, 2236 (2011).

[157] P. Moreno-García, A. La Rosa, V. Kolivoška, D. Bermejo, W. Hong, K. Yoshida, M. Baghernejad, S. Filippone, P. Broekmann, T. Wandlowski, and M. Nazario, *Charge transport in C60-based dumbbell-type molecules: mechanically induced switching between two distinct conductance states,* Journal of the American Chemical Society **137**, 2318 (2015).

[158] K. Ullmann, P. B. Coto, S. Leitherer, A. Molina-Ontoria, N. Martín, M. Thoss, and H. B. Weber, *Single-molecule junctions with epitaxial graphene nanoelectrodes,* Nano Letters **15**, 3512 (2015).

[159] S. Bilan, L. A. Zotti, F. Pauly, and J. C. Cuevas, *Theoretical study of the charge transport through C60-based single-molecule junctions,* Physical Review B **85**, 205403 (2012).

[160] G. Géranton, C. Seiler, A. Bagrets, L. Venkataraman, and F. Evers, *Transport properties of individual C60-molecules,* The Journal of Chemical Physics **139**, 234701 (2013).

[161] T. Morita and S. Lindsay, *Reduction-induced switching of single-molecule conductance of fullerene derivatives,* The Journal of Physical Chemistry B **112**, 10563 (2008).

[162] P. Peng, F.-F. Li, F. L. Bowles, V. S. P. K. Neti, A. J. Metta-Magana, M. M. Olmstead, A. L. Balch, and L. Echegoyen, *High yield synthesis of a new fullerene linker and its use in the formation of a linear coordination polymer by silver complexation,* Chemical Communications **49**, 3209 (2013).

[163] V. T. Annibale and D. Song, *Coordination chemistry and applications of versatile 4, 5-diazafluorene derivatives,* Dalton Transactions **45**, 32 (2016).

[164] R. M. Metzger, *Unimolecular electronics,* Chemical reviews **115**, 5056 (2015).

[165] C. A. Martin, D. Ding, H. S. van der Zant, and J. M. van Ruitenbeek, *Lithographic mechanical break junctions for single-molecule measurements in vacuum: Possibilities and limitations,* New Journal of Physics **10**, 065008 (2008).

[166] C. A. Martin, R. H. Smit, R. v. Egmond, H. S. van der Zant, and J. M. van Ruitenbeek, *A versatile low-temperature setup for the electrical characterization of single-molecule junctions,* Review of Scientific Instruments **82**, 053907 (2011).

[167] C. Seth, V. Kaliginedi, S. Suravarapu, D. Reber, W. Hong, T. Wandlowski, F. Lafolet, P. Broekmann, G. Royal, and R. Venkatramani, *Conductance in a bis-terpyridine based single molecular breadboard circuit,* Chemical Science **8**, 1576 (2017).

[168] A. Etcheverry-Berríos, I. Olavarría, M. L. Perrin, R. Díaz-Torres, D. Jullian, I. Ponce, J. H. Zagal, J. Pavez, S. O. Vásquez, H. S. J. van der Zant, D. Dulić, N. Aliaga-Alcalde, and M. Soler, *Multiscale approach to the study of the electronic properties of two thiophene curcuminoid molecules,* Chemistry - A European Journal **22**, 12808 (2016).

[169] L. Sun, Y. A. Diaz-Fernandez, T. A. Gschneidtner, F. Westerlund, S. Lara-Avila, and K. Moth-Poulsen, *Single-molecule electronics: from chemical design to functional devices,* Chemical Society Reviews **43**, 7378 (2014).

[170] G.-P. Zhang, Z. Xie, Y. Song, G.-C. Hu, and C.-K. Wang, *Towards rectifying performance at the molecular scale,* Topics in Current Chemistry **375**, 85 (2017).

[171] S. Y. Quek, M. Kamenetska, M. L. Steigerwald, H. J. Choi, S. G. Louie, M. S. Hybertsen, J. Neaton, and L. Venkataraman, *Mechanically controlled binary conductance switching of a single-molecule junction,* Nature Nanotechnology **4**, 230 (2009).

[172] T. A. Su, H. Li, M. L. Steigerwald, L. Venkataraman, and C. Nuckolls, *Stereoelectronic switching in single-molecule junctions,* Nature Chemistry **7**, 215 (2015).

[173] Y. Li, N. L. Haworth, L. Xiang, S. Ciampi, M. L. Coote, and N. Tao, *Mechanical stretching-induced electron-transfer reactions and conductance switching in single molecules,* Journal of the American Chemical Society **139**, 14699 (2017).

[174] R. Frisenda, G. D. Harzmann, J. A. Celis Gil, J. M. Thijssen, M. Mayor, and H. S. van der Zant, *Stretching-induced conductance increase in a spin-crossover molecule,* Nano Letters **16**, 4733 (2016).

[175] S. T. Schneebeli, M. Kamenetska, Z. Cheng, R. Skouta, R. A. Friesner, L. Venkataraman, and R. Breslow, *Single-molecule conductance through multiple π- π-stacked benzene rings determined with direct electrode-to-benzene ring connections,* Journal of the American Chemical Society **133**, 2136 (2011).

[176] D. Nozaki, A. Lücke, and W. G. Schmidt, *Molecular orbital rule for quantum interference in weakly coupled dimers: Low-energy giant conductivity switching induced by orbital level crossing,* The Journal of Physical Chemistry Letters **8**, 727 (2017).

[177] G. C. Solomon, J. Vura-Weis, C. Herrmann, M. R. Wasielewski, and M. A. Ratner, *Understanding coherent transport through π-stacked systems upon spatial dislocation,* The Journal of Physical Chemistry B **114**, 14735 (2010).

[178] C. Lambert, *Basic concepts of quantum interference and electron transport in single-molecule electronics,* Chemical Society Reviews **44**, 875 (2015).

[179] F. Schwarz, G. Kastlunger, F. Lissel, C. Egler-Lucas, S. N. Semenov, K. Venkatesan, H. Berke, R. Stadler, and E. Lörtscher, *Field-induced conductance switching by charge-state alternation in organometallic single-molecule junctions,* Nature Nanotechnology **11**, 170 (2016).

[180] N. Darwish, I. Díez-Pérez, P. Da Silva, N. Tao, J. J. Gooding, and M. N. Paddon-Row, *Observation of electrochemically controlled quantum interference in a single anthraquinone-based norbornylogous bridge molecule,* Angewandte Chemie International Edition **51**, 3203 (2012).

[181] H. Atesci, V. Kaliginedi, J. A. C. Gil, H. Ozawa, J. M. Thijssen, P. Broekmann, M.-a. Haga, and S. J. van der Molen, *Humidity-controlled rectification switching in ruthenium-complex molecular junctions,* Nature Nanotechnology **13**, 117 (2018).

[182] X. Li, A. Staykov, and K. Yoshizawa, *Orbital views on electron-transport properties of cyclophanes: insight into intermolecular transport,* Bulletin of the Chemical Society of Japan **85**, 181 (2012).

[183] C. Brown and A. Farthing, *Preparation and structure of di-p-xylylene,* Nature **164**, 915 (1949).

[184] N. V. Vorontsova, V. I. Rozenberg, E. V. Sergeeva, E. V. Vorontsov, Z. A. Starikova, K. A. Lyssenko, and H. Hopf, *Symmetrically tetrasubstituted [2.2] paracyclophanes: Their systematization and regioselective synthesis of several types of bis-bifunctional derivatives by double electrophilic substitution,* Chemistry–A European Journal **14**, 4600 (2008).

[185] M. Carlotti, A. Kovalchuk, T. Wächter, X. Qiu, M. Zharnikov, and R. C. Chiechi, *Conformation-driven quantum interference effects mediated by through-space conjugation in self-assembled monolayers,* Nature Communications **7**, 13904 (2016).

[186] H. Häkkinen, *The gold–sulfur interface at the nanoscale,* Nature Chemistry **4**, 443 (2012).

[187] J. L. Zafra, A. Molina Ontoria, P. Mayorga Burrezo, M. Peña Alvarez, M. Samoc, J. Szeremeta, F. J. Ramírez, M. D. Lovander, C. J. Droske, T. M. Pappenfus, *et al.*, *Fingerprints of through-bond and through-space exciton and charge π-electron delocalization in linearly extended [2.2] paracyclophanes,* Journal of the American Chemical Society **139**, 3095 (2017).

[188] D. S. Seferos, S. A. Trammell, G. C. Bazan, and J. G. Kushmerick, *Probing π-coupling in molecular junctions,* Proceedings of the National Academy of Sciences **102**, 8821 (2005).

[189] L. Bondarenko, I. Dix, H. Hinrichs, and H. Hopf, *Cyclophanes. part LII: Ethynyl [2.2] paracyclophanes-new building blocks for molecular scaffolding,* Synthesis **2004**, 2751 (2004).

[190] Z.-F. Shi, L.-J. Wang, H. Wang, X.-P. Cao, and H.-L. Zhang, *Synthesis of oligo (phenylene ethynylene) s with dendrimer "shells" for molecular electronics,* Organic letters **9**, 595 (2007).

[191] J. Xia, I. Diez-Perez, and N. Tao, *Electron transport in single molecules measured by a distance-modulation assisted break junction method,* Nano Letters **8**, 1960 (2008).

[192] M. Tsutsui, K. Shoji, M. Taniguchi, and T. Kawai, *Formation and self-breaking mechanism of stable atom-sized junctions,* Nano Letters **8**, 345 (2008).

[193] F. Pauly, J. K. Viljas, U. Huniar, M. Häfner, S. Wohlthat, M. Bürkle, J. C. Cuevas, and G. Schön, *Cluster-based density-functional approach to quantum transport through molecular and atomic contacts,* New Journal of Physics **10**, 125019 (2008).

[194] K. Yoshizawa, T. Tada, and A. Staykov, *Orbital views of the electron transport in molecular devices,* Journal of the American Chemical Society **130**, 9406 (2008).

[195] D. Krüger, H. Fuchs, R. Rousseau, D. Marx, and M. Parrinello, *Pulling monatomic gold wires with single molecules: an ab initio simulation,* Physical Review Letters **89**, 186402 (2002).

[196] C. Bruot, J. L. Palma, L. Xiang, V. Mujica, M. A. Ratner, and N. Tao, *Piezoresistivity in single dna molecules,* Nature Communications **6**, 8032 (2015).

[197] S. Y. Quek, L. Venkataraman, H. J. Choi, S. G. Louie, M. S. Hybertsen, and J. Neaton, *Amine- gold linked single-molecule circuits: experiment and theory,* Nano Letters **7**, 3477 (2007).

[198] S. Ballmann, R. Härtle, P. B. Coto, M. Elbing, M. Mayor, M. R. Bryce, M. Thoss, and H. B. Weber, *Experimental evidence for quantum interference and vibrationally induced decoherence in single-molecule junctions,* Physical Review Letters **109**, 056801 (2012).

[199] Y. Selzer, M. A. Cabassi, T. S. Mayer, and D. L. Allara, *Temperature effects on conduction through a molecular junction,* Nanotechnology **15**, S483 (2004).

[200] M. Kamenetska, J. Widawsky, M. Dell'Angela, M. Frei, and L. Venkataraman, *Temperature dependent tunneling conductance of single molecule junctions,* The Journal of Chemical Physics **146**, 092311 (2017).

[201] R. Ahlrichs, M. Bär, M. Häser, H. Horn, and C. Kölmel, *Electronic structure calculations on workstation computers: The program system turbomole,* Chemical Physics Letters **162**, 165 (1989).

[202] A. Schäfer, H. Horn, and R. Ahlrichs, *Fully optimized contracted gaussian basis sets for atoms li to kr,* The Journal of Chemical Physics **97**, 2571 (1992).

[203] J. P. Perdew, K. Burke, and M. Ernzerhof, *Generalized gradient approximation made simple,* Physical Review Letters **77**, 3865 (1996).

[204] D. C. Milan, O. A. Al-Owaedi, M.-C. Oerthel, S. Marqués-González, R. J. Brooke, M. R. Bryce, P. Cea, J. Ferrer, S. J. Higgins, C. J. Lambert, *et al.*, *Solvent dependence of the single molecule conductance of oligoyne-based molecular wires,* The Journal of Physical Chemistry C **120**, 15666 (2015).

[205] M. Kotiuga, P. Darancet, C. R. Arroyo, L. Venkataraman, and J. B. Neaton, *Adsorption-induced solvent-based electrostatic gating of charge transport through molecular junctions,* Nano Letters **15**, 4498 (2015).

[206] S. Tanimoto, M. Tsutsui, K. Yokota, and M. Taniguchi, *Dipole effects on the formation of molecular junctions,* Nanoscale Horizons **1**, 399 (2016).

[207] D. P. Long, J. L. Lazorcik, B. A. Mantooth, M. H. Moore, M. A. Ratner, A. Troisi, Y. Yao, J. W. Ciszek, J. M. Tour, and R. Shashidhar, *Effects of hydration on molecular junction transport,* Nature Materials **5**, 901 (2006).

[208] E. Leary, H. Höbenreich, S. J. Higgins, H. Van Zalinge, W. Haiss, R. J. Nichols, C. Finch, I. Grace, C. Lambert, R. McGrath, *et al.*, *Single-molecule solvation-shell sensing,* Physical Review Letters **102**, 086801 (2009).

[209] A. Tawara, T. Tada, and S. Watanabe, *Electrostatic and dynamical effects of an aqueous solution on the zero-bias conductance of a single molecule: A first-principles study,* Physical Review B **80**, 073409 (2009).

[210] B. Capozzi, Q. Chen, P. Darancet, M. Kotiuga, M. Buzzeo, J. B. Neaton, C. Nuckolls, and L. Venkataraman, *Tunable charge transport in single-molecule junctions via electrolytic gating,* Nano Letters **14**, 1400 (2014).

[211] K. Wang, *Dna-based single-molecule electronics: From concept to function,* Journal of functional biomaterials **9**, 8 (2018).

[212] M. S. Hybertsen, L. Venkataraman, J. E. Klare, A. C. Whalley, M. L. Steigerwald, and C. Nuckolls, *Amine-linked single-molecule circuits: systematic trends across molecular families,* Journal of Physics: Condensed Matter **20**, 374115 (2008).

[213] L. Grüter, M. T. González, R. Huber, M. Calame, and C. Schönenberger, *Electrical conductance of atomic contacts in liquid environments,* Small **1**, 1067 (2005).

[214] M. T. González, S. Wu, R. Huber, S. J. Van Der Molen, C. Schönenberger, and M. Calame, *Electrical conductance of molecular junctions by a robust statistical analysis,* Nano Letters **6**, 2238 (2006).

[215] W. Hong, H. Valkenier, G. Mészáros, D. Z. Manrique, A. Mishchenko, A. Putz, P. M. García, C. J. Lambert, J. C. Hummelen, and T. Wandlowski, *An MCBJ case study: The influence of π-conjugation on the single-molecule conductance at a solid/liquid interface,* Beilstein journal of nanotechnology **2**, 699 (2011).

[216] S. Nakashima, Y. Takahashi, and M. Kiguchi, *Effect of the environment on the electrical conductance of the single benzene-1, 4-diamine molecule junction,* Beilstein journal of nanotechnology **2**, 755 (2011).

[217] A. Arima, M. Tsutsui, T. Morikawa, K. Yokota, and M. Taniguchi, *Fabrications of insulator-protected nanometer-sized electrode gaps,* Journal of Applied Physics **115**, 114310 (2014).

[218] N. Muthusubramanian, E. Galan, C. Maity, R. Eelkema, F. C. Grozema, and H. S. van der Zant, *Insulator-protected mechanically controlled break junctions for measuring single-molecule conductance in aqueous environments,* Applied Physics Letters **109**, 013102 (2016).

[219] A. L. Jesus and J. Redinha, *Molecular insight into the amine–water interaction: A combined vibrational, energetic and nbo/neda study,* Computational and Theoretical Chemistry **1023**, 74 (2013).

[220] R. Frisenda, D. Stefani, and H. S. J. van der Zant, *Quantum transport through a single conjugated rigid molecule, a mechanical break junction study,* Accounts of Chemical Research **51**, 1359 (2018).

[221] S. Datta, *The non-equilibrium green's function (negf) formalism: An elementary introduction,* in *Electron Devices Meeting, 2002. IEDM'02. International* (IEEE, 2002) pp. 703–706.

[222] C. Verzijl, J. Seldenthuis, and J. Thijssen, *Applicability of the wide-band limit in dft-based molecular transport calculations,* The Journal of Chemical Physics **138**, 094102 (2013).

[223] G. t. Te Velde, F. M. Bickelhaupt, E. J. Baerends, C. Fonseca Guerra, S. J. van Gisbergen, J. G. Snijders, and T. Ziegler, *Chemistry with adf,* Journal of Computational Chemistry **22**, 931 (2001).

[224] A. Klamt and G. Schüürmann, *Cosmo: a new approach to dielectric screening in solvents with explicit expressions for the screening energy and its gradient,* Journal of the Chemical Society, Perkin Transactions 2 , 799 (1993).

[225] A. Klamt, *Conductor-like screening model for real solvents: a new approach to the quantitative calculation of solvation phenomena,* The Journal of Physical Chemistry **99**, 2224 (1995).

[226] A. Klamt, *COSMO-RS: from quantum chemistry to fluid phase thermodynamics and drug design* (Elsevier, 2005).

[227] T. K. Woo, L. Cavallo, and T. Ziegler, *Implementation of the imomm methodology for performing combined qm/mm molecular dynamics simulations and frequency calculations,* Theoretical Chemistry Accounts **100**, 307 (1998).

[228] C. Verzijl, J. Celis Gil, M. Perrin, D. Dulić, H. van der Zant, and J. Thijssen, *Image effects in transport at metal-molecule interfaces,* The Journal of Chemical Physics **143**, 174106 (2015).

[229] I. Bertini, H. B. Gray, H. Gray, E. I. Stiefel, E. Stiefel, and J. S. Valentine, *Biological inorganic chemistry: structure and reactivity* (University Science Books, 2007).

[230] P. Facci, *Biomolecular electronics: bioelectronics and the electrical control of biological systems and reactions* (William Andrew, 2014).

[231] C. Guo, S. Sarkar, S. Refaely-Abramson, D. A. Egger, T. Bendikov, K. Yonezawa, Y. Suda, T. Yamaguchi, I. Pecht, S. Kera, *et al.*, *Electronic structure of dipeptides in the gas-phase and as an adsorbed monolayer,* Physical Chemistry Chemical Physics **20**, 6860 (2018).

[232] C. Guo, X. Yu, S. Refaely-Abramson, L. Sepunaru, T. Bendikov, I. Pecht, L. Kronik, A. Vilan, M. Sheves, and D. Cahen, *Tuning electronic transport via hepta-alanine peptides junction by tryptophan doping,* Proceedings of the National Academy of Sciences **113**, 10785 (2016).

[233] L. Sepunaru, S. Refaely-Abramson, R. Lovrinčić, Y. Gavrilov, P. Agrawal, Y. Levy, L. Kronik, I. Pecht, M. Sheves, and D. Cahen, *Electronic transport via homopeptides: The role of side chains and secondary structure,* Journal of the American Chemical Society **137**, 9617 (2015).

[234] M. Baghbanzadeh, C. M. Bowers, D. Rappoport, T. Żaba, M. Gonidec, M. H. Al-Sayah, P. Cyganik, A. Aspuru-Guzik, and G. M. Whitesides, *Charge tunneling along short oligoglycine chains,* Angewandte Chemie International Edition **54**, 14743 (2015).

[235] N. Amdursky, *Electron transfer across helical peptides,* ChemPlusChem **80**, 1075 (2015).

[236] R. A. Malak, Z. Gao, J. F. Wishart, and S. S. Isied, *Long-range electron transfer across peptide bridges: The transition from electron superexchange to hopping,* Journal of the American Chemical Society **126**, 13888 (2004).

[237] H. S. Mandal and H.-B. Kraatz, *Electron transfer mechanism in helical peptides,* The Journal of Physical Chemistry Letters **3**, 709 (2012).

[238] A. Shah, B. Adhikari, S. Martic, A. Munir, S. Shahzad, K. Ahmad, and H.-B. Kraatz, *Electron transfer in peptides,* Chemical Society Reviews **44**, 1015 (2015).

[239] J. R. Horsley, J. Yu, K. E. Moore, J. G. Shapter, and A. D. Abell, *Unraveling the interplay of backbone rigidity and electron rich side-chains on electron transfer in peptides: the realization of tunable molecular wires,* Journal of the American Chemical Society **136**, 12479 (2014).

[240] J. Feng, R. B. Pandey, R. J. Berry, B. L. Farmer, R. R. Naik, and H. Heinz, *Adsorption mechanism of single amino acid and surfactant molecules to au {111} surfaces in aqueous solution: design rules for metal-binding molecules,* Soft Matter **7**, 2113 (2011).

[241] F. Iori, R. Di Felice, E. Molinari, and S. Corni, *Golp: An atomistic force-field to describe the interaction of proteins with au (111) surfaces in water,* Journal of computational chemistry **30**, 1465 (2009).

[242] E. W. Schlag, S.-Y. Sheu, D.-Y. Yang, H. L. Selzle, and S. H. Lin, *Distal charge transport in peptides,* Angewandte Chemie International Edition **46**, 3196 (2007).

[243] X. Xiao, B. Xu, and N. Tao, *Conductance titration of single-peptide molecules,* Journal of the American Chemical Society **126**, 5370 (2004).

[244] J. M. Brisendine, S. Refaely-Abramson, Z.-F. Liu, J. Cui, F. Ng, J. B. Neaton, R. L. Koder, and L. Venkataraman, *Probing charge transport through peptide bonds,* The Journal of Physical Chemistry Letters **9**, 763 (2018).

[245] M. Kamenetska, M. Koentopp, A. Whalley, Y. Park, M. Steigerwald, C. Nuckolls, M. Hybertsen, and L. Venkataraman, *Formation and evolution of single-molecule junctions,* Physical Review Letters **102**, 126803 (2009).

[246] K. A. Walther, F. Gräter, L. Dougan, C. L. Badilla, B. J. Berne, and J. M. Fernandez, *Signatures of hydrophobic collapse in extended proteins captured with force spectroscopy,* Proceedings of the National Academy of Sciences **104**, 7916 (2007).

[247] G. Stirnemann, D. Giganti, J. M. Fernandez, and B. Berne, *Elasticity, structure, and relaxation of extended proteins under force,* Proceedings of the National Academy of Sciences **110**, 3847 (2013).

[248] H. Dietz, F. Berkemeier, M. Bertz, and M. Rief, *Anisotropic deformation response of single protein molecules,* Proceedings of the National Academy of Sciences **103**, 12724 (2006).

[249] M. Rief, M. Gautel, F. Oesterhelt, J. M. Fernandez, and H. E. Gaub, *Reversible unfolding of individual titin immunoglobulin domains by afm,* Science **276**, 1109 (1997).

[250] K.-C. Liao, L.-Y. Hsu, C. M. Bowers, H. Rabitz, and G. M. Whitesides, *Molecular series-tunneling junctions,* Journal of the American Chemical Society **137**, 5948 (2015).

[251] D. Stefani, K. J. Weiland, M. Skripnik, C. Hsu, M. L. Perrin, M. Mayor, F. Pauly, and H. S. J. van der Zant, *Large conductance variations in a mechanosensitive single-molecule junction,* Nano Letters **18**, 5981 (2018).

[252] T. S. Balaban, *Tailoring porphyrins and chlorins for self-assembly in biomimetic artificial antenna systems,* Accounts of chemical research **38**, 612 (2005).

[253] S. Horn, K. Dahms, and M. O. Senge, *Synthetic transformations of porphyrins–advances 2004-2007,* Journal of Porphyrins and Phthalocyanines **12**, 1053 (2008).

[254] M. Jurow, A. E. Schuckman, J. D. Batteas, and C. M. Drain, *Porphyrins as molecular electronic components of functional devices,* Coordination chemistry reviews **254**, 2297 (2010).

[255] T. Lash, K. Kadish, K. Smith, and R. Guilard, *The porphyrin handbook,* Kadish, KM , 125 (2000).

[256] Z. Liu, A. A. Yasseri, J. S. Lindsey, and D. F. Bocian, *Molecular memories that survive silicon device processing and real-world operation,* Science **302**, 1543 (2003).

[257] T. Tanaka and A. Osuka, *Conjugated porphyrin arrays: synthesis, properties and applications for functional materials,* Chemical Society Reviews **44**, 943 (2015).

[258] T. Stuyver, M. Perrin, P. Geerlings, F. De Proft, and M. Alonso, *Conductance switching in expanded porphyrins through aromaticity and topology changes,* Journal of the American Chemical Society **140**, 1313 (2018).

[259] G. Sedghi, K. Sawada, L. J. Esdaile, M. Hoffmann, H. L. Anderson, D. Bethell, W. Haiss, S. J. Higgins, and R. J. Nichols, *Single molecule conductance of porphyrin wires with ultralow attenuation,* Journal of the American Chemical Society **130**, 8582 (2008).

[260] Z. Li and E. Borguet, *Determining charge transport pathways through single porphyrin molecules using scanning tunneling microscopy break junctions,* Journal of the American Chemical Society **134**, 63 (2011).

[261] E. Leary, B. Limburg, A. Alanazy, S. Sangtarash, I. Grace, K. Swada, L. J. Esdaile, M. Noori, M. T. González, G. Rubio-Bollinger, *et al.*, *Bias-driven conductance increase with length in porphyrin tapes,* Journal of the American Chemical Society **140**, 12877 (2018).

[262] W. R. Browne and B. L. Feringa, *Making molecular machines work,* Nature Nanotechnology **1**, 25 (2006).

[263] V. Balzani, A. Credi, F. M. Raymo, and J. F. Stoddart, *Artificial molecular machines,* Angewandte Chemie International Edition **39**, 3348 (2000).

[264] J. Michl and E. C. H. Sykes, *Molecular rotors and motors: Recent advances and future challenges,* ACS Nano **3**, 1042 (2009).

[265] R. Eelkema, M. M. Pollard, J. Vicario, N. Katsonis, B. S. Ramon, C. W. Bastiaansen, D. J. Broer, and B. L. Feringa, *Molecular machines: nanomotor rotates microscale objects,* Nature **440**, 163 (2006).

[266] B. L. Feringa and W. R. Browne, *Molecular switches* (John Wiley & Sons, 2011).

[267] M. L. Perrin, F. Prins, C. A. Martin, A. J. Shaikh, R. Eelkema, J. H. van Esch, T. Briza, R. Kaplanek, V. Kral, J. M. van Ruitenbeek, *et al.*, *Influence of the chemical structure on the stability and conductance of porphyrin single-molecule junctions,* Angewandte Chemie International Edition **50**, 11223 (2011).

[268] R. H. M. Smit, Y. Noat, C. Untiedt, N. D. Lang, M. C. van Hemert, and J. M. van Ruitenbeek, *Measurement of the conductance of a hydrogen molecule,* Nature **419**, 906 (2002).

[269] L. Venkataraman, J. E. Klare, I. W. Tam, C. Nuckolls, M. S. Hybertsen, and M. L. Steigerwald, *Single-molecule circuits with well-defined molecular conductance,* Nano Letters **6**, 458 (2006).

[270] L. Wang, L. Wang, L. Zhang, and X. D., *Advance of mechanically controllable break junction for molecular electronics.* Topics in Current Chemistry **375** (2017), 10.1007/s41061-017-0149-0.

[271] L. Venkataraman, J. E. Klare, C. Nuckolls, M. S. Hybertsen, and M. L. Steigerwald, *Dependence of single-molecule junction conductance on molecular conformation,* Nature **442**, 904 (2006).

[272] J. Ulrich, D. Esrail, W. Pontius, L. Venkataraman, D. Millar, and L. H. Doerrer, *Variability of conductance in molecular junctions,* The Journal of Physical Chemistry B **110**, 2462 (2006).

[273] M. Lemmer, M. S. Inkpen, K. Kornysheva, N. J. Long, and T. Albrecht, *Unsupervised vector-based classification of single-molecule charge transport data,* Nature Communications **7**, 12922 (2016).

[274] J. M. Hamill, X. Zhao, G. Mészáros, M. Bryce, and M. Arenz, *Fast data sorting with modified principal component analysis to distinguish unique single molecular break junction trajectories,* Phys. Rev. Lett. **120**, 016601 (2018).

[275] A. Géron, *Hands-on machine learning with Scikit-Learn and TensorFlow: concepts, tools, and techniques to build intelligent systems* (O'Reilly Media, Inc., 2017).

[276] G. James, D. Witten, T. Hastie, and R. Tibshirani, *An introduction to statistical learning*, Vol. 112 (Springer, 2013).

[277] K. P. Lauritzen, A. Magyarkuti, Z. Balogh, A. Halbritter, and G. C. Solomon, *Classification of conductance traces with recurrent neural networks,* J. Chem. Phys. **148**, 084111 (2018).

[278] T. Albrecht, G. Slabaugh, E. Alonso, and S. M. R. Al-Arif, *Deep learning for single-molecule science,* Nanotechnology (2017).

[279] M. S. Inkpen, M. Lemmer, N. Fitzpatrick, D. C. Milan, R. J. Nichols, N. J. Long, and T. Albrecht, *New insights into single-molecule junctions using a robust, unsupervised approach to data collection and analysis,* Journal of the American Chemical Society **137**, 9971 (2015).

[280] B. Li, M. Famili, E. Pensa, I. Grace, N. J. Long, C. Lambert, T. Albrecht, and L. F. Cohen, *Cross-plane conductance through a graphene/molecular monolayer/Au sandwich,* Nanoscale **10**, 19791 (2018).

[281] B. H. Wu, J. A. Ivie, T. K. Johnson, and O. L. Monti, *Uncovering hierarchical data structure in single molecule transport,* The Journal of Chemical Physics **146**, 092321 (2017).

[282] D. Arthur and S. Vassilvitskii, *K-means++: The advantages of careful seeding,* in *Proceedings of the eighteenth annual ACM-SIAM symposium on Discrete algorithms* (Society for Industrial and Applied Mathematics, 2007) pp. 1027–1035.

[283] J. S. Martin Ester, Hans-Peter Kriegel and X. Xu, *A density-based algorithm for discovering clusters in large spatial databases with noise,* in *ACM DL Logo Preview Check out a preview of the next ACM DL Proceedings of the Second International Conference on Knowledge Discovery and Data Mining* (American Association for Artificial Intelligence, 1996) pp. 226–231.

[284] R. J. Campello, D. Moulavi, and J. Sander, *Density-based clustering based on hierarchical density estimates,* in *Pacific-Asia conference on knowledge discovery and data mining* (Springer, 2013) pp. 160–172.

[285] M. E. Tipping and C. M. Bishop, *Mixtures of probabilistic principal component analyzers,* Neural computation **11**, 443 (1999).

[286] D. E. Gustafson and W. C. Kessel, *Fuzzy clustering with a fuzzy covariance matrix,* in *Decision and Control including the 17th Symposium on Adaptive Processes, 1978 IEEE Conference on* (IEEE, 1979) pp. 761–766.

[287] Y. P. Raykov, A. Boukouvalas, F. Baig, and M. A. Little, *What to do when K-means clustering fails: a simple yet principled alternative algorithm,* PloS one **11**, e0162259 (2016).

ACKNOWLEDGEMENTS

These last four years have been a remarkable journey. I take great pride in having met and worked with wonderful people and brilliant scientists. As a result, I learnt a lot and I think I have grown both as a scientist and as a person. There were many happy moments but also tough times, and I had the privilege of going through them with the support of many people that I would like to acknowledge in this section.

I want to start by thanking my promotor and supervisor, *Herre van der Zant*. You have always been there for me when I needed your advice and directions. And not only did you provide fast feedback (if it was not fast enough it was always because of me), you always kept my personal happiness in great regard and were very effective in motivating me when I was losing hope. I learnt a lot from you and both on the professional and personal side. I admire how fast and efficient you are in your work, which is something that I still struggle to imitate, and you know how to enjoy life outside of it. I want to thank you from the bottom of my heart for being my supervisor and I wish you all the best.

I also want to thank *Marcel Mayor* for being my second promotor. The projects we collaborated on have always been very exciting and generated interesting discussions from which I learnt a lot. I had heard some rumors before meeting her, but nothing could have prepared me for the Diana experience. One day you arrived in the lab and immediately started directing works with your captivating energy as if you were back home. I wish you all the best in your pursuit of an European comeback. I am grateful to *Nicolás Agraıt* for welcoming me in his lab in Madrid and for giving me helpful tips (pun intended) about measurements and about swimming. I am very happy that you accepted to be part of the committee. *Peter Steeneken*, I enjoyed every interaction we had and I always appreciated your positive spirit. I am glad you accepted to be a member of my committee. *Jos Thijssen*, thank you for being part of my committee and for the collaboration on the solvents project. *Tim Albrecth* and *Yaroslav Blanter*, thank you for being part of my committee.

Next, I want to thank *Mickael Perrin* and *Riccardo Frisenda* for patiently introducing me in the world of molecular electronics. Riccardo, thank you for teaching me the ropes of the work, for your precious advice and for easying my adjustment to the new environment. I think you are an amazing scientist and I wish you all the best for your carreer, which I am sure will be great. Mickael, I really appreciated the time we spent together in and outside the lab. I admire your motivation, your efficency, work-life balance and your seemingly unbreakable good spirit. You are part of many of my good memories from these four years and I hope we will make new ones in the future (I have not given up on the idea of that multi-pitch climb!). And finally, thank you very much for being part of my defence committee. *Chris Bruot* was another very important person in the lab for me. Although his stay was short, we became quite close by spending a lot of time together in the clean room and in the climbing gym. I am going to keep my promise of visiting you, please wait for me and

show me the best sides of the States.

Once all the more senior members were gone, I was left in the lab with *Ignacio Olavarria*, with whom I shared crazy discussions, crazier runs, conferences, dinners, games and long office days, always joined together by a 'twisted kind of humor', as you nicely put it. I was honoured to be your paranymph and I hope I will visit you soon in Chile. *Sabina Caneva* is the first Italian with whom I have hardly ever spoken Italian. Thank you for always being supportive and helping me out in my first steps in Blender. I enjoyed spending time with you in and out of the university and you know very well I approve of your great passion for chocolate. *Damien Cabosart* introduced the lab to the wonders of machine learning. I wish you great success in your future endeavours.

Maria El Abbassi, despite the annoying music in the lab, you are a wonderful addition to the atmosphere of the lab, always organizing events to bring people together. On top of that, you are an amazing scientists, extremely hard working and with unlimited knowledge and thirst for discovery. I am incredibly happy to have witnessed the end of your bureaucratic odyssey towards Baguetteship. Merci pour tes aide et tes soutien. *Alfredo Rates*, you are incredibly kind and I am sure your wonderful approach to everything will bring you a lot of happiness and satisfcation. I wish you all the best in the next big steps in your life! *Chunwei Hsu*, it was a pleasure to work with you and to be your supervisor. You are a gifted scientist and I am sure you can accomplish amazing results. Thank you for all the time we spent in the lab in Delft and in Madrid, and for accomodating my attempts to divert the discussion to videogames. *Luca Ornago*, you have the heavy responsibility of carrying the Italian flag in the lab, but I am sure with your motivation you will be able to do great things! Overall, I leave the (El Abbassi?) lab in very capable hands and I am sure you will prosper in the next years.

I would also like to thank the students I had the chance to supervise. *Matthijs Doelman*, I enjoyed working with you and spending time with you in the lab. You were my only chance to learn Dutch, no wonder I lost it all after you left. I wish you all the best. *Luuk de Niet*, keep going to great concerts and organize climbing events! Best of luck with your new job. *Beatrice ~~Vollmer~~ Bednarz*, I hope we will be able to do some of the things I promised you once you are back from Taiwan. Please always preserve your positive energy and constant smile, it's a joy to be around you! And the Chilean double agents *Pablo Cabello* (I will always remember the time in Paris, especially the rush through the Louvre to win the bet with Maria!) and *Jacqueline Labra-Muñoz*.

I want to acknowledge the rest of the group for creating a nice atmosphere. *Rocco Gaudeni* for his endless preaching and romanticism. I thoroughly enjoyed working with you and getting to know you better. Thank you for your support an best of luck in your future to you and Katja. I am sure you will be a great dad! *Max Koole* for showing me that Dutch people regularly biking long distances in the rain are not just a myth. *Anastasia Holovchenko* for your support and for trying to get me to start fencing. *Alexandra Fursina* for your kindness. *Enrique Burzuri*, my first office mate. *Julien Dugay*, for the discussions on veganism. *Joshua Island*, for how you told your crazy stories with the quietest smile. *Nandini Muthusubramanian*, for helping me adjust to the PhD life. *Joeri de Bruijckere*, for persevering and prospering despite the incredible amount of bad luck with the fridge. I wish you a stellar carreer in research. *Pascal Gehring*, for your neverending flow of crazy ideas. *Benjamin Lehner*, your determination is incredibly inspiring. I wish you all the best for the

future. *Vera Janssen*, best of luck navigating to the end of your PhD! *Michele Buscema*, for being around even after your graduation.

I also need to mention some of the people who enabled me to do any measurements at all by synthesizing the molecules that are the protagonist of this thesis. Through our collaboration, these people become more than colleagues and for this reason I want to mention them now. *Cansel Temiz* is the Potion Mistress from Delft who was always incredibly kind and helpful with any chemistry-related question I had. *Kevin Weiland* and *Patrick Zwick* are the two crazy scientists from Basel. I thoroughly enjoyed working with you and your visits to Delft. *Cunlan Guo*, you are an amazing and passionate worker, I wish you the best in your career.

I consider myself lucky to have started my PhD when there was still MED, so that I could experience amazing events like the beach volleyball matches, the paintball or the boat trip. Then there was the transition to QN, and I want to take this opportunity to congratulate and wish the best for their future research to *Sander Otte*, *Gary Steele*, *Simon Gröblacher*, *Andrea Caviglia*, *Peter Steeneken*, *Kobus Kuipers*, *Sonja Conesa-Boj* and *Toeno van der Sar*. Even after the end of MED, many wonderful people walked the corridors and labs of QN and deserve to be mentioned here. *Dejan Davidovikj*, for our always interesting discussions, not only about games. *Ranko Toskovic*, because I love our eternal love-hate relationship. *Clemens Schäfermeier* is another person that I wish I could spend more time with. You are a brilliant scientist and a wonderful and inspiring person. I am looking forward to climbing together again soon. Despite the little time we shared, you became a dear friend and I hope we will stay in touch in the future. *Santiago Cartamil*, for your stories that kept me entairtained through countless hours. For the GrapheneX and GrapheneY projects and for the Nintendomania. Thank you for your support and advice. Best of luck to you and Gabi in your new life as parents! *Giordano Mattoni*, for being this impossible (or very sensible?) combination of genius and crazy. *Nicola Manca*, for the omnipresent banana and for introducing me to the deliciousness of the Baci di Alassio. *Igor Marinković*, for your amazing personality and for allowing me to pierce through your outer layer. *Andreas Wallucks*, for being an ever pleasant company and for climbing with me. *Richard Norte*, for your always positive attitude. *Moritz Forsch*, for your enthusiasm. *Nikos Papadopoulos* for being the master DJ. *Felix Schmidt* and *Sarwan Peiter*, for becoming Vikings with me. *Emre Mulazimoglu*, for being the sultan. *Marc Westig*, for the late night meetings your always encouraging and wise words. *Holger Thierschmann*, for being always present when things become fun. *Dima Afanasiev* and *Thierry van Tiel*, for the climbing experiences. *Eduard Lesne*, for his strong opinions generating interesting conversations. *Yildiz Gözde Sağlam*, for being with me at the summer school in Les Houches. *Filippo Alpeggiani, Lorenzo de Angelis* e *Iacopo Bertelli* for bringing the number of Italians in the department back to acceptable levels. *Luigi Maduro*, for his crazy martial artistry. I also want to remember my everlasting office mate *Behnam Mirzaei* and *Jan Girovsky* for his kidness and motivating words.

I want to remember the amazing PowPowPow trip with Mickael, Dejan, Giordano, Nicola and Max. I thoroughly enjoyed skiing with you guys. I want to reiterate my gratitude to Santiago, Rocco and Vera for the times of GrapheneX and GrapheneY. They have been a nice change of pace to the PhD life. We shared very stressful times but I am very

proud of what we achieved and that I could do this with you. I also remember fondly the trip to Courchevel for (and preceding) the Winter Retreat, and the Summer School in Les Houches, where I met amazing people like *Sasha Vrbica, Jimmy Hutasoit, Nikita Lebedev, Hannes Coners, Michal Pacholski, Pacome Armagnat, Lauriane Contamin, Corentin Bertrand, Patryk Kubiczek, Benoit Rossignol, Kristof Harms, Sonja Fischer, Xavier Bonet, Hristo Barakov and Zhenya Repin*.

I also want to express my gratitude to all the Quantum Nanoscience staff and in particular to *Heleen Woldhuis, Etty van der Leij, Maria Roodenburg-van Dijk, Marije Boonstra, Dorine Verhoeven, and Ronald Bode*. Special thanks go to *Tino Kool* for being part of the group not only during office hours. I would also like to thank the Kavli Nanolab staff, *Frank Dirne, Marc Zuiddam, Eugene Straver, Ewan Hendriks, Charles de Boer, Marco van der Krogt, Arnold van Run, van Langen-Suurling, Roel Mattern, Hozanna Miro, Pauline Stevic*, and *Marco Bakker* for their help and for ensuring the smooth operation of the cleanroom.

Finally, I want to thank the people that helped me the most on a personal level and whose support allowed me to get to this point. *João Moura*, I cannot thank enough the luck that made us share an office, because it started one of the most cherished friendships of my life. I want to thank you with all my heart for your constant and infallible support. We have done this whole journey together, so I never had a doubt that I wanted you to be next to me when this is over. *Dirk Groenendijk*, between everything we've gone through together, you have become one of my dearest friends. You have helped me countless times in a myriad of different ways and for this I want to thank you from the bottom of my heart. I commend you for joining me in my crazy training programs and runs. Thank you for being my paranymph. *Mafalda Monteiro*, you are an inspiration for your passion and determination. You work harder than anyone to reach your goals and I always admired you for this. *Flávio Fonseca*, thank you for your always kind and comforting words. *Alice Borghese* e *Irene Battisti*, grazie con tutto il cuore per il vostro sostegno. Anche se non ci siamo visti tanto quanto avrei sperato, non mi siete mai state lontane. *Johannes Jobst*, you are amazingly talented and I admire you in many ways. Thank you for your always eye-opening advice and for the many joyful moments we shared. *Sander Blok*, kabeltrein, kokosroomijs, don't touch the alien... BOOOM!!! *Gesa Welker*, thank you for always being there for me whenever I needed to talk. Your advice and comfort has always been extremely helpful. *Elisa Marchesi*, grazie di cuore per tutte le volte in cui hai sopportato i miei lamenti e per i tuoi preziosi consigli. Se ti ascoltassi di più, sarei sicuramente una persona più serena. Grazie per tutta la consulenza gratuita che mi hai fatto per questioni di design. Spero d'ora in poi di mandarti più spesso foto di viaggi o ricette ben riuscite. *Zhenya Cheipesh*, thank you for your neverending support and encouraging words, they always mean a lot even if I don't show it.

Vorrei cogliere l'occasione per ringraziare tutti i miei compagni di università, dato che la storia del mio dottorato comincia proprio da lì. I cinque anni a Padova sono stati fra i più belli della mia vita e questo è solo merito vostro, *Massimiliano Smania, Carlo Rigoni, Sonia Vigolo, Luca Costantin, Carlo Montevecchi, Damiano Verardo, Stefano Vecchio, Alessando Ciriali, Alessio Boletti, Beatrice Foffani, Giulia Rigoni, Emanuele Michielin, Andrea Bertolucci, Alberto Cappellaro, ~~Alessandro~~ Mimo, Sofia Cristofaro, Mattia Maren-*

da, Marina Fico. Nonostante il tempo o la distanza, quando ci ritroviamo sembra che non sia passato un giorno dall'ultima volta. Mi auguro che sia così ancora per molti anni a venire.

Per concludere vorrei ringraziare la mia famiglia. Grazie ai miei genitori, perché mi avete sempre sostenuto e incoraggiato nelle mie scelte lasciandomi il massimo della libertà. Grazie ai miei nonni, perché non c'è cosa più bella di sapere che i propri nonni sono orgogliosi di te. E voi non me lo avete mai fatto dubitare. Grazie all'Anna, perché anche se non ci sentiamo spesso sei sempre una persona importante per me. Grazie al Marco, per i tuoi consigli sempre puntuali e per la tua infinita saggezza. Grazie ad Andrea e Corinna, perché mi aiutate sempre incondizionatamente. Grazie a tutti gli zii e le zie, perché immancabilmente mi fate festa ogni volta che torno a casa, anche se torno così di rado. Vi voglio bene.

I have most certainly not given justice to all the gratitude that I feel for everyone listed here and I surely forgot someone very important. For this I apologize and I hope that I will compensate with my actions rather than through my words.
To all of you, thank you.

Curriculum Vitæ

Davide Stefani

15-05-1990 Born in Vicenza, Italy.

Education

2004–2009 High School
Liceo Scientifico G.B. Quadri
Vicenza, Italy.

2009–2012 Bachelor of science in Physics
Università degli Studi di Padova
Padova, Italy
Thesis: Motion of a drop driven by a vibrating substrate
Supervisor: Prof. G. Mistura

2012–2014 Master of science in Physics
Università degli Studi di Padova
Padova, Italy
Thesis: Growth and characterization of nanostructured Au doped Zinc oxide thin films by RF Magnetron Co-Sputtering
Supervisors: Prof. G. Mattei & Prof. L. Soriano de Arpe

2015–2019 PhD in Applied Physics
Delft University of Technology
Delft, The Netherlands
Thesis: Various aspects of quantum transport through single molecules: a mechanical break-junction study
Promotor: Prof. Dr. Ir. H. S. J. van der Zant

List of Publications

12. R. Gaudenzi, **D. Stefani**, S. J. Cartamil-Bueno, *Light-induced propulsion of graphene-on-grid sails in microgravity*, in preparation.

11. P. Zwick, **D. Stefani**, H. S. J. van der Zant, M. Mayor, *Unexpected three-fold macrocyclization of a porphyrin precursor*, in preparation.

10. **D. Stefani**, C. Guo, D. Cabosart, D. Cahen and H. S. J. van der Zant, *Importance of peptide length and composition on charge transport*, in preparation.

9. M. El Abbassi, A. Soriano, P. Zwick, **D. Stefani**, A. Prescimone, M. Mayor, H. S. J. van der Zant, D. Dulić, *Tuning of the electrical properties of porphyrin molecules by chemical design*, in preparation.

8. **D. Stefani**, N. O. Kavadias, M. Perrin, M. Doelman, E. Galán, F. C. Grozema, J. M. Thijssen, and H. S. J. van der Zant, *The influence of a water environment on single–molecule conductance*, in preparation.

7. T. Brandl, M. El Abbassi, **D. Stefani**, R. Frisenda, G. D. Harzmann, H. S. J. van der Zant and M. Mayor, *Enhanced Separation Concept (ESC): removing the functional subunit from the electrode by molecular design*, European Journal of Organic Chemistry, Submitted (2019).

6. D. Cabosart, M. El Abbassi, **D. Stefani**, R. Frisenda, M. Calame, H. S. J. van der Zant and M. L. Perrin, *A reference-free clustering method for the analysis of molecular break-junction measurements*, Applied Physics Letters, Accepted (2019).

5. S. Caneva, P. Gehring, V. M. García-Suárez, A. García-Fuente, **D. Stefani**, I. J. Olavarria-Contreras, J. Ferrer, C. Dekker, H. S. J. van der Zant, *Mechanically Controlled Quantum Interference in Graphene Break Junctions*, Nature Nanotechnology **13**, 1126–1131 (2018).

4. **D. Stefani**, K. Weiland, M. Skripnik, C. Hsu, M. L. Perrin, M. Mayor, F. Pauly, H. S. J. van der Zant, *Large Conductance Variations in a Mechanosensitive Single-Molecule Junction*, Nano Letters **18** (9), 5981–5988 (2018).

3. **D. Stefani**, M. L. Perrin, C. A. Gutierréz-Cerron, A. Aragonès, J. Labra-Muñoz, R. Carrasco, Y. Matsushita, Z. Futera, J. Labuta, T. Ngo, K. Ariga, I. Díez-Pérez, D. Dulić, H. S. J. van der Zant, J. P. Hill, *Mechanical Tuning of Through-Molecule Conductance in a Conjugated Calix[4]pyrrole*, ChemistrySelect **3** (23), 6473–6478 (2018).

2. R. Frisenda, **D. Stefani**, H. S. J. van der Zant, *Quantum transport through a single conjugated rigid molecule, a mechanical break junction study*, Accounts of Chemical Research **51** (6), 1359–1367 (2018).

1. **D. Stefani**, C. A. Gutierréz-Cerron, D. Aravena, J. Labra-Muñoz, C. Suarez, S. Liu, M. Soler, L. Echegoyen, H. S.J. van der Zant, and D. Dulić, *Charge Transport through a Single Molecule of* trans-*1*-bis- *Diazofluorene [60]fullerene*, Chemistry of Materials **29** (17), 7305–7312 (2017).